Efficient Measurement Techniques in Reverberation Chamber

by

Zhihao Tian

Submitted in accordance with the requirements for the award of the degree of Doctor of Philosophy of the University *of* Liverpool

September 2017

Copyright

To my family: Thank you for all of your efforts and for your support.

Table of Contents

Copyright ..... *i*

Table of Contents ..... *iii*

Acronyms and Abbreviations ..... *vii*

Acknowledgements ..... *ix*

List of Publications ..... *x*

Abstract ..... *xiv*

Chapter 1: Introduction 1

1.1 Background 1

1.1.1 Anechoic Chamber 1

1.1.2 TEM Cells 2

1.1.3 Reverberation Chamber 4

1.2 Motivation and Objective 6

1.3 Organisation of the Thesis 7

1.4 References 9

Chapter 2: Theories of Reverberation Chamber 12

2.1 Introduction 12

2.2 Deterministic Theory 13

2.2.1 Resonant Modes 13

2.2.2 Modes inside a Lossy Cavity 20

2.2.3 Lowest Usable Frequency 22

2.2.4 Number of Cavity Modes 23

2.2.5 Green's Function 26

2.3 Stirring Techniques 29

2.3.1 Mechanical Stirring 30

2.3.2 Frequency Stirring 31

2.3.3 Source Stirring 32

2.4 Statistical Theory 33

2.4.1 Plane-wave Integration Model 33

2.4.2 Statistical Properties of Fields 36

2.4.3 Probability Density Functions for the Fields 38

2.4.4 Loss Mechanism and *Q* Factor 41

2.4.5 Chamber Decay Time 43

2.4.6 Stirred and Unstirred Power 45

2.4.7 Enhanced Backscatter Effect 51

2.5 Summary 54

2.6 References 54

Chapter 3: Efficient Averaged Absorption Cross Section Measurement 61

3.1 Introduction 61

3.2 Theory 62

3.2.1 Frequency Domain 63

3.2.2 Time Domain 65

3.3 Measurement 66

3.4 Convergence Property 74

3.5 ACS Measurement without Calibration 78

3.6 Discussions and Conclusion 83

3.7 References 85

Chapter 4: Volume Measurement Using Averaged Absorption Cross Section .. 90

4.1 Introduction 90

4.2 Theory 91

4.3 Measurement 92

4.4 Discussions and Conclusion 105

4.5 References 105

Chapter 5: Simplified Shielding Effectiveness Measurement of Small Cavity 109

5.1 Introduction 109

5.2 Theory 110

5.2.1 Frequency Domain 110

5.2.2 Time Domain 112

5.3 Measurement 114

5.4 Convergence Behaviour 122

5.5 Discussions and Conclusion 128

5.6 References 129

Chapter 6: Antenna Array Efficiency Measurement 133

6.1 Introduction 133

6.2 The Problem 134

6.2.1 Single Antenna Case 134

6.2.2 Antenna Array Case 141

6.3 Improved Method 142

6.4 Measurement Uncertainty 150

6.5 Discussions and Conclusion 153

6.6 References 154

Chapter 7: Conclusions and Future Work 157

References 160

Appendix A. Vector and Dyadic Analysis 162

Appendix B. Probability Density Function 165

References 166

Acronyms and Abbreviations

AC	Anechoic Chamber
ACS	Absorption Cross Section
AUT	Antenna under Test
CST	Computer Simulation Technology
DC	Direct Current
EM	Electromagnetic
EMC	Electromagnetic Compatibility
EUT	Equipment under Test
FD	Frequency Domain
IEEE	Institute of Electrical and Electronics Engineers
IFT	Inverse Fourier Transform
IFFT	Inverse Fast Fourier Transform
LoS	Line-of-Sight
LPDA	Log Periodic Dipole Antenna
LUF	Lowest Usable Frequency
NLoS	Non-Line-of-Sight
OUT	Object under Test
1D	One Dimensional
PDF	Probability Density Function
PDP	Power Delay Profile

PEC	Perfect Electrical Conductor
RAM	Radio Absorbing Material
RC	Reverberation Chamber
RMS	Root Mean Square
RMSE	Root Mean Square Error
SAR	Specific Absorption Rate
SE	Shielding Effectiveness
SI	International System of Units
3D	Three Dimensional
TD	Time Domain
TE	Transverse Electric
TEM	Transverse Electromagnetic
TM	Transverse Magnetic
VNA	Vector Network Analyser
VSWR	Voltage Standing Wave Ratio

Acknowledgements

First and foremost, I would like to express my sincere gratitude to my supervisors Professor Yi Huang and Professor Yaochun Shen. I thank you both for your invaluable guidance and persistent support for my research. Without your help, this dissertation would not have been possible. I would also like to thank Dr. Qian Xu. I learned a lot from him during our many discussions about reverberation chamber measurement and analysis techniques. I feel lucky to be working in a research group that stimulates original ideas and insightful thoughts. I really enjoy the intellectual delight in our group. The beneficial discussions and selfless help from my colleagues are much appreciated.

This work would not be completed without the financial support of CSC (China Scholarship Council). I would like to acknowledge the important role of them.

Finally, I would like to thank my research lab colleagues and my friends: Prof. Chenjiang Guo, Dr. Stephen Boyes, Dr. Shufeng Sun, Dr. Saqer Alja'afreh, Dr. Gaosheng Li, Dr. Neda Khiabani, Dr. Lei Xing, Alieldin Ahmed, Dr. Ping Cao, Dr. Jingwei Zhang, Saidatul Izyanie, Dr. Sheng Yuan, Chaoyun Song, Manoj Stanley, Zhouxiang Fei, Dr. Muayad Kod, Dr. Rula Alrawashdeh, Muaad Hussein, Aznida Abu Bakar Sajak, Dr. Amir Kotb, Abed Pour Sohrab, Anqi Chen, Yuan Zhuang, Umniyyah Ulfa, Yukun Zhao, Shuang Li, Bahaa Al-Juboori, Chen Xu, Wenzhang Zhang, Sumi Joseph, Tianyuan Jia, Dr. Tian-Hong Loh, and Dr. Chong Li. I have enjoyed working with you all and I appreciate the help and support that you gave me.

List of Publications

Journal Publications

[1] **Z. Tian**, Y. Huang, Q. Xu, and G. Li, "A Rapid Method for Measuring the Volume of a Large Cavity Using Averaged Absorption Cross Section," *IEEE Access*, 2017, DOI: 10.1109/ACCESS.2017.2745698.

[2] **Z. Tian**, Y. Huang, and Q. Xu, "Efficient Methods of Measuring Shielding Effectiveness of Electrically Large Enclosures Using Nested Reverberation Chambers with Only Two Antennas," *IEEE Transactions on Electromagnetic Compatibility*, vol. 59, no. 6, pp. 1872-1879, December 2017.

[3] **Z. Tian**, Y. Huang, and Q. Xu, "An Improved Method for Efficiency Measurement of All-Excited Antenna Array in Reverberation Chamber Using Power Divider," *IEEE Transactions on Antennas and Propagation*, vol. 65, no. 6, pp. 3005-3013, June 2017.

[4] **Z. Tian**, Y. Huang, Y. Shen, and Q. Xu, "Efficient and Accurate Measurement of Absorption Cross Section of a Lossy Object in Reverberation Chamber Using Two One-Antenna Methods," *IEEE Transactions on Electromagnetic Compatibility*, vol. 58, no. 3, pp. 686-693, June 2016.

[5] M. Stanley, Y, Huang, H. Wang, Z. Hai, **Z. Tian**, and Q. Xu, "A Novel Reconfigurable Metal Rim Integrated Open Slot Antenna for Octa-band Smartphone Applications", *IEEE Transactions on Antennas and Propagation*, vol. 65, no. 7, pp. 3352-3363, July 2017.

[6] C. Li, T. H. Loh, **Z. Tian**, Q. Xu, and Y. Huang, "Evaluation of Chamber Effects on Antenna Efficiency Measurements Using Non-reference Antenna Methods in Two Reverberation Chambers," *IET Microwaves, Antennas & Propagation*, June 2017, DOI: 10.1049/iet-map.2015.0838.

[7] Q. Xu, Y. Huang, L. Xing, C. Song, **Z. Tian**, S. Alja'afreh, and M. Stanley, "3D Antenna Radiation Pattern Reconstruction in a Reverberation Chamber Using Spherical Wave Decomposition," *IEEE Transactions on Antennas and Propagation*, vol. 65, no. 4, pp. 1728-1739, April 2017.

[8] Q. Xu, Y. Huang, L. Xing, **Z. Tian**, J. Zhou, A. Chen, and Y. Zhuang, "Average Absorption Coefficient Measurement of Arbitrarily Shaped Electrically Large Objects in a Reverberation Chamber," *IEEE Transactions on Electromagnetic Compatibility*, vol. 58, no. 6, pp. 1776-1779, December 2016.

[9] Q. Xu, Y. Huang, L. Xing, **Z. Tian**, M. Stanley, and S. Yuan, "B-scan in a reverberation chamber," *IEEE Transactions on Antennas and Propagation*, vol. 64, no. 5, pp. 1740-1750, May 2016.

[10] Q. Xu, Y. Huang, L. Xing, **Z. Tian**, C. Song, and M. Stanley, "The Limit of the Total Scattering Cross Section of Electrically Large Stirrers in a Reverberation Chamber," *IEEE Transactions on Electromagnetic Compatibility*, vol. 58, no. 2, pp. 623-626, April 2016.

[11] Q. Xu, Y. Huang, L. Xing, and **Z. Tian**, "Extract the Decay Constant of a Reverberation Chamber Without Satisfying Nyquist Criterion," *IEEE Microwave and Wireless Components Letters*, vol. 26, no. 3, pp. 153-155, March 2016.

[12] Q. Xu, Y. Huang, S. Yuan, L. Xing, and **Z. Tian**, "Two alternative methods to measure the radiated emission in a reverberation chamber," *International Journal of Antennas and Propagation*, vol. 2016, Article ID: 5291072, 7 pages, February 2016.

[13] Q. Xu, Y. Huang, X. Zhu, L. Xing, **Z. Tian**, and C. Song, "A Modified Two-Antenna Method to Measure the Radiation Efficiency of Antennas in a Reverberation Chamber," *IEEE Antennas and Wireless Propagation Letters*, vol. 15, pp. 336-339, February 2016.

[14] Q. Xu, Y. Huang, X. Zhu, L. Xing, **Z. Tian**, and C. Song, "Shielding effectiveness measurement of an electrically large enclosure using one antenna," *IEEE Transactions on Electromagnetic Compatibility*, vol. 57, no. 6, pp. 1466-1471, December 2015.

[15] Q. Xu, Y. Huang, L. Xing, **Z. Tian**, Z. Fei, and L. Zheng, "A fast method to measure the volume of a large cavity," *IEEE Access*, vol. 3, pp. 1555-1561, September 2015.

[16] Q. Xu, Y. Huang, X. Zhu, S. Alja'afreh, L. Xing, and **Z. Tian**, "Diversity gain measurement in a reverberation chamber without extra antennas," *IEEE Antennas and Wireless Propagation Letters*, vol. 14, pp. 1666-1669, August 2015.

Conference Publications

[1] **Z. Tian**, Y. Huang, and Q. Xu, "Efficient Measurement Techniques on OTA Test in Reverberation Chamber", 2017 IEEE AP-S Symposium on Antennas and Propagation and USNC-URSI Radio Science Meeting, San Diego, U.S., 2017.

[2] **Z. Tian**, Y. Huang, and Q. Xu, "Enhanced Backscatter Coefficient Measurement at High Frequencies in Reverberation Chamber", International Workshop on Electromagnetics (iWEM), London, U.K., 2017.

[3] **Z. Tian**, Y. Huang, and Q. Xu, "Measurement of Absorption Cross Section of a Lossy Object in Reverberation Chamber without the Need for Calibration", Loughborough Antennas and Propagation Conference (LAPC), Loughborough, U.K., 2016.

[4] **Z. Tian**, Y. Huang, and Q. Xu, "Stirring effectiveness characterization based on Doppler spread in a reverberation chamber," European Conference on Antennas and Propagation (EuCAP), Davos, Switzerland, 2016.

[5] **Z. Tian**, Y. Huang, and Q. Xu, "A further investigation of the source stirred chamber method for antenna efficiency measurements," 8th UK, Europe, China Conference on Millimetre Waves and Terahertz Technologies (UCMMT), Cardiff, U.K., 2015.

[6] **Z. Tian**, Y. Huang, Y. Shen, and Q. Xu, "An electrical stirring method for a reverberation chamber," Antennas and Propagation Conference (LAPC), U.K., Loughborough, 2014.

[7] Q. Xu, Y. Huang, Y. Zhao, L. Xing, **Z. Tian**, and T. H. Loh, "Investigation of Bandpass Filters in the Time Domain Signal Analysis of Reverberation Chamber", 2017 URSI General Assembly and Scientific Symposium (GASS), Montreal, Canada, 2017.

[8] C. Li, T. Loh, **Z. Tian**, Q. Xu, and Y. Huang, "A comparison of antenna efficiency measurements performed in two reverberation chambers using non-reference antenna methods," Loughborough Antennas and Propagation Conference (LAPC), Loughborough, U.K., 2015. (Best Non-student Paper Award)

[9] Q. Xu, Y. Huang, X. Zhu, L. Xing, and **Z. Tian**, "Antenna radiation efficiency measurement in a reverberation chamber without the need for calibration," IEEE AP-S Symposium on Antennas and Propagation (APS), Vancouver, Canada, 2015.

[10] Q. Xu, Y. Huang, X. Zhu, L. Xing, and **Z. Tian**, "Permittivity measurement of spherical objects using a reverberation chamber," Loughborough Antennas and Propagation Conference (LAPC), Loughborough, U.K., 2014. (Best Student Paper Award)

Abstract

The rapid expansion of electronic industry calls for effective and efficient electromagnetic (EM) measurements, including the characterization of devices under test (DUT), such as antennas or wireless devices, and the electromagnetic compatibility (EMC) testing.

In the real world, EM measurements can be influenced by a number of uncontrollable factors which will afflict the measurements. These factors make the measurements very difficult especially when the measurements require high precision and/or low power relative to the background noise. To conduct EM measurements accurately, many different facilities/environments have been developed, including anechoic chambers (ACs), transverse electromagnetic (TEM) Cells, and reverberation chambers (RCs). These three environments have different characteristics.

Over the past several decades, RCs have been enjoying growing popularity as a promising facility for the characterization of wireless devices and for the EMC testing. The RC measurement method exhibits much competitive superiority over the AC method and TEM Cell method, such as low cost, enhanced test repeatability, a more realistic test environment, and easily achieved high-field environment. The application of the RC for performing EMC testing was first proposed by H. A. Mendes in 1968. In the recent IEC 61000-4-21 standard, the importance of EMC testing using RCs as an alternative measurement technique has been recognized.

To make the RC well stirred, a large number of independent samples (stirrer positions) are required. Consequently, the measurement time is usually long (typically several hours), which has greatly restricted the engineering applications of the RC measurement techniques.

The purpose of this thesis is to present our studies on improving the measurement efficiency of RCs in recent years, including the efficient measurement of the averaged absorption cross section (ACS) with only one antenna, the rapid volume measurement method using the averaged ACS, the simplified shielding effectiveness

(SE) measurement using the nested RC with two antennas, and the improved antenna array efficiency measurement in an RC.

For ACS measurement, the proposed one-antenna methods in both the frequency domain and the time domain are presented. The measurement setup is greatly simplified and the measurement time is significantly shortened. The efficient measurement of the ACS can be used to obtain the volume of a chamber, which leads to the rapid volume measurement method. For the SE measurement of electrically large enclosures using a nested RC, four improved measurement methods are proposed. Both the frequency-domain and time-domain methods are studied. The proposed methods require only two antennas and provide efficient measurement of SE without losing the accuracy. Finally, the accurate array efficiency measurement method in an RC using a power divider is presented. A power divider is used to excite the feeding ports of the array elements simultaneously. Thus, the efficiency measurement of the entire array can be effectively treated in a manner similar to a single port antenna, which would simplify the measurement procedure and reduce the overall measurement time. By introducing proper attenuators between the array elements and the power divider to alleviate the effect of the reflected power from the array to the insertion loss of the power divider, the array efficiency can be measured accurately even when the elements of the array are not well-matched with the power divider. The proposed method is advantageous especially for wideband antenna arrays where good impedance matching of array elements is difficult to maintain.

In this thesis, it is shown that our proposed methods have greatly improved the RC measurement efficiency and simplified the measurement setup at the same time. These contributions could promote the industrial application of RCs.

Chapter 1: Introduction

1.1 Background

With the blooming electronic industry, electromagnetic (EM) measurements are becoming more and more important, including the characterization of devices under test (DUT), such as antennas or wireless devices, and the electromagnetic compatibility (EMC) testing. Real world EM measurements can be easily affected by the surroundings where a number of uncontrollable factors exist. The surroundings will afflict the measurements. Consequently, field experiments can be difficult to perform, especially if the measurements require high precision and/or low power relative to the background noise [1]. Nevertheless, for the EM characterization of a DUT, to determine if the DUT can operate correctly in the environment it is intended for, field experiments are essential. In practice, these tests are performed after the DUT has been fully characterized under idealized environments which are close to analytic or numerical models. For EMC testing, its purpose is to keep all electronic products not disturbing the proper operation of the other products and inversely withstanding EM radiation emitted from surrounding devices [1] – [2]. An important aspect of a successful electronic product development is therefore the efficient and effective EMC testing [1].

Over the past decades, to conduct EM measurements accurately, many different facilities have been developed, including anechoic chambers (ACs), transverse electromagnetic (TEM) Cells, and reverberation chambers (RCs). Each of these three facilities creates an idealized environment that allows measurements to be compared with various analytic or numerical models.

1.1.1 Anechoic Chamber

An AC is a room lined with radio absorbing materials (RAMs) on the walls, floor, and ceiling – non-reflecting boundaries are created [3] – [4]. EM waves are allowed to propagate away from the source as if they were in free space. Thus, all outdoor EM measurements can be conducted inside an indoor environment which is not subject to any interference [4]. As such,

ACs are very suitable for characterizing quantities as a function of angles, such as antennas and wireless devices radiation patterns. In addition, measurements in ACs can be directly compared with models assuming no boundary reflections, as is typically done for antennas [5]. The 3D model of an AC is shown in Figure 1.1(a) and a typical AC measurement is shown in Figure 1.1(b). However, the expensive RAMs are often prohibitive for potential users [4]. In addition, during the measurement, the DUT needs to be mounted on a positioner to be reoriented which limits the size and the form factor of the test objects [5].

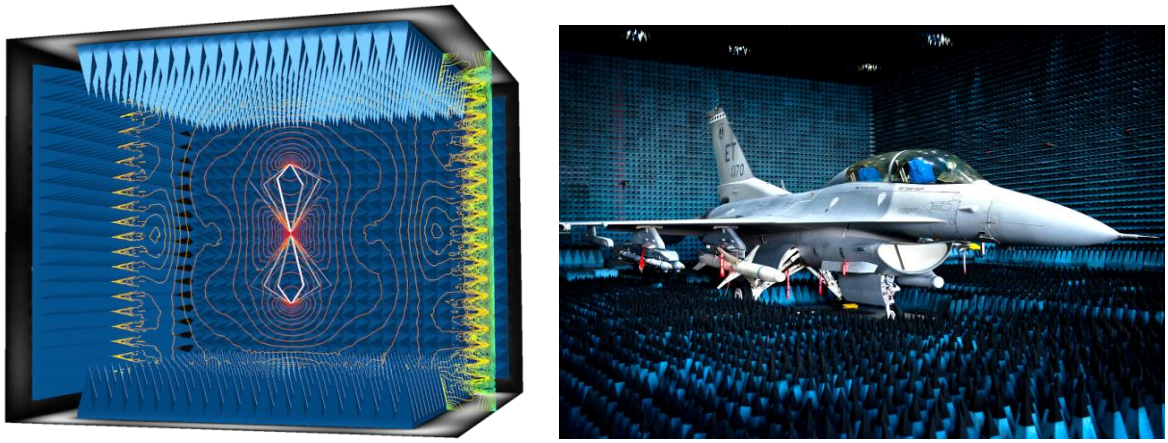

(a) **(b)**

Figure 1.1 Anechoic chamber (a) 3D model [6], (b) flight test in the anechoic chamber [7].

1.1.2 TEM Cells

TEM Cells are essentially large transmission lines used for establishing standard EM fields in a shielded environment. The cell consists of a section of rectangular coaxial transmission line tapered at each end to adapt to standard coaxial connectors [8]. A diagram and a picture of a TEM Cell are shown in Figure 1.2(a) and (b), respectively. The waves traveling through the cell are similar to plane waves in the test area [9], thus providing a close approximation to a far-field plane propagating in free space. A TEM cell operates from DC (0 Hz) up to a cut-off frequency, determined by the dimensions of the cell. A DUT is subjected to a well-characterized (ideally uniform) field in TEM Cells, or conversely, the radiation from the DUT can couple into the TEM mode of the cell. TEM Cells can be used for emission testing of small equipment, for calibration of radio frequency (RF) probes, and for biomedical

experiments. TEM Cells are far less expensive than ACs. However, the cell also has limitations, among which is that the upper useful frequency is bound by its physical dimensions which, in turn, constrain the size of a DUT that can be tested with the cell [5]. Additionally, larger TEM Cells have lower cut-off frequencies for the higher order modes. This makes large objects test be very difficult at higher frequencies in TEM Cells.

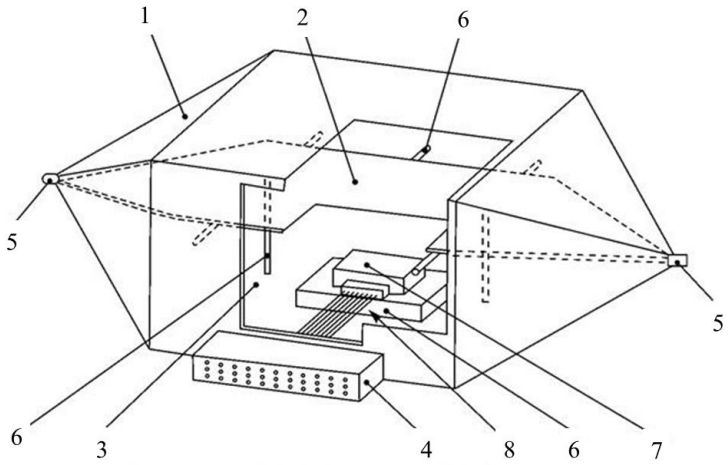

1. Outer shield 2. Septum (inner conductor) 3. Access door 4. Interface panel
5. Coaxial connector 6. Dielectric support 7. DUT 8. Input and output

(a)

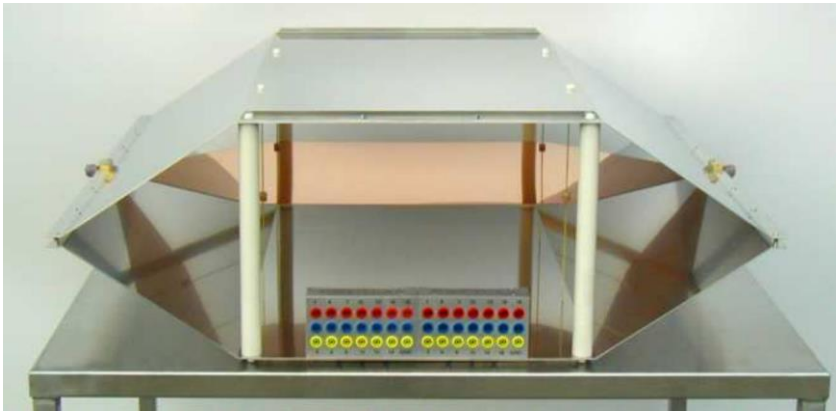

(b)

Figure 1.2 TEM Cell: (a) TEM Cell diagram [10], (b) photograph of the prototype of the open TEM Cell [11].

1.1.3 Reverberation Chamber

An RC is an electrically large, highly conductive cavity or chamber, furnished with a mechanism for altering/stirring its modes, to perform EM measurements on electronic equipment [12]. A diagram of a typical RC is shown in Figure 1.3. A photograph of a measurement setup in the RC at the University of Liverpool is shown in Figure 1.4. The RC is designed to work in an "over-mode" condition. Generally, the dimensions of an RC should be large with respect to the wavelength at the lowest usable frequency (LUF). And also, it should be large enough to accommodate the DUT, the stirrers, and the antennas used in the measurement. The RC is normally equipped with mechanical stirrers whose dimensions are

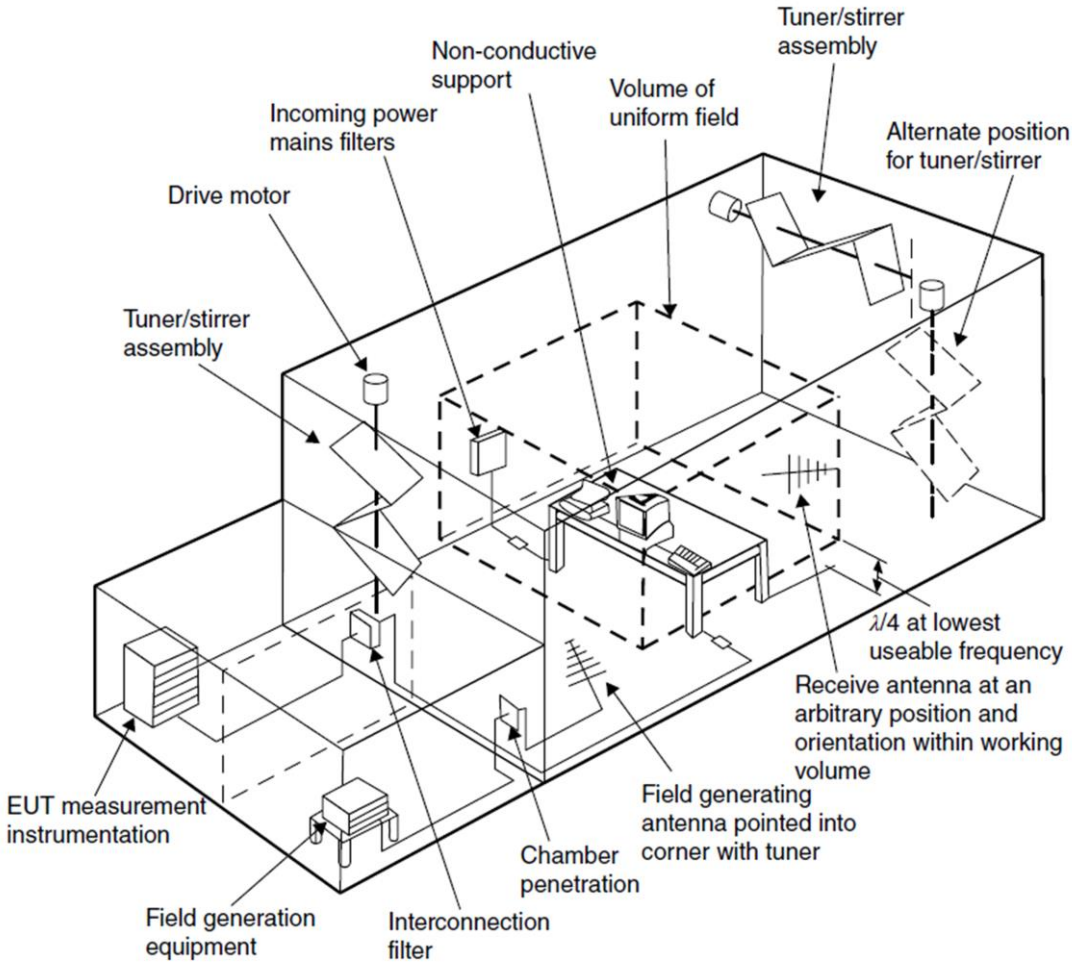

Figure 1.3 A typical RC facility [12].

Figure 1.4 Photograph of a typical measurement setup in the RC at the University of Liverpool.

significant fractions of the RC dimensions and of the wavelength at the LUF [12]. The mechanical stirrers can be rotated stepwise by a drive motor to different positions and thus the multi-mode EM environment can be stirred. After averaging over a sufficient number of stirrer positions, the resulting field is statistically uniform, isotropic (i.e., energy coming from all aspect angles), and randomly polarised (i.e., waves having all possible polarisation directions) [12].

To stir the RC well, many samples that are used to perform the statistical analysis should be collected. An effective stirring process will produce highly independent samples (low correlation). If enough statistically independent samples can be obtained, then the average of the power measured at any location within the working volume of the RC will be constant (within some standard deviation) and the RC is said to be spatially uniform [13]. Therefore, the RC measurements can be compared to models of a DUT subjected to incident EM fields from all directions and all polarization angles. Conversely, the total radiating field of a source can be measured without moving the source itself. In the RC, the mode density increases with

frequency, consequently, large-form-factor DUTs can be measured at high frequencies as long as they are relatively small compared with the RC. Although the DUT size is a factor that needs to be considered when selecting the size of the RC, generally it is the lowest operating frequency that determines how large the RC needs to be for a particular test [12]. Low-frequency measurements require big size RCs. For tens-of-MHz measurements, the dimensions of the RC should be at least several meters. However, above 1.0 GHz, an RC can be small enough to fit on a lab table [5]. RCs are generally more expensive than TEM Cells but they are much less expensive than ACs. And also, RCs have many advantages over ACs and TEM Cells, such as enhanced test repeatability, a more realistic test environment, and easily achieved high-field environment [1], [5], [12]. Therefore, RCs have been enjoying growing popularity as a promising facility for EM measurements in the past decades.

1.2 Motivation and Objective

The selection of a measurement environment is an important consideration when performing EM measurements. While ACs, TEM Cells, and RCs are often used to conduct the same types of measurements, they have different properties from one another. Because of the aforementioned competitive superiorities of RCs over ACs and TEM Cells, RCs are becoming more prevalent for EM measurements. However, a large number of stirring positions are required to well stir an RC. Therefore, the measurement in an RC is normally time-consuming (typically several hours), which has greatly restricted the industrial applications of the RC measurement techniques.

Although much research has been performed on RCs over the past decades, the research on improving the measurement efficiency is relatively lacking. The aim of this thesis is to improve the measurement efficiency of RCs, including the efficient measurement of the averaged absorption cross section with only one antenna [14], the rapid volume measurement method using the averaged absorption cross section [15], the simplified shielding effectiveness measurement using the nested RC with two antennas [16], and the improved antenna array efficiency measurement in an RC [17].

In this thesis, it is shown that our proposed methods have greatly improved the RC measurement efficiency and simplified the measurement setup at the same time. These contributions could promote the industrial application of RCs.

1.3 Organisation of the Thesis

The contents of this thesis are organized in the following manner.

Chapter 2 is to review and discuss the theories of the RC. Relevant concepts and the theoretical foundations are established in this chapter.

In Chapter 3, one-antenna methods are presented for determining the averaged absorption cross section of a lossy object in both the frequency domain and the time domain. The commonly used RC technique for determining the averaged absorption cross section of a lossy object requires two antennas and the radiation efficiency of the two antennas should be known. In this chapter, the one-antenna method in the frequency domain is first presented which requires only one antenna (with known efficiency) by making use of enhanced backscatter effect. Thus, the measurement setup is simplified. Then, the one-antenna method in the time domain is presented which needs no knowledge of the efficiency of the antenna. The experimental setup is illustrated and measurement results are presented. It seems that the measured averaged absorption cross sections by the three methods (the conventional two-antenna method, the proposed frequency-domain one-antenna method, and the proposed time-domain one-antenna method) are in good agreement. Furthermore, the robustness of the chamber decay time and the convergence speed of the three methods are investigated. It is found that the time-domain method converges much faster than the frequency-domain methods. A rapid and accurate measurement can be achieved in the time domain based on this finding by using source stirring technique. Moreover, in the time-domain approach, the RC can be replaced by a suitable electrically large conducting cavity, which will greatly reduce the hardware requirement. It is demonstrated that the time-domain method is much more efficient and its hardware requirement is much lower than the frequency-domain method.

Chapter 4 concerns a rapid and accurate measurement method for estimating the volume of a large cavity using the averaged absorption cross section. A piece of RAM with a known averaged absorption cross section is selected to aid the measurement. Using this method the cavity volume can be obtained by measuring its decay time constants with and without the RAM. The proposed method has been validated with both theory and measurement studies. It is found that the measurement can be completed rapidly with a simple measurement setup using this method, which makes it an attractive way for the cavity volume measurement. Furthermore, by using acoustic waves, the proposed method can be generalized and the cavity under test does not have to be of conducting material.

In Chapter 5, the nested RC measurement is considered. The two-antenna methods for the shielding effectiveness measurement using the nested RC in both the frequency domain and the time domain have been presented. These two-antenna methods have simplified the measurement setup and improved the measurement efficiency. It is demonstrated that the measured shielding effectiveness using the proposed two-antenna methods and the conventional three-antenna method agrees well. The time-domain method goes to convergence much faster than the frequency-domain methods. Consequently, in the time domain, fast and accurate measurement can be realized by using the source stirring technique, which will result in fast shielding effectiveness measurement in reality. Furthermore, in the time-domain approach, by replacing the RC with a suitable conducting cavity (electrically large) and using the source stirring technique, the hardware requirement will be greatly reduced. It is found that the time-domain method outperforms the frequency-domain method with much higher measurement efficiency and much lower hardware requirement.

Chapter 6 concerns the characterization of antenna arrays using an RC. An improved measurement-based method to obtain the efficiency of an all-excited antenna array in an RC is proposed. When measuring the efficiency of an antenna array in an RC, to make the array work in an “all-excited” manner, a power divider is normally employed to excite the feeding ports of the array elements simultaneously, that is, all the array elements are excited through a series of power dividers by merely a single excitation source. Thus, the efficiency measurement of the entire array can be effectively treated in a manner similar to a single port antenna, which would simplify the measurement procedure and reduce the overall measurement time. However, the introduction of the power divider will inevitably bring in

insertion loss which needs to be quantified and calibrated out. The previous method is correct if each element of the antenna array is well matched. However, if some elements of the array antenna are not well matched, a considerable error may occur. In this chapter, the power dissipated on the isolation resistance of the power divider has been minimized by introducing 10-dB attenuators between array elements and power divider ports. The attenuators would alleviate the reflection from the array antenna to the power divider and thus reduce the dissipated power on the power divider. Moreover, because the attenuation of the attenuator is known, thus we can calibrate it out accurately. It is shown that this method is effective to measure the efficiency of an antenna array especially for an antenna array that some elements of it are not well matched. It is advantageous especially for wideband antenna arrays where good impedance matching of array elements is difficult to maintain.

In Chapter 7, all the work in this thesis is summarized, the key contributions and potential problems are identified, and the future work is discussed.

1.4 References

[1] Christian Bruns, "Three-dimensional Simulation and Experimental Verification of a Reverberation Chamber," Ph.D. dissertation, Swiss Federal Institute of Technology Zurich, Zurich, Switzerland, 2005.

[2] P. A. Chatterton, and M. A. Houlden, EMC: Electromagnetic Theory to Practical Design, West Sussex, UK: Wiley, 1992.

[3] W. H. Emerson, "Electromagnetic wave absorbers and anechoic chamber through the years," *IEEE Trans. Antennas Propag.*, vol. 21, no. 4, pp. 484-490, Jul. 1973.

[4] Q. Xu, "Anechoic and Reverberation Chamber Design and Measurements," Ph.D. dissertation, Dept. of Elect. Eng. and Electr., Univ. of Liverpool, Liverpool, UK, 2015.

[5] C. R. Dunlap, "Reverberation chamber characterization using enhanced backscatter coefficient measurements," Ph.D. dissertation, Dept. of Elect., Comput. and Eng., Univ. of Colorado, Boulder, USA, 2013.

[6] [Online]. Available: https://www.comsol.jp/blogs/how-to-adapt-the-real-world-for-electromagnetics-simulations/. [Accessed: 18-Apr-2017].

[7] [Online]. Available: https://www.flickr.com/photos/usairforce/15710179866/. [Accessed: 18-Apr-2017].

[8] M. L. Crawford, "Generation of Standard EM Fields Using TEM Transmission Cells," *IEEE Trans. Electromagn. Compat.*, vol. EMC-16, no. 4, pp. 189-195, Nov. 1974.

[9] M. L. Crawford, J. L. Workman, and C. L. Thomas, "Generation of EM Susceptibility Test Fields Using a Large Absorber-Loaded TEM Cell," *IEEE Trans. Instrum. Meas.*, vol. 26, no. 3, pp. 225-230, Sept. 1977.

[10] M. T. Ma, M. Kanda, M. L. Crawford, and E. B. Larsen, "A review of electromagnetic compatibility/interference measurement methodologies," *Proc. IEEE*, vol. 73, no. 3, pp. 388-411, Mar. 1985.

[11] [Online]. Available: http://www.montena.com/fileadmin/technology_tests/documents/data_sheets/Data_sheet_TEM_cell_open.pdf. [Accessed: 18-Apr-2017].

[12] *Electromagnetic Compatibility (EMC) part 4–21: Testing and measurement techniques-Reverberation chamber test methods*, IEC 61000-4-21, 2003.

[13] D. A. Hill, Electromagnetic Fields in Cavities: Deterministic and Statistical Theories. New York, NY, USA: Wiley-IEEE Press, 2009.

[14] Z. Tian, Y. Huang, Y. Shen, and Q. Xu, "Efficient and Accurate Measurement of Absorption Cross Section of a Lossy Object in Reverberation Chamber Using Two One-Antenna Methods," *IEEE Trans. Electromagn. Compat.*, vol. 58, no. 3, pp. 686-693, Jun. 2016.

[15] Z. Tian, Y. Huang, Q. Xu, and G. Li, "A Rapid Method for Measuring the Volume of a Large Cavity Using Averaged Absorption Cross Section," *IEEE ACCESS*, in revision.

[16] Z. Tian, Y. Huang, and Q. Xu, "Efficient Methods of Measuring Shielding Effectiveness of Electrically Large Enclosures Using Nested Reverberation Chambers with Only Two Antennas," *IEEE Trans. Electromagn. Compat.*, doi: 10.1109/TEMC.2017.2696743.

[17] Z. Tian, Y. Huang, and Q. Xu, "An Improved Method for Efficiency Measurement of All-Excited Antenna Array in Reverberation Chamber Using Power Divider," *IEEE Trans. Antennas Propag.*, doi: 10.1109/TAP.2017.2684133.

Chapter 2: Theories of Reverberation Chamber

2.1 Introduction

This chapter is intended to review the concepts and introduce the theories that will later be referred to and relied upon in the following chapters, including the deterministic theory and the statistical theory.

First of all, the deterministic theory is presented in Section 2.2. The cavity discussed in Section 2.2 consists of a rectangular region (because most of the RCs are of rectangular shape) bounded by conducting walls and filled with a uniform dielectric (usually free space). After a brief discussion of fundamentals of EM theory, the general properties of cavity modes will be given. Subsequently, the detailed expressions for the modal resonant frequencies, modes number/density, and Dyadic Green's Function are given.

The deterministic theory is convenient for regularly designed cavities. The cavity details, such as shape, dimensions, and fill contents are well known. The cavity is generally of a simple/separable geometry. However, for electrically large, complex cavities those are not regularly designed, the details of the cavity geometry and loading objects are not expected to be precisely known [1]. In such cases, the deterministic mode theory is not appropriate for predicting the field properties while the statistical theory is [2] – [6]. An RC is a complex cavity and many stirrer positions are employed in RC measurements [7], therefore a statistical model is required to determine the statistics of the fields and DUT response. In this thesis, the well-known plane-wave integral representation for the electric and magnetic fields is selected [1], [8] – [9]. This model is consistent with Maxwell's equations and also includes the statistical properties expected for a well-stirred field. The statistical nature of the fields is introduced through the plane-wave coefficients that are taken to be random variables with fairly simple statistical properties [1], [9]. Because the theory uses only propagating plane waves, it is fairly easy to use to calculate the responses of DUTs.

The International System of Units (SI) is used throughout the thesis.

2.2 Deterministic Theory

An RC is a metallic room with stirrers installed inside. To better understand its basic operating principles, the RC is first abstracted to an empty, rectangular cavity resonator with walls made of perfect electrical conductor (PEC).

2.2.1 Resonant Modes

As it is well known, a cavity resonator can be formed by closing the separated ends of a rectangular waveguide [10] – [11]. If the geometrical dimensions of this resonator reach certain lengths, at a given frequency an EM field within this resonator forms a standing wave pattern – resonant modes [12]. The geometry of a typical rectangular cavity is shown in Figure 2.1.

Generally, in order to construct the resonant modes in a rectangular cavity, the modes that are transverse electric (TE) or transverse magnetic (TM) to one of the three axes need to be derived [10]. In our thesis, the *z* axis is chosen to keep with standard waveguide notation. The TE modes are normally called magnetic modes because the E_z component is zero. Similarly, the TM modes are normally called electric modes because the H_z component is zero [1], [10].

This standing wave pattern can be mathematically described by solving Maxwell's equations. The general form of time-varying Maxwell's equations can be written in the differential form as [10]

$$\nabla \times \vec{E} = -\frac{\partial \vec{B}}{\partial t} \tag{2.1}$$

$$\nabla \times \vec{H} = \frac{\partial \vec{D}}{\partial t} + \vec{J} \tag{2.2}$$

$$\nabla \cdot \vec{D} = \rho \tag{2.3}$$

$$\nabla \cdot \vec{B} = 0 \tag{2.4}$$

The quantities in these equations represent time-varying vector fields and are real functions

of spatial coordinates *x*, *y*, *z*, and the time variable *t*. These quantities are defined as follows [10]

$\vec{E}$ is the electric field, in volts per meter (V/m).

$\vec{H}$ is the magnetic field, in amperes per meter (A/m).

$\vec{D}$ is the electric flux density, in coulombs per meter squared (C/m^2).

$\vec{B}$ is the magnetic flux density, in webers per meter squared (Wb/m^2).

$\vec{J}$ is the electric current density, in amperes per meter squared (A/m^2).

ρ is the electric charge density, in coulombs per meter cubed (C/m^3).

The sources of the EM fields are the electric current $\vec{J}$ and the electric charge density ρ. In order to derive the numerical formulation valid inside an ideal cavity, it is assumed that there are no sources inside the computational volume *V*, i.e. $\rho = 0$ and $\vec{J} = \vec{0}$. Furthermore the properties of the materials in which EM fields exist are taken to be linear, homogeneous, and

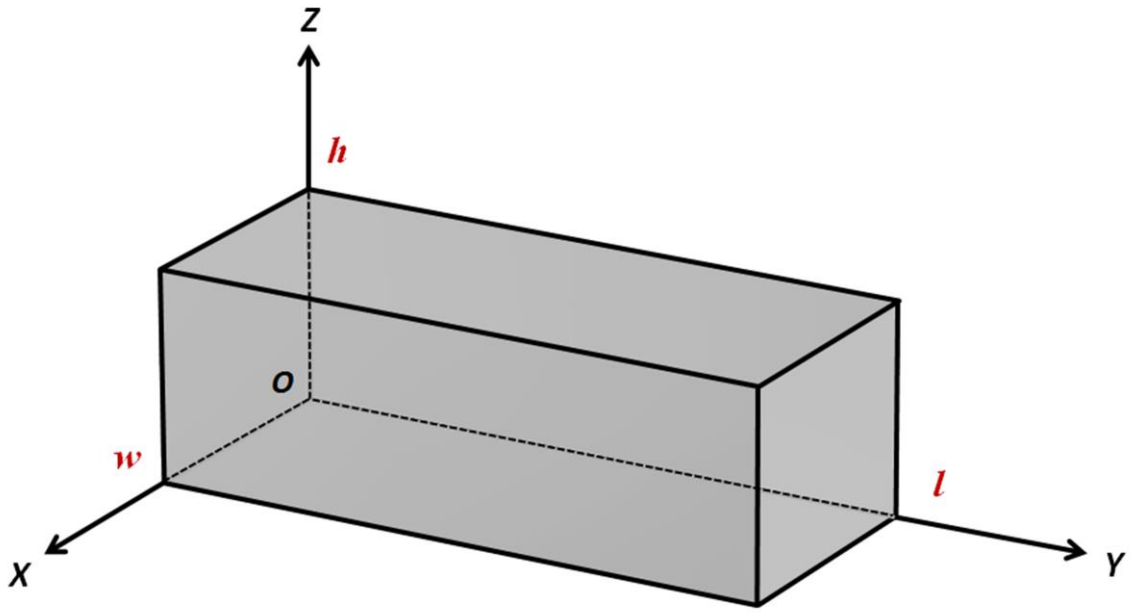

Figure 2.1 Geometry of a rectangular cavity.

isotropic so that the constitutive equations will be [10] – [12],

$$\vec{D} = \varepsilon\vec{E} \tag{2.5}$$

$$\vec{B} = \mu\vec{H} \tag{2.6}$$

Herein ε denotes the dielectric permittivity and μ the magnetic permeability. In free space, the corresponding permittivity $\varepsilon_0 = 8.854\times10^{-12}$ farad/m, and the corresponding permeability $\mu_0 = 4\pi\times10^{-7}$ henry/m [10]. In a dielectric, $\varepsilon = \varepsilon_r\varepsilon_0$ and $\mu = \mu_r\mu_0$, where ε_r and μ_r are the relative permittivity and permeability of the material inside the cavity, respectively. For time-harmonic fields with an $e^{j\omega t}$-dependence, utilizing the material equations (2.5) – (2.6), (2.1) – (2.4) can be simplified to

$$\nabla\times\vec{E} = -j\omega\mu\vec{H} \tag{2.7}$$

$$\nabla\times\vec{H} = j\omega\varepsilon\vec{E} \tag{2.8}$$

$$\nabla\cdot\vec{E} = 0 \tag{2.9}$$

$$\nabla\cdot\vec{H} = 0 \tag{2.10}$$

Applying the vector identity in Appendix A

$$\nabla\times\left(\nabla\times\vec{A}\right) = \nabla\left(\nabla\cdot\vec{A}\right) - \Delta\vec{A} \tag{2.11}$$

to (2.7) and (2.8), the electrical and magnetic wave equations can be derived as

$$\Delta\vec{E} - \frac{1}{c^2}\frac{\partial^2\vec{E}}{\partial t^2} = 0 \tag{2.12}$$

$$\Delta\vec{H} - \frac{1}{c^2}\frac{\partial^2\vec{H}}{\partial t^2} = 0 \tag{2.13}$$

which can be used to describe the fields within a cavity. c denotes the propagation speed of the EM wave in the medium and is given by

$$c = \frac{c_0}{\sqrt{\varepsilon_r\mu_r}} \tag{2.14}$$

with c_0 = 3×10^8 m/s being the speed of an EM wave in vacuum. The partial differential equations (2.12) and (2.13) can be solved by the method of separation of variables [10] using boundary conditions. The boundary conditions can be derived for both the tangential components and normal components. For the tangential components of the electric and the magnetic field, respectively, it can be derived

$$\overrightarrow{e_n} \times \left(\overrightarrow{E_2} - \overrightarrow{E_1}\right) = \vec{0} \tag{2.15}$$

$$\overrightarrow{e_n} \times \left(\overrightarrow{H_2} - \overrightarrow{H_1}\right) = \overrightarrow{J_S}, \tag{2.16}$$

wherein $\overrightarrow{J_S}$ is the electric surface current density that may exist on the interface. The vector $\overrightarrow{e_n}$ represents a normal vector pointing from dielectric 1 into dielectric 2.

For the normal components of the electric and magnetic field, the boundary conditions are enforced by

$$\overrightarrow{e_n} \cdot \left(\overrightarrow{D_2} - \overrightarrow{D_1}\right) = \rho_s \tag{2.17}$$

$$\overrightarrow{e_n} \cdot \left(\overrightarrow{B_2} - \overrightarrow{B_1}\right) = 0, \tag{2.18}$$

where ρ_s is the surface charge density on the interface. For an interface between two dielectric materials (normally no charge or surface current densities will exist), equations (2.15) – (2.18) state that the normal components of $\vec{B}$ and $\vec{D}$ are continuous across the interface, and the tangential components of $\vec{E}$ and $\vec{H}$ are continuous across the interface [10].

For an ideal cavity, from (2.15) and (2.18), it can obtained

$$\vec{E}_{\parallel} = \vec{0} \tag{2.19}$$

$$H_{\perp} = 0, \tag{2.20}$$

which is valid on the PEC wall surface of the cavity for the tangential components of the electrical field $\vec{E}_{\parallel}$ and the normal component of the magnetic field $H_{\perp}$. Applying (2.19) and (2.20) to the rectangular cavity shown in Figure 2.1 yields

$$x = 0 \text{ and } x = w: \quad E_y = 0, E_z = 0, H_x = 0 \tag{2.21}$$

$$y = 0 \text{ and } y = l: \quad E_x = 0, E_z = 0, H_y = 0 \tag{2.22}$$

$$z = 0 \text{ and } z = h: \quad E_x = 0, E_y = 0, H_z = 0 \tag{2.23}$$

Using the boundary conditions (2.21) – (2.23), the wave equations (2.12) and (2.13) can be solved and the certain EM field standing wave patterns (cavity modes) can be obtained. These cavity modes can be classified into two main categories: the TE modes with $E_z = 0$ and the TM modes with $H_z = 0$. As a result, for the field components of TM_{mnp} modes in an ideal rectangular cavity, it can be derived

$$E_x(x,y,z) = -\frac{1}{k_{mn}^2}\left(\frac{m\pi}{w}\right)\left(\frac{p\pi}{l}\right) E_0 \cos\left(\frac{m\pi}{w}x\right) \sin\left(\frac{n\pi}{h}y\right) \sin\left(\frac{p\pi}{l}z\right) \tag{2.24}$$

$$E_y(x,y,z) = -\frac{1}{k_{mn}^2}\left(\frac{n\pi}{h}\right)\left(\frac{p\pi}{l}\right) E_0 \sin\left(\frac{m\pi}{w}x\right) \cos\left(\frac{n\pi}{h}y\right) \sin\left(\frac{p\pi}{l}z\right) \tag{2.25}$$

$$E_z(x,y,z) = E_0 \sin\left(\frac{m\pi}{w}x\right) \sin\left(\frac{n\pi}{h}y\right) \cos\left(\frac{p\pi}{l}z\right) \tag{2.26}$$

$$H_x(x,y,z) = \frac{j\omega\varepsilon}{k_{mn}^2}\left(\frac{n\pi}{h}\right) E_0 \sin\left(\frac{m\pi}{w}x\right) \cos\left(\frac{n\pi}{h}y\right) \cos\left(\frac{p\pi}{l}z\right) \tag{2.27}$$

$$H_y(x,y,z) = -\frac{j\omega\varepsilon}{k_{mn}^2}\left(\frac{m\pi}{w}\right) E_0 \cos\left(\frac{m\pi}{w}x\right) \sin\left(\frac{n\pi}{h}y\right) \cos\left(\frac{p\pi}{l}z\right) \tag{2.28}$$

$$H_z(x,y,z) = 0 \tag{2.29}$$

with the integer numbers m, n = 1, 2, 3, ⋯ and p = 0, 1, 2, ⋯. The indices m, n, and p denote the number of half wavelengths in x-, y-, and z-direction, respectively. E_0 is a constant with a unit of V/m. Similarly, for TE_{mnp} modes, the following equations can be derived

$$E_x(x,y,z) = \frac{j\omega\mu}{k_{mn}^2}\left(\frac{n\pi}{h}\right) H_0 \cos\left(\frac{m\pi}{w}x\right) \sin\left(\frac{n\pi}{h}y\right) \sin\left(\frac{p\pi}{l}z\right) \tag{2.30}$$

$$E_y(x,y,z) = -\frac{j\omega\mu}{k_{mn}^2}\left(\frac{m\pi}{w}\right) H_0 \sin\left(\frac{m\pi}{w}x\right) \cos\left(\frac{n\pi}{h}y\right) \sin\left(\frac{p\pi}{l}z\right) \tag{2.31}$$

$$E_z(x,y,z) = 0 \tag{2.32}$$

$$H_x(x,y,z) = -\frac{1}{k_{mn}^2}\left(\frac{m\pi}{w}\right)\left(\frac{p\pi}{l}\right)H_0 \sin\left(\frac{m\pi}{w}x\right)\cos\left(\frac{n\pi}{h}y\right)\cos\left(\frac{p\pi}{l}z\right) \tag{2.33}$$

$$H_y(x,y,z) = -\frac{1}{k_{mn}^2}\left(\frac{n\pi}{h}\right)\left(\frac{p\pi}{l}\right)H_0 \cos\left(\frac{m\pi}{w}x\right)\sin\left(\frac{n\pi}{h}y\right)\cos\left(\frac{p\pi}{l}z\right) \tag{2.34}$$

$$H_z(x,y,z) = H_0 \cos\left(\frac{m\pi}{w}x\right)\cos\left(\frac{n\pi}{h}y\right)\sin\left(\frac{p\pi}{l}z\right) \tag{2.35}$$

with m, n = 0, 1, 2, 3, ⋯ and p = 1, 2, 3, ⋯, with the only exception that $m = n = 0$ is not allowed. H_0 is a constant with a unit of A/m. The wave number $k = 2\pi/\lambda$, λ is the wavelength. The constant k_{mn} utilized as an abbreviation in (2.24) – (2.29) and (2.30) – (2.35) is given as

$$k_{mn} = \sqrt{\left(\frac{m\pi}{w}\right)^2 + \left(\frac{n\pi}{h}\right)^2} \tag{2.36}$$

The angular frequency ω as employed in (2.24) – (2.35) can be calculated from

$$\frac{\omega}{c} = \frac{2\pi f}{c} = k_{mnp} = \sqrt{\left(\frac{m\pi}{w}\right)^2 + \left(\frac{n\pi}{h}\right)^2 + \left(\frac{p\pi}{l}\right)^2} \tag{2.37}$$

with c as given by (2.14) and f as the frequency. In an ideal cavity, i.e., a lossless cavity, the cut-off frequencies of the individual modes are described by

$$f_{mnp} = \frac{c}{2\pi}\sqrt{\left(\frac{m\pi}{w}\right)^2 + \left(\frac{n\pi}{h}\right)^2 + \left(\frac{p\pi}{l}\right)^2} \tag{2.38}$$

The modes with the lowest cut-off frequencies can be TM_{110}, TE_{011}, or TE_{101} mode depending on the actual dimensions of a cavity, i.e. the relation between w, h, and l. Assuming $w < h < l$, the lowest resonant frequency occurs for TE_{011} mode. It is important to note that there can be several modes having the same cut-off frequency. If several modes exhibit the same cut-off frequency they are called "degenerate modes". For the RC at the University of Liverpool, its dimension is l = 5.8 m, w = 3.6 m, and h = 4.0 m. The first five resonant modes that can exist are shown in Table 2.1. The theoretical mode distribution as a function of frequency for our RC in 40 – 200 MHz is shown in Figure 2.2. Each mode represents a unique spatial field

variation or modal structure. It can be seen that at the lower frequencies, the modal population of the RC is sparse and it is with frequency gaps of different size. With the increase of the frequency, the mode structure becomes finer. The lowest resonant frequency (the first resonance) of our RC occurs at 45.55 MHz corresponding to the TE_{011} mode in Table 2.1.

Table 2.1: The first five resonant modes in the RC at the University of Liverpool

Mode number	*m*	*n*	*p*	Resonant frequency (MHz)
1	0	1	1	45.55
2	1	0	1	49.04
3	1	1	0	56.06
4	1	1	1	61.73
5	0	1	2	63.89

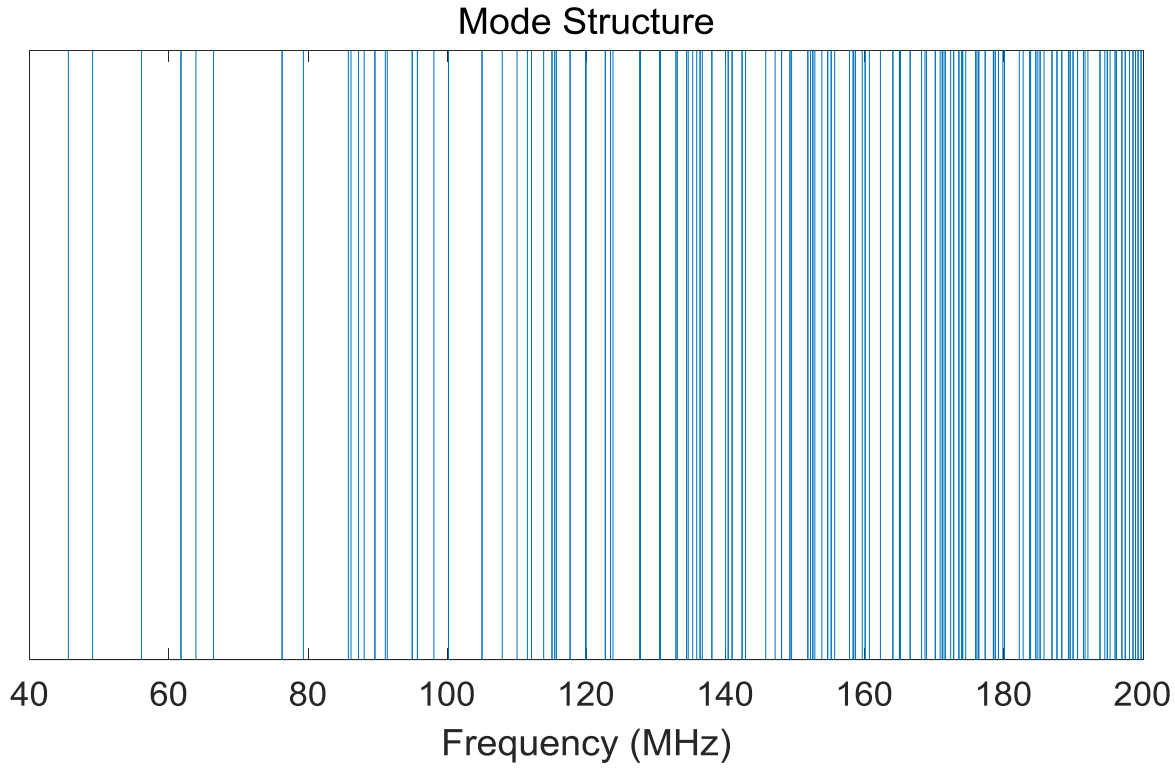

Figure 2.2 Theoretical modal structures for the RC at the University of Liverpool.

2.2.2 Modes inside a Lossy Cavity

For an ideal, lossless cavity the mode spectrum is discrete. Theoretically, a resonance only occurs at the frequency f_0 corresponding to the exact frequency of the resonant mode [13] – [14]. However, in a finitely conducting cavity, modes over a certain "modal bandwidth" Δf exist. The modal bandwidth can be defined as "The bandwidth over which the excited power in a particular cavity mode with resonance frequency f_0 is larger than half the excited power at f_0" [15]. For simplicity it is assumed that the modes can only be excited within the range:

$$f_0 - \Delta f/2 \leq f_{res} \leq f_0 + \Delta f/2 \tag{2.39}$$

wherein f_{res} is the resonant frequency, therefore the mode spectrum is not fully discrete anymore. Outside of its modal bandwidth, the contribution of a mode to the overall field distribution can be neglected [12]. From a certain frequency on, the modal bandwidths for different resonant frequencies start to overlap and consequently, multiple modes can be excited at a single frequency. The number of modes that can be excited simultaneously at a given frequency varies depending on the quality factor Q of the lossy cavity. At this point, the cavity turns into multi-mode operation regime. The field distribution obtained within the cavity for multi-mode operation is the superposition of the individual modes [7]. In practice, the modal bandwidth can be formulated by

$$\Delta f = f/Q \tag{2.40}$$

The modal bandwidth is measured in our RC. Both the "unloaded" scenario and the "loaded" scenario are studied. In both scenarios, the transmitting antenna (antenna 1) is a log periodic antenna (LPDA), and the receiving antenna (antenna 2) is a folded diploe antenna. The efficiency of the two antennas is with known efficiency values. In the "loaded" configuration, the RC has been loaded with two pieces of RAMs placed in the two corners of the chamber to illustrate the loading effect on the average mode bandwidth. The measurement setup can be seen from Figure 2.3(a) and (b). The measurement results are depicted in Figure 2.4. It can be seen that the modal bandwidth is slightly decreasing for increasing frequency, which means the window in which subsequent modes can be excited grows smaller at higher frequencies. However, at higher frequencies the mode density is higher, meaning that many modes can still be excited.

(a) **(b)**

Figure 2.3 The measured setup for modal bandwidth measurement under (a) unloaded and (b) loaded scenarios.

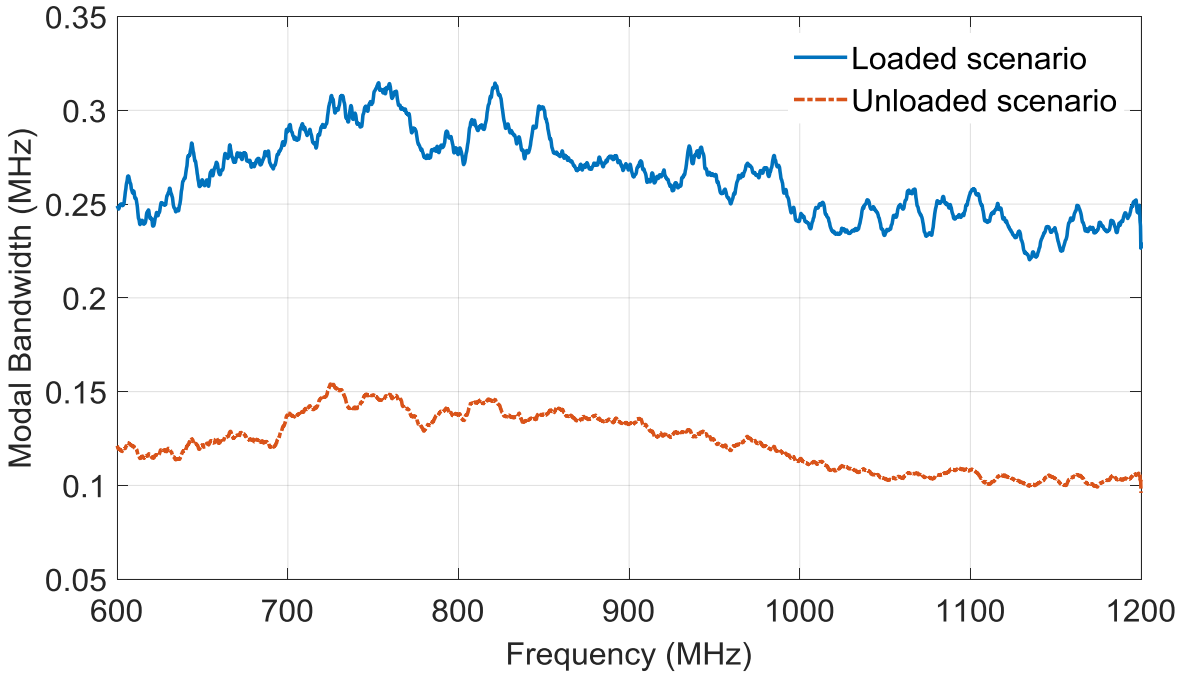

Figure 2.4 Measured modal bandwidth in the RC at the University of Liverpool.

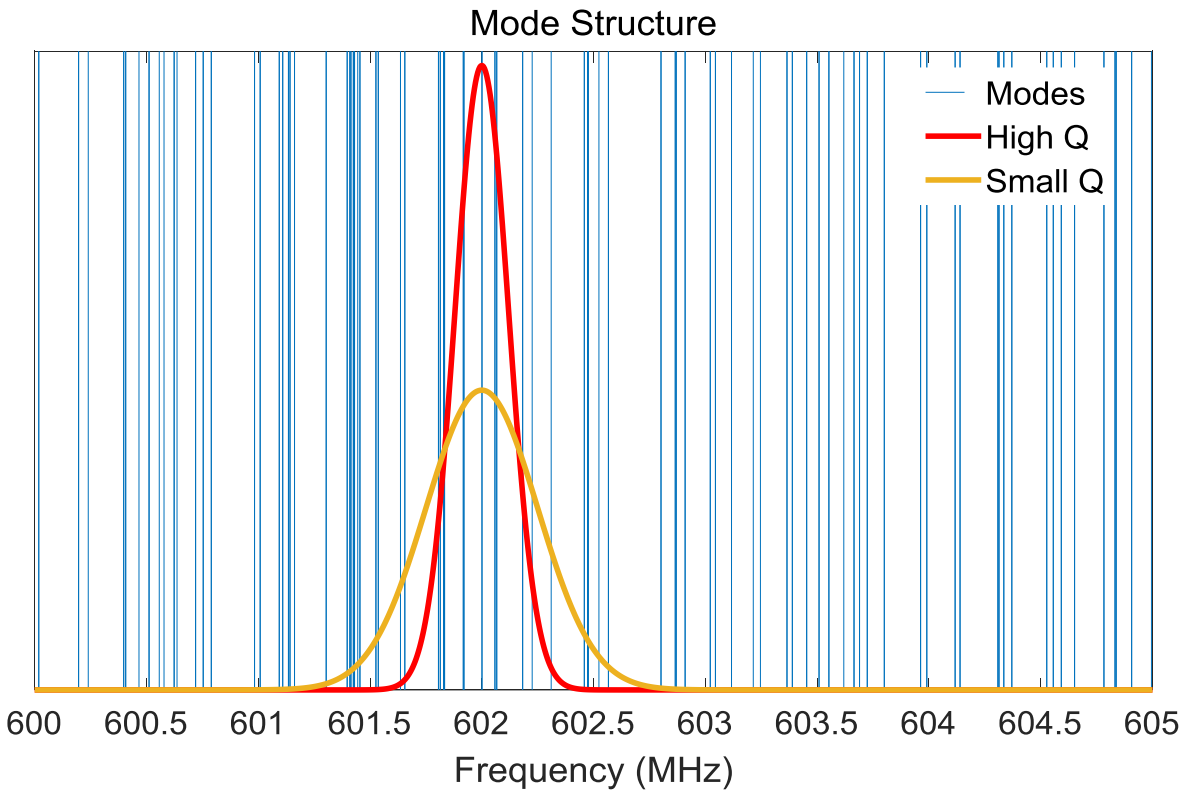

Figure 2.5 Modal Structure with small and high *Q* superimposed at 602 MHz in the RC at the University of Liverpool.

The effect of decreasing the *Q* of the RC is shown in Figure 2.5. In this case, additional modes can be excited when the cavity is driven at the frequency of about 602 MHz because of the broader modal overlap due to lower *Q*. The effective modal structure is the vector sum of the excited modes with different weighting factors of amplitudes. The spatial field variation will now be different from that obtained with the higher *Q* RC. Thus, varying the *Q* of the RC can change the "effective" modal structure. It should be noted that if the frequency were increased, more modes would be available within a given modal bandwidth, giving rise to a finer structure of the field. Again, the effective modal structure would be the vector sum of the modes.

2.2.3 Lowest Usable Frequency

The lowest usable frequency (LUF) f_{LUF} is commonly defined as the frequency from which

the RC meets the operational requirements [7], [16]. There are several definitions for the LUF:

- The LUF is three times the cut-off frequency f_c of the fundamental mode of a cavity with the same dimensions as the RC, i.e., $f_{LUF} = 3f_c$ [7].
- The LUF is defined as the frequency at which 60 ··· 100 modes within an ideal cavity of the same dimensions as the RC are above cut-off frequency and at least 1.5 modes/MHz are present [7], [17].
- The LUF is defined as the lowest frequency at which specified field uniformity can be achieved over a volume constrained by eight corner locations [7].

It is worth mentioning that the first two definitions are relatively qualitative criteria which offer only a rough overview on whether an RC begins to meet the operational requirements from a certain frequency. The third definition is much more stringent because it involves measurements within the RC and also considers the desired measurement uncertainties and confidence intervals to be obtained for a given number of stirrer positions. The LUF can be determined by the RC size, shape, quality factor, and the effectiveness of the stirrers [7].

2.2.4 Number of Cavity Modes

In order to evaluate from which frequency f_{LUF} on an RC begins to satisfy the operational requirements, the cumulated number of modes and the mode density must be known. Again, computation of these parameters assumes an empty RC without any stirrers, i.e., a rectangular cavity resonator.

There are three common methods to assess the number of modes that are present in a given cavity. The first method is termed as "mode counting" which can be performed by the repeated solution of (2.38) for both TE and TM modes [13]. And then the total number of modes present with eigenvalues less than or equal to k_{mnp} will be counted. Theoretically, N as a function of k_{mnp} is discrete, but people have derived a smooth approximation referred to as "Weyl's formula" [1], which is valid for cavities of general shape and can be written as

$$N(f) = \frac{8\pi}{3}(l \times w \times h)\frac{f^3}{c^3} \tag{2.41}$$

where $N(f)$ is the cumulated number of modes. The third method is a modified version of Weyl's formula specific to rectangular cavities [1] and is stated in (2.42).

$$N(f) = \frac{8\pi}{3}(l \times w \times h)\frac{f^3}{c^3} - (l + w + h)\frac{f}{c} + \frac{1}{2} \tag{2.42}$$

It can be seen that the RC volume has the major impact on the cumulated number of modes, as shown by the first part of (2.42). The second part of (2.42) represents the contribution of the combined edge length of an RC. A comparison of the modal numbers presented in the RC at the University of Liverpool by mode counting, Weyl's formula, and modified Weyl's formula is shown in Figure 2.6. It can be seen that the extra terms in (2.42) improve the agreement obtained with the mode counting method as opposed to using the original Weyl's formula in (2.41). With the increase of frequency, it can be seen that the number of modes increases with respect to the cavity volume and the third power of frequency. As noted above, for a proper operation of an RC usually at least 60 modes above the cut-off frequency are required. As noted from Figure 2.6, the LUF for our RC is about 140 MHz.

The mode density $\partial N/\partial f$ (number of modes per frequency interval) can be calculated from (2.43) to be

$$\frac{\partial N}{\partial f} = 8\pi \cdot lwh \cdot \frac{f^2}{c^3} - (l + w + h)\frac{1}{c} \tag{2.43}$$

The f^2 dependence in (2.43) indicates that the mode density also increases rapidly for high frequencies [1]. To achieve sufficient statistical field uniformity and isotropy, a common RC specification is to have at least $\partial N/\partial f$ = 1.5 modes/MHz above cut-off frequencies [18]. A plot of the mode density can be seen in Figure 2.7. It can be seen that the chamber has a mode density of at least 1.5 modes per megahertz from about 140 MHz upwards, i.e., the corresponding LUF is about 140 MHz, which agrees well with the prediction from Figure 2.6. A low mode density in any given chamber means that chamber would not have adequate performance, as the mode density is too small to obtain spatial field uniformity [7].

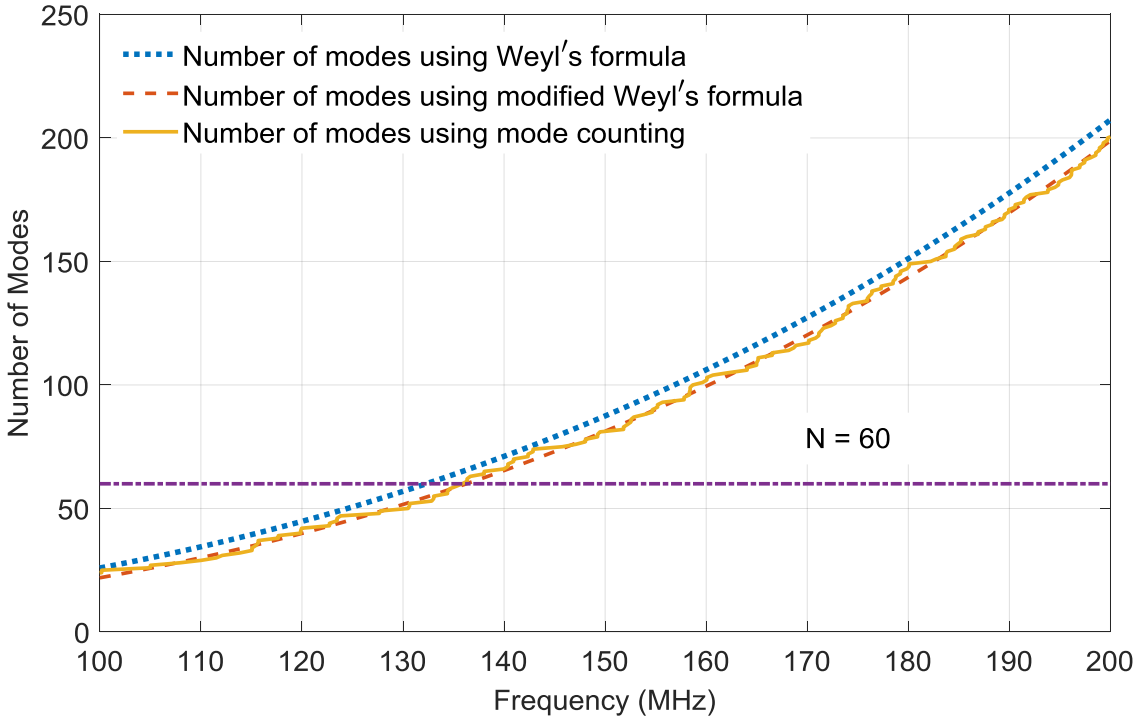

Figure 2.6 **Number of modes versus frequency for the RC at the University of Liverpool.**

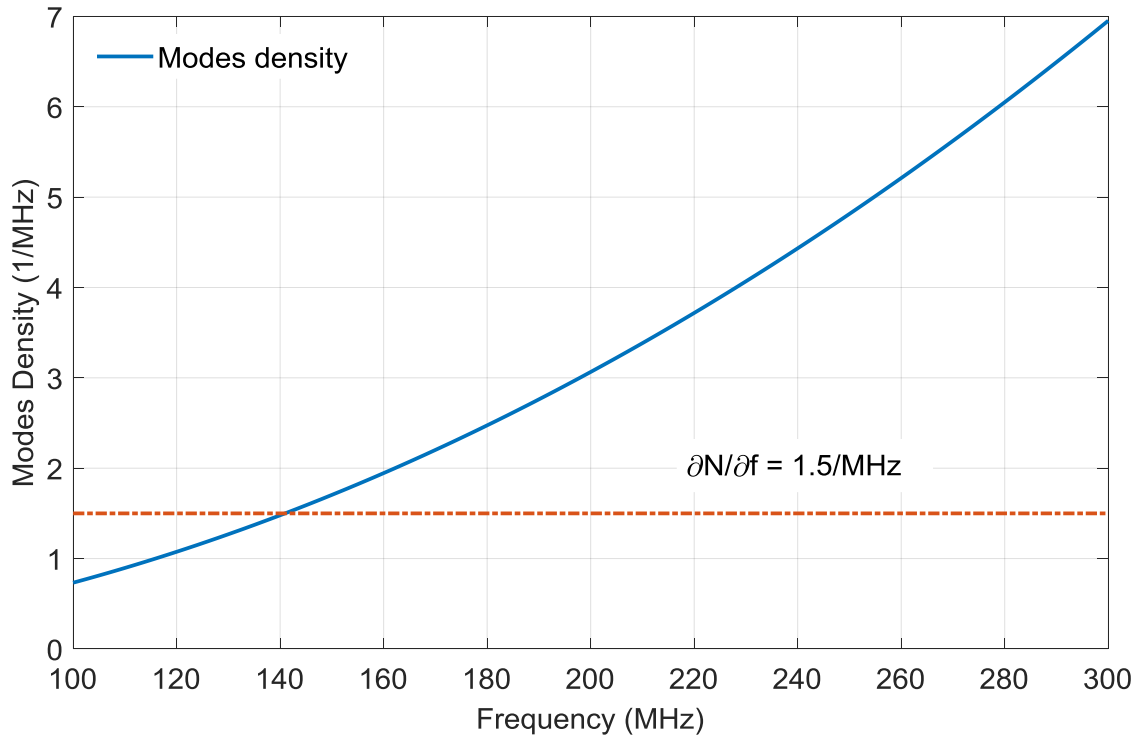

Figure 2.7 **Modes density versus frequency for the RC at the University of Liverpool.**

2.2.5 Green's Function

The Dyadic Green's function is a bridge to link the excitation source and its generated electric and magnetic fields [19] – [20]. Different from the prior field equations in (2.24) to (2.35), it is advantageous to visualise these fields in a "non-empty" cavity, i.e., with a realistic excitation involved [13]. The EM fields inside a rectangular cavity outside of the source area are purely the superposition of all TE and TM modes generated within it. In the source area, special treatment is required [1], [13], [19] – [20], but the Dyadic Green's functions are still useful there. Modes inside the cavity can be controlled by choosing the polarisation and location of the excitation source [19] – [20].

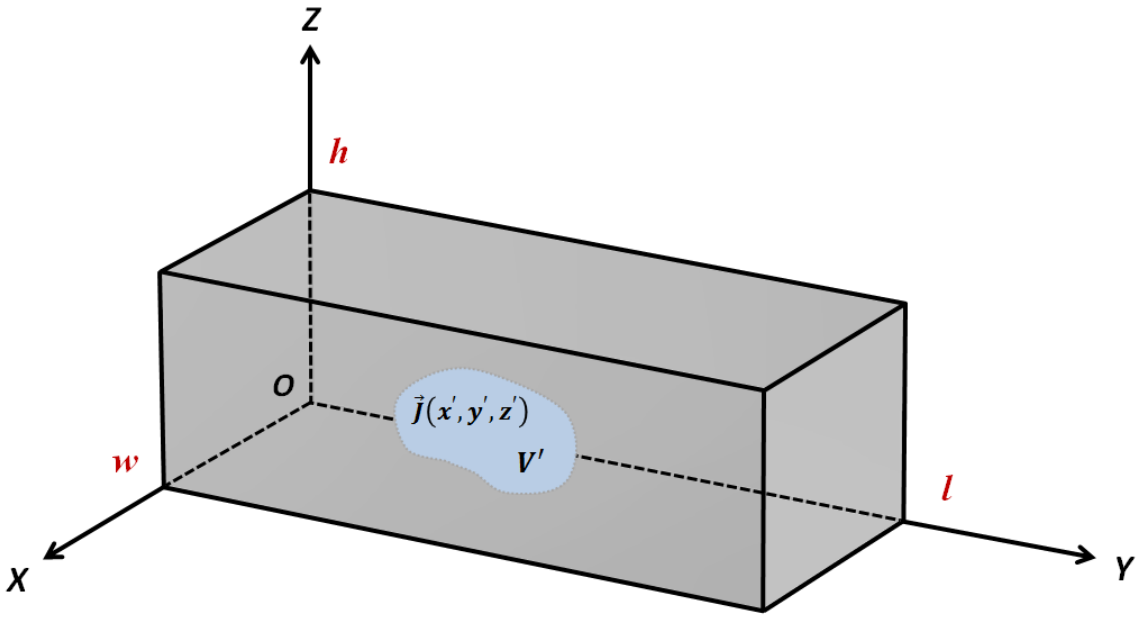

Figure 2.8 A volume current density $\vec{J}(x',y',z')$ confined to a volume V' in a rectangular cavity.

In [20], a computationally efficient series of equations based on Dyadic Green's functions was derived in order to study the resultant electric field inside shielded enclosures (the magnetic field can also be derived similarly). Consider a volume current density $\vec{J}(x',y',z')$ confined to a volume V' in a rectangular cavity, as shown in Figure 2.8. The resulting electric field was deduced using (2.44), (2.45) and (2.46).

$$\vec{E} = \frac{1}{j\omega\varepsilon} \int_{source} \overleftrightarrow{G} \cdot \vec{J}(x', y', z') dV' \tag{2.44}$$

where $\overleftrightarrow{G}$ is the Dyadic Green's function. The double arrow above the Green's functions indicates a three by three dyadic. It can be expressed as

$$\begin{aligned}
\overleftrightarrow{G} = & \sum_{p=0}^{\infty}\sum_{m=0}^{\infty} \frac{2\varepsilon_{0m}}{hw\alpha sin\alpha l} sink_z z' cosk_x x' \Big\{ k_z k_x cosk_z z sink_x x \begin{bmatrix} sin\alpha y sin\alpha(l-y') & y<y' \\ sin\alpha y' sin\alpha(l-y) & y>y' \end{bmatrix} \hat{z}\hat{x} \\
& + (k_x^2 - k^2) sink_z z cosk_x x \begin{bmatrix} sin\alpha y sin\alpha(l-y') & y<y' \\ sin\alpha y' sin\alpha(l-y) & y>y' \end{bmatrix} \hat{x}\hat{x} \\
& + k_x \alpha sink_z z sink_x x \begin{bmatrix} cos\alpha y sin\alpha(l-y') & y<y' \\ -sin\alpha y' cos\alpha(l-y) & y>y' \end{bmatrix} \hat{y}\hat{x} \Big\} \\
& + \sum_{m=0}^{\infty}\sum_{n=0}^{\infty} \frac{2\varepsilon_{0n}}{wl\beta sin\beta h} sink_x x' cosk_y y' \Big\{ k_x k_y cosk_x x sink_y y \begin{bmatrix} sin\beta z sin\beta(h-z') & z<z' \\ sin\beta z' sin\beta(h-z) & z>z' \end{bmatrix} \hat{x}\hat{y} \\
& + \left(k_y^2 - k^2\right) sink_x x cosk_y y \begin{bmatrix} sin\beta z sin\beta(h-z') & z<z' \\ sin\beta z' sin\beta(h-z) & z>z' \end{bmatrix} \hat{y}\hat{y} \\
& + k_y \beta sink_x x sink_y y \begin{bmatrix} cos\beta z sin\beta(h-z') & z<z' \\ -sin\beta z' cos\beta(h-z) & z>z' \end{bmatrix} \hat{z}\hat{y} \Big\} \\
& + \sum_{n=0}^{\infty}\sum_{p=0}^{\infty} \frac{2\varepsilon_{0p}}{lh\gamma sin\gamma w} sink_y y' cosk_z z' \Big\{ k_y k_z cosk_y y sink_z z \begin{bmatrix} sin\gamma x sin\gamma(w-x') & x<x' \\ sin\gamma x' sin\gamma(w-x) & x>x' \end{bmatrix} \hat{y}\hat{z} \\
& + (k_z^2 - k^2) sink_y y cosk_z z \begin{bmatrix} sin\gamma x sin\gamma(w-x') & x<x' \\ sin\gamma x' sin\gamma(w-x) & x>x' \end{bmatrix} \hat{z}\hat{z} \\
& + k_z \gamma sink_y y sink_z z \begin{bmatrix} cos\gamma x sin\gamma(w-x') & x<x' \\ -sin\gamma x' cos\gamma(w-x) & x>x' \end{bmatrix} \hat{x}\hat{z} \Big\}
\end{aligned} \tag{2.45}$$

where $k_x = m\pi/w$, $k_y = n\pi/l$, $k_z = p\pi/h$, $\alpha = \sqrt{k^2 - k_z^2 - k_x^2}$, $\beta = \sqrt{k^2 - k_y^2 - k_x^2}$, $\gamma = \sqrt{k^2 - k_z^2 - k_y^2}$, and $\varepsilon_{0m(n,p)} = \begin{cases} 1, & m\,(n,p) = 0 \\ 2, & m\,(n,p) \neq 0 \end{cases}$.

Assuming the current source used to generate the field inside the RC is a *y* polarised unit element, the resultant electric field on an *xz* plane can be obtained using (2.46) [13] [19] – [20]

$$\vec{E} = \frac{1}{j\omega\varepsilon}\sum_{m=0}^{\infty}\sum_{n=0}^{\infty}\frac{2\varepsilon_{0n}}{wl\beta sin\beta h} sink_x x' cosk_y y'$$

$$\left\{\begin{array}{c} k_x k_y cosk_x x sink_y y \begin{bmatrix} sin\beta z sin\beta(h-z') & z<z' \\ sin\beta z' sin\beta(h-z) & z>z' \end{bmatrix}\hat{x} \\ +\left(k_y^2 - k^2\right) sink_x x cosk_y y \begin{bmatrix} sin\beta z sin\beta(h-z') & z<z' \\ sin\beta z' sin\beta(h-z) & z>z' \end{bmatrix}\hat{y} \\ +k_y \beta sink_x x sink_y y \begin{bmatrix} cos\beta z sin\beta(h-z') & z<z' \\ -sin\beta z' cos\beta(h-z) & z>z' \end{bmatrix}\hat{z} \end{array}\right\} \quad (2.46)$$

The E_y electric field distribution at 200 MHz, 600 MHz, and 1200 MHz on the *xz* plane in the RC at the University of Liverpool is plotted in Figure 2.9(a), (b), and (c), respectively. The observation plane in all the depicted plots is $y = l/2$ (the mid-point in length of the RC). The current source is located at x_1 = 0.4 m, x_2 = 0.5 m, y_1 = 1.35 m, y_2 = 1.4 m and z_0 = 0.5 m, which is corresponding to the corner of the RC [13]. It can be seen from Figures 2.9, the electric fields inside the RC are formed as a result of standing waves that have a sine and cosine dependence. With the increase of frequency, the fields begin to vary in a more complex manner. The magnitudes of the fields have significantly different values from point to point.

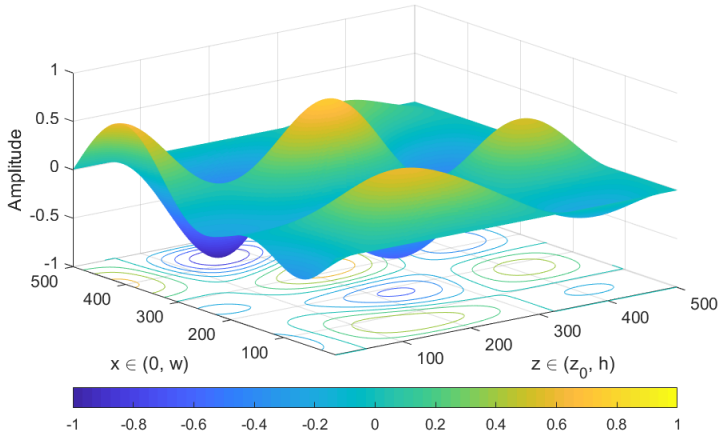

(a)

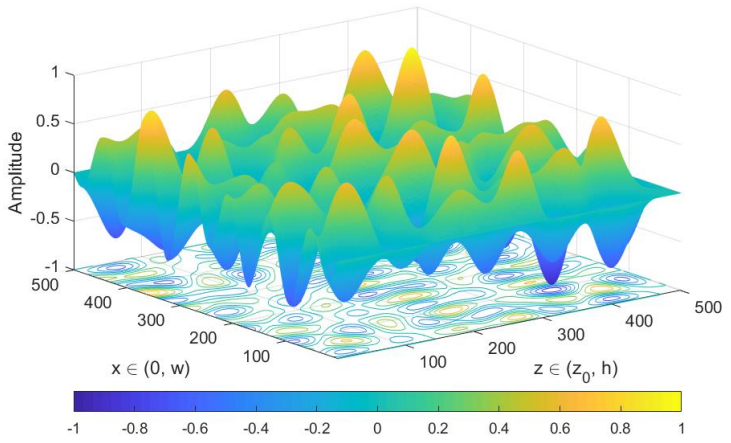

(b)

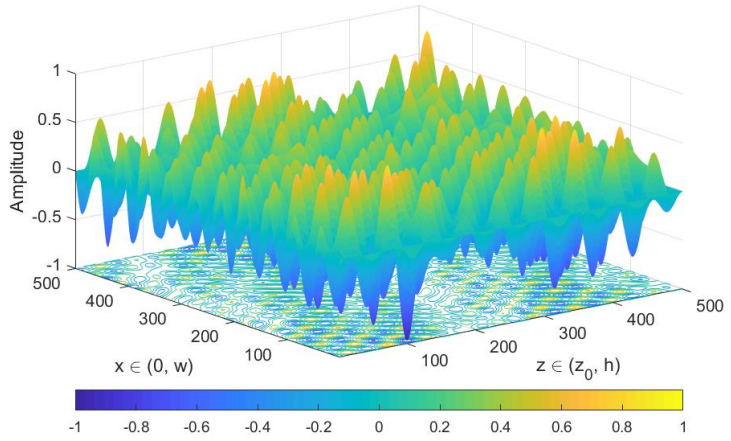

(c)

Figure 2.9 Normalised E_y field distribution in the RC at the University of Liverpool at (a) 200 MHz, (b) 600 MHz, and (c) 1200 MHz.

2.3 Stirring Techniques

The statistical nature of the fields in the RC is realized by employing stirring techniques. The purpose of these techniques is to make the fields statistically uniform and isotropic on average. In practice, the analysis of the measured data in RCs is always based on some limited number of stirring samples (stirring positions). In this section, these frequently used stirring techniques will be introduced and how they are implemented is explained.

2.3.1 Mechanical Stirring

The mechanical stirring technique, also called mode stirring technique, is the most common technique employed to stir the fields inside an RC. This stirring technique is realized by rotating the electrically large stirrers. By "electrically large", it means the size of the stirrer is at least comparable with respect to the wavelength of operation. When this is not the case, the stirrers' performance in significantly changing the field distribution will diminish. The stirrers are designed to be non-symmetric and arbitrarily shaped to generate more independent samples. An example of mechanical stirrer design in the University of Liverpool RC can be viewed in Figure. 1.4.

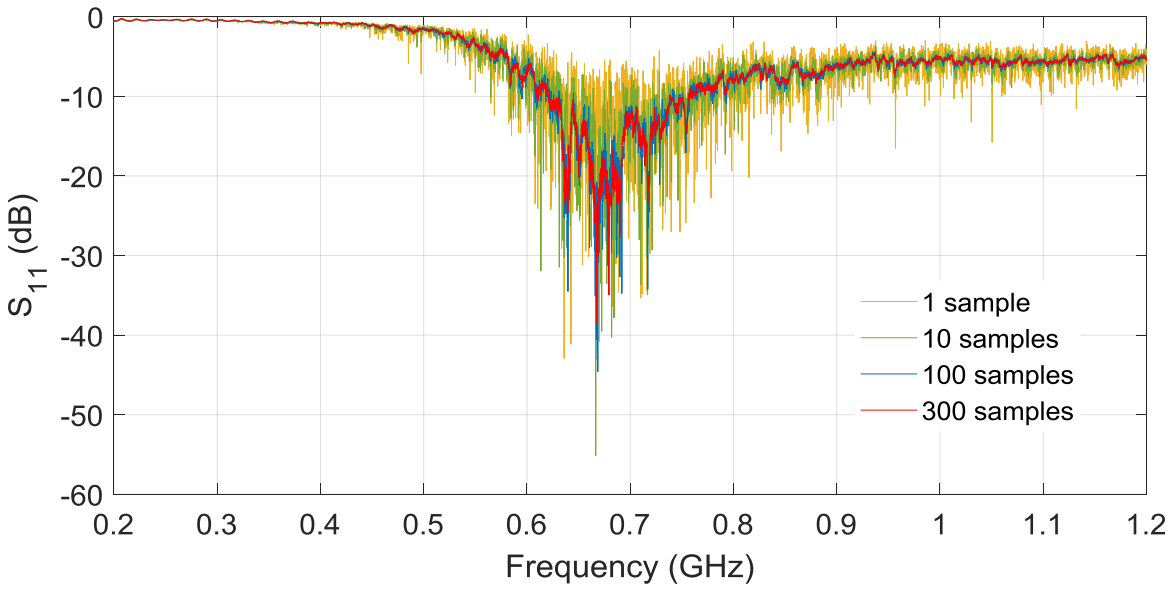

Figure 2.10 The effect of using the mechanical stirring technique to obtain statistical values of S_{11}.

The stirrers can be rotated in a stepwise or continuous manner and thus the boundary conditions for the EM field inside the RC vary [7]. The effect of changing the boundary conditions for the field means that the high and low field magnitudes, called hot and cold spots, throughout the RC will change as a function of location. This means that the field distribution can be rendered statistically homogeneous and isotropic on average from many stirrer positions. Wu and Chang [21] pointed out that the rotating stirrers continuously change

the resonant frequencies of the RC modes and that mechanical stirring has some equivalence to the frequency modulation of the source. The mechanical stirring technique can be quite effective [22], but it is fairly slow. Figure 2.10 shows the effect of using the mechanical stirring technique to obtain statistical values of *S*-parameters (S_{11} here). As can be seen with the increase of the number of samples, S_{11} becomes smoother because the effect caused by stochastic factors is averaged.

2.3.2 Frequency Stirring

Frequency stirring technique or electronic stirring technique is used to achieve the spatially uniform field by sweeping the source frequency over some narrow bandwidth of frequencies [23]. As the centre frequency is changed the hot spots and cold spots spatially move around the chamber. The power measured at the various discrete frequency points within a window of frequencies is averaged. The average computed from the window of frequencies is then attributed to the centre frequency in the window [24]. By sliding the same bandwidth window, measurements over the full frequency span are accomplished. It should be careful about the window bandwidth when performing frequency stirring. If too large smoothing bandwidth is taken, the loss of frequency resolution in any measured data will occur. Frequency stirring is similar to smoothing the data over frequency, but frequency stirring must be applied to the raw measured data (typically complex data), while smoothing is generally applied to the final computation of the desired quantity [13], [24]. For example, *S*-parameters measurements collected with a vector network analyzer (VNA) can be frequency stirred in order to obtain the average reflection coefficient, as shown in Figure 2.11. Frequency stirring with different certain bandwidth is adopted. As can be seen, S_{11} is averaged just as mechanical stirred data is averaged over all measured stirrer positions. Theoretically, if the RC is spatially uniform, the frequency stirring and mechanical stirring techniques should give the same average result. In addition, when smoothing the raw data a rectangular window must be used because the frequency stirring technique is meant to be an un-weighted average just as other stirring techniques are [24].

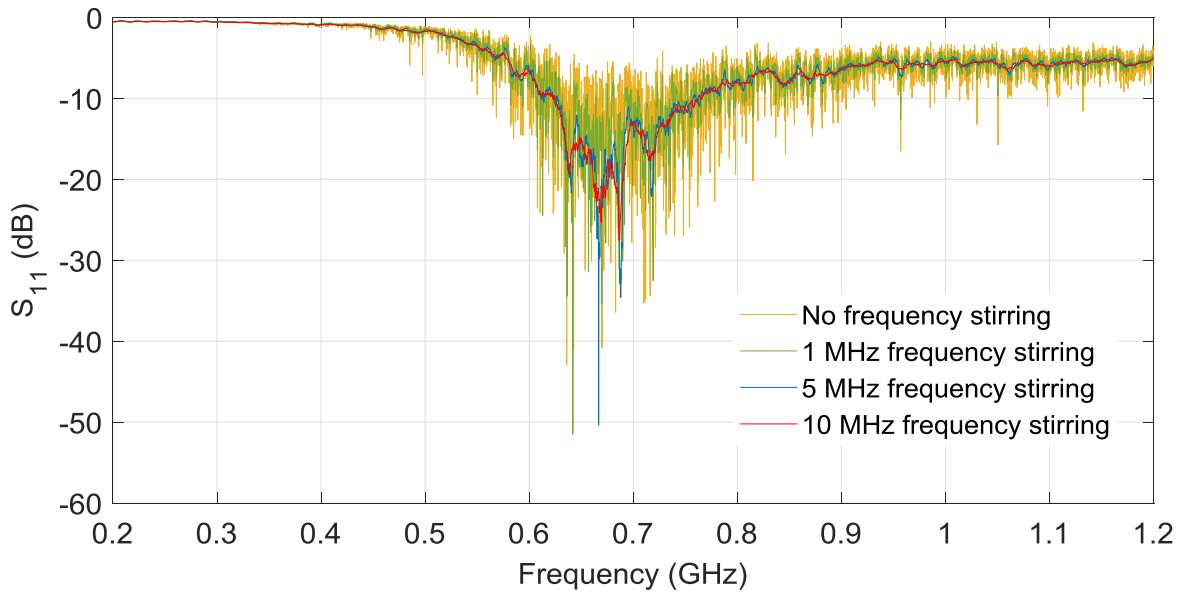

Figure 2.11 The effect of using the frequency stirring technique to obtain statistical values of S_{11}.

2.3.3 Source Stirring

The source stirring technique was first proposed by Y. Huang and D. J. Edwards in 1992 using Dyadic Green's functions [19] – [20]. It advocates the displacement or reorientation of an excitation source and an overall average is taken from measured samples at each individual location or orientation [13]. This technique eliminates mechanical stirrers inside the chamber and enlarges the available testing area. Unlike the mechanical stirring technique, there is no change of the eigenfrequency or eigenmode in source stirring technique. The only thing changed is the weighting factor of eigenmode. Hence the chamber which is reverberated by controlling the excitation can be named as the source-stirred chamber [20]. This technique has been proved in [25] to be an effective way of improving the field uniformity of an RC at lower frequencies. Thus it is valid for immunity test at lower frequencies in RCs. The field perturbation effect of using source stirring technique is visualized in Figure 2.9.

It should be noted that no stirring technique is perfect and using a combination of stirring techniques is useful in acquiring a sufficient number of statistically independent samples. It is up to the test engineer to determine a stirring technique, or a combination of stirring

techniques, in order to minimise the statistical error and reinforce the confidence attributed to the statistically determined field values [24].

2.4 Statistical Theory

For carefully designed cavities, the cavity details such as shape, dimensions, and materials are precisely known, and the cavity is generally of a simple/separable geometry. In such cases, deterministic theories are appropriate. However, in practice, the details of the cavity geometry and loading objects, such as cable bundles, scatterers, and absorbers are not expected to be well known [1]. Consequently, for many applications in EMC and wireless communications, people have to deal with problems where only a partial knowledge of the cavity geometry and its interior loading are known. Over the past two decades, techniques in statistical electromagnetics have been developed to deal with such a kind of problems [2], [3], [26] – [27]. The RC is a good example of a cavity with a complex interior. Clearly, all the information (scatters, loading object characteristics, and apertures, etc.) will not be known in detail. Statistical models for angle of arrival have been found useful for characterizing EM propagation in RCs [28].

2.4.1 Plane-wave Integration Model

As discussed above, it is not convenient to predict the field properties in electrically large, complex cavities using deterministic theories. Since many samples (stirrer positions) are employed in RC measurements, a statistical method [26] – [28] is required to determine the statistics of the fields and test object response. Moreover, the associated EM theory must be consistent with Maxwell's equations. The well-known plane-wave integration model for the EM fields has been found to be successful [1], [8]. This model satisfies Maxwell's equations and at the same time includes the statistical properties expected for a well-stirred field [8]. The plane-wave coefficients in the model are random variables with fairly simple statistical properties, thus, the fields are of statistical nature. Because the theory uses only propagating plane waves, it is fairly easy to calculate the responses of test objects or reference antennas using this model [1].

In a source-free, finite volume, the electric field $\vec{E}$ at location $\vec{r}$ can be represented by integrating plane waves from all directions

$$\vec{E}(\vec{r}) = \iint_{4\pi} \vec{F}(\Omega)\, exp\left(i\vec{k}\cdot\vec{r}\right) d\Omega \tag{2.47}$$

where Ω is the solid angle and dΩ = sinθdθdφ. θ and φ the elevation and azimuth angles, respectively. The geometry of a plane-wave component is shown in Figure 2.12. The vector wavenumber $\vec{k}$ is

$$\vec{k} = -k(\hat{x}sin\theta sin\varphi + \hat{y}sin\theta sin\varphi + \hat{z}cos\theta) \tag{2.48}$$

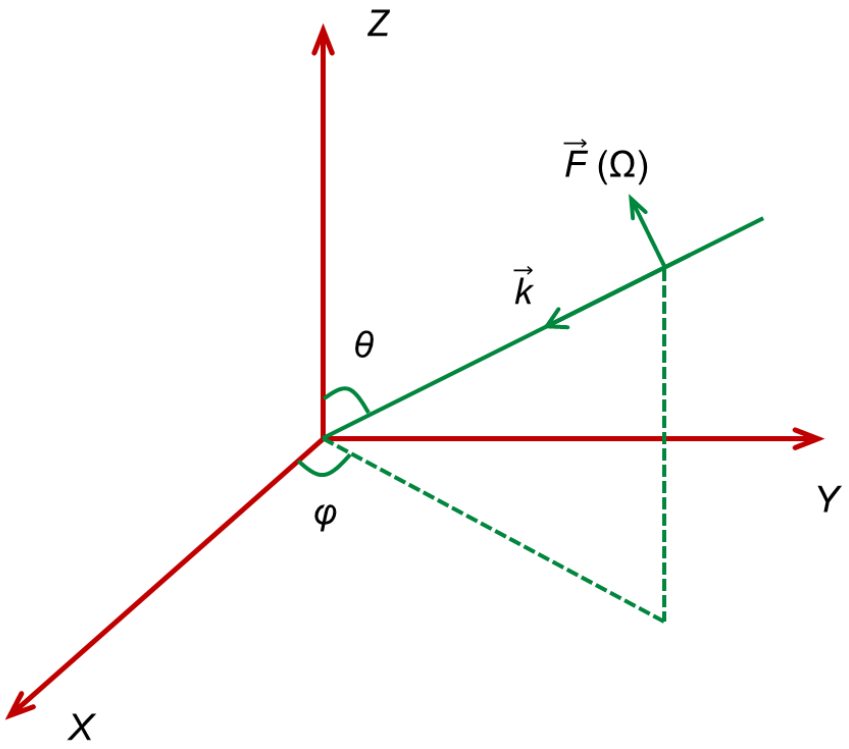

Figure 2.12 Plane-wave integration model.

So (2.47) can be re-written as

$$\vec{E}(\vec{r}) = \int_0^{2\pi}\int_0^{\pi} \vec{F}(\theta,\varphi)exp(i\vec{k}\cdot\vec{r})sin\theta d\theta d\varphi \tag{2.49}$$

The angular spectrum $\vec{F}(\Omega)$ can be written more explicitly in two polarisations

$$\vec{F}(\Omega) = \hat{\theta}F_{\theta}(\Omega) + \hat{\varphi}F_{\varphi}(\Omega) \tag{2.50}$$

where $\hat{\theta}$ and $\hat{\varphi}$ are unit vectors that are orthogonal to each other and to $\vec{k}$. Both F_θ and F_φ are complex and can be written in terms of their real and imaginary parts (to represent the phase)

$$F_{\theta}(\Omega) = F_{\theta r}(\Omega) + iF_{\theta i}(\Omega) \quad \text{and} \quad F_{\varphi}(\Omega) = F_{\varphi r}(\Omega) + iF_{\varphi i}(\Omega) \tag{2.51}$$

The angular spectrum $\vec{F}(\Omega)$ is taken to be a random variable in RCs. It depends on stirrer positions, i.e., $\vec{F}(\Omega)$ is different for each stirrer position. The statistical properties of the angular spectrum $\vec{F}(\Omega)$ are defined as follows

$$\langle F_{\theta}(\Omega)\rangle = \langle F_{\varphi}(\Omega)\rangle = 0 \tag{2.52}$$

$$\begin{aligned}
&\langle F_{\theta r}(\Omega_1)F_{\theta i}(\Omega_2)\rangle = \langle F_{\varphi r}(\Omega_1)F_{\varphi i}(\Omega_2)\rangle = \\
&\langle F_{\theta r}(\Omega_1)F_{\varphi r}(\Omega_2)\rangle = \langle F_{\theta r}(\Omega_1)F_{\varphi i}(\Omega_2)\rangle = \\
&\langle F_{\theta i}(\Omega_1)F_{\varphi r}(\Omega_2)\rangle = \langle F_{\theta i}(\Omega_1)F_{\varphi i}(\Omega_2)\rangle = 0
\end{aligned} \tag{2.53}$$

$$\begin{aligned}
&\langle F_{\theta r}(\Omega_1)F_{\theta r}(\Omega_2)\rangle = \langle F_{\theta i}(\Omega_1)F_{\theta i}(\Omega_2)\rangle = \\
&\langle F_{\varphi r}(\Omega_1)F_{\varphi r}(\Omega_2)\rangle = \langle F_{\varphi i}(\Omega_1)F_{\varphi i}(\Omega_2)\rangle = C_E\delta(\Omega_1 - \Omega_2)
\end{aligned} \tag{2.54}$$

where $\langle\ \rangle$ represents an ensemble average over all samples, δ is the Dirac delta function [29]. C_E is a constant with units of $(\mathrm{V/m})^2$ and it is proportional to the square of the electric field strength, as shown in the following section. It is useful to interpret the physical meaning of (2.52) – (2.54). (2.52) indicates the mean value of the angular spectrum is zero because the rays from all directions are with random phases. (2.53) means angular spectrum components with orthogonal polarizations or quadrature phase is uncorrelated. (2.54) indicates angular spectrum components arriving from different directions are uncorrelated because they have taken very different multiple scattering paths.

From (2.53) and (2.54), the following useful relationships can also be obtained

$$\langle F_\theta(\Omega_1)F_\varphi^*(\Omega_2)\rangle = 0 \tag{2.55}$$

$$\langle F_\theta(\Omega_1)F_\theta^*(\Omega_2)\rangle = \langle F_\varphi(\Omega_1)F_\varphi^*(\Omega_2)\rangle = 2C_E\delta(\Omega_1 - \Omega_2) \tag{2.56}$$

where * denotes complex conjugate.

2.4.2 Statistical Properties of Fields

In this section, some useful field properties will be derived using (2.47) and (2.52) – (2.56). First of all, the mean value of the electric field $\langle\vec{E}(\vec{r})\rangle$ can be derived as

$$\langle\vec{E}(\vec{r})\rangle = \iint_{4\pi}\langle\vec{F}(\Omega)\rangle exp\left(i\vec{k}\cdot\vec{r}\right)d\Omega = 0 \tag{2.57}$$

This result is expected in a well-stirred RC where the field is the sum of many multipath rays with random phases.

From (2.47), the square of the absolute value of the electric field can be written as

$$\left|\vec{E}(\vec{r})\right|^2 = \iint_{4\pi}\iint_{4\pi}\vec{F}(\Omega_1)\,\vec{F}^*(\Omega_2)exp\left(i\left(\vec{k}_1 - \vec{k}_2\right)\cdot\vec{r}\right)d\Omega_1 d\Omega_2 \tag{2.58}$$

By applying (2.55) and (2.56), the mean-square value of the electric field can be obtained [1]

$$\langle\left|\vec{E}(\vec{r})\right|^2\rangle = 4C_E\iint_{4\pi}d\Omega_2 = 16\pi C_E = E_0^2 \tag{2.59}$$

From (2.59), it can be seen that $\langle\left|\vec{E}(\vec{r})\right|^2\rangle$ is independent of position. This is the spatial uniformity property of an ideal RC.

Similarly, the mean-square values of the rectangular components of the electric field can be derived as

$$\langle|E_x|^2\rangle = \langle\left|E_y\right|^2\rangle = \langle|E_z|^2\rangle = \frac{E_0^2}{3} \tag{2.60}$$

This indicates the isotropy property of an ideal RC.

The magnetic field $\vec{H}$ has the similar statistical properties and the results are listed as follows

$$\langle \vec{H}(\vec{r}) \rangle = 0 \tag{2.61}$$

$$\langle \left| \vec{H}(\vec{r}) \right|^2 \rangle = \frac{E_0^2}{\eta^2} \tag{2.62}$$

$$\langle |H_x|^2 \rangle = \langle \left| H_y \right|^2 \rangle = \langle |H_z|^2 \rangle = \frac{E_0^2}{3} \tag{2.63}$$

where η is the characteristic impedance of the free space.

The energy density W can be written as [10] – [11]

$$W(r) = \frac{1}{2}\left[\varepsilon \left| \vec{E}(\vec{r}) \right|^2 + \mu \left| \vec{H}^*(\vec{r}) \right|^2 \right] \tag{2.64}$$

$$\langle W(r) \rangle = \frac{1}{2}\left[\varepsilon \langle \left| \vec{E}(\vec{r}) \right|^2 \rangle + \mu \langle \left| \vec{H}^*(\vec{r}) \right|^2 \rangle \right] = \varepsilon E_0^2 \tag{2.65}$$

It can be seen that the average value of the energy density is also independent of position.

The power density or Poynting vector $\vec{S}$ can be written as

$$\vec{S}(\vec{r}) = \vec{E}(\vec{r}) \times \vec{H}^*(\vec{r}) \tag{2.66}$$

The mean value of $\vec{S}$ is

$$\langle \vec{S}(\vec{r}) \rangle = 0 \tag{2.67}$$

A physical interpretation of (2.67) is that each plane wave carries equal power in any direction so that the vector sum over the whole space is zero [1]. The result shows that $\vec{S}$ is not the proper quantity to characterize the field strength in an RC while $\langle W(r) \rangle$ is an appropriate quantity.

Similar to the plane wave in free space, a scalar power density can be defined as

$$S = c\langle W \rangle = \frac{E_0^2}{\eta} \tag{2.68}$$

2.4.3 Probability Density Functions for the Fields

The knowledge of the probability density functions (PDF) of the filed quantities can be very useful for analysis of measured data in an RC because the measured data in an RC is always based on a limited number of samples. The rectangular components can be written in terms of their real and imaginary parts as

$$E_x = E_{xr} + iE_{xi}, \quad E_y = E_{yr} + iE_{yi}, \quad E_z = E_{zr} + iE_{zi} \tag{2.69}$$

where E_{xr} / E_{yr} / E_{zr} and E_{xi} / E_{yi} / E_{zi} are the real and imaginary part of E_x / E_y / E_z. From (2.52) – (2.54), it can be derived that the mean values of all the real and imaginary parts in (2.69) are zero

$$\langle E_{xr} \rangle = \langle E_{xi} \rangle = \langle E_{yr} \rangle = \langle E_{yi} \rangle = \langle E_{zr} \rangle = \langle E_{zi} \rangle = 0 \tag{2.70}$$

and the variances of the real and imaginary parts are half the result for the complex components in (2.60)

$$\langle E_{xr}^2 \rangle = \langle E_{xi}^2 \rangle = \langle E_{yr}^2 \rangle = \langle E_{yi}^2 \rangle = \langle E_{zr}^2 \rangle = \langle E_{zi}^2 \rangle = \frac{E_0^2}{6} \equiv \sigma^2 \tag{2.71}$$

If the mean and variance are specified for a PDF over the range from - ∞ to ∞, then the maximum entropy theorem [30] or central limit theorem [31] predicts a Gaussian PDF. So the PDF of E_{xr} is

$$f(E_{xr}) = \frac{1}{\sqrt{2\pi}\sigma} exp\left[-\frac{E_{xr}^2}{2\sigma^2}\right] \tag{2.72}$$

where σ is defined in (2.71). The other real and imaginary parts of the electric components have the same PDF.

It has also been proved that the real and imaginary parts of the electric field components are uncorrelated, i.e.,

$$\langle E_{xr}(\vec{r}) E_{xi}(\vec{r}) \rangle = 0 \tag{2.73}$$

For now, it has been known that the real and imaginary parts of the rectangular components of the electric field are independent, normally distributed with zero mean and equal variances. Therefore, the following conclusions can be deduced

$$f(|E_x|) = \frac{|E_x|}{\sigma^2} exp\left[-\frac{|E_x|^2}{2\sigma^2}\right] \tag{2.74}$$

That is the magnitude of E_x has a Rayleigh distribution [31]. The comparison of (2.74) with measured data at 2.0 GHz in the University of Liverpool RC is shown in Figure 2.13. The two stirrers are stepwise rotated simultaneously. The total number of samples is 120. As can be seen, good agreement between measured data and theoretical prediction is obtained.

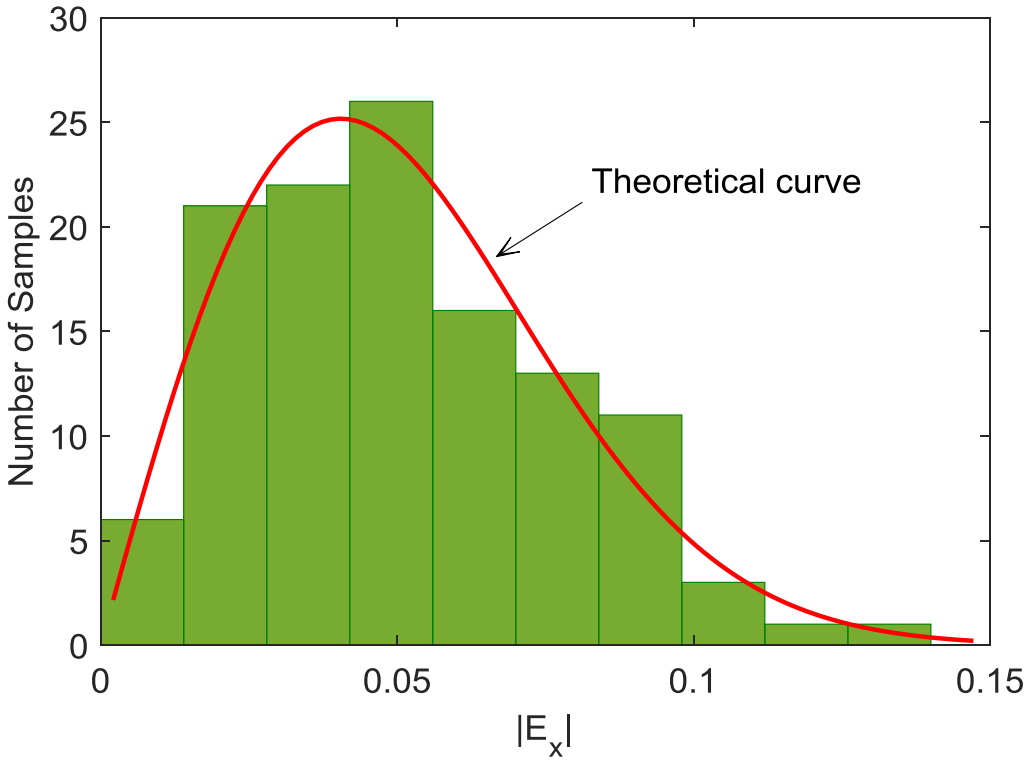

Figure 2.13 Comparison of the measured PDF of $|E_x|$ with theoretical Rayleigh distribution.

The squared magnitude of E_x is chi-square distributed with two degrees of freedom (exponential distribution) [31]

$$f(|E_x|^2) = \frac{1}{2\sigma^2} exp\left[-\frac{|E_x|^2}{2\sigma^2}\right] \tag{2.75}$$

The comparison of (2.75) with measured data at 2.0 GHz in the University of Liverpool RC is shown in Figure 2.14. (2.74) and (2.75) also hold for E_y and E_z.

The total electric field magnitude is chi distributed with six degrees of freedom [31]

$$f(|\vec{E}|) = \frac{|\vec{E}|^5}{8\sigma^6} exp\left[-\frac{|\vec{E}|^2}{2\sigma^2}\right] \tag{2.76}$$

The squared magnitude of the total electric field is chi-square distributed with six degrees of freedom [31]

$$f\left(|\vec{E}|^2\right) = \frac{|\vec{E}|^4}{16\sigma^6} exp\left[-\frac{|\vec{E}|^2}{2\sigma^2}\right] \tag{2.77}$$

The dual PDFs for the magnetic field can be obtained by the aforementioned procedure. And the dual of the results in (2.74) – (2.77) can be obtained by replacing E by H and σ by σ_H [1].

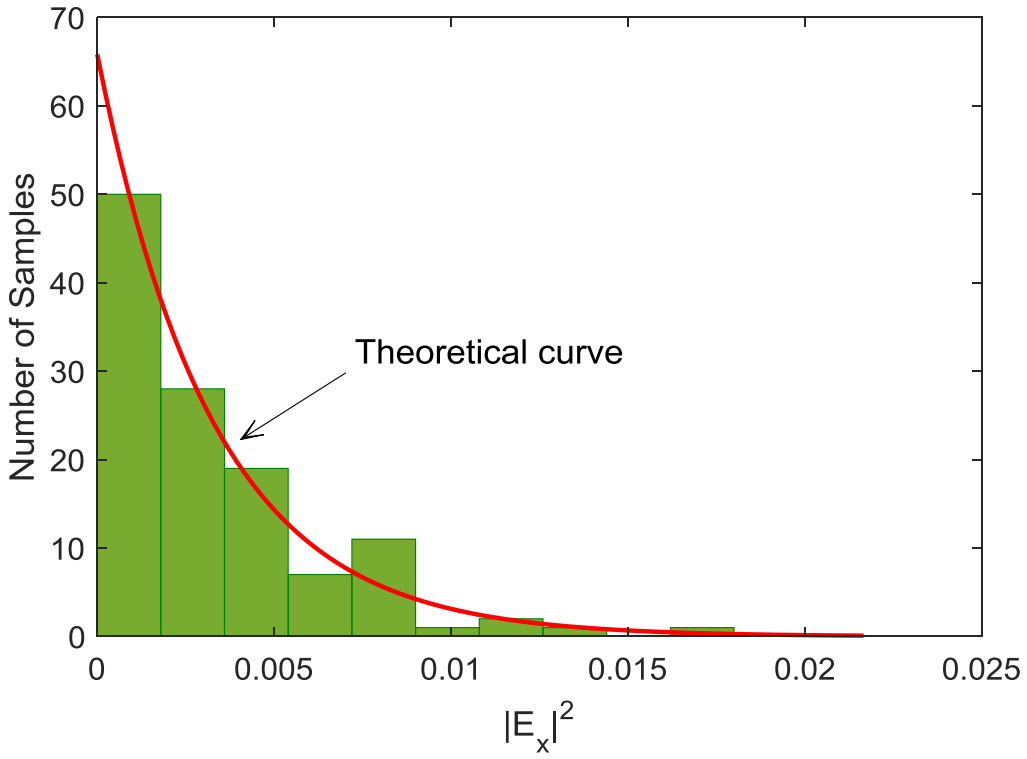

Figure 2.14 Comparison of the measured PDF of $|E_x|^2$ with theoretical exponential distribution.

2.4.4 Loss Mechanism and *Q* Factor

The *Q* factor describes the rate at which an RC loses energy due to the overall losses inside [3] [32]. Generally, there are four loss terms in an RC: the RC wall loss (Q_1), the loss due to aperture leakage (Q_2), the loss of lossy objects (Q_3), and the antenna loss (Q_4).

The total *Q* factor can be defined as [1], [3] [33].

$$Q = \omega U_s / P_d \tag{2.78}$$

where ω is the angular frequency, U_s is the steady state energy and P_d is the power dissipated.

$$U_s = WV \tag{2.79}$$

where *V* is the volume of the RC and *W* is the energy density as defined before.

$$W = \varepsilon_0 E^2 \tag{2.80}$$

where ε_0 is the permittivity of the medium in the RC (free space) and *E* is the RMS (root-mean-square) electric field. The power density S_c in the RC can be expressed as

$$S_c = \frac{E^2}{\eta_0} = cW \tag{2.81}$$

where $\eta_0 = \sqrt{\mu_0/\varepsilon_0}$ is the intrinsic impedance of the medium in the RC.

To calculate the *Q* factor of the RC, all losses should be accounted for. Thus, it can be derived

$$P_d = P_{d1} + P_{d2} + P_{d3} + P_{d4} \tag{2.82}$$

where P_{d1} is the power dissipated in the cavity walls, P_{d2} is the power absorbed by lossy objects within the cavity, P_{d3} is the power leaked through apertures, and P_{d4} is the power dissipated on receiving antennas [3]. By substituting (2.82) into (2.78) the following expression can be written for the inverse of *Q*

$$Q^{-1} = Q_1^{-1} + Q_2^{-1} + Q_3^{-1} + Q_4^{-1} \tag{2.83}$$

where

$$Q_1 = \omega U_s/P_{d1}, \quad Q_2 = \omega U_s/P_{d2} \quad Q_3 = \omega U_s/P_{d3} \quad Q_4 = \omega U_s/P_{d4} \tag{2.84}$$

The separate loss terms Q_1 to Q_4 can analysed as follows

$$Q_1 = \frac{3V}{2\mu_{wr} S_a \delta} \tag{2.85}$$

where $\delta = \sqrt{1/\pi f \mu_w \sigma_w}$, $\mu_{wr} = \mu_w/\mu_0$. μ_w and σ_w are the permeability and conductivity of the wall material, respectively. μ_{wr} is the relative permeability of the wall material. δ is the skin depth and S_a is the RC surface area.

$$Q_2 = \frac{2\pi V}{\lambda \langle \sigma_a \rangle} \tag{2.86}$$

where $\langle \sigma_a \rangle$ is the averaged absorption cross section of the lossy objects loading the chamber and λ is the wavelength. A measurement procedure to deduce this term can be found in [33] – [37].

$$Q_3 = \frac{4\pi V}{\lambda \langle \sigma_l \rangle} \tag{2.87}$$

where $\langle \sigma_l \rangle$ is the average transmission cross section of any apertures.

$$Q_4 = \frac{16\pi^2 V}{m\lambda^3} \tag{2.88}$$

where m is the impedance mismatch factor (m = 1 for a matched load).

Under steady-state conditions, the power transmitted into the chamber (P_t) is equal to the power dissipated by the overall loss, i.e.,

$$P_t = P_d \tag{2.89}$$

By substituting (2.78), (2.79), (2.81) into (2.89), the power density in the RC can be rewritten as

$$S_c = \frac{\lambda Q P_t}{2\pi V} \tag{2.90}$$

If an impedance matched antenna is used, then the received power (P_r) is a product of the effective area $\lambda^2/8\pi$ [38] – [39] and the received power can be expressed as

$$P_r = \frac{\lambda^3 Q}{16\pi^2 V} P_t \tag{2.91}$$

Solving (2.91) in terms of Q yields the chamber Q factor in terms of the measured power ratio (P_r/P_t). Thus (2.92) represents a commonly used frequency-domain approach to measure the chamber Q factor [40] – [41]. The equation assumes well matched and lossless antennas.

$$Q = \frac{16\pi^2 V}{\lambda^3} \times \frac{P_r}{P_t} \tag{2.92}$$

where

$$\frac{P_r}{P_t} = \frac{\langle |S_{21}|^2 \rangle}{(1 - |\langle S_{11} \rangle|^2)(1 - |\langle S_{22} \rangle|^2)} \tag{2.93}$$

where S_{11} and S_{22} are the reflection coefficients of antenna 1 and antenna 2, respectively and S_{21} is the transmission coefficient of the two antennas. It should be noted that if the antennas are not ideal, the antenna loss (including ohmic loss and mismatch loss) should be calibrated out when using (2.92) and (2.93).

2.4.5 Chamber Decay Time

Up to this point, only the frequency-domain response of the RC has been considered. In the following part, the time-domain response will be considered which is of interest for transient applications. The case of field decay where the excitation source is instantaneously turned off is first considered. The following differential equation can be obtained

$$dU = -P_d dt \tag{2.94}$$

where dU is the energy change in the RC over a time increment dt. Use (2.78) to replace P_d in (2.94)

$$dU = -(\omega U/Q)dt = -\frac{U}{\tau} dt \tag{2.95}$$

where the chamber decay time (or chamber time constant) $\tau = Q/\omega$. Using the initial condition $U = U_s$ at $t = 0$, (2.95) can be solved as

$$U = U_s exp(-t/\tau), \quad t > 0 \tag{2.96}$$

The chamber decay time τ has been measured by fitting the decay curve in (2.96) to experimental data [40] – [44]. Once τ has been determined, the frequency-dependent Q is determined from

$$Q = \omega\langle\tau\rangle \tag{2.97}$$

where $\langle\ \rangle$ signifies the ensemble average. Equation (2.97) offers a time-domain method to measure Q. The comparison of the measured Q with the frequency-domain method and time-domain method is shown in Figures 2.15. A good agreement between the time-domain Q and the frequency-domain Q is shown when the antenna loss is removed. When the antenna loss is included, the frequency-domain Q is lower than the time-domain Q. Actually, for this case, the ratio of the frequency-domain Q and the time-domain Q contains the information of the antenna efficiency. Three antenna efficiency measurement techniques based on this fact is discussed in detail in [40].

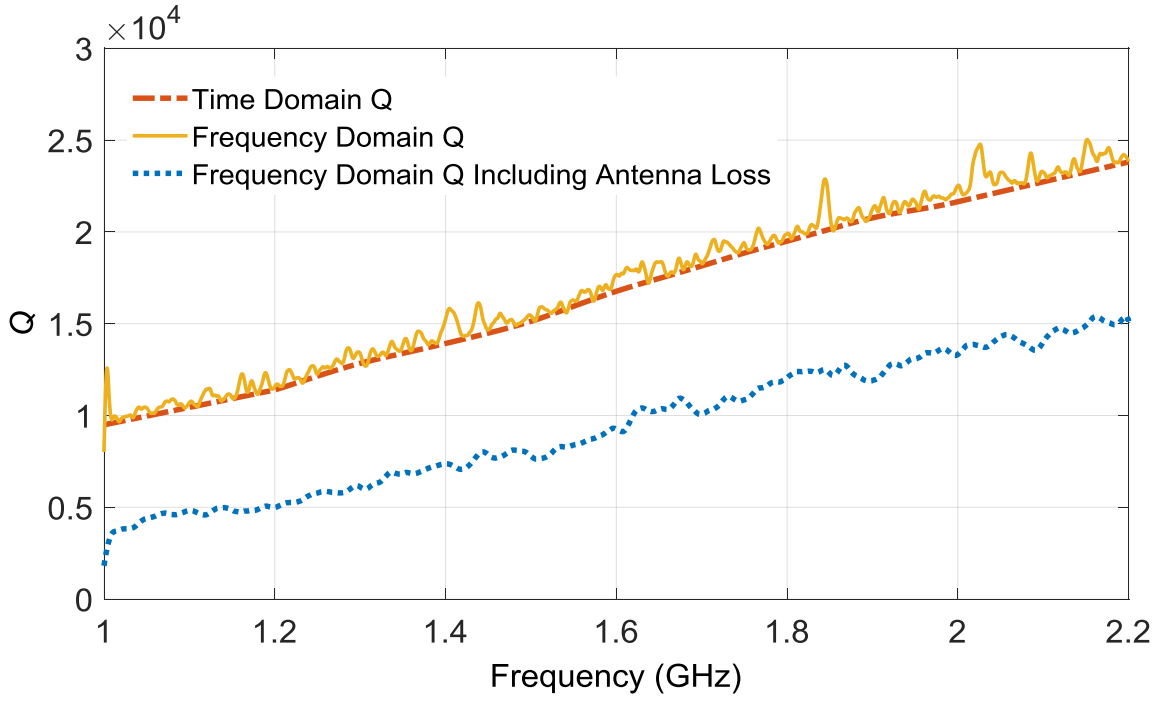

Figure 2.15 Comparison of the frequency-domain *Q* and the time-domain *Q*.

2.4.6 Stirred and Unstirred Power

As stated above, the magnitude of any of the electric field components is statistically Rayleigh distributed in theory. However, if any line-of-sight (LoS) path exists in an RC, the stirred power and the unstirred power together will manifest itself as being Rician distributed [13]. The unstirred power is the power that is coupled directly from the transmitting antenna to the receiving antenna without interaction with any mode stirrers. The stirred power results from the power radiating from a transmitting antenna that fully interacts with the mode stirrers before being captured by the receiving antenna [13], [45] – [46]. In practice, the RC could be used to emulate a Rician environment if desired [45]. However, for most of the measurements in an RC, any unstirred power is supposed to be minimised and a Rayleigh environment is desired.

The unstirred multipath propagation in the RC can be characterized by the Rician *K*-factor. A brief derivation of this quantity is summarised as follows.

Any transmission measurement in an RC essentially comprises of the chamber's physical and statistical properties [13]. This measured complex transmission coefficient S_{21} consists of two parts: the unstirred part ($S_{21,u}$) and the stirred part ($S_{21,s}$).

$$S_{21} = S_{21,u} + S_{21,s} \tag{2.98}$$

$$S_{21,u} = S_{21,u}^{r} + iS_{21,u}^{i} \tag{2.99}$$

$$S_{21,s} = S_{21,s}^{r} + iS_{21,s}^{i} \tag{2.100}$$

The unstirred components $S_{21,u}^{r}$ and $S_{21,u}^{i}$ are constants with zero variance for a given measurement configuration, and the stirred components $S_{21,s}^{r}$ and $S_{21,s}^{i}$ are supposed to be independent Gaussian random variables with zero mean and identical variance σ^2 under ideal RC conditions, i.e., pure non-line-of-sight (NLoS) environment. That is

$$\langle S_{21,s} \rangle = 0 \tag{2.101}$$

$$S_{21,s}^{r} \sim N(0, \sigma^2) \quad \text{and} \quad S_{21,s}^{i} \sim N(0, \sigma^2) \tag{2.102}$$

where $\langle\ \rangle$ signifies the ensemble average. Then it can be derived

$$S_{21}^{r} \sim N\left(S_{21,u}^{r}, \sigma^2\right) \quad \text{and} \quad S_{21}^{i} \sim N\left(S_{21,u}^{i}, \sigma^2\right) \tag{2.103}$$

From the above distribution analysis, the stirred and unstirred power can be express as

$$\text{stirred power} = \langle |S_{21} - \langle S_{21} \rangle|^2 \rangle = 2\sigma^2 \tag{2.104}$$

$$\text{unstirred power} = |\langle S_{21} \rangle|^2 = d \tag{2.105}$$

This is seen visually by referring to the scattering plots in Figure 2.16(a) and (b). *d* is the distance of the centroid (green dot) of the clutter from the origin (red dot). As can be seen from Figure 2.16(b), the bias of the cluster of data from the origin is very small, which represents the case where very weak direct antenna coupling is present. This is desired for a well-stirred RC.

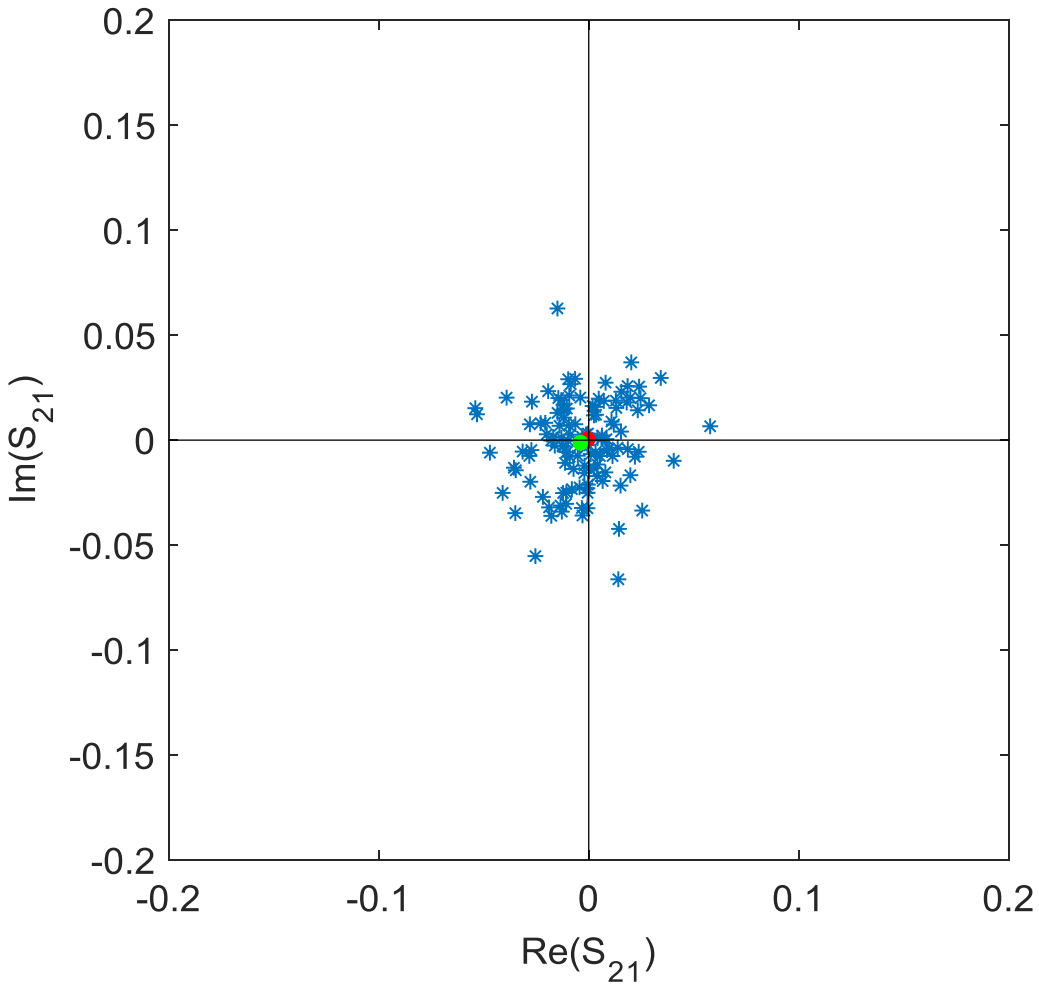

(a)

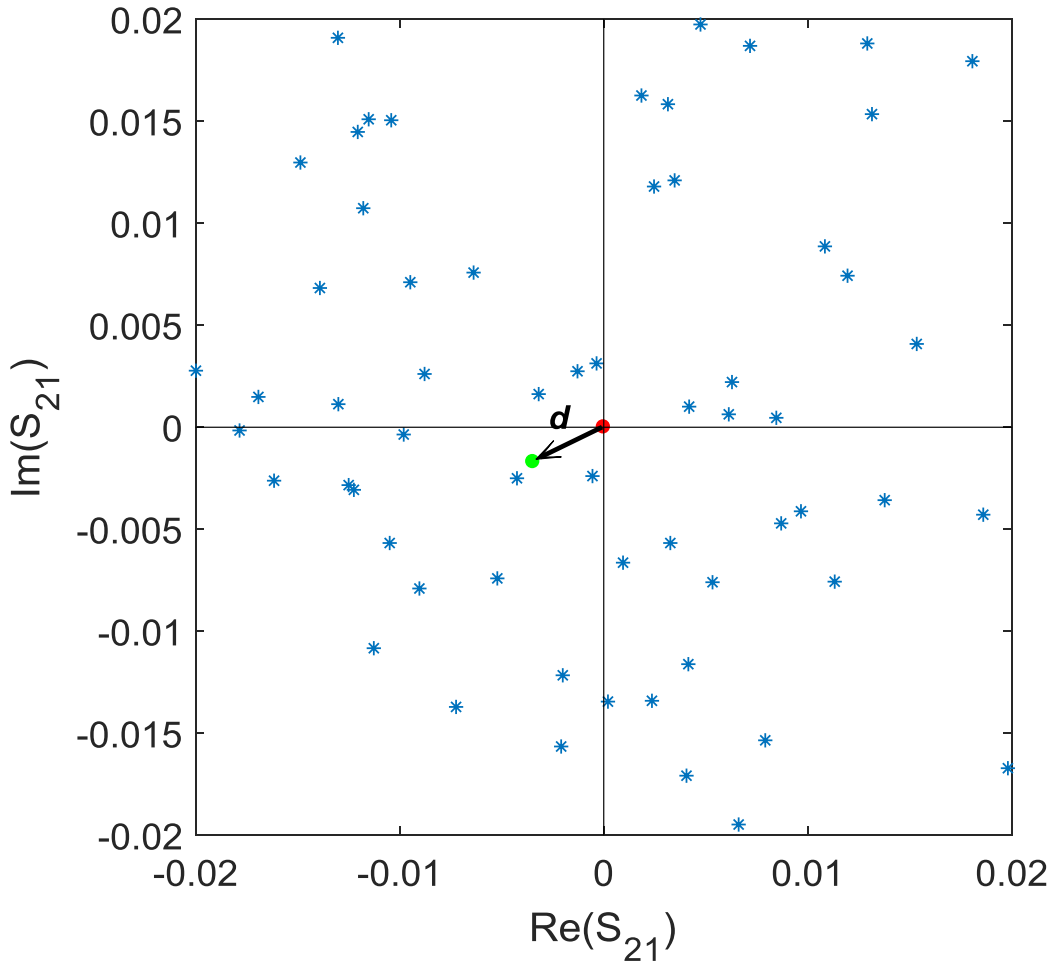

(b)

Figure 2.16 Scatter plot of measured S_{21} at 4.0 GHz: (a) normal view, and (b) zoom in.

The Rician *K*-factor defined as the ratio of the unstirred power to the stirred power can be expressed as [46] – [48]

$$K = \frac{d^2}{2\sigma^2} = \frac{|\langle S_{21}\rangle|^2}{\langle |S_{21} - \langle S_{21}\rangle|^2\rangle} \tag{2.106}$$

It is an important characteristic parameter for a wireless fading channel since it is a measure of the distribution of the components of the received signal resulting from various interactions with the surrounding environment. Here, the *K*-factor for an RC setup exhibiting good field uniformity is estimated, i.e., for a chamber with lower values of *K*-factor. [49]. A

well-stirred RC should typically have a Rician *K*-factor value below 0.1 [49]. RC setups with such low *K*-factors enable low measurement uncertainty for over-the-air tests [50].

Figure 2.17(a) and (b) depict the measurement setup and the measured Rician *K*-factor as a function of frequency in the RC at the University of Liverpool, respectively. During the measurement, antenna 1 directed to one corner of the RC and antenna 2 directed to the vertical stirrer to avoid LoS illumination. It can be seen that the stirred power in the RC is dominant as the measured *K*-factor value is below 0.1. That means any LoS path is very small and as a result, the statistical form of the magnitudes will tend towards a Rayleigh distribution as opposed to a Rician distribution (ideal Rayleigh distribution: $K \rightarrow 0$).

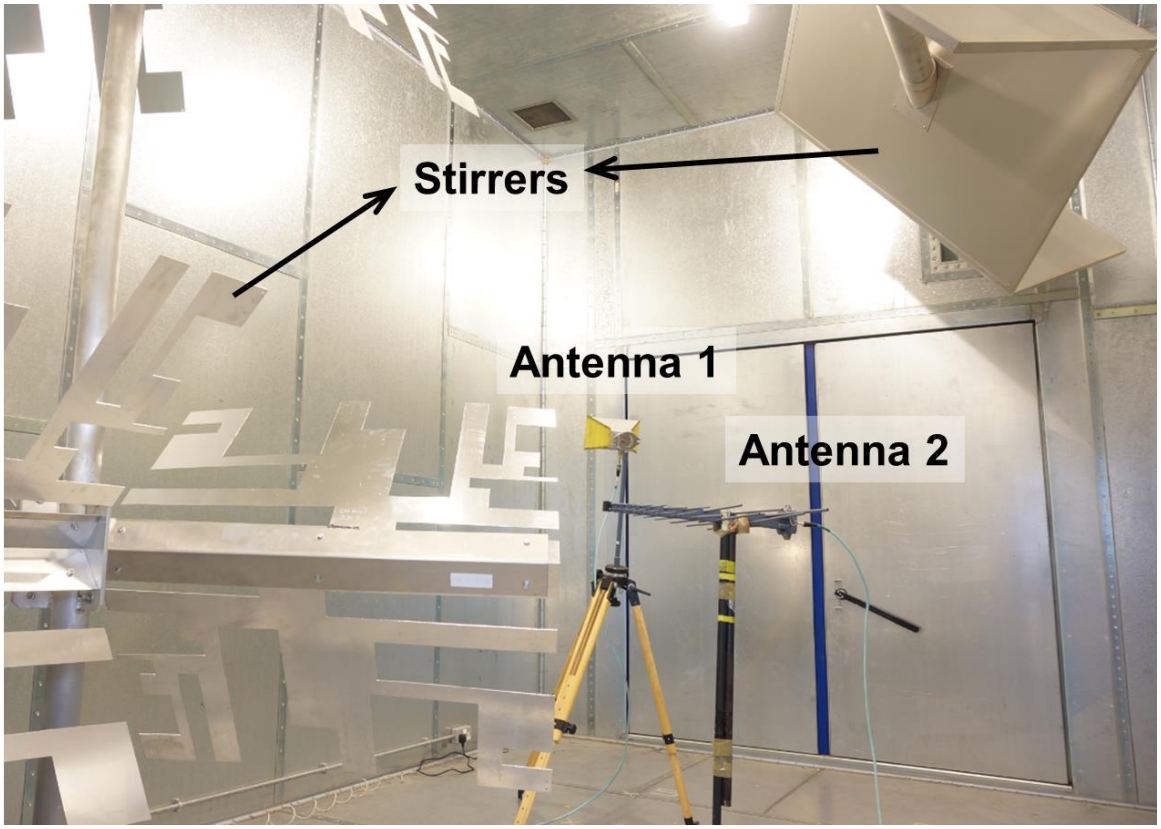

(a)

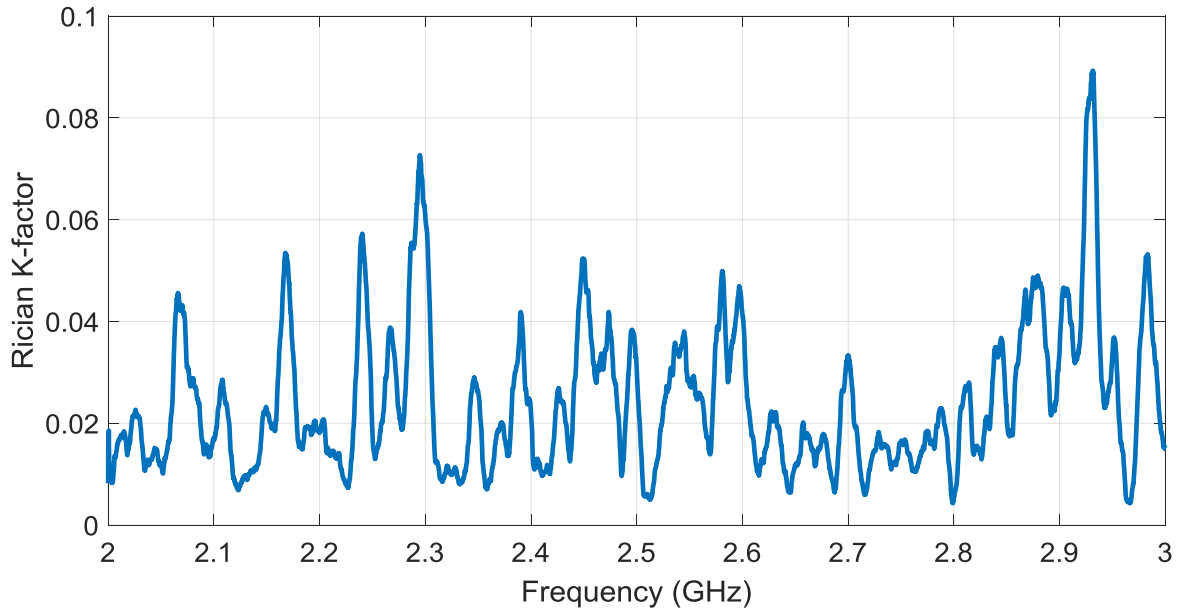

(b)

Figure 2.17 Rician *K*-factor from 2.0 to 3.0 GHz: (a) measurement setup, (b) measured results.

Similar to the transmission coefficient, the reflection coefficient measured in the RC also comprises of the stirred part ($S_{11,s}$) and the unstirred part ($S_{11,u}$)

$$S_{11} = S_{11,u} + S_{11,s} \tag{2.107}$$

The unstirred part $S_{11,u}$ includes the contribution of the antenna mismatch (free space response) and the unstirred energy in the RC. If the RC is ideally stirred [44], i.e., the RC environment in a pure Rayleigh environment, the stirred part $S_{11,s}$ is of Gaussian distribution with zero mean. Thus, the following relationship can be derived

$$\langle S_{11} \rangle = \langle S_{11,u} \rangle = S_{11,fs} \tag{2.108}$$

where $S_{11,fs}$ is the free-space antenna reflection coefficient. The $S_{11,fs}$ is measured in the RC and in the AC, respectively, as shown in Figure 2.18(a) and (b). An LPDA was selected as the antenna under test (AUT). The complex *S*-parameters measured in the RC were averaged over 360 stirrer positions. 10,001 points were sampled in the frequency range of 0 to 10 GHz. A comparison of measured results in both amplitude and phase is depicted in Figure 2.19(a)

and (b), respectively. In Figure 2.19(b), only 0 – 2 GHz is selected for the clearer show. It can be seen that the measured results in the RC and the AC agree very well. At the lower frequency band (from 200 – 600 MHz), the RC is not very well stirred, and therefore some small difference shows. From 0 – 200 MHz, the two curves also agree well, but it is because of the antenna mismatch (radiation is low) while not the well-stirred field.

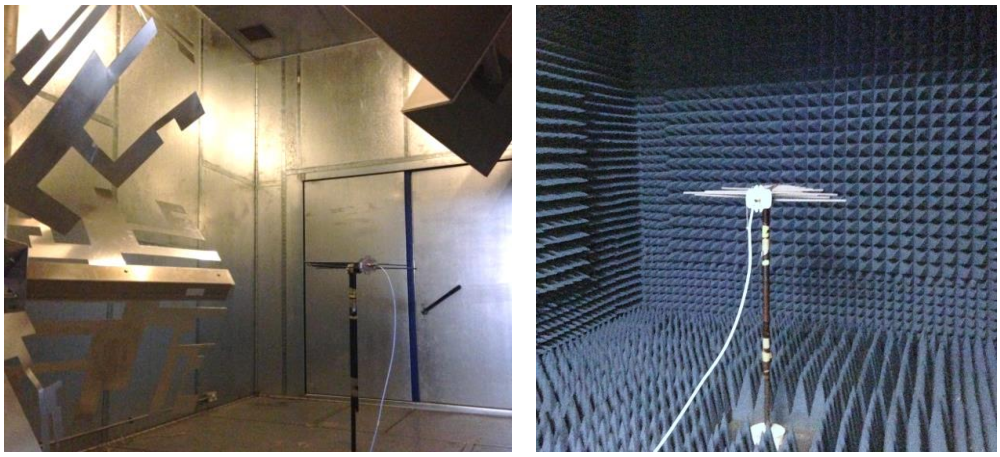

(a) **(b)**

Figure 2.18 Free-space antenna reflection coefficient measurement setups: (a) in the RC, and (b) in the AC, respectively.

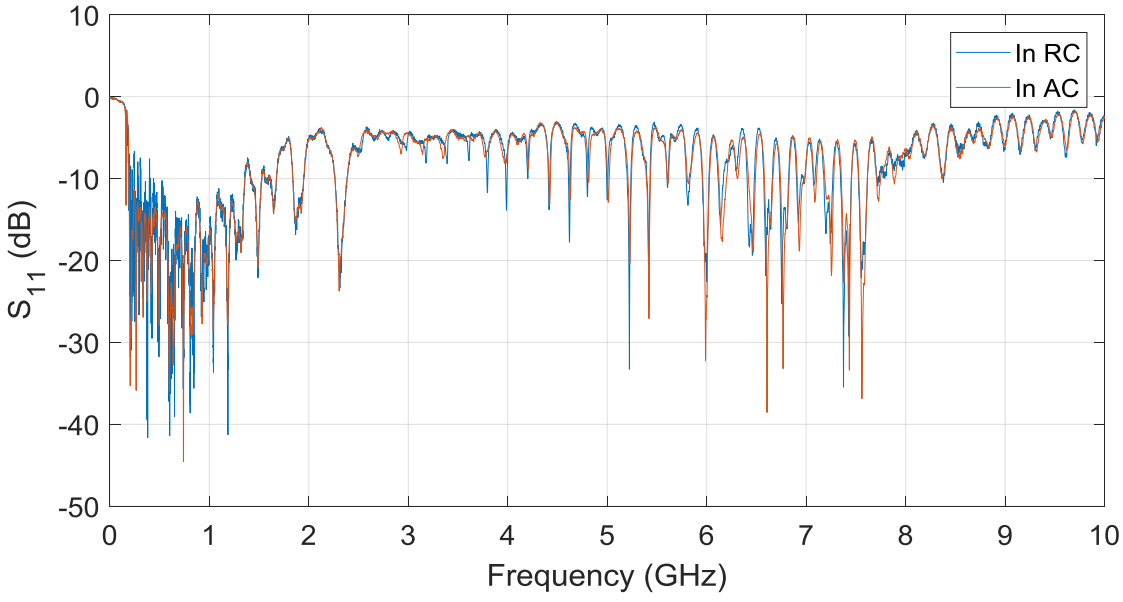

(a)

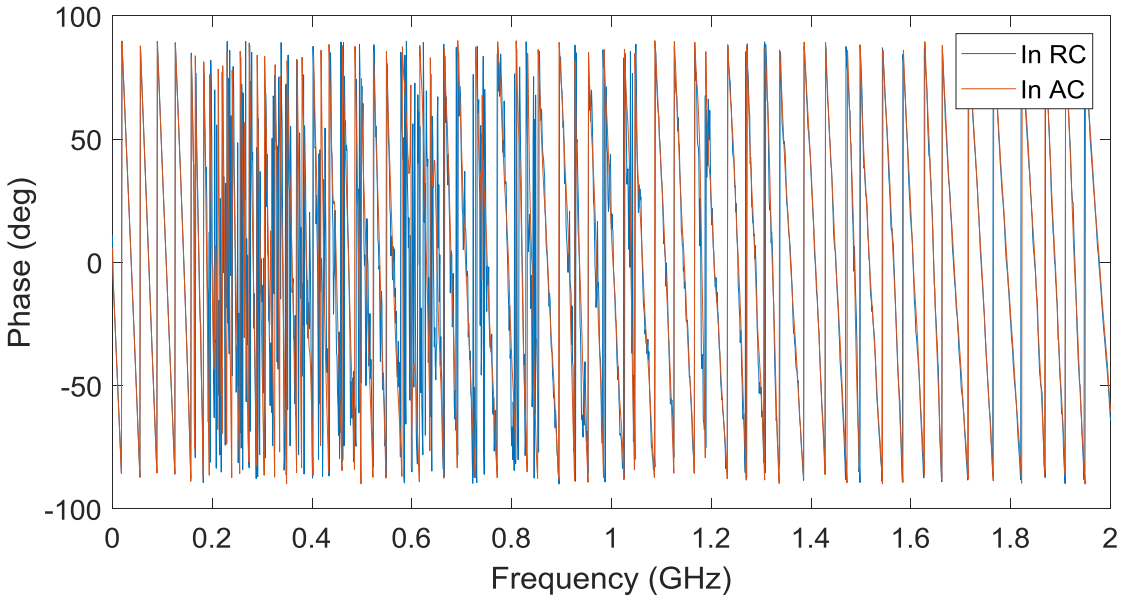

(b)

Figure 2.19 Comparison of measured free-space antenna reflection coefficient in RC and AC in both (a) amplitude and (b) phase.

2.4.7 Enhanced Backscatter Effect

The enhanced backscatter effect was first observed by John M. Ladbury and David A. Hill in the year of 2007 [51] and subsequently used to characterize the performance of RCs [52] and measure the radiation efficiency of antennas [40], [53] – [54]. It states that the power received by the source antenna is higher than that at any other random location in the RC [52]. Using the infinite plane wave integration model it is found that

$$\langle P_{rf} \rangle = e_b \langle P_{rx} \rangle \tag{2.109}$$

where P_{rx} is the power incident at the receiving antenna, P_{rf} is the power reflected back to the transmitting antenna, e_b is defined as the enhanced backscatter coefficient, and $\langle\ \rangle$, as before, indicates the ensemble average. For idealized antennas (well-matched, lossless)

$$e_b = 2 \tag{2.110}$$

That is, in an ideally stirred RC the average power received by the transmitter is twice as the

power received by the receiver [1], [52]. This phenomenon is observed in other disciplines as well, such as scattering from the rough surface in optics [55], and reverberant acoustical fields [56] – [57].

Under the assumption that the field can be described as an infinite sum of plane waves and the antennas used are perfectly matched and lossless, e_b can be related to the *S*-parameters by

$$\langle |S_{11}|^2 \rangle = e_b \langle |S_{21}|^2 \rangle \tag{2.111}$$

However, for real antennas of non-ideal characteristics, (2.111) needs to be modified. The final result is obtained by

$$e_b = \frac{\langle |S_{11,s}|^2 \rangle}{\langle |S_{21,s}|^2 \rangle} \tag{2.112}$$

where

$$S_{11,s} = S_{11} - \langle S_{11} \rangle, \text{ and } S_{21,s} = S_{21} - \langle S_{21} \rangle \tag{2.113}$$

An experimental verification of (2.111) in the University of Liverpool RC is shown in Figure 2.20. As can be seen, the agreement with the factor of 2 is good above 200 MHz where the mode density of the RC is sufficiently high. The number of samples at each frequency is 120.

For now, it is known that the enhanced backscatter factor is 2 for an ideally stirred RC, but what is the size of the region over which the enhanced backscatter occurs? It has been proved that the enhanced backscatter constant varies as a function of distance *r* [1]

$$e_b = 1 + \frac{sin(2kr)}{2kr} \tag{2.114}$$

where *r* is the distance between the source and the random location in the RC. Considering two extreme cases $r = 0$ and $r \to \infty$. It is easy to conclude that when $r = 0$, $e_b = 2$, which is consistent with the uniform-field result in (2.110). And when $r \to \infty$, $e_b = 1$, i.e., no enhanced backscatter effect occurs. (2.114) is plotted in Figure 2.21. It can be seen that when $r > \lambda/4$, e_b is close to 1. The region of enhanced backscatter can be defined as the distance from which $e_b = 1$. Hence, the region of enhanced backscatter is a fairly small (especially for high frequency) sphere of radius $\lambda/4$ [1].

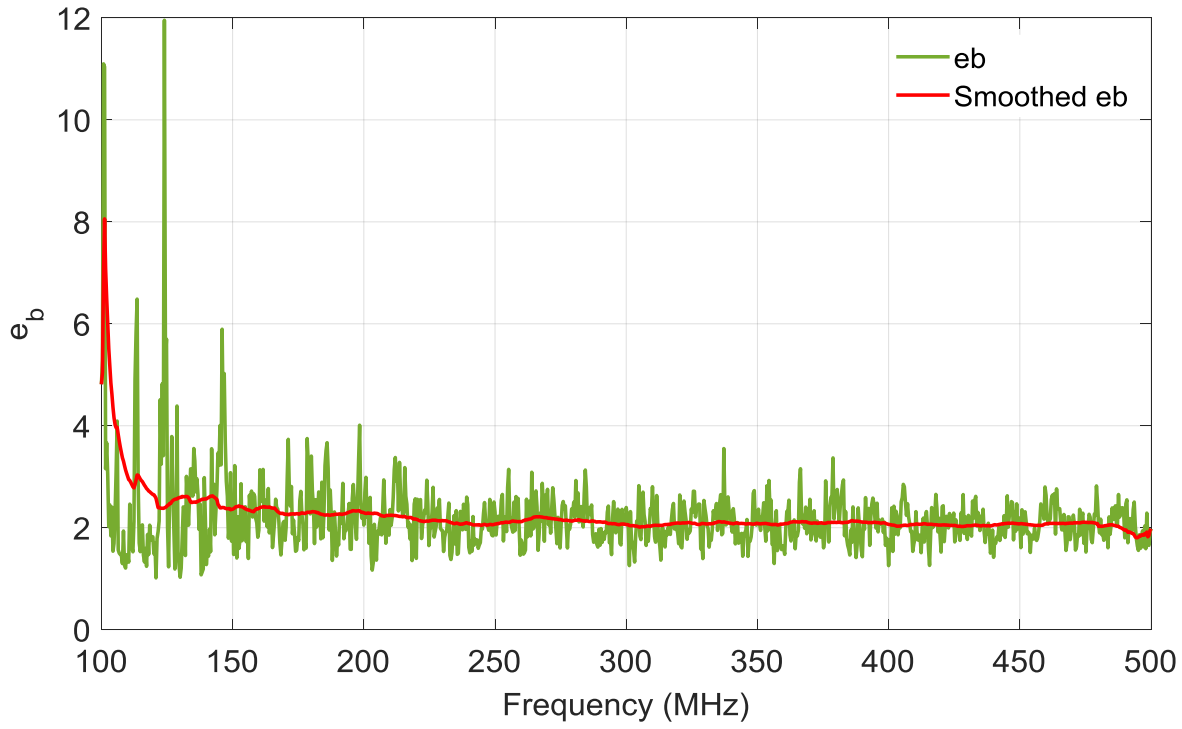

Figure 2.20 Enhanced backscatter coefficient from 100 MHz to 500 MHz.

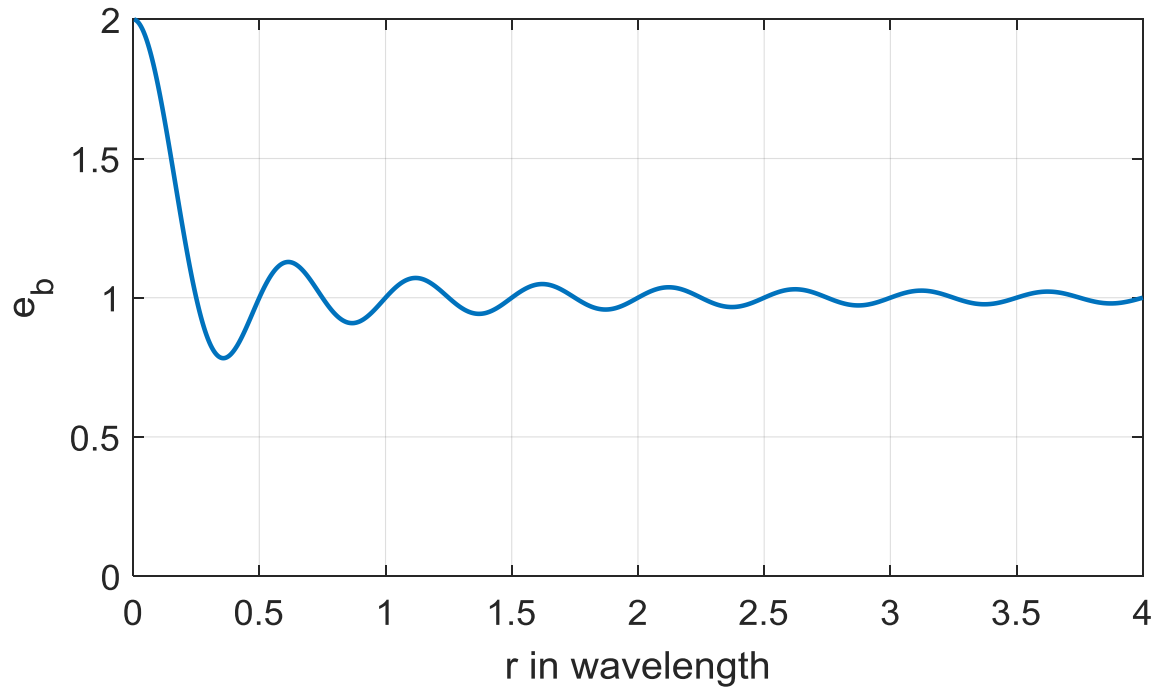

Figure 2.21 Enhanced backscatter coefficient as a function of distance *r*.

2.5 Summary

In this chapter, the fundamental concepts, parameters, and theories of an RC were introduced. In the beginning, the deterministic theory was introduced. The RC was abstracted to an empty rectangular cavity. The TE and TM modes, the number of modes, the modal density, and the Green's function were presented. The cavity modes could be used to derive the guidelines for the LUF of an RC but not sufficient to analyse the actual EM field distribution within an RC. With the help of Green's function, the EM field distribution could be stringently analysed and vividly visualized. In a next step, the statistical theory was introduced. The RC was described as a statistical test environment and the EM fields were analysed using plane-wave integration model. The statistical properties of fields, the loss mechanism, the stirred and unstirred power, and the enhanced backscatter effect were presented. These concepts and theories are used extensively throughout the following chapters and establish the foundation on which the RC measurement is built.

2.6 References

[1] D. A. Hill, Electromagnetic Fields in Cavities: Deterministic and Statistical Theories. New York, NY, USA: Wiley-IEEE Press, 2009.

[2] T.H. Lehman, "A statistical theory of electromagnetic fields in complex cavities," EMP Interaction Note 494, 1993.

[3] D. A. Hill, M. T. Ma, A. R. Ondrejka, B. F. Riddle, M. L. Crawford, and R. T. Johnk, "Aperture excitation of electrically large, lossy cavities," *IEEE Trans. Electromagn. Compat.*, vol. 36, pp. 169-178, 1994.

[4] J. B. Gros, U. Kuhl, O. Legrand, F. Mortessagne, and E. Richalot, "Universal intensity statistics in a chaotic reverberation chamber to refine the criterion of statistical field uniformity," in *Proc. IEEE Metrology for Aerospace (MetroAeroSpace)*, Benevento, 2015, pp. 225-229.

[5] X. Chen, "Generalized Statistics of Antenna Efficiency Measurement in a Reverberation Chamber," *IEEE Trans. Antenna Propag.*, vol. 62, no. 3, pp. 1504-1507, Mar. 2014.

[6] A. Cozza, "A statistics-based definition of the overmoded condition for reverberation chambers," *2011 URSI General Assembly and Scientific Symposium*, Istanbul, 2011, pp. 1-4.

[7] *Electromagnetic Compatibility (EMC) part 4-21: Testing and measurement techniques-Reverberation chamber test methods*, IEC 61000-4-21, 2003.

[8] D. A. Hill, "Plane wave integral representation for fields in reverberation chambers," *IEEE Trans. Electromagn. Compat.*, vol. 40, pp. 209-217, 1998.

[9] D. A. Hill, "Electromagnetic Theory of Reverberation Chambers," NIST Technical Note 1506, Dec. 1998.

[10] David M. Pozar, Microwave Engineering. Singapore: Wiley, *4th* ed., 2011.

[11] R. E. Collin, Foundations for Microwave Engineering. New York, NY: McGraw-Hill, 1966.

[12] Christian Bruns, "Three-dimensional Simulation and Experimental Verification of a Reverberation Chamber," Ph.D. dissertation, Swiss Federal Institute of Technology Zurich, Zurich, Switzerland, 2005.

[13] S. J. Boyes, and Yi Huang, Reverberation Chambers: Theories and Applications to EMC and Antenna Measurements, West Sussex, WS, UK: Wiley, 2016.

[14] K. Rosengren, and P. S. Kildal, "Study of distributions of modes and plane waves in reverberation chambers for the characterization of antennas in a multipath environment," *Microw. Opt. Technol. Lett.*, vol. 30, pp. 386-391, 2001.

[15] P. S. Kildal, X. Chen, C. Orlenius, M. Franzen, and C. S. L. Patane, "Characterization of Reverberation Chambers for OTA Measurements of Wireless Devices: Physical Formulations of Channel Matrix and New Uncertainty Formula," *IEEE Trans. Antennas Propag.*, vol. 60, pp. 3875-3891, 2012.

[16] L. R. Arnaut, "Operation of electromagnetic reverberation chambers with wave diffractors at relatively low frequencies," *IEEE Trans. Electromagn. Compat.*, vol. 43, no. 4, pp. 637-653, Nov. 2001.

[17] *Requirement for the Control of Electromagnetic Interference Characteristics of Subsystems and Equipment*, MIL-STD-461E, 1999.

[18] B. H. Liu, D. C. Chang, and M. T. Ma, "Eigenmodes and the composite quality factor of a reverberating chamber," National Bureau of Standards (NBS), Tech. Rep., 1983.

[19] Y. Huang, and D. J. Edwards, "A novel reverberating chamber: the source-stirred chamber," in *Proc. 8th Int. Conf. Electromagn. Compat.*, Edinburgh, U.K., Sept. 1992, pp. 120-124.

[20] Y. Huang, "The investigation of chamber for electromagnetic systems," Ph.D. dissertation, Dept. of Eng. Sci., Univ. of Oxford, Oxford, U.K., 1993.

[21] D. I. Wu, and D. C. Chang, "The effect of an electrically large stirrer in a mode-stirred chamber," *IEEE Trans. Electromagn. Compat.*, vol. 31, no. 2, pp. 164-169, May 1989.

[22] M. L. Crawford, and G. H. Koepke, "Design, Evaluation, and Use of a Reverberation Chamber for Performing Electromagnetic Susceptibility/Vulnerability Measurements," NBS Technical Note 1092, Apr. 1986.

[23] D. A. Hill, "Electronic mode stirring for reverberation chambers," *IEEE Trans. Electromagn. Compat.*, vol. 36, no. 4, pp. 294-299, Nov. 1994.

[24] C. R. Dunlap, "Reverberation chamber characterization using enhanced backscatter coefficient measurements," Ph.D. dissertation, Dept. of Elect., Comput. and Eng., Univ. of Colorado, Boulder, USA, 2013.

[25] A. De Leo, V. M. Primiani, P. Russo, and G. Cerri, "Low-Frequency Theoretical Analysis of a Source-Stirred Reverberation Chamber," *IEEE Trans. Electromagn. Compat.*, vol. 59, no. 2, pp. 315-324, Apr. 2017.

[26] R. H. Price, H. T. Davis, and E. P. Wenaas, "Determination of the statistical distribution of electromagnetic-field amplitudes in complex cavities," Phys. Rev. E, vol. 48, pp. 4716-4729, 1993.

[27] R. Holland, and R. St. John, Statistical Electromagnetics. Philadelphia: Taylor & Francis, 1999.

[28] W. Spencer, M. Rice, B. Jeffs, and M. Jensen, "A statistical model for angle of arrival in indoor multipath propagation," *Proc. VTC'97*, pp. 1415-1419, 1997.

[29] G. B. Arfken, H. J. Weber, and F. E. Harris, Mathematical Methods for Physicists (7th Edition), Academic Press, Boston, USA, 2013.

[30] J. N. Kapur, and H. K. Kesavan, Entropy Optimization Principles with Applications. Boston: Academic Press, 1992.

[31] A. Papoulis, *Probability, Random Variables, and Stochastic Processes*. New York: McGraw-Hill Book Co., 1965.

[32] C. L. Holloway, D. A. Hill, J. M. Ladbury, and G. Koepke, "Requirements for an effective reverberation chamber: unloaded or loaded," *IEEE Trans. Electromagn. Compat.*, vol. 48, no. 1, pp. 187-194, Feb. 2006.

[33] U. Carlberg, P. S. Kildal, A. Wolfgang, O. Sotoudeh, and C. Orlenius, "Calculated and measured absorption cross sections of lossy objects in reverberation chamber," *IEEE Trans. Electromagn. Compat.*, vol. 46, no. 2, pp. 146-154, May 2004.

[34] G. C. R. Melia, M. P. Robinson, I. D. Flintoft, A. C. Marvin, and J. F. Dawson, "Broadband Measurement of Absorption Cross Section of the Human Body in a Reverberation Chamber," *IEEE Trans. Electromagn. Compat.*, vol. 55, no. 6, pp. 1043-1050, Dec. 2013.

[35] I. D. Flintoft, G. C. R. Melia, M. P. Robinson, J. F. Dawson, and A. C. Marvin. "Rapid and accurate broadband absorption cross-section measurement of human bodies in a reverberation chamber," *Meas. Sci. Technol.*, vol. 26, no. 6, pp. 65701-65709, Jun. 2015.

[36] P. Hallbjorner, U. Carlberg, K. Madsen, and J. Andersson, "Extracting electrical material parameters of electrically large dielectric objects from reverberation chamber measurements of absorption cross section," *IEEE Trans. Electromagn. Compat.*, vol. 47, no. 2, pp. 291-303, May 2005.

[37] Z. Tian, Y. Huang, Y. Shen, and Q. Xu, "Efficient and Accurate Measurement of Absorption Cross Section of a Lossy Object in Reverberation Chamber Using Two One-Antenna Methods," *IEEE Trans. Electromagn. Compat.*, vol. 58, no. 3, pp. 686-693, Jun. 2016.

[38] C. T. Tai, "On the definition of effective aperture of antennas," *IEEE Trans. Antennas Propagat.*, vol. AP-9, pp. 224-225, 1961.

[39] Yi Huang, and Kevin Boyle, Antennas: from Theory to Practice. West Sussex, UK: Wiley, 2008.

[40] C. L. Holloway, H. A. Shah, R. J. Pirkl, W. F. Young, D. A. Hill, and J. Ladbury, "Reverberation chamber techniques for determining the radiation and total efficiency of antennas," *IEEE Trans. Antennas Propag*., vol. 60, no. 4, pp. 1758-1770, Apr. 2012.

[41] C. L. Holloway, H. A. Shah, R. J. Pirkl, K. A. Remley, D. A. Hill, and J. Ladbury, "Early Time Behavior in Reverberation Chambers and Its Effect on the Relationships Between Coherence Bandwidth, Chamber Decay Time, RMS Delay Spread, and the Chamber Buildup Time," *IEEE Trans. Electromagn. Compat*., vol. 54, no. 4, pp. 714-725, Aug. 2012.

[42] Q. Xu, Y. Huang, L. Xing, and Z. Tian, "Extract the Decay Constant of a Reverberation Chamber Without Satisfying Nyquist Criterion," *IEEE Microwave and Wireless Components Letters*, vol. 26, no. 3, pp. 153-155, Mar. 2016.

[43] Q. Xu, Y. Huang, X. Zhu, L. Xing, Z. Tian, and C. Song, "Shielding effectiveness measurement of an electrically large enclosure using one antenna," *IEEE Transactions on Electromagnetic Compatibility*, vol. 57, no. 6, pp. 1466-1471, Dec. 2015.

[44] Q. Xu, Y. Huang, L. Xing, Z. Tian, M. Stanley, and S. Yuan, "B-scan in a reverberation chamber," *IEEE Transactions on Antennas and Propagation*, vol. 64, no. 5, pp. 1740-1750, May 2016.

[45] C. L. Holloway, D. A. Hill, J. M. Ladbury, P. F. Wilson, G. Koepke, and J. Coder, "On the Use of Reverberation Chambers to Simulate a Rician Radio Environment for the Testing of Wireless Devices," *IEEE Trans. Antennas Propag.*, vol. 54, no. 11, pp. 3167-3177, Nov. 2006.

[46] P. S. Kildal, X. Chen, C. Orlenius, M. Franzen, and C. S. L. Patane, "Characterization of Reverberation Chambers for OTA Measurements of Wireless Devices: Physical Formulations of Channel Matrix and New Uncertainty Formula," *IEEE Trans. Antennas Propag.*, vol. 60, no. 8, pp. 3875-3891, Aug. 2012.

[47] C. Lemoine, E. Amador, P. Besnier, J. M. Floc'h, and A. Laisné, "Antenna Directivity Measurement in Reverberation Chamber From Rician K-Factor Estimation," *IEEE Trans. Antennas Propag.*, vol. 61, no. 10, pp. 5307-5310, Oct. 2013.

[48] X. Chen, P. S. Kildal, and S. H. Lai, "Estimation of Average Rician K-Factor and Average Mode Bandwidth in Loaded Reverberation Chamber," *IEEE Antennas Wireless Propag. Lett.*, vol. 10, pp. 1437-1440, 2011.

[49] C. M. J. Wang, *et al*., "Parameter Estimation and Uncertainty Evaluation in a Low Rician K-Factor Reverberation-Chamber Environment," *IEEE Trans. Electromagn. Compat.*, vol. 56, no. 5, pp. 1002-1012, Oct. 2014.

[50] X. Chen, P. S. Kildal, and J. Carlsson, "Verification of the Rician K-factor-based uncertainty model for measurements in reverberation chambers," *IET Sci. Meas. Techn.*, vol. 9, no. 5, pp. 534-539, Aug. 2015.

[51] J. M. Ladbury, and D. A. Hill, "Enhanced Backscatter in a Reverberation Chamber: Inside Every Complex Problem is a Simple Solution Struggling to Get Out," in *Proc. IEEE Int. Symp. on Electromagn. Compat.*, Jul. 2007, pp. 1-5.

[52] C. R. Dunlap, "Reverberation chamber characterization using enhanced backscatter coefficient measurements," Ph.D. dissertation, Dept. of Elect., Comput. and Eng., Univ. of Colorado, Boulder, USA, 2013.

[53] C. L. Holloway *et al*., "Validation of a two-antenna reverberation-chamber technique for estimating the total and radiation efficiency of antennas," in *Proc. IEEE Int. Symp. on Electromagn. Compat.*, Rome, IT, 2012, pp. 1-6.

[54] C. L. Holloway *et al*., "Validation of a one-antenna reverberation-chamber technique for estimating the total and radiation efficiency of an antenna," in *Proc. IEEE Int. Symp. on Electromagn. Compat.*, Pittsburgh, PA, 2012, pp. 205-209.

[55] M. T. Ma, M. Kanda, M. L. Krawford, and E. B. Larsen. "A Review of Electromagnetic Compatibility/Interference Measurement Methodologies," *Proc IEEE*, vol. 73, no. 3, pp. 388-412, Mar. 1985.

[56] F. Jacobsen, and A. R. Molares. "Sound Power Emitted by a Pure-Tone Source in a Reverberation Room," *Journal of the Acoustical Society of America*, vol. 126, no. 2, pp. 676-684, Aug. 2009.

[57] F. Jacobsen, and A. R. Molares, "The Ensemble Variance of Pure-Tone Measurements in Reverberation Rooms," *Journal of the Acoustical Society of America*, vo. 127, no. 1, pp. 233-237, Jan. 2010.

Chapter 3: Efficient Averaged Absorption Cross Section Measurement

3.1 Introduction

RCs have been widely used for radiated power measurement [1] – [9]. Recently, it has been shown that the RC can also be used to measure the averaged absorption cross section (ACS) of a lossy object, which is averaged over all angles of incidence and polarization [10] – [11]. The measurement of the ACS of a lossy object is required for many applications including the characterization of the effect of lossy objects in multipath environments such as interiors of mass transit vehicles or aircraft loaded with cargoes or passengers [12], biometrics EM exposure studies such as human's specific absorption rate (SAR) [13].

The ACS of a lossy object is defined as the ratio of the power dissipated in the object to the power density of the incident plane wave. The averaged statistic power transfer function of an RC is proportional to its quality factor. The ACS contribution to the quality factor was derived mathematically in [14], which offers an opportunity to measure the averaged ACS of an object from the quality factor of the RC.

For ACS measurement, the common approach is to place a transmitting antenna inside a chamber along with a generic receiving antenna and extract the power transfer function by measuring the transmission coefficient S_{21}, and reflection coefficients S_{11} and S_{22}. The problem with this approach is that it requires two antennas with known efficiency – this could be a problem in reality. An alternative technique given in [15] is to use the coherence bandwidth which is estimated from the complex correlation function of the loaded and unloaded chambers, but it has its own approximations and limitations because of the ambiguity introduced by selecting the threshold for determining the bandwidth of the modes. In this chapter, both the frequency-domain and the time-domain information is proposed to be used to obtain ACS. Our method requires only one antenna and provides an accurate measurement of ACS without the above-mentioned limitations and approximations.

3.2 Theory

The quality factor Q of an RC is a key quantity in calculating the ACS of a lossy object. Generally, as mentioned in Section 2.4.4, in an electrically large cavity, Q is defined as

$$Q = \omega U_s / P_d \tag{3.1}$$

When the cavity is unloaded, i.e., there are no lossy objects within the chamber, the dissipated power can be written as the summation of three items [14]

$$P_{du} = P_{d1} + P_{d3} + P_{d4} \tag{3.2}$$

where P_{du} is the total power dissipated under the unloaded scenario, P_{d1}, P_{d3}, and P_{d4} are as defined in (2.82).

By substituting (3.2) to (3.1), the following equation can be written for the inverse of Q

$$Q_u^{-1} = Q_1^{-1} + Q_3^{-1} + Q_4^{-1} \tag{3.3}$$

where Q_u is the chamber quality factor under the unloaded scenario. Q_1, Q_3, and Q_4 are as defined in (2.83).

When the cavity is loaded with lossy objects, the total dissipated power can be rewritten as

$$P_{dl} = P_{d1} + P_{d2} + P_{d3} + P_{d4} \tag{3.4}$$

where P_{dl} is the total power dissipated under the loaded scenario, P_{d2} is the power absorbed by lossy objects as mentioned in Section 2.4.4.

The corresponding inverse of Q becomes

$$Q_l^{-1} = Q_1^{-1} + Q_2^{-1} + Q_3^{-1} + Q_4^{-1} \tag{3.5}$$

Q_2 is the contribution of the ACS to the cavity Q and can be expressed as

$$Q_2 = 2\pi V / \lambda \langle \sigma_a \rangle \tag{3.6}$$

where V is the RC volume and λ is the wavelength.

The averaged ACS $\langle\sigma_a\rangle$ of a lossy object can determine it from its contribution to chamber Q from (3.6)

$$\langle\sigma_a\rangle = \frac{2\pi V}{\lambda} Q_2^{-1} \tag{3.7}$$

where $\langle\ \rangle$ indicates average with respect to the incidence angle and polarization.

From (3.3), (3.5) and (3.7), the averaged ACS can be rewritten in terms of the measured loaded and unloaded chamber Q factors Q_l and Q_u

$$\langle\sigma_a\rangle = \frac{2\pi V}{\lambda} (Q_l^{-1} - Q_u^{-1}) \tag{3.8}$$

Thus two pieces of information are still needed, Q_l and Q_u, in order to determine $\langle\sigma_a\rangle$. Basically, the chamber Q factor can be measured either in the frequency domain or in the time domain. In the frequency domain, the chamber Q can be evaluated from the averaged net power transfer function T by using Hill's formulas in [14]. In the time domain, the chamber Q can be obtained from the chamber decay time τ [2], [16] – [18]. Both the averaged net power transfer function and the chamber decay time can be extracted using only one antenna [2]. In the following part of this section, the formulas required for the one-antenna method to determine the ACS of lossy objects within an RC will be derived in both the frequency domain and the time domain.

3.2.1 Frequency Domain

In the frequency domain, the averaged statistic power transfer function of an RC is proportional to its quality factor Q_{FD} [14]. The subscript "FD" is used to emphasize that it is measured in the frequency domain.

$$Q_{FD} = \frac{16\pi^2 V}{\lambda^3} \frac{\langle P_r\rangle}{P_t} \tag{3.9}$$

where $\langle P_r \rangle$ is the average received power, P_t is the power transmitted into the chamber, and $\langle\ \rangle$ means average over all stirrer positions. The second item on the right-hand side of (3.9) is related to the *S*-parameters measured using a VNA as

$$\frac{\langle P_r \rangle}{P_t} = \langle |S_{21}|^2 \rangle \tag{3.10}$$

A simple measurement of this *S*-parameter would account for contributions from dissipative and mismatch loss of antennas. The contributions from the stirred (energy that interacts with the stirrers) and unstirred energy (energy that does not interact with the stirrers) in the chamber are included as well. Thus, $\langle |S_{21}|^2 \rangle$ can be regarded as the uncalibrated chamber transfer function. By calibrating out the dissipative and mismatch loss of antennas the unstirred contributions of *S*-parameters can be removed. The net power transfer function *T* can be extracted as [19]

$$T = \frac{\langle |S_{21,s}|^2 \rangle}{(1 - |\langle S_{11} \rangle|^2)(1 - |\langle S_{22} \rangle|^2)\eta_1^{rad}\eta_2^{rad}} \tag{3.11}$$

where $S_{21,s}$ is the stirred part of S_{21} which can be obtained by the vector average subtraction [20]

$$S_{*,s} = S_* - \langle S_* \rangle \tag{3.12}$$

$\langle\ \rangle$ means the averaged value of the *S*-parameters, as defined earlier, but here it is linked to the stirring method (mode stirring, frequency stirring, source stirring, *etc*.), η_1^{rad} and η_2^{rad} are the radiation efficiency of antenna 1 and antenna 2 that are used in the measurement, respectively.

Substituting (3.9) – (3.12) into (3.8), the averaged ACS $\langle \sigma_a \rangle$ can be determined from the net power transfer function with and without the lossy objects (T_l, T_u)

$$\langle \sigma_a \rangle = \frac{\lambda^2}{8\pi}(T_l^{-1} - T_u^{-1}) \tag{3.13}$$

Typically, the net power transfer function is measured with two low-loss antennas using (3.11). The radiation efficiency of the two antennas (η_1^{rad}, η_2^{rad}) should be known in advance,

or, for a rough measurement, the efficiency could be assumed to be unity, which will actually introduce systematic errors.

For a well performed RC, the enhanced backscatter coefficient [2] – [21]

$$e_b = \sqrt{\langle |S_{11,s}|^2 \rangle \langle |S_{22,s}|^2 \rangle} \Big/ \langle |S_{21,s}|^2 \rangle = 2 \tag{3.14}$$

Assuming two identical antennas are used in the measurement, it can be derived $\langle |S_{11,s}|^2 \rangle = \langle |S_{22,s}|^2 \rangle = 2 \langle |S_{21,s}|^2 \rangle$. Now, equation (3.11) can be expressed as

$$T = \frac{\langle |S_{11,s}|^2 \rangle}{2(1 - |\langle S_{11} \rangle|^2)^2 (\eta_1^{rad})^2} \tag{3.15}$$

Thus, only one antenna is needed to complete this measurement, and the radiation efficiency of only one antenna needs to be known, which will greatly simplify the measurement.

3.2.2 Time Domain

The time-domain method is realized by performing the measurement in the frequency domain and then transforming the results to the time domain. In the time domain, the loaded and unloaded chamber *Q* can be determined from the chamber decay time. [2], [22] have shown $Q_{TD} = \omega\tau$. Similarly, the subscript "TD" is used to emphasize that the measurement is conducted in the time domain. ω is the angular frequency and τ is the chamber decay time. The loaded and unloaded *Q* can be written as

$$Q_l = \omega \langle \tau_l \rangle \text{ and } Q_u = \omega \langle \tau_u \rangle \tag{3.16}$$

where $\langle \tau_l \rangle$ is the average loaded chamber decay time and $\langle \tau_u \rangle$ is the average unloaded chamber decay time. Substituting (3.16) into (3.8), the ACS can also be obtained in the following form [22]

$$\langle \sigma_a \rangle = \frac{V}{c} (\langle \tau_l \rangle^{-1} - \langle \tau_u \rangle^{-1}) \tag{3.17}$$

where c is the speed of light in the chamber (equal to c_0). This technique requires the knowledge of the chamber decay time τ. It is worth mentioning that τ can be measured in the time domain directly or in the frequency domain. In this thesis, the frequency-domain measurement is adopted because it normally gives a larger dynamic range than the time-domain measurement. The time-domain response is obtained from the inverse Fourier transform (IFT) of the measured frequency-domain response. Here, to obtain τ, the power delay profile (PDP) of the RC is first needs to be obtained from the IFT of S_{11}. Because the time-domain power in the RC decays exponentially, thus τ can be obtained from the slope of *ln*(power) in the time domain. The details for extracting τ from the *S*-parameters can be found in [16]. Compared with the frequency-domain method, the time-domain method is simpler and more accurate because the knowledge of the antenna efficiency is not required and the systematic error caused by antenna efficiency estimation can be avoided.

3.3 Measurement

To validate the proposed methods, measurements were performed from 4.0 – 5.0 GHz in the University of Liverpool RC which has a size of 3.6 m × 4 m × 5.8 m. It has two mode-stir paddles: the vertical one is mounted in a corner while the horizontal one is set close to the ceiling. Two double-ridged waveguide horn antennas were used as antenna 1 (SATIMO® SH 2000) and antenna 2 (Rohde & Schwarz® HF 906). Antenna 1 was mounted on a turn-table platform to introduce source stirring positions and connected to port 1 of a VNA via a cable running through the bulkhead of the chamber, and antenna 2 was connected to port 2 of the VNA via another cable through the bulkhead of the chamber. During the measurement, the turn-table platform was moved stepwise to 3 source stirring positions (20 degrees for each step). At each source stirring position the two paddles were moved simultaneously and stepwise to 100 positions (3.6 degrees for each step). At each mode stirring position and for each source stirring position, a full frequency sweep was performed by the VNA and the *S*-parameters were collected. Thus, for each frequency, 300 stirring positions are obtained (3 source stirring positions, and 100 mode stirring positions for each source stirring position). A piece of RAM was selected as an object under test (OUT). The measurement setups without

and with the OUT are shown in Figure 3.1(a) and (b), respectively. The whole measurement system is shown in Figure 3.1(c).

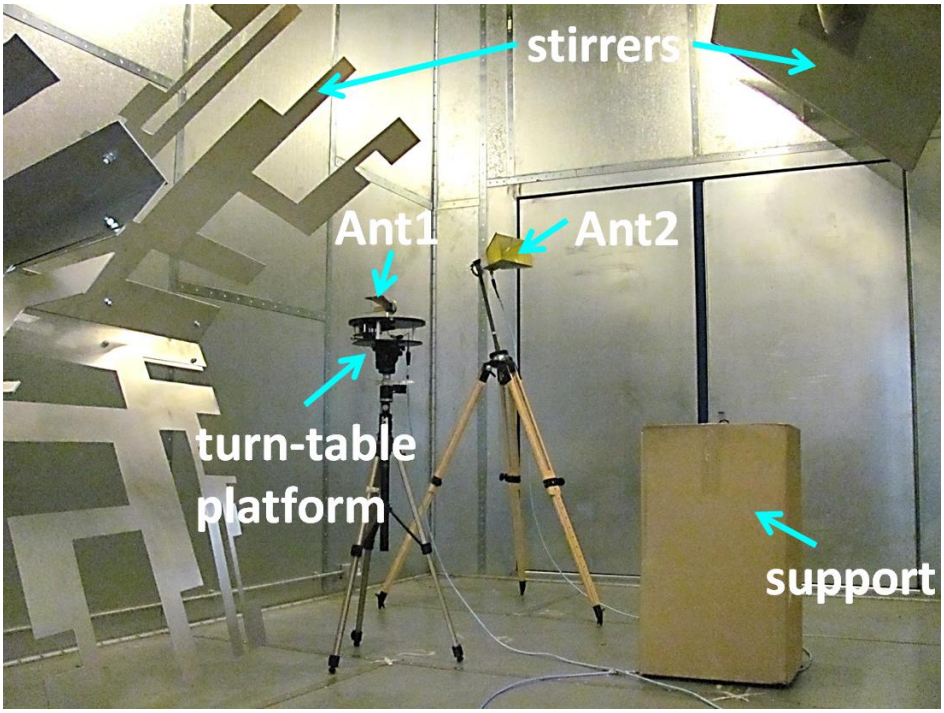

(a)

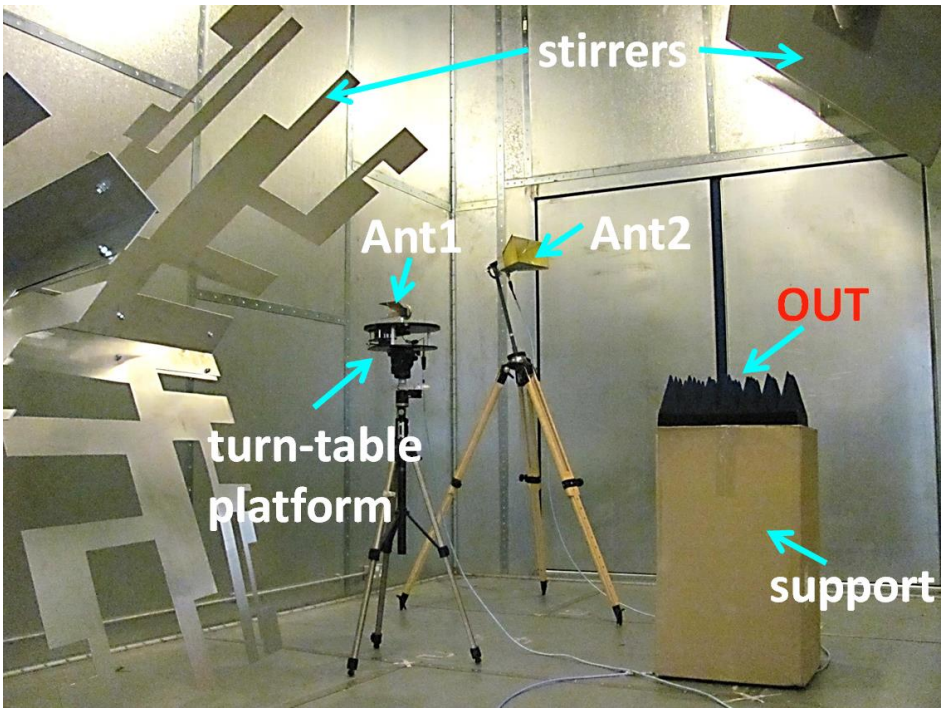

(b)

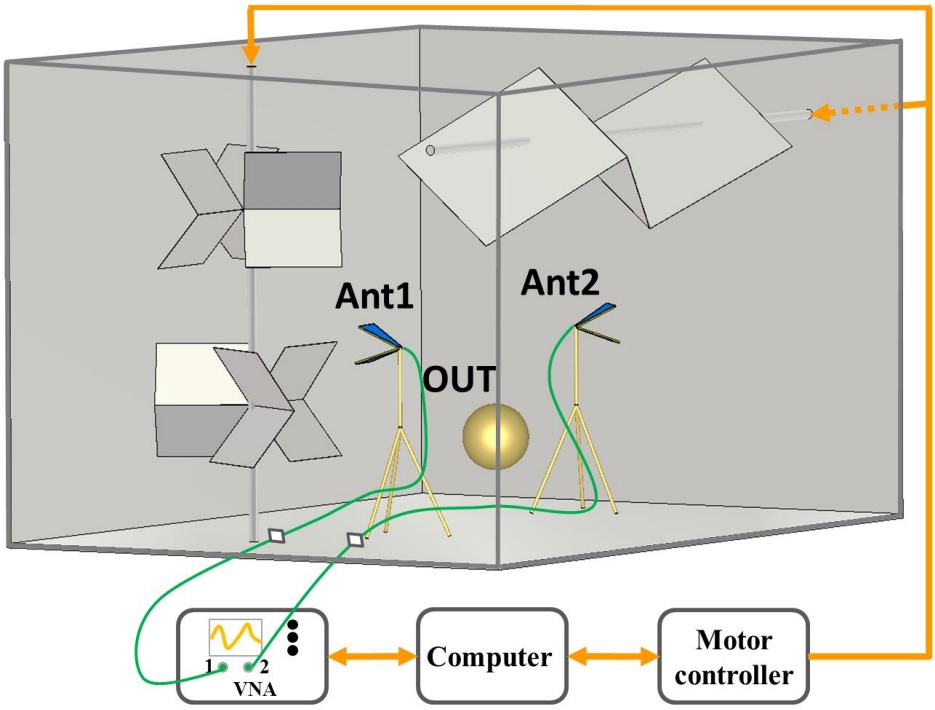

(c)

Figure 3.1 ACS measurement setup in the RC: (a) unloaded scenario, (b) loaded scenario, (c) measurement system.

The measurement procedure is given as follows.

Step 1: Calibrate the VNA including the cables according to the standard calibration procedure.

Step 2: Place the two antennas, the turn-table platform and the support (excluding the OUT) inside the RC.

Step 3: Connect antenna 1 to port 1 of the VNA and antenna 2 to port 2 of the VNA, and collect the full *S*-parameters for each stirring position.

Step 4: Keep the previous measurement setup unchanged and place the OUT on the support, and repeat Step 3.

In this measurement, 10,001 points were sampled in the frequency range from 3.8 to 5.2 GHz. The ACS of the OUT was calculated using the conventional two-antenna method ($ACS_{FD,2}$),

the one-antenna method in the frequency domain ($ACS_{FD,\,1}$) and the one-antenna method in the time domain ($ACS_{TD,\,2}$), respectively. The first subscript "FD" or "TD" is used to indicate that the measurement is conducted in the frequency domain or in the time domain, respectively, and the second subscript "1" or "2" is used to indicate that one antenna or two antennas were used in the measurement. In the frequency domain, the enhanced backscatter coefficients (e_b) under the loaded and unloaded scenarios are obtained and shown in Figure 3.2. It can be seen that they are very close to 2, which means the RC is well stirred and measurement setup is reasonable [23].

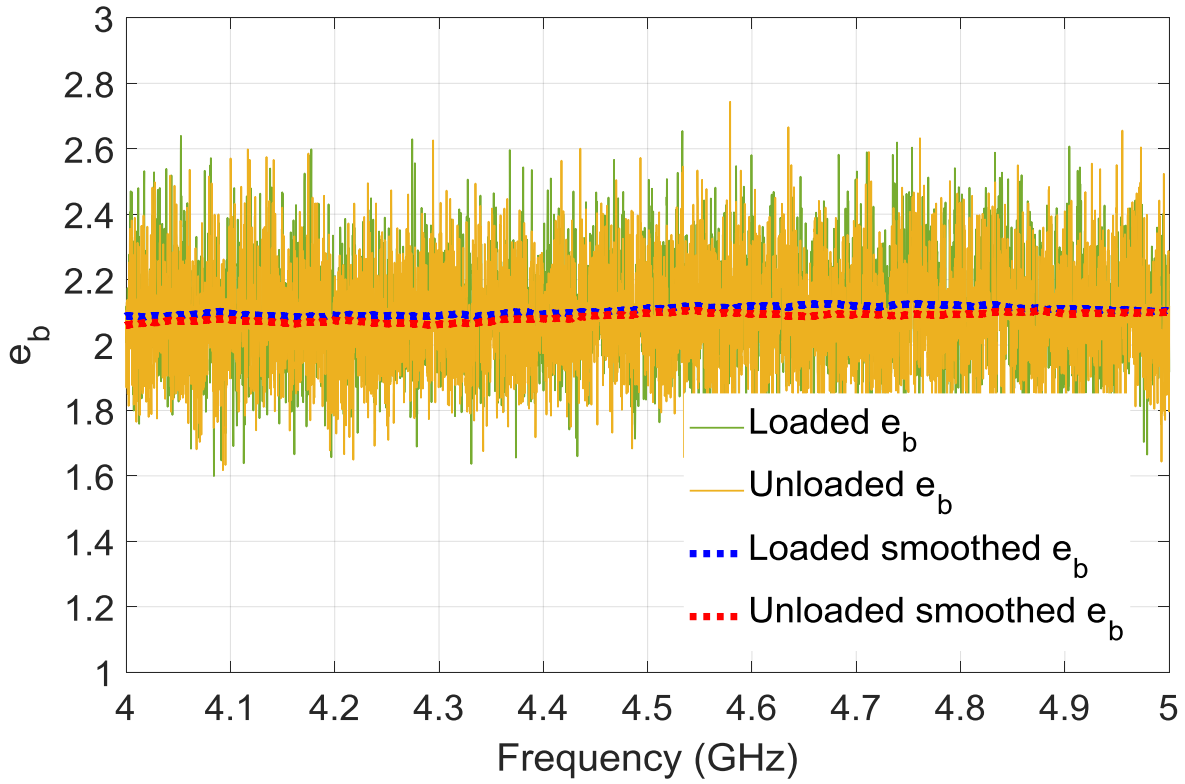

Figure 3.2 e_b under the loaded and unloaded scenarios.

The chamber transfer functions using one antenna method ($T_{FD,1}$) and two-antenna method ($T_{FD,2}$) under loaded and unloaded scenarios are shown in Figure 3.3. As can be seen, the chamber transfer function is reduced when the chamber is loaded because of the increase of the power loss. $T_{FD,1}$ is very close to $T_{FD,2}$ for both loaded and unloaded scenarios, which manifests the effectiveness of the one-antenna method in the frequency domain.

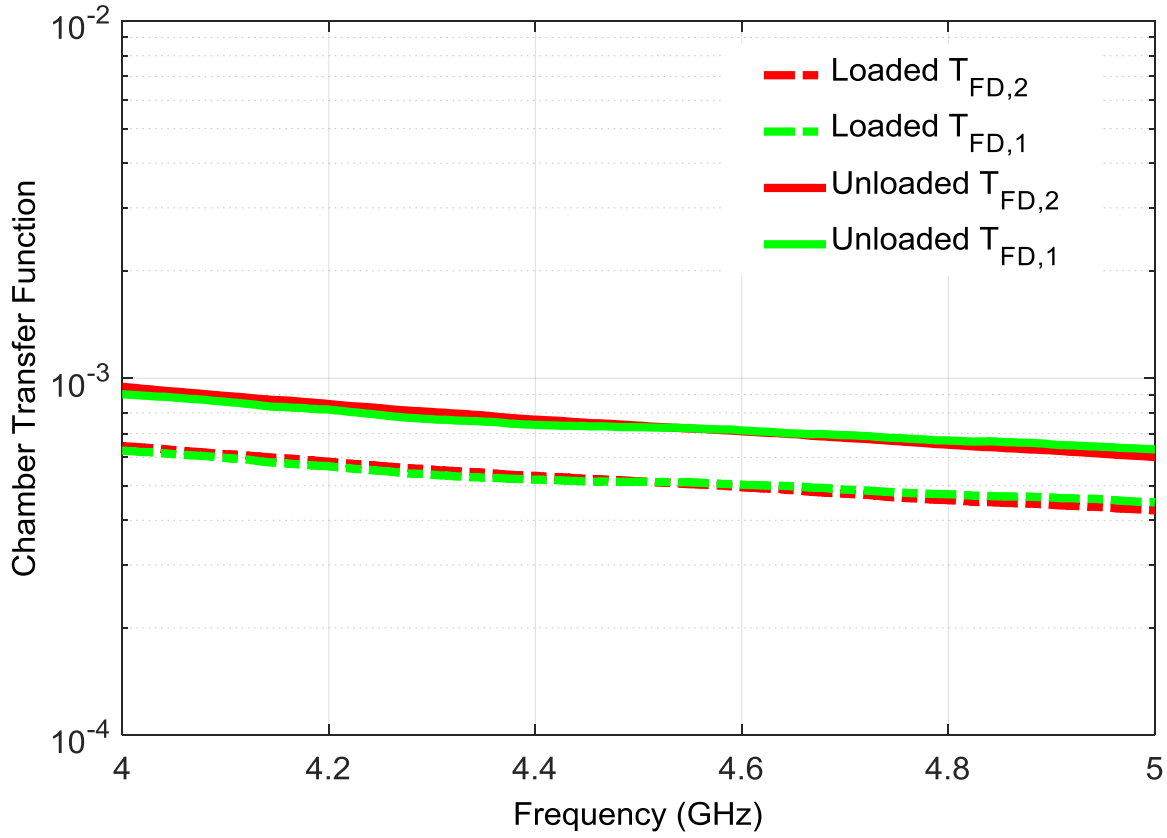

Figure 3.3 The measured chamber transfer function using one-antenna and two-antenna methods under loaded and unloaded scenarios.

In the time domain, a band-pass elliptic filter of order 10 is used to filter S_{11} with 200 MHz bandwidth, as shown in Figure 3.4(a), and then the inverse fast Fourier transform (IFFT) is applied to the filtered S_{11}. Since the time-domain power decays exponentially ($e^{-t/\tau}$) in the RC, the least-square fit is applied to *ln*(power) to obtain the slope, and τ can be extracted by getting the negative inverse of the slope. To avoid the fit error caused by the noise level, only part of the signal is used for least-square fit, as shown in Figure 3.4(b).

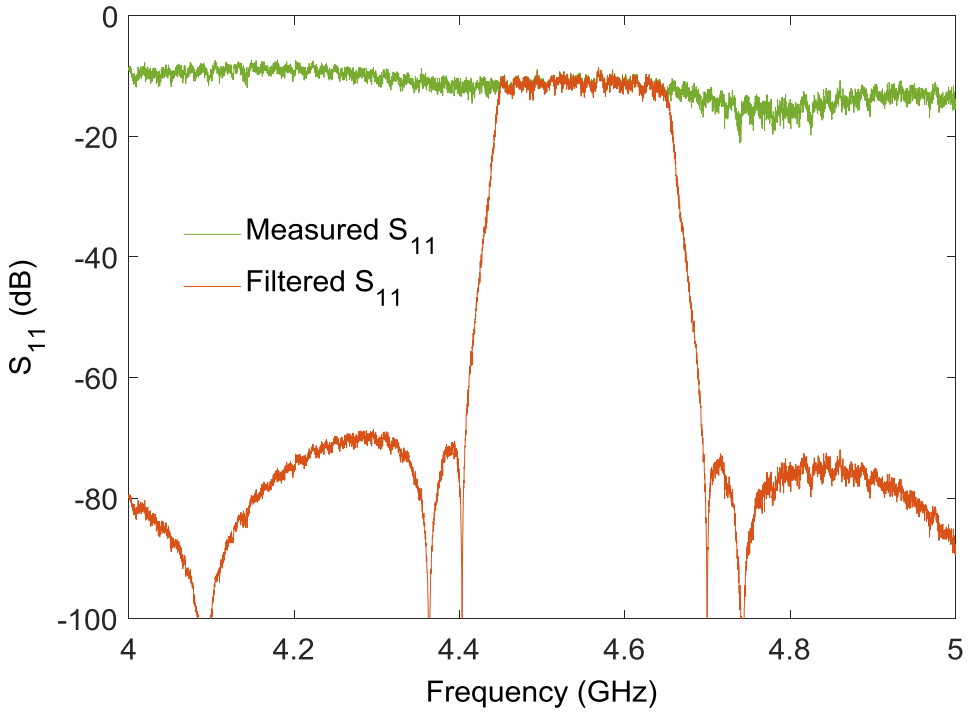

(a)

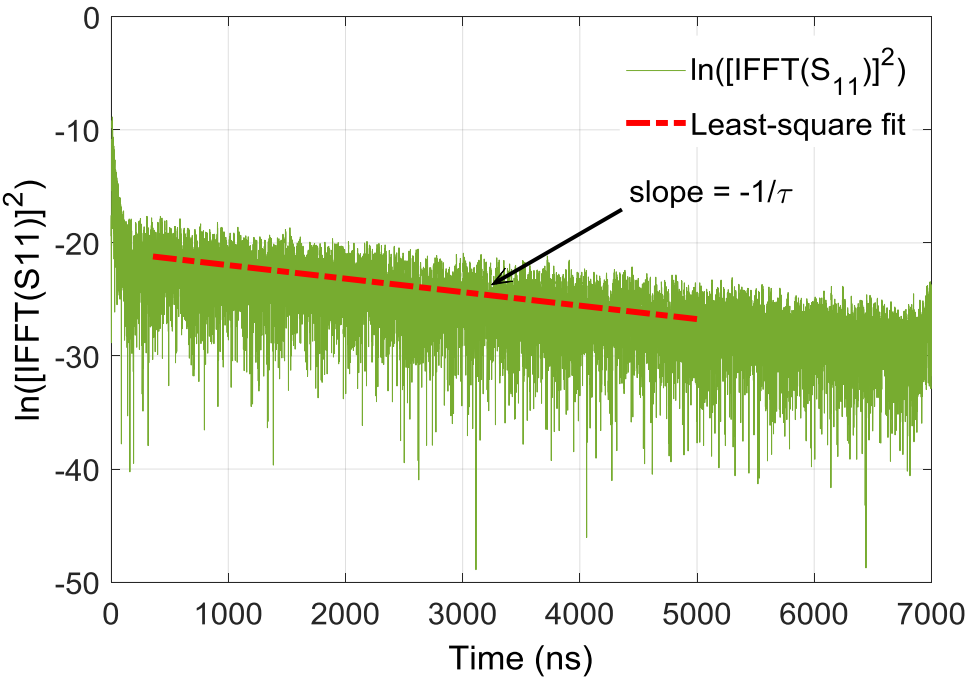

(b)

Figure 3.4 Extracting τ from S_{11}: (a) measured S_{11} and filtered S_{11}, (b) time-domain response: ln([IFFT(S_{11})]^2) and least-square fit.

By sweeping the centre frequency of the filter, τ at different centre frequencies is obtained. The measured chamber decay time using one-antenna method under loaded and unloaded scenarios are depicted in Figure 3.5.

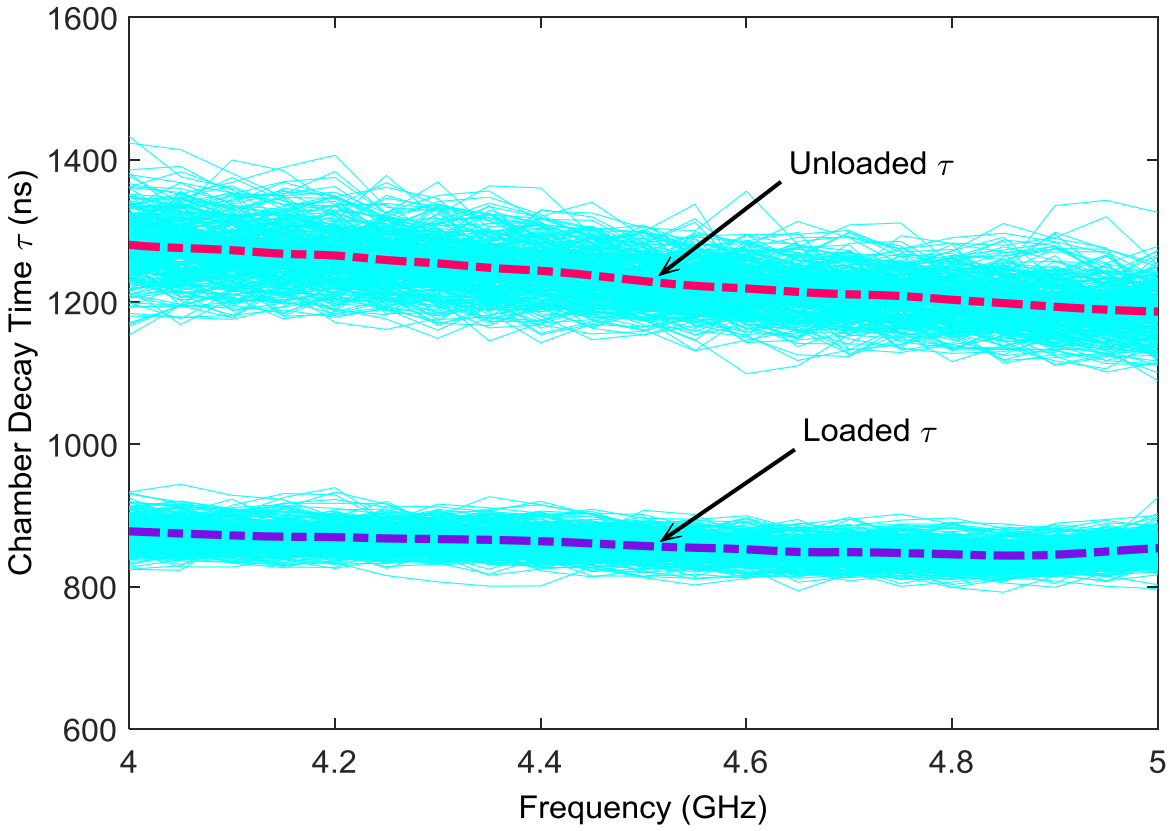

Figure 3.5 The measured chamber decay time using one-antenna method under loaded and unloaded scenarios.

The thin cyan curves are the measured τ for different stirring samples and the thick dash curves are the averaged τ for all samples. As expected, the chamber decay time is reduced when the chamber is loaded. Another thing to be noted is that τ is very robust in the full frequency span, i.e., τ does not vary much for different stirring samples. The reason can be explained as follows: the chamber decay time τ is determined by the chamber loss. For a given frequency, the chamber loss will vary due to the change of the paddle positions and the change of the chamber modes. When the number of resonant modes is massive (1,657,518 modes in 4.0 GHz in our RC according to Weyl's formula [22]), the positions of the peaks and troughs of the resonant mode will not change much for different boundary conditions,

and the loss variation is relatively small for different paddle positions. Hence, the chamber decay time is very robust. As shown in Figure 3.5, under the unloaded scenario, the variation between the τ for one sample and the averaged τ is within about ±10%. And under the loaded scenario, the variation is within about ±5%. It is easy to understand when the RC is loaded, the majority of the power is consumed by the lossy objects, the power loss is not sensitive to the boundary condition of the RC, and hence the loaded τ is more robust than the unloaded τ. The robustness of the chamber decay time actually offers an opportunity to extract τ by merely a few stirring samples, thus the ACS can be measured rapidly and accurately, which will be detailed later.

The ACS measurement results are shown in Figure 3.6. In the frequency domain, 200 MHz frequency stirring is adopted. The efficiency of antenna 1 and antenna 2 in 4.0 – 5.0 GHz are 78% and 95%, respectively. It can be seen clearly that the measured ACSs using the three methods are all around 0.1 m^2 and the maximum variation is within 10%.

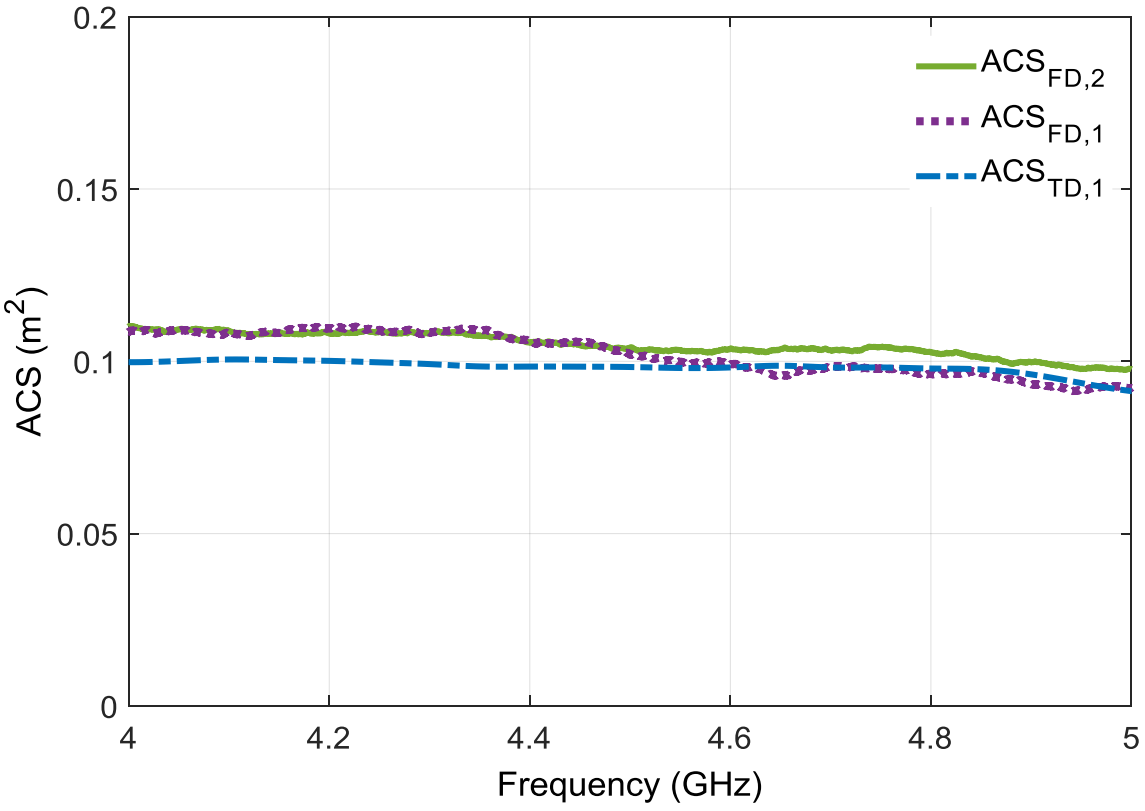

Figure 3.6 The measured ACS of the OUT.

3.4 Convergence Property

The convergence properties of the three methods are also studied. The root-mean-square-error (RMSE) of the measured ACS from 4.0 – 5.0 GHz with different numbers of stirring positions to the ACS measured with 300 stirring positions is adopted to evaluate the convergence, and the algorithm is expressed as

$$\mathrm{RMSE}_i = \sqrt{\frac{\sum_{j=1}^{N}\left(\mathrm{ACS}_{i,j} - \mathrm{ACS}_{M,j}\right)^2}{N}} \tag{3.18}$$

where i is the number of stirring positions, M is the maximum number of stirring positions, j is the frequency sampling point number, N is the number of frequency sampling points in 4.0 – 5.0 GHz. In our case, M = 300 and N = 7143. The calculated results are shown in Figure 3.7.

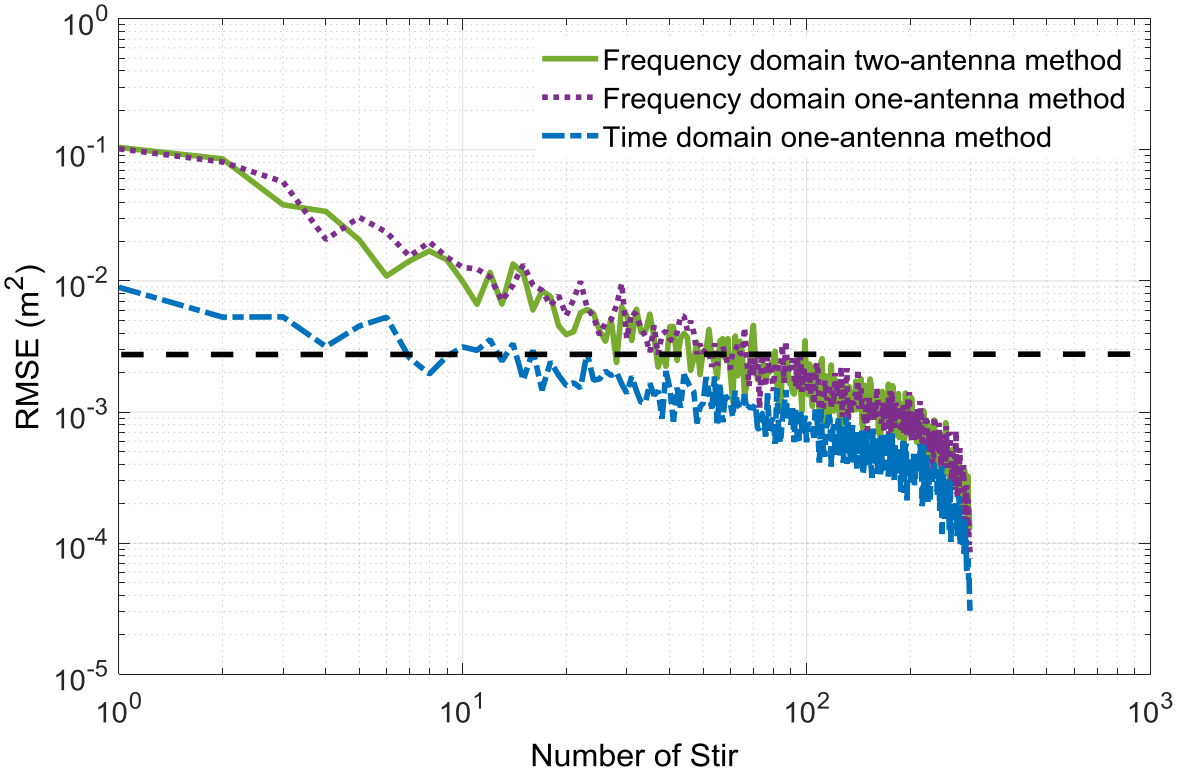

Figure 3.7 The RMSE with the increase of the number of stirring positions for different methods.

As can be seen, the convergence speeds of the one-antenna method and the two-antenna method in the frequency domain are close but the time-domain method converges faster than the frequency-domain methods. This is because the chamber decay time τ is not sensitive to the boundary conditions and only depends on the overall loss of the RC. While the chamber transfer function and e_b depend on how well the RC is stirred. Thus, $ACS_{TD,\,1}$ converges faster than $ACS_{FD,\,1}$ and $ACS_{FD,\,2}$. It is worth mentioning that, in the time domain, the RMSE is always below 10% (compared with the averaged ACS in the full frequency span, about 0.1 m^2 from Figure 3.6) and drops below 3% after 15 stirring positions. However, in the frequency domain, the one-antenna method and the two-antenna method have similar convergence behaviour, the RMSEs are always above 10% before the first 10 stirring positions and drop down slowly afterwards. They are below 3% after 100 stirring positions.

As implied in (3.14) and (3.15), the one-antenna method in the frequency domain requires $e_b = 2$. Inaccurate results may be obtained if e_b deviates from 2. To show the influence of the deviation of e_b from 2 to the validity of the measurement in the frequency domain based on one-antenna approach, the convergence behaviour of the measured e_b (under both loaded and unloaded scenarios) and $ACS_{FD,\,1}$ at 4.5 GHz has been checked, as shown in Figure 3.8. The $e_b = 2$ level and $ACS_{FD,\,1} = 0.1$ m^2 level are marked out with dash lines. As can be seen, at the first dozens of stirs, the deviation of e_b from 2 fluctuates drastically, the measured ACS is unreliable. However, with the increase of the number of stir, e_b converges to 2 gradually. The convergence behaviour of $ACS_{FD,\,1}$ is very similar to e_b. After about 150 stirs, the variation of e_b from 2 becomes small (within 10% variation) and the measured $ACS_{FD,\,1}$ becomes stable (it converges to 0.1 m^2). That means the accuracy of the frequency-domain one-antenna approach depends on $e_b = 2$, i.e., how well the chamber is stirred.

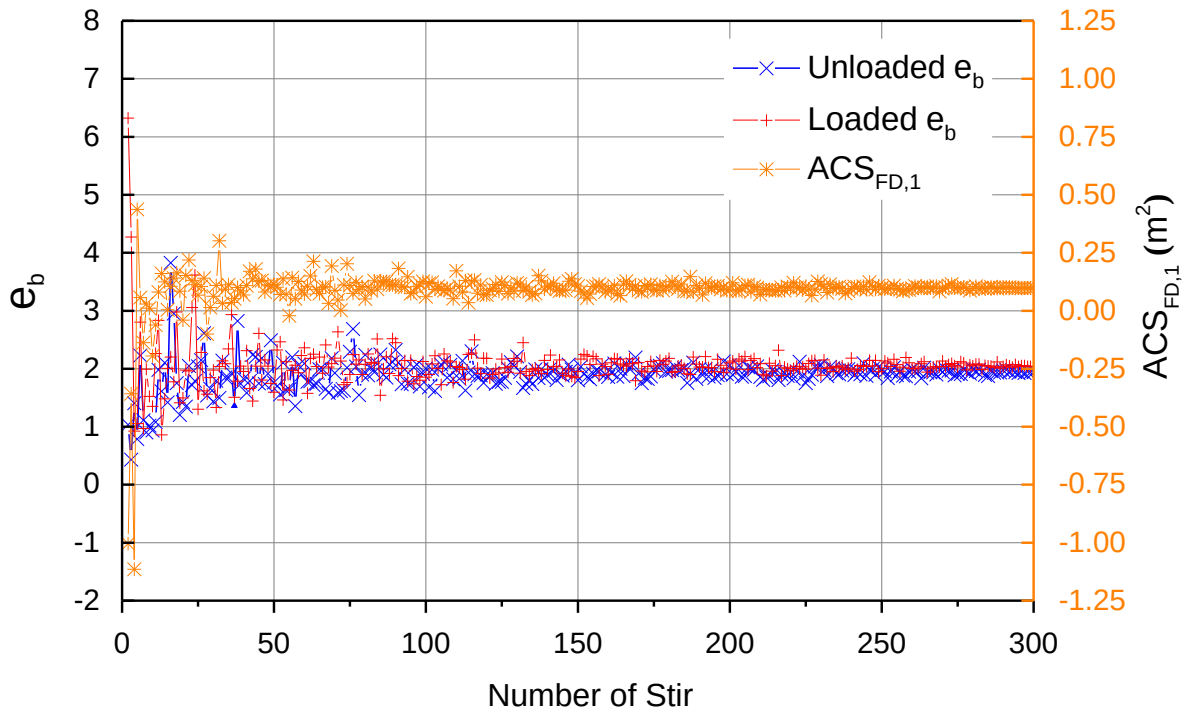

Figure 3.8 The convergence behavior of the measured e_b and $ACS_{FD,1}$ @ 4.5 GHz.

Considering the robustness of the chamber decay time and the fast convergence property of the time-domain method, the measurement setup can be further simplified by using an electrically large conducting cavity, i.e., an RC is not necessary. To verify this idea, the paddles of the RC were set stationary, therefore, no mode stirring was introduced during the measurement, and thus the RC would merely act as an electrically large cavity. To extract the correct τ of the electrically large cavity, a simple source stirring was introduced by rotating the turn-table platform. Based on the convergence speed of the one-antenna method in the time domain, 20 source stirring positions was adopted in our measurement. The turn-table platform was moved stepwise to 20 source stirring positions (18 degrees for each step). A double-ridged waveguide horn antenna (SATIMO® SH 2000) was mounted on the turn-table platform and connected to port 1 of a VNA via a cable running through the bulkhead of the cavity. The measurement procedure was similar to that in the RC. The cavity decay time with and without OUT was extracted from S_{11}. The measurement results are shown in Figure 3.9. As can be seen, the results from the mode stirring and source stirring are in good agreement. The difference is within 4% and the whole measurement time for the source stirring was about 7 minutes while the measurement time for the mode stirring was more than 8 hours,

which means that the ACS can be measured in the time domain rapidly and accurately. The major contribution to the measurement time is the damping time of the turn-table platform between the steps and the time of transferring data from the VNA to the computer. The measurement time of this method is comparable with that of the rapid method proposed in [24] and therefore, it is quite suitable for applications requiring discriminations between subjects due to its high accuracy and short measurement time. It should be pointed out that the cavity should be large enough to support sufficient cavity modes to ensure enough independent samples to be obtained at the lowest frequency of the measurement, or the OUT could not fully "submerge" into the field-uniform area and the measurement result could be wrong. This is the main consideration for the selection of the size of the conducting cavity in the measurement.

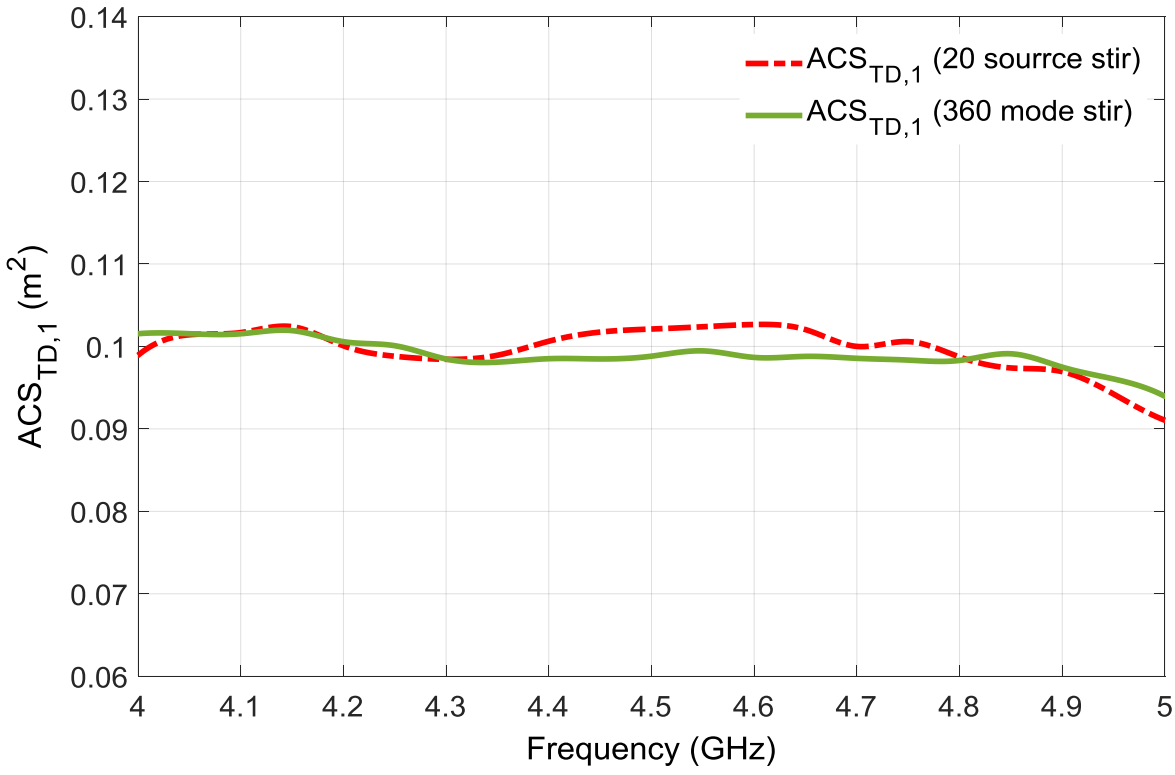

Figure 3.9 The comparison of the measured ACS in the time domain with 20 source stirring positions and 360 mode stirring positions.

3.5 ACS Measurement without Calibration

In this section, it is shown that the ACS can be measured accurately without calibration. This is realized by making use of the fact that the chamber decay time is independent of the insertion loss of cables in the measurement. Measurements have been done to verify the proposed procedure. It has been shown that the measurement process is simplified and the measurement time is shortened at the same time.

As mentioned in Section 3.3, in order to extract the chamber decay time, a full two-port (for two-antenna methods) or one-port (for one-antenna method) calibration must be carried out before collecting the *S*-parameters of the antennas. In such measurements, the reference planes are calibrated at the end of the cables, as shown in Figure 3.10(a) with dot lines. However, the calibration process is tedious and time-consuming. Nowadays, some VNAs are pre-calibrated with the reference planes at the output connectors of the VNAs, when the VNA is pre-set the reference planes are restored [25]. This offers an opportunity to perform the measurement without the need for calibration. The antennas and the cables after the reference planes can be regarded as integrated antennas. Since the chamber decay time does not depend on the insertion loss of cables used in the measurement and it is only determined by the diffused loss in the RC. The ACS can be measured accurately without calibration, which will simplify the measurement process and shorten the measurement time.

To validate the proposed method, measurements were performed from 4.0 – 5.0 GHz in our RC. The two-antenna method was adopted. Antenna 1 (SATIMO® SH 2000) was connected to port 1 of a VNA and antenna 2 (Rohde & Schwarz® HF 906) was connected to port 2 of the VNA as in Section 3.3. During the measurement, the two stirrers were moved simultaneously and stepwise to 120 positions (3 degrees for each step). At each mode stirring position, a full frequency sweep was performed by the VNA and the full *S*-parameters were collected. A piece of RAM was selected as an OUT. The measurement setup is shown in Figure 3.10(a). The measurement setups without and with the OUT are shown in Figure 3.10(b) and (c), respectively.

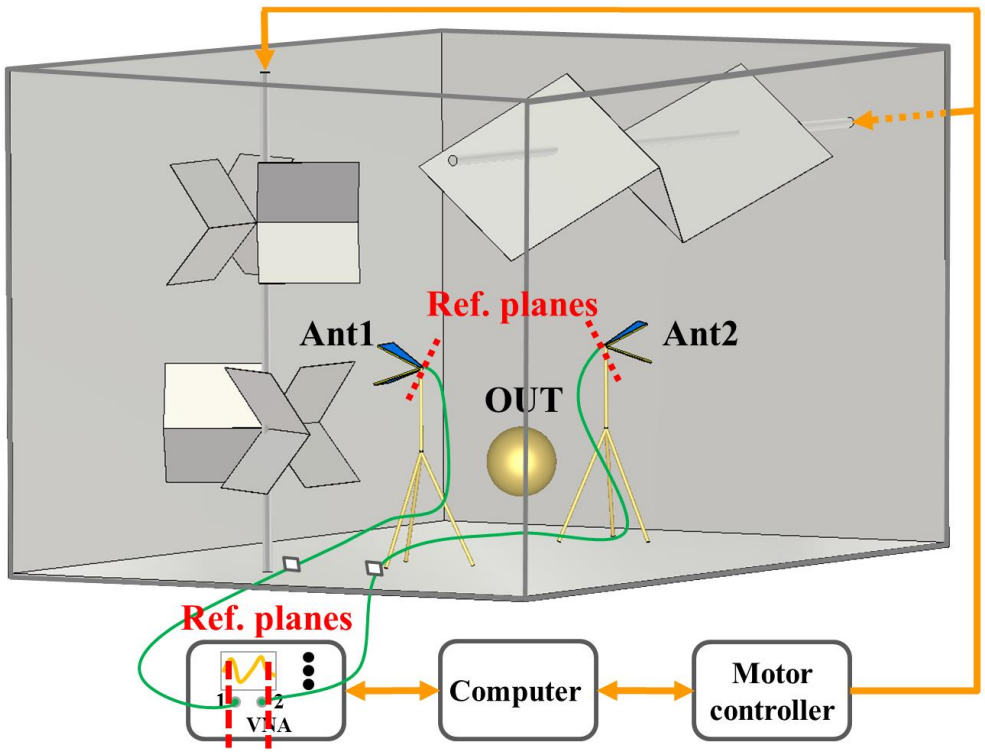
Ref. planes
Ant1
Ant2
OUT
Ref. planes
1
2
VNA
Computer
Motor controller

(a)

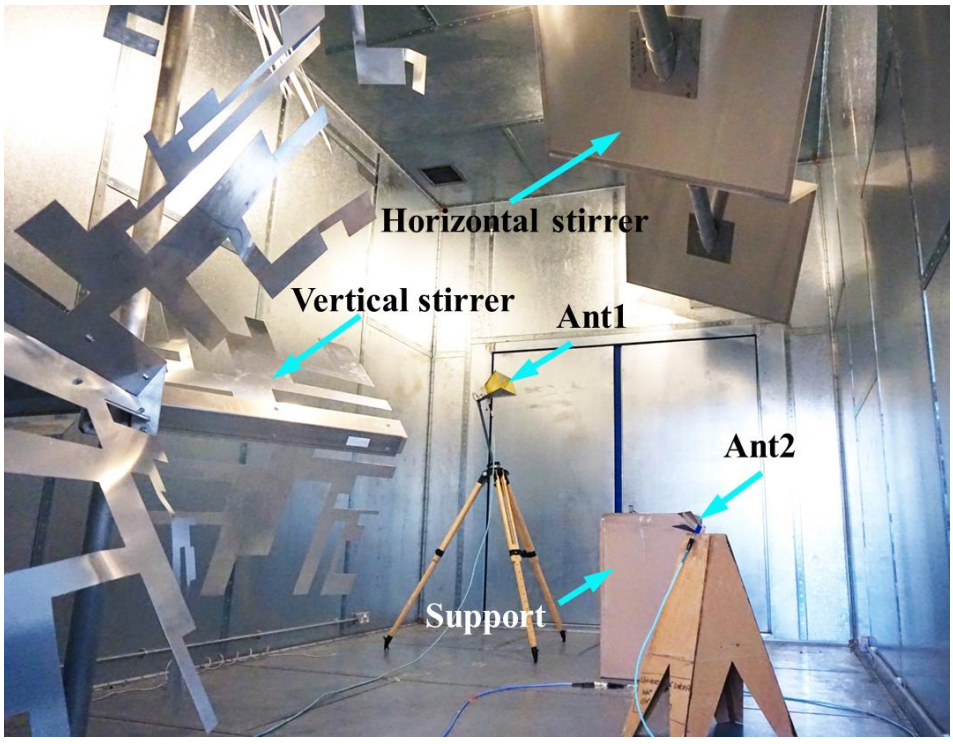
Horizontal stirrer
Vertical stirrer
Ant1
Ant2
Support

(b)

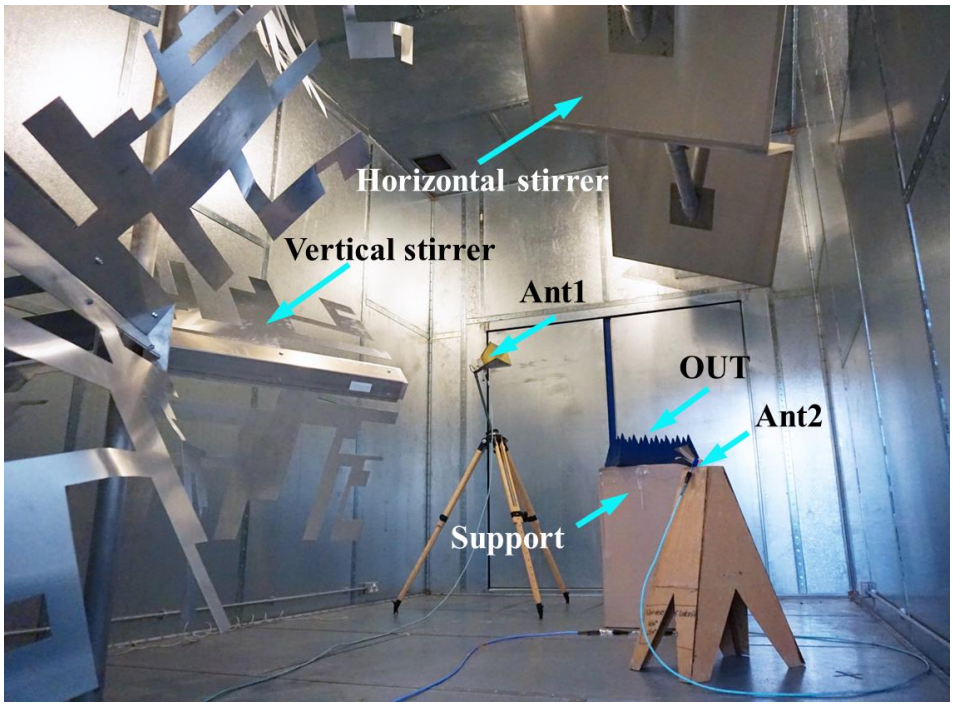

(c)

Figure 3.10 ACS measurement setup in the RC: (a) measurement system, (b) unloaded scenario, (c) loaded scenario.

The measurement procedure is given as follows.

Step 1: Calibrate the VNA including the cables according to the standard calibration procedure.

Step 2: Place the two antennas and the support (excluding the OUT) inside the RC.

Step 3: Connect antenna 1 to port 1 of the VNA and antenna 2 to port 2 of the VNA, and collect the full *S*-parameters for each stirring position.

Step 4: Keep the previous measurement setup unchanged and place the OUT on the support, and repeat Step 3.

Step 5: Preset the VNA to shift the reference planes, and repeat Step 3 without calibration. Move the OUT out of the RC, and repeat Step 3 without calibration.

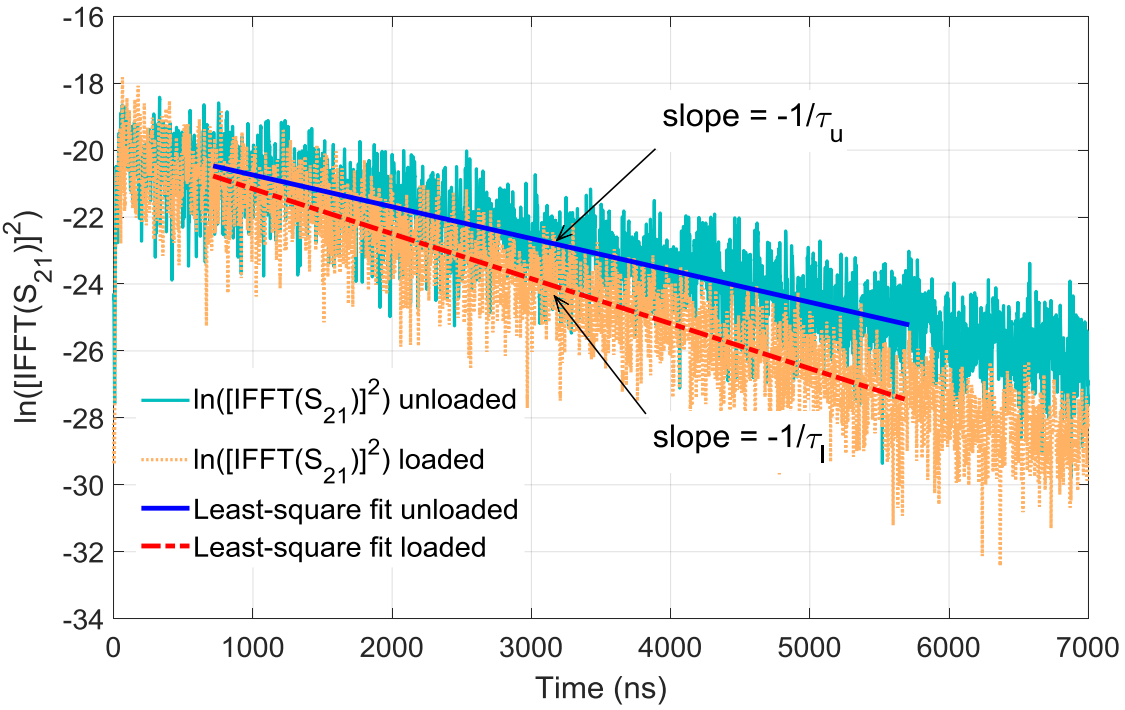

Figure 3.11 Time-domain response with calibration: $\ln([IFFT(S_{21})]^2)$ and least-square fit under loaded and unloaded scenarios.

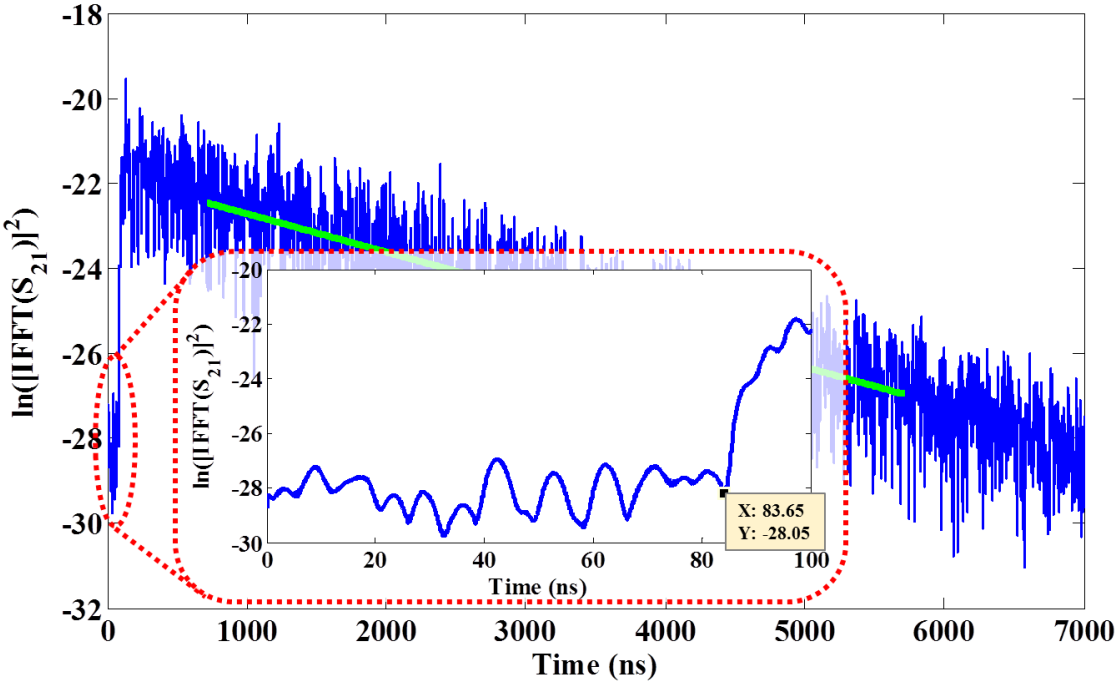

Figure 3.12 Time-domain response with no calibration and the close-up of the early-time behavior.

In this measurement, 10,001 points were sampled in the frequency range from 3.8 to 5.2 GHz. The ACS of the OUT was calculated using (3.17). A band-pass elliptic filter of order 10 is used to filter S_{21} with 200 MHz bandwidth, and then the IFFT is applied to the filtered S_{21}. The chamber decay time τ can be extracted by the same procedure as described in Section 3.3, as shown in Figure 3.11. The average chamber decay time $\langle\tau\rangle$ is then obtained from the ensemble average of the τ for different stirring positions. The early time behaviour is depicted in detail in Figure 3.12. As can be seen, in the first 83.65 ns, the chamber is not charged, this is the time that the wave travels in the cables. In our case, the total length of the two cables is about 16 m and the travelling speed of the wave inside the cables is about 2×10^8 m/s [26]. Thus, the 83.65 ns corresponds to 16.73 m which agrees well with the total length of our cables used in the measurement (our VNA is pre-calibrated with the reference planes at the output connectors of the VNA, when the VNA is pre-set the reference planes are restored). By sweeping the centre frequency of the filter, τ at different centre frequencies is obtained. The measured chamber decay time with and without calibration under loaded and unloaded scenarios is shown in Figure 3.13.

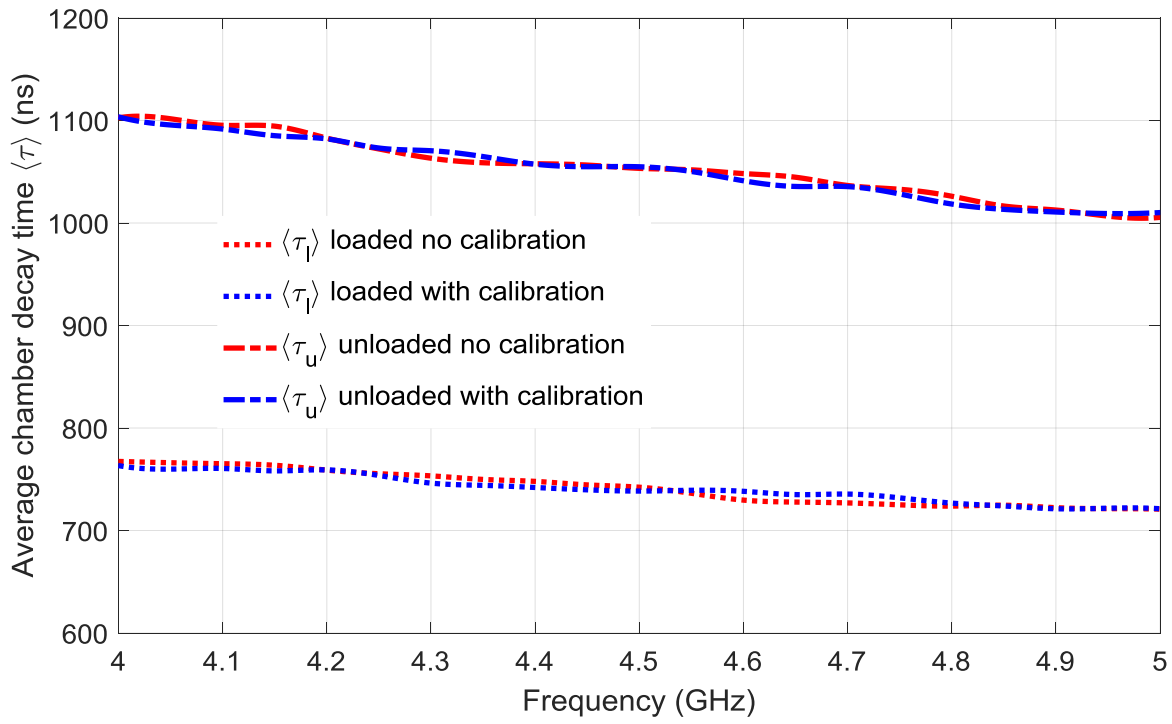

Figure 3.13 The comparison of the average chamber decay time with and without calibration under loaded and unloaded scenarios.

As expected, the chamber decay time is reduced when the chamber is loaded. The chamber decay time with calibration and that without calibration agree well, i.e., the chamber decay time can be measured accurately without calibration. The measured ACSs with and without calibration are depicted in Figure 3.14. As can be seen, they agree well and the maximum difference is within 2%, which manifests the effectiveness of the proposed method.

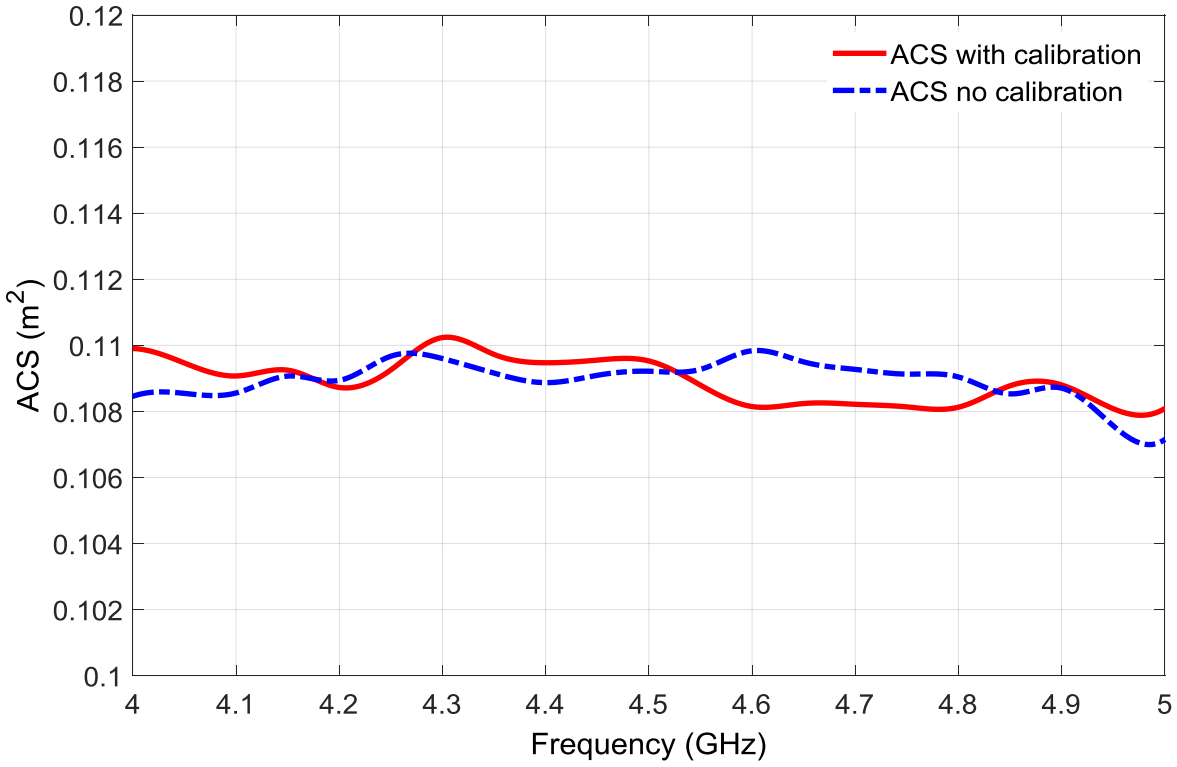

Figure 3.14 The comparison of the measured ACS with and without calibration.

3.6 Discussions and Conclusion

In this chapter, one-antenna methods for determining the ACS of the OUT in the frequency domain and in the time domain were presented at the beginning. The commonly used RC technique for determining the ACS of the OUT requires two antennas and the radiation efficiency of the two antennas should be known. In this chapter, the one-antenna method in the frequency domain was first presented which requires only one antenna (with known efficiency) by making use of enhanced backscatter effect. Thus, the measurement setup was

simplified. Then, the one-antenna method in the time domain was presented which needs no knowledge of the efficiency of the antenna. The experimental setup was illustrated and measurement results were presented. It seems that the measured ACSs by the three methods are in good agreement. The robustness of the chamber decay time and the convergence speed of the three methods were investigated. It is found that the time domain method converges much faster than the frequency domain methods. A rapid and accurate measurement can be achieved in the time domain based on this finding by using source stirring technique, which makes it quite suitable for human absorption and exposure measurement. Furthermore, in the time domain approach, the RC can be replaced by a suitable electrically large conducting cavity, which will greatly reduce the hardware requirement. The method was validated in the RC by setting the paddles stationary and the results agree well with that measured in the RC using mode stirring. The comparison of the measurement methods mentioned above is shown in Table 3.1. It is demonstrated that the time domain method is much more efficient and its hardware requirement is much lower than the frequency domain method.

Table 3.1: Comparison of Different Measurement Methods

Measurement methods	Number of antennas	Time	Facility
FD two-antenna method	2	approx. 8 hrs	RC
FD one-antenna method	1	approx. 8 hrs	RC
TD one-antenna method (mode stirring)	1	approx. 7 mins	RC
TD one-antenna method (source stirring)	1	approx. 7 mins	electrically large cavity

Following the previous work, a reliable and simple no-calibration method was proposed for the measurement of the averaged ACS of a lossy object based on the time-domain measurement in an RC. By making use of the fact that the chamber decay time is independent of the insertion loss in the system, the ACS can be measured accurately without calibration, which will simplify the measurement process and shorten the measurement time at the same time. Measurement has been done to validate the proposed method. The results show that the

averaged ACS of the OUT can be accurately measured using the proposed method with no calibration process.

There are some points that need to be emphasized. Firstly, the proposed methods presented in this chapter assume that the RC was well stirred. When the RC is not well stirred, the OUT could not fully "submerge" in the field-uniform area. The measured chamber transfer function and chamber decay time will be inaccurate, hence the measured ACS will be of considerable errors. Secondly, the antennas used in the measurement should be of high efficiency in the time domain method, i.e., the losses in the RC are dominated by the chamber wall loss and OUT loss rather than by the losses of the antennas used in the measurement. Otherwise, the power will not decay exponentially and chamber decay time cannot be extracted correctly. However, in the frequency domain, the antennas used do not have to be of high efficiency because the antenna efficiency has been calibrated out in the net power transfer function. Thirdly, during the measurement, the OUT should be set far away (more than 10λ is recommended) from the antennas to avoid the proximity effect [27]. Last but not least, the calculation of the ACS requires the difference in the net power transfer function (in the frequency domain) or the chamber decay time (in the time domain) with and without the OUT, as seen in (3.13) and (3.17). If the loss of the OUT is too small compared with that of the chamber itself, it will be very difficult for the chamber to distinguish the difference of the loss (i.e., the difference of the Q factors between loaded and unloaded scenarios), which will result in the inaccuracy of the measurement. However, for most of the applications, like the measurement of the human body absorption cross section, the loss of the OUT is normally large enough for the chamber to see and thus the ACS can be accurately calculated.

3.7 References

[1] *Electromagnetic Compatibility (EMC) part 4-21: Testing and measurement techniques-Reverberation chamber test methods*, IEC 61000-4-21, 2003.

[2] C. L. Holloway, H. A. Shah, R. J. Pirkl, W. F. Young, D. A. Hill, and J. Ladbury, "Reverberation chamber techniques for determining the radiation and total efficiency

of antennas," *IEEE Trans. Antennas Propag*., vol. 60, no. 4, pp. 1758-1770, Apr. 2012.

[3] C. L. Holloway, R. Smith, C. Dunlap, R. Pirkl, J. Ladbury, W. Young, B. Hansell, M. Shadish, and K. Sullivan, "Validation of a one-antenna reverberation-chamber technique for estimating the total and radiation efficiency of an antenna," in *Proc. IEEE Int. Symp. on Electromagn. Compat.*, Aug. 2012, pp. 205-209.

[4] H. G. Krauthauser, and M. Herbrig, "Yet another antenna efficiency measurement method in reverberation chambers," in *Proc. IEEE Int. Symp. on Electromagn. Compat.*, Jul. 2010, pp. 536-540.

[5] *IEEE Standard Method for Measuring the Effectiveness of Electromagnetic Shielding Enclosures*, IEEE Standard 299, 2006.

[6] C. L. Holloway, D. A. Hill, M. Sandroni, J. M. Ladbury, J. Coder, G. Koepke, A. C. Marvin, and Yuhui He, "Use of Reverberation Chambers to Determine the Shielding Effectiveness of Physically Small, Electrically Large Enclosures and Cavities," *IEEE Trans. Electromagn. Compat*., vol.50, no.4, pp. 770-782, Nov. 2008.

[7] D. Fedeli, G. Gradoni, V. M. Primiani, and F. Moglie, "Accurate analysis of reverberation field penetration into an equipment-level enclosure," *IEEE Trans. Electromagn. Compat.*, vol. 51, no. 2, pp. 170-180, May 2009.

[8] G. B. Tait, C. Hager, M. B. Slocum, and M. O. Hatfield, "On Measuring Shielding Effectiveness of Sparsely-Moded Enclosures in a Reverberation Chamber," *IEEE Trans. Electromagn. Compat.*, vol. 55, no. 2, pp. 231-240, Apr. 2013.

[9] H. G. Krauthäuser, "On the measurement of total radiated power in uncalibrated reverberation chambers," *IEEE Trans. Electromagn. Compat*., vol. 49, no. 2, pp. 270-279, 2007.

[10] U. Carlberg, P.-S. Kildal, A. Wolfgang, O. Sotoudeh, and C. Orlenius, "Calculated and measured absorption cross sections of lossy objects in reverberation chamber," *IEEE Trans. Electromagn. Compat*., vol. 46, no. 2, pp. 146-154, May 2004.

[11] E. Amador, M. Andries, C. Lemoine, and P. Besnier, "Absorbing material characterization in a reverberation chamber," in *Proc. IEEE Int. Symp. on Electromagn. Compat.*, Sept. 2011, pp. 117-122.

[12] G. C. R. Melia, M. P. Robinson, I. D. Flintoft, A. C. Marvin, and J. F. Dawson, "Broadband Measurement of Absorption Cross Section of the Human Body in a Reverberation Chamber," *IEEE Trans. Electromagn. Compat*., vol. 55, no. 6, pp. 1043-1050, Dec. 2013.

[13] A. Bamba, D. P. Gaillot, E. Tanghe, G. Vermeeren, W. Joseph, M. Lienard, and L. Martens, "Assessing Whole-Body Absorption Cross Section For Diffuse Exposure From Reverberation Chamber Measurements," *IEEE Trans. Electromagn. Compat*., vol. 57, no. 1, pp. 27-34, Feb. 2015.

[14] D. A. Hill, M. T. Ma, A. R. Ondrejka, B. F. Riddle, M. L. Crawford, and R. T. Johnk, "Aperture excitation of electrically large, lossy cavities," *IEEE Trans. Electromagn. Compat*., vol. 36, no. 3, pp. 169-178, Aug. 1994.

[15] M. I. Andries, P. Besnier, and C. Lemoine, "On the prediction of the average absorbing cross section of materials from coherence bandwidth measurements in reverberation chamber," in *Proc. IEEE Int. Symp. on Electromagn. Compat.*, Sept. 2012, pp. 1-6.

[16] C. L. Holloway, H. A. Shah, R. J. Pirkl, K. A. Remley, D. A. Hill, and J. Ladbury, "Early Time Behavior in Reverberation Chambers and Its Effect on the Relationships Between Coherence Bandwidth, Chamber Decay Time, RMS Delay Spread, and the Chamber Buildup Time," *IEEE Trans. Electromagn. Compat*., vol. 54, no. 4, pp. 714-725, Aug. 2012.

[17] D. L. Green, V. Rajamani, C. F. Bunting, B. Archambeault, and S. Connor, "One-port time domain measurement technique for quality factor of loaded and unloaded cavities," in *Proc. IEEE Int. Symp. on Electromagn. Compat.*, Aug. 2013, pp. 747-750.

[18] C. Vyhlidal, V. Rajamani, C. F. Bunting, P. Damacharla, and V. Devabhaktuni, "Estimation of absorber performance using reverberation techniques and artificial neural network models," in *Proc. IEEE Int. Symp. on Electromagn. Compat.*, Aug. 2015, pp. 897-901.

[19] S. J. Boyes, P. J. Soh, Y. Huang, G. A. E. Vandenbosch, and N. Khiabani, "Measurement and Performance of Textile Antenna Efficiency on a Human Body in a Reverberation Chamber," *IEEE Trans. Antennas Propag*., vol.61, no.2, pp. 871-881, Feb. 2013.

[20] C. L. Holloway, D. A. Hill, J. M. Ladbury, P. F. Wilson, G. Koepke, and J. Coder, "On the Use of Reverberation Chambers to Simulate a Rician Radio Environment for the Testing of Wireless Devices," *IEEE Trans. Antennas Propag*., vol.54, no.11, pp. 3167-3177, Nov. 2006.

[21] J. M. Ladbury, and D. A. Hill, "Enhanced Backscatter in a Reverberation Chamber: Inside Every Complex Problem is a Simple Solution Struggling to Get Out," in *Proc. IEEE Int. Symp. on Electromagn. Compat.*, Jul. 2007, pp. 1-5.

[22] D. A. Hill, Electromagnetic Fields in Cavities: Deterministic and Statistical Theories. New York, NY, USA: Wiley-IEEE Press, 2009.

[23] C. R. Dunlap, "Reverberation chamber characterization using enhanced backscatter coefficient measurements," Ph.D. dissertation, Dept. of Elect., Comput. and Eng., Univ. of Colorado, Boulder, USA, 2013.

[24] I. D. Flintoft, G. C. R. Melia, M. P. Robinson, J. F. Dawson, and A. C. Marvin. "Rapid and accurate broadband absorption cross-section measurement of human bodies in a reverberation chamber," *Meas. Sci. Technol*., vol. 26, no. 6, pp. 65701-65709, Jun. 2015.

[25] Q. Xu, Y. Huang, X. Zhu, L. Xing, and Z. Tian, "Measure the radiation efficiency of antennas in a reverberation chamber without calibration," in *Proc. IEEE int. Symp. on Antennas Propag.*, Vancouver, BC, 2015, pp. 1178-1179.

[26] [Online] Available: http://web.physics.ucsb.edu/~lecturedemonstrations/Composer/Pages/76.18.html. [Accessed: 18-Apr-2017]

[27] W. T. C. Burger, K. A. Remley, C. L. Holloway, and J. M. Ladbury, "Proximity and antenna orientation effects for large-form-factor devices in a reverberation chamber," in *Proc. IEEE Int. Symp. on Electromagn. Compat.*, Aug. 5-9, 2013, pp. 671-676.

Chapter 4: Volume Measurement Using Averaged Absorption Cross Section

4.1 Introduction

In last chapter, the ACS measurement methods in an RC have been discussed. In this chapter, an interesting practical application of the ACS measurement methods will be introduced – cavity volume measurement.

The measurement of the volume of a large cavity is required especially in shipping and aircraft industry. In practice, to optimize the capacity of the cargo compartment of a ship or an aircraft, it is necessary to get the knowledge of its volume. An example is shown in Figure. 4.1. However, the volume of such a cavity is not easy to obtain because of its irregular shape and the complex inner environment. Normally, a 3D laser scanner can be employed [2]. The laser scanner first scans the whole profile of the cavity under test and builds its 3D model. Subsequently, the volume of the cavity can be calculated from the 3D model. However, this method is time-consuming and costly. It may not be available for some companies or institutes. And also, before scanning the profile of the cavity, the contents that may block the laser beam in the cavity should be removed, which could be tedious or sometimes impossible in reality. Since such a cavity is normally made of metal, an alternative method based on the statistical theory of EM waves was proposed in [3]. In this method, the volume of a cavity is extracted by comparing the cavity quality factors in the frequency domain and in the time domain [4] – [7]. This method is economical, but it is not efficient enough because many stirring positions are required during the measurement. A more efficient method is in demand for practical purpose.

In this chapter, a new rapid method to measure the volume of a large cavity is presented. This method is based on the measurement of the cavity decay time constants with and without a lossy object. A lossy object with a known averaged ACS [8] – [14] is required for the measurement. It is found that only one antenna is required in this method. Hence, the hardware requirement is very simple, which makes the method very economical. Also, this

method is very efficient because only a few stirring positions are needed to complete the measurement. Consequently, the measurement time can be greatly shortened. Furthermore, by using acoustic waves instead of EM waves, this method can be generalized and the cavity under test does not have to be metallic.

Figure 4.1 The cargo compartment of an aircraft and the demand of measuring its volume [1].

4.2 Theory

Before studying how to measure the cavity volume using the ACS, it is useful to first introduce how the ACS is measured in an electrically large cavity using an electromagnetic method. It has been detailed in Chapter 3 that the averaged ACS $\langle\sigma_a\rangle$ can be measured in the time domain [9], [15] as

$$\langle\sigma_a\rangle = \frac{V}{c}(\langle\tau_l\rangle^{-1} - \langle\tau_u\rangle^{-1}) \tag{4.1}$$

The definitions of V, c, $\langle\tau_l\rangle$, and $\langle\tau_u\rangle$ can be found in Section 3.2.

It can be clearly seen from (4.1), the cavity volume V is required to calculate the ACS. (4.1) can be transformed to the form

$$V = c \cdot \frac{\langle\sigma_a\rangle}{\langle\tau_l\rangle^{-1} - \langle\tau_u\rangle^{-1}} \tag{4.2}$$

It can be seen that if the averaged ACS of an OUT is known or pre-calibrated, (4.2) provides a method to obtain the cavity volume. The quantities that needs to be measured is τ_l and τ_u. In this method, only one antenna is required since τ can be obtained from S_{11}. Furthermore, because τ is very robust [9], only a very few stirring positions are needed to extract it accurately. Thus, this method can be very efficient.

4.3 Measurement

To verify the proposed method, measurements were conducted in the frequency range of 2.8 to 4.2 GHz in the RC at the University of Liverpool. The volume of the RC is 3.6 m × 4.0 m × 5.8 m = 83.52 m^3. A double-ridged waveguide horn antenna (SATIMO® SH 2000) was used in the measurement. The antenna was mounted on a turn-table platform to introduce source stirring positions [16] – [17]. It was connected to port 1 of the VNA via a cable running through the bulkhead of the RC. A piece of RAM was selected as the OUT which was placed on the support (a carton box). In the measurement, the turn-table platform was rotated stepwise to 18 different positions (10 degrees for each step). At each source stirring position, the VNA swept the *S*-parameters over the full frequency span. It should be noted that the antenna should direct away from the OUT to avoid LoS illumination (to provide a random environment). Therefore, a directional antenna was used and the turn-table platform was rotated 180 ° instead of 360 °. During the measurement, the two stirrers of the RC were not used because in practice it may not have a stirring system in a cavity. A general measurement setup is shown in Figure 4.2(a). The measurement setups without and with the OUT are shown in Figure 4.2(b) and (c), respectively.

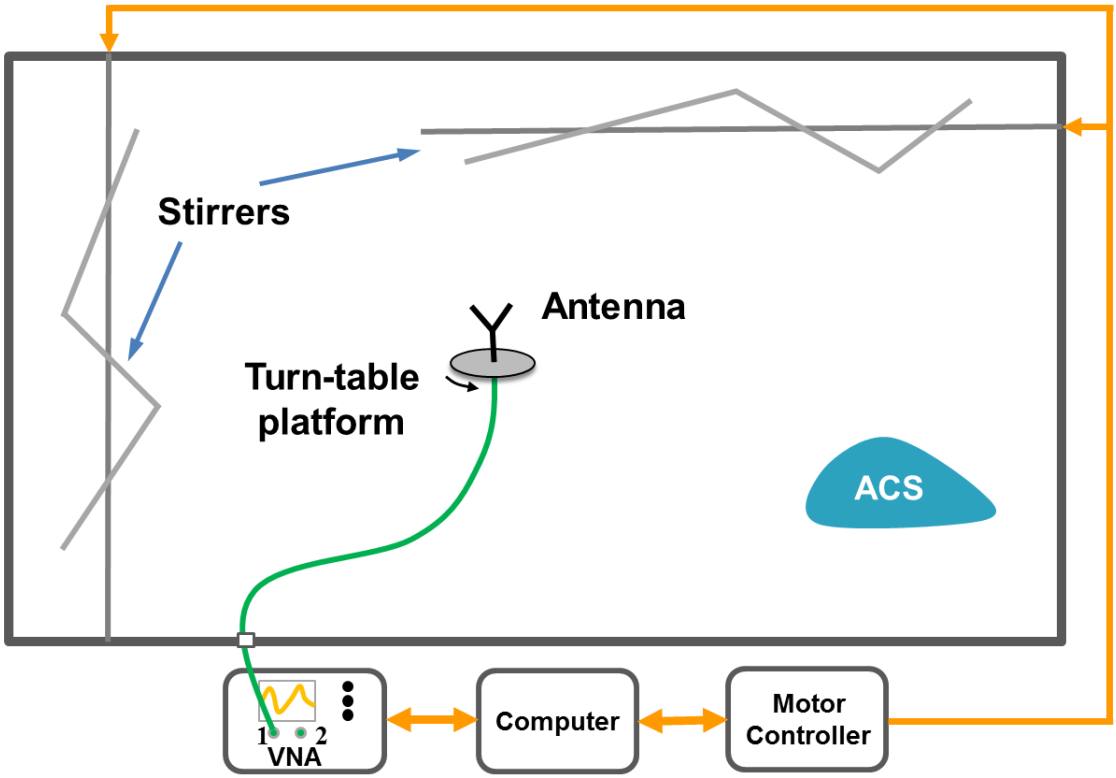
Stirrers
Antenna
Turn-table platform
ACS
1
2
VNA
Computer
Motor Controller

(a)

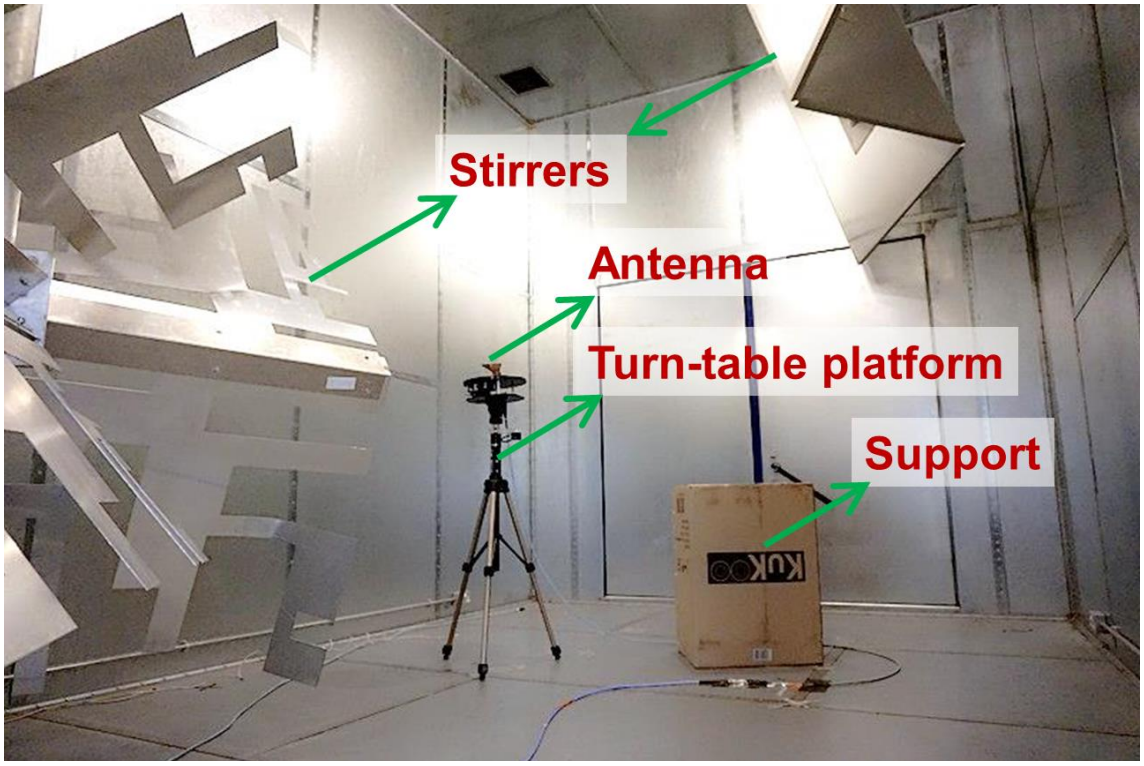
Stirrers
Antenna
Turn-table platform
Support

(b)

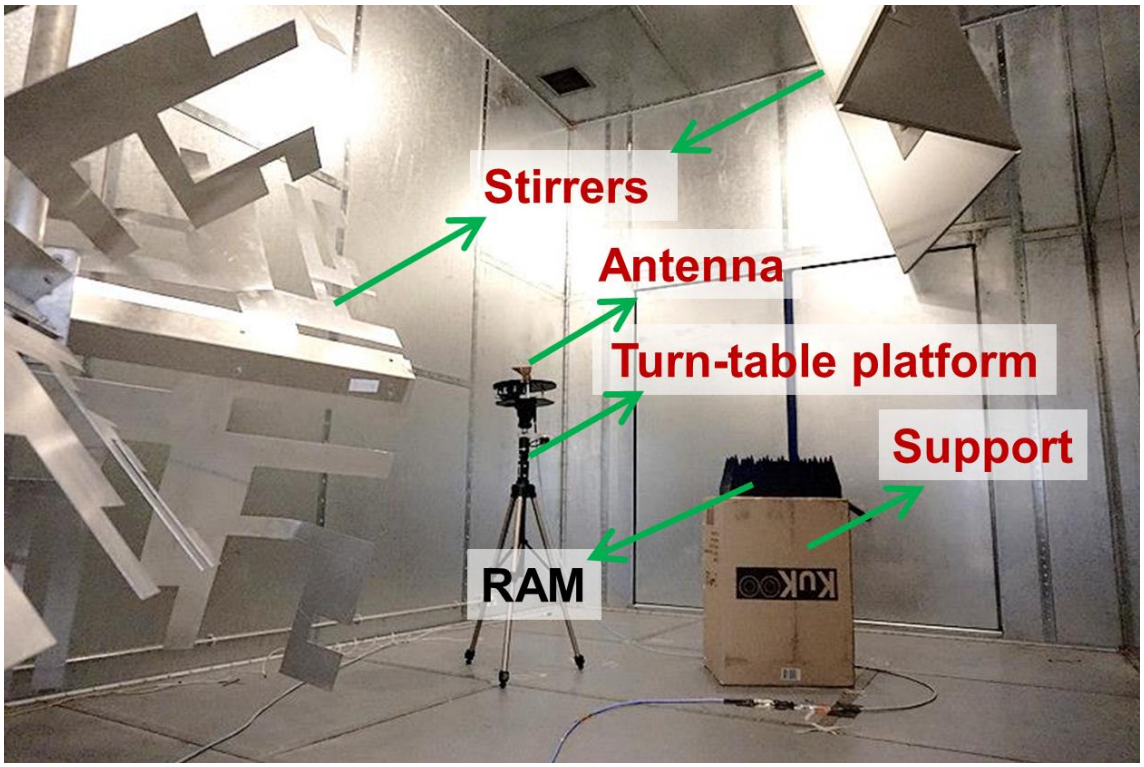

(c)

Figure 4.2 Measurement setup in the RC: (a) global measurement system, (b) without ACS, (c) with ACS.

The measurement was conducted with the following five steps.

Step 1: Calibrate the VNA including the cables.

Step 2: Place the antenna, the turn-table platform and the support inside the RC, excluding the OUT.

Step 3: Connect the antenna to the cable connected to VNA port 1 and record the *S*-parameters S_{11} at each source stirring position.

Step 4: Keep the measurement setup unchanged, place the OUT on the support and repeat Step 3.

Step 5: Extract the cavity decay time constants with and without the OUT and calculate the volume of the RC using (4.2).

In our measurement, 10,001 points were sampled in the frequency range of 2.8 – 4.2 GHz. S_{11} in this frequency span at each source stirring position was collected. The cavity decay time constant was extracted with the same procedure detailed in Section 3.3. The results are shown in Figure 4.3.

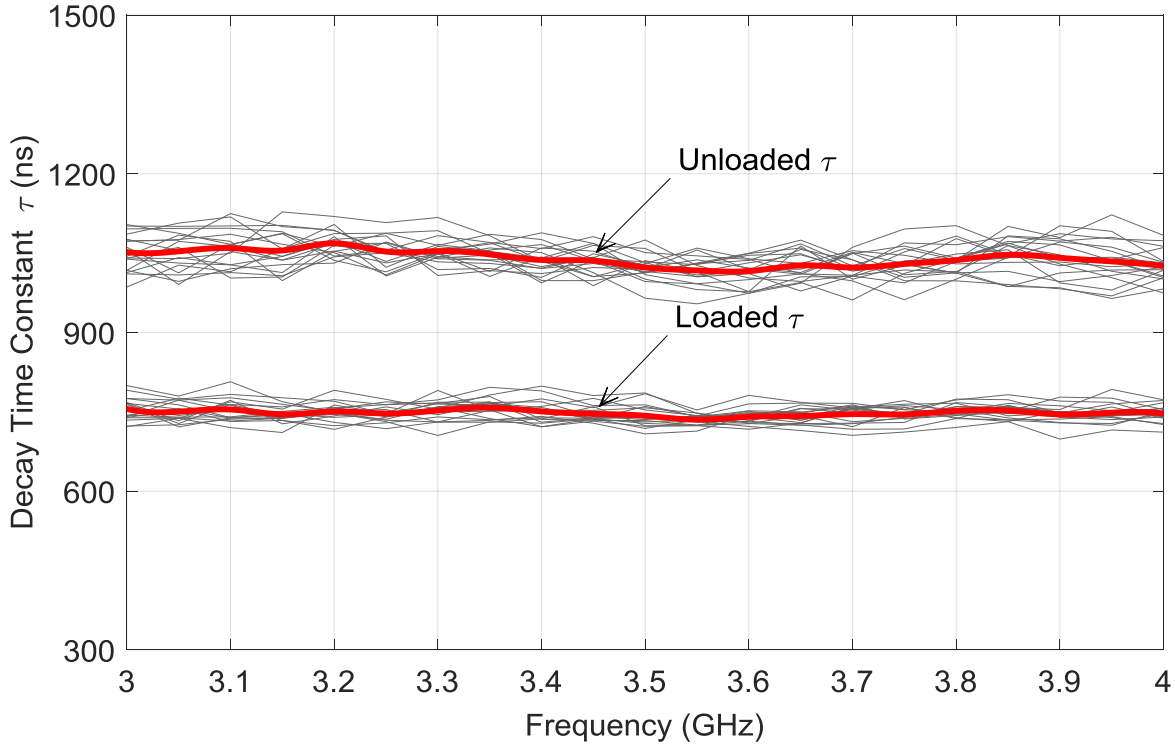

Figure 4.3 Measured cavity decay time constants τ under loaded and unloaded scenarios.

The thin curves are the measured τ for each source stirring position and the thick curves are the averaged τ for all the 18 source stirring positions. The averaged τ was used to calculate the cavity volume. The robustness of τ can be observed in Figure 4.3. As can be seen, under the unloaded scenario (without OUT), the variation between the τ for one stirring position and the averaged τ is within about $\pm$ 10% and under the loaded scenario (with OUT), it is within about $\pm$ 5%. This is because τ is determined by the diffuse loss of the RC which is not sensitive to the source stirring positions [9].

To measure the volume of the RC, the ACS of the OUT was first calibrated in the frequency range of interest, as shown in Figure 4.4. It can be seen that the ACS of the OUT is 0.1078 m^2 in the frequency band of 3.0 – 4.0 GHz. And also, the ACS seems frequency independent.

The reason is, when the OUT is electrically large, the ACS only determined by its surface area which does not depend on the frequency [8]. Actually, this provides a faster method to obtain the ACS of a RAM and consequently, a faster and simpler method to measure the cavity volume with ACS. This point will be discussed later.

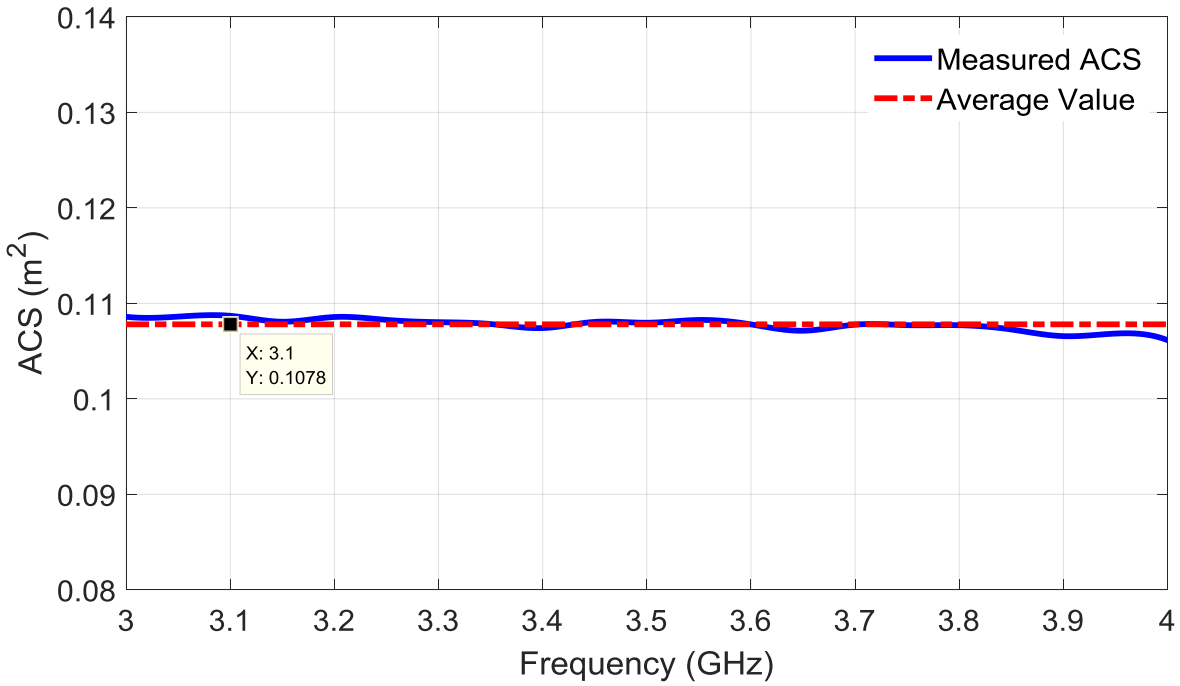

Figure 4.4 The averaged ACS of the OUT in 3.0 – 4.0 GHz.

In practice, a cavity is hardly vacant or well shielded. It may be loaded with cargoes or have apertures (such as windows or ventilation openings). To verify the validity of the proposed method in a practical environment, the volume of the RC in three different scenarios were measured: the well-shielded scenario, the open-door scenario, and the cargo-loaded scenario, as shown in Figure 4.5(a), (b) and (c), respectively. In the following part, the measurement results under these three different scenarios using the proposed method are detailed.

(a)

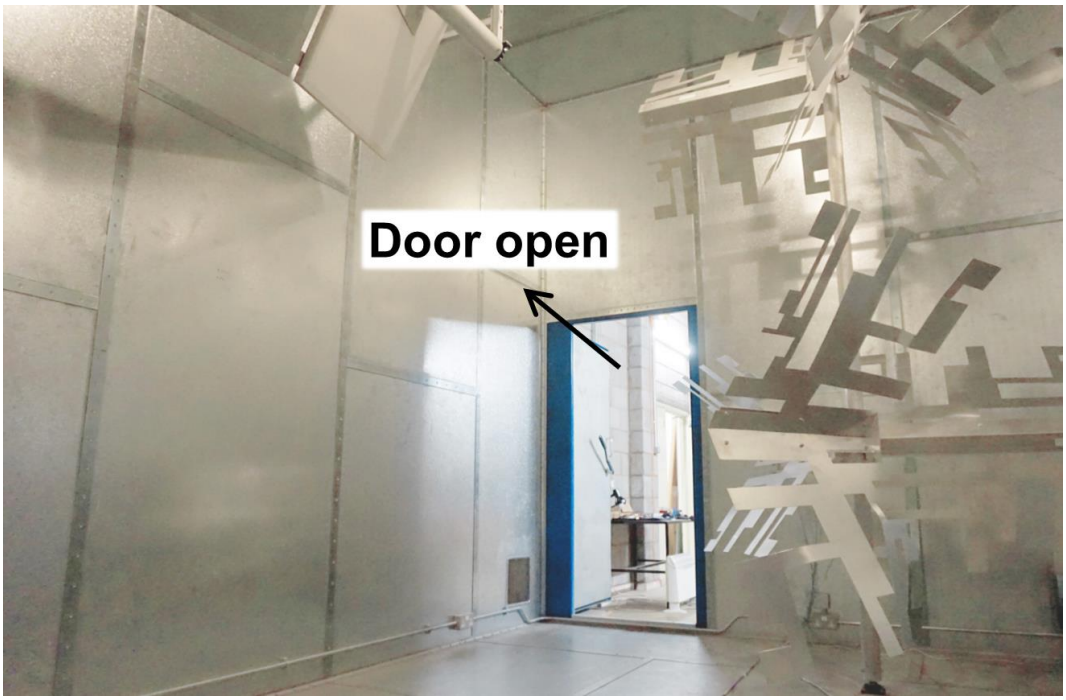

(b)

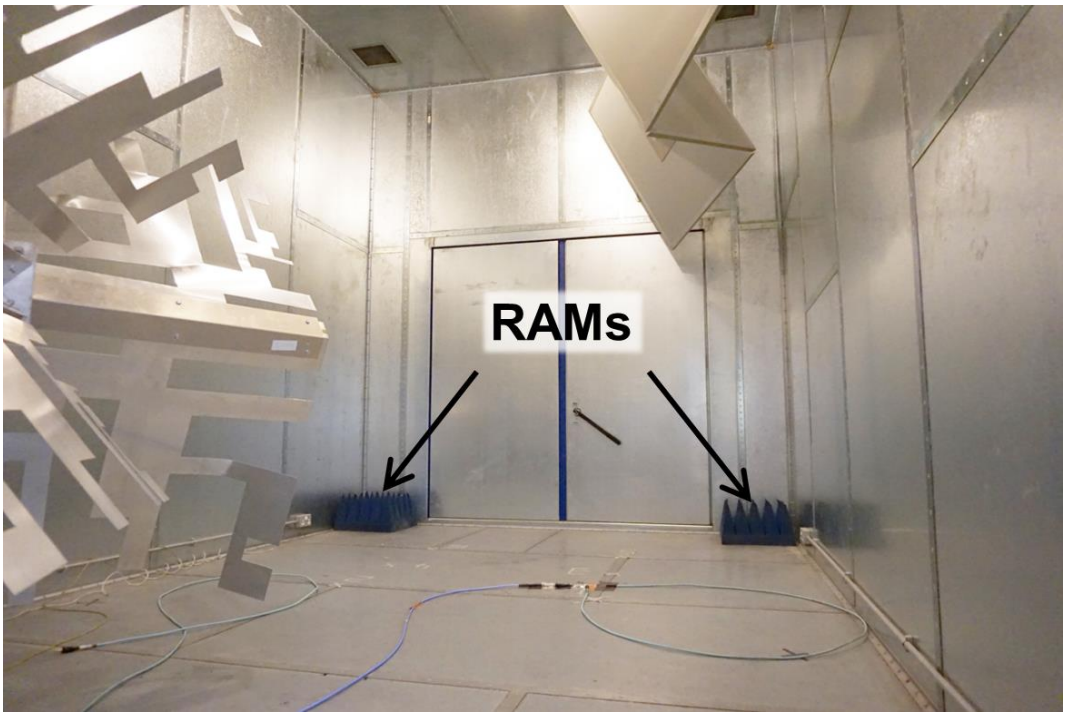

(c)

Figure 4.5 Three different test scenarios: (a) well-shielded scenario, (b) open-door scenario, and (c) cargo-loaded scenario.

In the well-shielded scenario, the door of the RC was closed. This scenario is corresponding to a cavity with a high *Q* factor. The measurement result is shown in Figure 4.6(a). The reference value (the real value of the RC volume, 83.52 m^3 here) and the average value (the averaged value of the RC volume in the frequency span of interest) are also plotted. It can be seen that the measured value is close to the reference value. The maximum difference is about 6.8% at 3.403 GHz. The difference between the average value and the reference value is only about 1.2%, which is very small. In practice, there may be some apertures on a cavity, such as windows, ventilation openings or open doors. This scenario is corresponding to a cavity with a relatively low *Q* factor. To emulate a cavity with apertures, the front door of the RC was opened and the whole measurement using the proposed method was repeated. The results are shown Figure 4.6(b). As can be seen, the maximum difference between the measured value and the reference value is approximately 5.8% at 3.423 GHz. The difference between the average value and the reference value is only approximately 0.26%, which is negligible. Sometimes a cavity is loaded with cargoes, such as the compartment of an aircraft

or the refrigerated warehouse of a supermarket. When a cavity is loaded with cargoes, its *Q* factor will decrease. To emulate a cavity loaded with cargoes, two pieces of RAM were placed at the corners of the RC to decrease its *Q* factor. The measurement result is depicted in Figure 4.6(c). As can be seen, the maximum difference between the measured value and the reference value is around 5% at 3.182 GHz. The difference between the average value and the reference value is around 0.5%, which can be neglected.

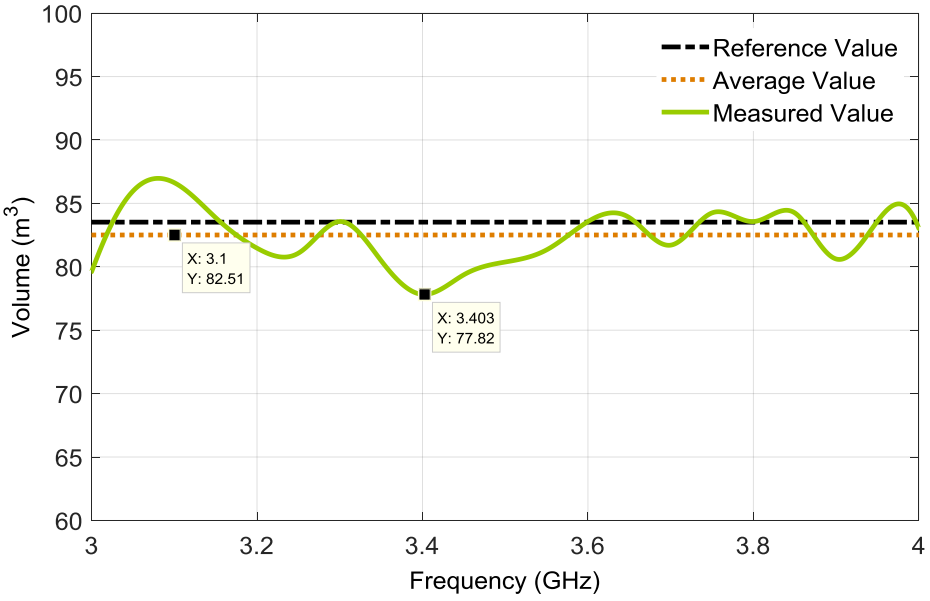

(a)

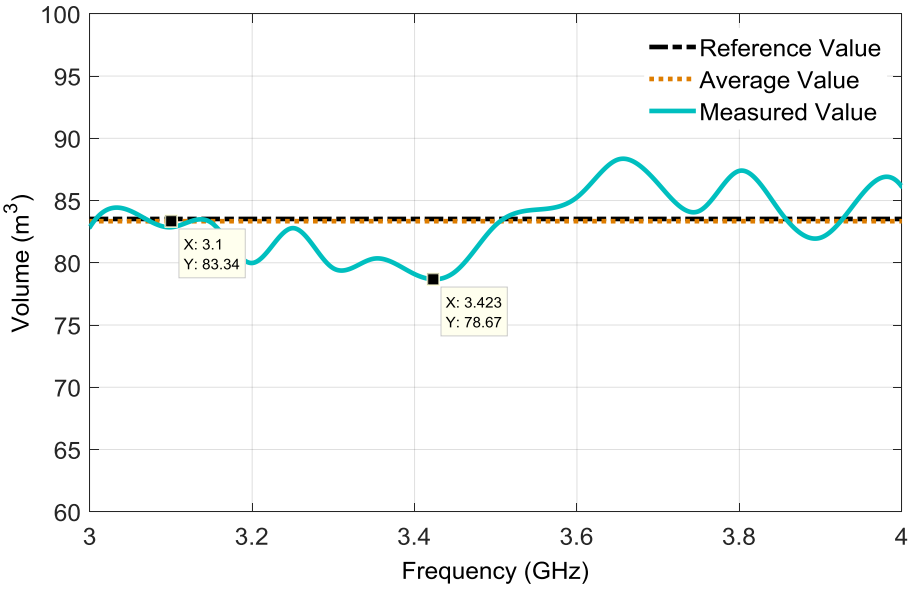

(b)

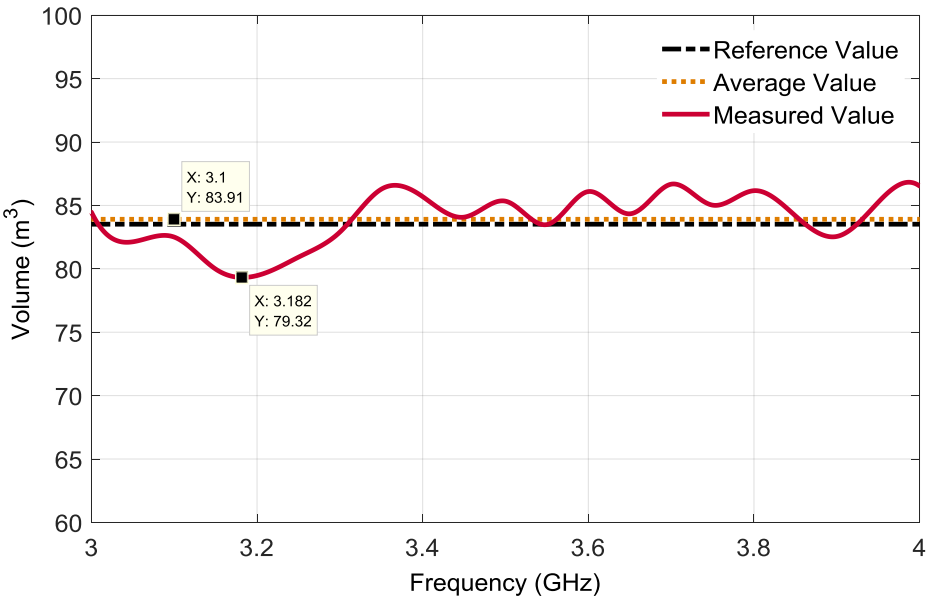

(c)

Figure 4.6 The measured RC volume under three different scenarios: (a) well-shielded scenario, (b) open-door scenario, and (c) cargo-loaded scenario.

It should be noted that in practice it may not have a chance to calibrate the ACS of the OUT. Fortunately, it has been proved that, for an electrically large RAM of convex shape, its ACS and surface area S satisfy ACS = $S/4$ [8]. That is, the ACS of a RAM is a quarter of its surface area. By utilizing this theory, the proposed method can be further simplified and the calibration of the ACS of the OUT is not needed. To validate this idea, another piece of RAM was selected as the OUT. The size of the base of the RAM was 0.5 m $\times$ 0.5 m $\times$ 0.06 m. The pyramids of the RAM were fully covered with aluminum foil (because the surface area of the pyramids was not easy to measure) and only the base was subject to absorption, as can be seen from Figure 4.7. Thus, the surface area absorbing the EM waves is 0.37 m^2 and its theoretical ACS is 0.0925 m^2. The measured and the theoretical ACS are compared in Figure 4.8. As can be seen, the average value of the measured ACS is about 0.0825 m^2 in the frequency range of 3.0 – 4.0 GHz which is 0.01 m^2 smaller (10.8% smaller) than the theoretical value. The reason is, in reality, the RAM is not an ideal "black body", i.e., it cannot absorb all the EM waves that hit on its surface because of the scattering, the diffraction, and the reflection. Consequently, the measured ACS is smaller than the theoretical value.

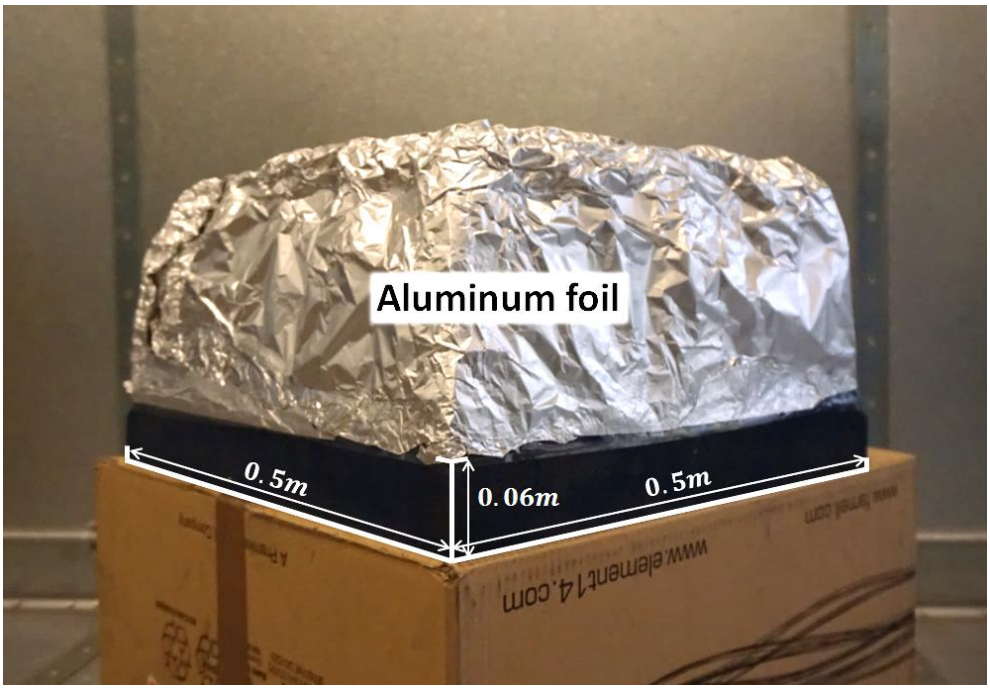

Figure 4.7 The RAM with its pyramids covered by aluminum foil. The size of its base is marked.

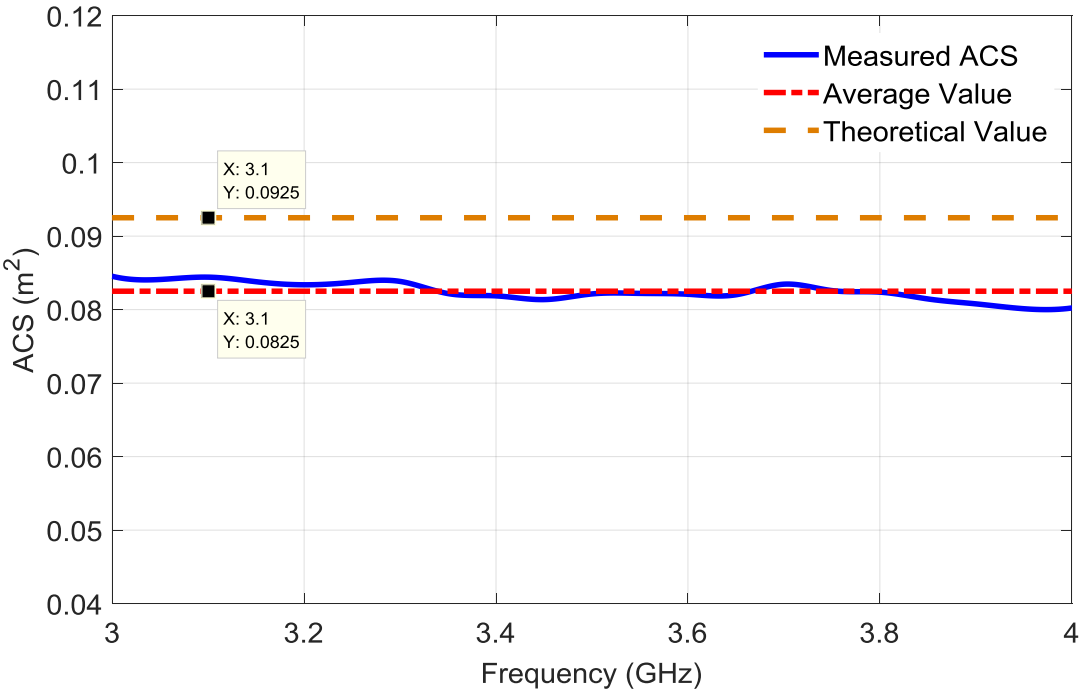

Figure 4.8 The measured ACS of the OUT. Its theoretical value and average value are marked out as well.

It is worth mentioning that for ease of surface area calculation, a RAM of regular shape (such as rectangular parallelepiped or spherical shape) is preferred. Again, the measurement was conducted by following the aforementioned procedure and three different scenarios (well-shielded scenario, open-door scenario, and cargo-loaded scenario) were studied. The theoretical ACS value is used to calculate the volume of the RC. The results are shown in Figure 4.9.

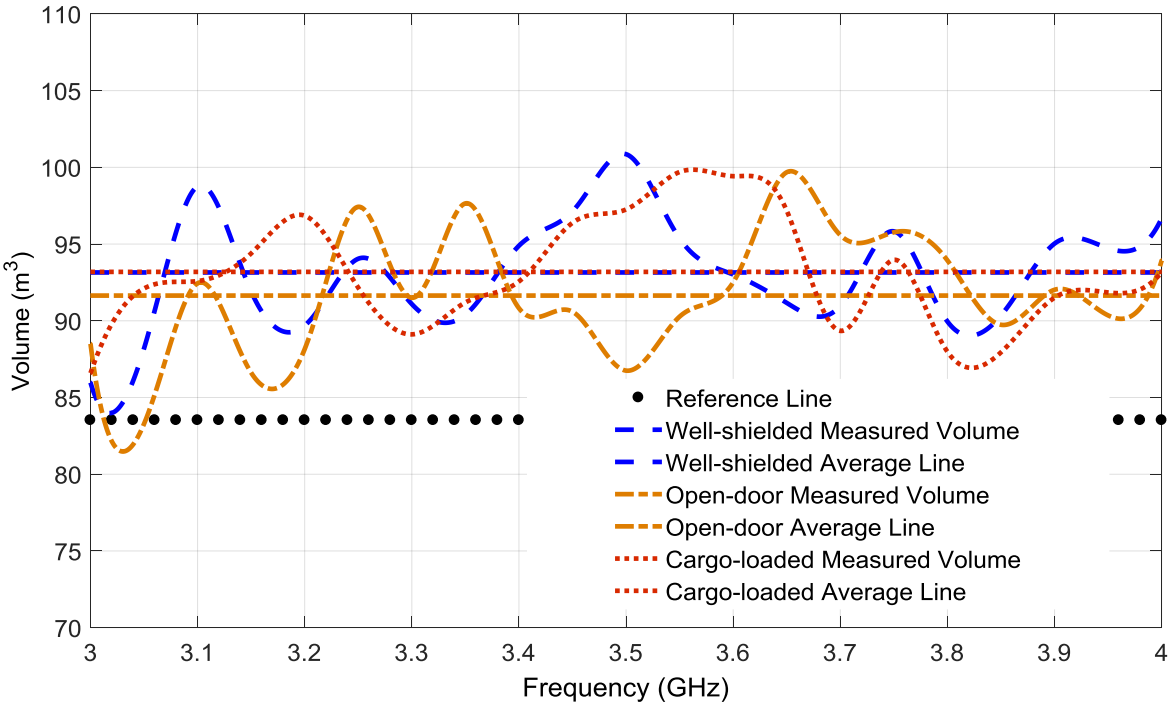

Figure 4.9 The measured RC volume under three different scenarios (the average lines of the three different scenarios are the corresponding horizontal lines).

It can be seen that the measured RC volume under the three different scenarios is close to the reference value. The maximum differences under the well-shielded scenario, the open-door scenario, and the cargo-loaded scenario are about 20.8%, 19.4%, and 19.5%, respectively. From (4.2), it can be obtained

$$\frac{dV}{V} = \frac{d\langle\sigma_a\rangle}{\langle\sigma_a\rangle} \tag{4.3}$$

That is, the measurement error margin of the cavity volume is determined by that of the ACS. From Figure 4.8, it is known that

$$\frac{d\langle\sigma_a\rangle}{\langle\sigma_a\rangle} = \frac{0.0925 - 0.0825}{0.0825} \times 100\% \approx 12\% \tag{4.4}$$

Therefore, the difference of cavity volume between the measured average value and the reference value should be around 12%. As shown in Figure 4.9, the differences between the average value and the reference value under the well-shielded scenario, the open-door scenario, and the cargo-loaded scenario are about 11.5%, 11.6%, and 9.7%, respectively, which agree well with the theoretical prediction in (4.4).

The measurement results are summarized in Table 4.1. A comparison between this proposed method and the method proposed in [3] is made. It can be seen that the proposed one-antenna method using source stirring and calibrated ACS can finish the measurement with minimum errors in the shortest time. The proposed one-antenna method using source stirring and theoretical ACS has the merit of short measurement time as well, but its measurement errors are relatively bigger.

It should be pointed out that the method of using EM waves is only valid for conducting cavities and the OUT should absorb radio waves. If the cavity is made of non-conducting materials such as concrete or bricks, acoustic waves should be used to detect the volume of the cavity. In acoustics, it can be derived [18]

$$\langle\sigma_a\rangle = \frac{24(ln10)V}{c_s}(T_{60,l}^{-1} - T_{60,u}^{-1}) \tag{4.5}$$

where $\langle\ \rangle$ represents the average over different microphone positions. $\langle\sigma_a\rangle$ is the averaged ACS of the OUT (acoustic wave absorbers), V is the volume of the cavity and c_s is the sound speed in the air. $T_{60,l}$ and $T_{60,u}$ are the reverberation time (the decay time for a 60 dB sound pressure level decrease) of the cavity with and without the OUT inside, respectively. (4.5) can be converted to

$$V = \frac{c_0}{24(ln10)} \cdot \frac{\langle\sigma_a\rangle}{T_{60,l}^{-1} - T_{60,u}^{-1}} \tag{4.6}$$

$T_{60,l}$ and $T_{60,u}$ can be extracted from the PDPs of the cavity with and without the OUT inside. Thus, the feasibility of the proposed method is generalized. It is not only limited to conducting cavities.

Table 4.1: Comparison of Measured RC Volume

Measurement methods	Scenarios	Maximum relative error	Mean relative error	Standard deviation	Measurement time
One-antenna method in [3] (mechanical stirring)	Well-shielded	N/A	N/A	N/A	Approx. 2 hrs
	Open-door (90°)	17.3%	7.3%	2.84	Approx. 2 hrs
	Cargo-loaded	10.2%	1.7%	2.19	Approx. 2 hrs
One-antenna method in [3] (source stirring)	Well-shielded	N/A	N/A	N/A	Approx. 40 mins
	Open-door (90°)	26.9%	2.6%	6.05	Approx. 40 mins
	Cargo-loaded	13.8%	1.8%	3.67	Approx. 40 mins
Proposed one-antenna method (source stirring & calibrated ACS)	Well-shielded	6.8%	1.2%	2.15	Approx. 10 mins
	Open-door (90°)	5.8%	0.2%	2.59	Approx. 10 mins
	Cargo-loaded	5.0%	0.5%	2.06	Approx. 10 mins
Proposed one-antenna method (source stirring & theoretical ACS)	Well-shielded	20.8%	11.5%	3.44	Approx. 10 mins
	Open-door (90°)	19.4%	11.6%	3.95	Approx. 10 mins
	Cargo-loaded	19.5%	9.7%	3.47	Approx. 10 mins

Source stirring & calibrated ACS means using source stirring technique and the calibrated ACS value; source stirring & theoretical ACS means using source stirring technique and the theoretical ACS value; 90° means the door is open with 90 degrees.

4.4 Discussions and Conclusion

In this chapter, a rapid and accurate measurement method has been developed to measure the volume of a large cavity. A RAM with a known averaged ACS is selected as an OUT to aid the measurement. Using this method, the cavity volume can be obtained by measuring its decay time constants with and without the OUT. The proposed method has been validated with both theory and measurement studies. It is found that the measurement can be completed rapidly with a simple measurement setup using this method, which makes it an ideal way of measuring the cavity volume. Furthermore, by using acoustic waves, the proposed method can be generalized and the cavity under test does not have to be conducting.

The preconditions of the proposed method should be pointed out. First, the environment inside the cavity under test should be reverberant, i.e., the Q factor of the cavity should not be too low. If its Q is very low, i.e., the cavity is very lossy, it will be very difficult to realize a statistically uniform field inside the cavity. Second, the loss of the OUT should not be too small. As can be seen from (4.2), the calculation of the cavity volume requires the difference of the cavity decay time constants with and without the OUT. If the OUT loss is too small compared with the cavity loss, it may not be possible for the cavity to perceive the difference of the loss (i.e., the difference of the Q factors with and without OUT), which will result in an inaccurate measurement. Third, during the measurement, the LoS illumination of the antenna to the OUT should be avoided. Or the inaccurate measurement of τ_l could occur because most of the power from the antenna will be captured and absorbed by the OUT before being reverberated by the cavity. Last but not least, the proposed method is valid for a single cavity while not for coupled cavities because for coupled cavities, the loss mechanism is different [19] – [21] and (4.1) is no longer hold.

4.5 References

[1] [Online]. Available: https://www.airtransport.cc. [Accessed: 03-Mar-2017].

[2] S. S. Bhat, and D. J. Smith, "Laser and sound scanner for non-contact 3D volume measurement and surface texture analysis," Physiological Meas., vol. 15, no. 1, pp. 7988, 1994.

[3] Q. Xu, Y. Huang, L. Xing, Z. Tian, Z. Fei, and L. Zheng, "A Fast Method to Measure the Volume of a Large Cavity," *IEEE Access*, vol. 3, pp. 1555-1561, 2015.

[4] C. L. Holloway, H. A. Shah, R. J. Pirkl, W. F. Young, D. A. Hill, and J. Ladbury, "Reverberation chamber techniques for determining the radiation and total efficiency of antennas," *IEEE Trans. Antennas Propag*., vol. 60, no. 4, pp. 1758-1770, Apr. 2012.

[5] J. M. Ladbury, and D. A. Hill, "Enhanced backscatter in a reverberation chamber: Inside every complex problem is a simple solution struggling to get out," in *Proc. IEEE Int. Symp. Electromagn. Compat.*, pp. 1-5, Jul. 2007.

[6] E. Amador, C. Lemoine, P. Besnier, and A. Laisné, "Reverberation chamber modeling based on image theory: Investigation in the pulse regime," *IEEE Trans. Electromagn. Compat.*, vol. 52, no. 4, pp. 778-789, Nov. 2010.

[7] E. Genender, C. L. Holloway, K. A. Remley, J. M. Ladbury, G. Koepke, and H. Garbe, "Simulating the multipath channel with a reverberation chamber: Application to bit error rate measurements," *IEEE Trans. Electromagn. Compat.*, vol. 52, no. 4, pp. 766-777, Nov. 2010.

[8] U. Carlberg, P. S. Kildal, A. Wolfgang, O. Sotoudeh, and C. Orlenius, "Calculated and measured absorption cross sections of lossy objects in reverberation chamber," *IEEE Trans. Electromagn. Compat.*, vol. 46, no. 2, pp. 146-154, May 2004.

[9] Z. Tian, Y. Huang, Y. Shen, and Q. Xu, "Efficient and Accurate Measurement of Absorption Cross Section of a Lossy Object in Reverberation Chamber Using Two One-Antenna Methods," *IEEE Trans. Electromagn. Compat.*, vol. 58, no. 3, pp. 686-693, Jun. 2016.

[10] E. Amador, M. Andries, C. Lemoine, and P. Besnier, "Absorbing material characterization in a reverberation chamber," in *Proc. IEEE Int. Symp. on Electromagn. Compat.*, Sept. 2011, pp. 117-122.

[11] G. C. R. Melia, M. P. Robinson, I. D. Flintoft, A. C. Marvin, and J. F. Dawson, "Broadband Measurement of Absorption Cross Section of the Human Body in a Reverberation Chamber," *IEEE Trans. Electromagn. Compat*., vol. 55, no. 6, pp. 1043-1050, Dec. 2013.

[12] A. Bamba, D. P. Gaillot, E. Tanghe, G. Vermeeren, W. Joseph, M. Lienard, and L. Martens, "Assessing Whole-Body Absorption Cross Section For Diffuse Exposure From Reverberation Chamber Measurements," *IEEE Trans. Electromagn. Compat*., vol. 57, no. 1, pp. 27-34, Feb. 2015.

[13] D. A. Hill, M. T. Ma, A. R. Ondrejka, B. F. Riddle, M. L. Crawford, and R. T. Johnk, "Aperture excitation of electrically large, lossy cavities," *IEEE Trans. Electromagn. Compat*., vol. 36, no. 3, pp. 169-178, Aug. 1994.

[14] M. I. Andries, P. Besnier, and C. Lemoine, "On the prediction of the average absorbing cross section of materials from coherence bandwidth measurements in reverberation chamber," in *Proc. IEEE Int. Symp. on Electromagn. Compat.*, Sept. 2012, pp. 1-6.

[15] D. A. Hill, Electromagnetic Fields in Cavities: Deterministic and Statistical Theories. New York, NY, USA: Wiley-IEEE Press, 2009.

[16] Y. Huang, and D. J. Edwards, "A novel reverberating chamber: the source-stirred chamber," in *Proc. 8th Int. Conf. Electromagn. Compat.*, Edinburgh, U.K., Sept. 1992, pp. 120-124.

[17] Y. Huang, "The investigation of chamber for electromagnetic systems," Ph.D. dissertation, Dept. of Eng. Sci., Univ. of Oxford, Oxford, U.K., 1993.

[18] M. Kleiner,,and J. Tichy, *Acoustics of Small Rooms*. Boca Raton, FL, USA: CRC Press, 2014 [Online]. Available: https://www.airtransport.cc. [Accessed: 03-Mar-2017].

[19] G. B. Tait, R. E. Richardson, M. B. Slocum, and M. O. Hatfield, "Time-Dependent Model of RF Energy Propagation in Coupled Reverberant Cavities," *IEEE Trans. Electromagn. Compat.*, vol. 53, no. 3, pp. 846-849, Aug. 2011.

[20] G. B. Tait, R. E. Richardson, M. B. Slocum, M. O. Hatfield, and M. J. Rodriguez, "Reverberant Microwave Propagation in Coupled Complex Cavities," *IEEE Trans. Electromagn. Compat.*, vol. 53, no. 1, pp. 229-232, Feb. 2011.

[21] R.Richardson, "Reverberant microwave propagation," Naval Surface Warfare Center, Dahlgren Division, Dahlgren, VA, Tech. Rep. NSWCDD/TR-08/127, Oct. 2008.

Chapter 5: Simplified Shielding Effectiveness Measurement of Small Cavity

5.1 Introduction

Chapter 3 and Chapter 4 have considered measurements in a single cavity (i.e., RC only). However, in practice, the nested-cavity or cascade-connected-cavity method is required for some measurements, e.g., the EM shielding of enclosures or materials. In this chapter, the measurement of the EM shielding of physically small but electrically large enclosures using nested RC will be considered.

EM shielding has become a significant issue due to the proliferation of electronic devices in the world. Shielding enclosures are used to either protect or control immunity and/or emission of electronic devices for many applications. The shielding effectiveness (SE) is an important figure of merit to characterize the EM isolation performance of enclosures.

Generally, an IEEE standard can be followed for measuring the SE of EM shielding enclosures [1] in an AC. The idea is to illuminate the equipment under test (EUT) with a plane wave, and consequently, the results are only valid for specific incidence directions and polarizations tested in practice. However, in real-life, equipment is seldom exposed to a single plane wave; a more realistic scenario would be waves coming from different directions. Recently, the RC technique is becoming prevalent for the SE measurement [2] – [9]. The use of RCs for determining the SE has the advantage over other techniques in that the RC offers a more realistic environment. That is, in an RC, the fields are incident on the EUT with various polarizations and angles of incidence [10].

Conventionally, to measure the SE of an electrically large enclosure in an RC, it is required to set a transmitting antenna (T_x) along with a receiving antenna in the large RC (R_{xo}) and a receiving antenna inside the nested small enclosure (R_{xi}). By comparing the power transfer functions between $T_x - R_{xo}$ and between $T_x - R_{xi}$ in the frequency domain, the SE of the small enclosure can be extracted. However, this approach requires three antennas with known

efficiency of the two receiving antennas, which could be problematic sometimes in practice. An optional time-domain method proposed in [5] is to use the decay time of the enclosure to extract SE. But it needs to cover and uncover the aperture of the enclosure which may not be applicable for some equipment with complex structures. And also, when the EUT is well shielded, the measurement uncertainty increases very quickly.

5.2 Theory

It has been shown that for a well-stirred electrically large enclosure, the SE of the enclosure is defined as follows

$$\mathrm{SE} = -10\log_{10}\frac{\langle P_{in}\rangle}{\langle P_{out}\rangle} \tag{5.1}$$

or

$$\mathrm{SE} = -10\log_{10}\frac{\langle S_{in}\rangle}{\langle S_{out}\rangle} \tag{5.2}$$

where P_{in} and P_{out} are the power levels inside and outside the enclosure, S_{in} and S_{out} are the power density levels inside and outside the enclosure, respectively. $\langle\ \rangle$ denotes an ensemble average for all stirring sequences.

5.2.1 Frequency Domain

In the frequency domain, the existing measurement method of determining the SE is to compare the power transfer functions between $T_x - R_{xo}$ and between $T_x - R_{xi}$. As stated in Section 3.2.1, the power transfer function can be obtained from the *S*-parameter as [11]

$$\frac{\langle P_r\rangle}{P_t} = \langle|S_{21}|^2\rangle \tag{5.3}$$

$\langle|S_{21}|^2\rangle$ is an uncalibrated power transfer function including the ohmic loss of antennas, the antennas mismatch, and also, both the stirred and unstirred power. The net power transfer

function T can be obtained by removing the ohmic loss and mismatch of antennas and the unstirred power as [3], [11] – [13]

$$T = \frac{\langle |S_{21,s}|^2 \rangle}{(1 - |\langle S_{11} \rangle|^2)(1 - |\langle S_{22} \rangle|^2)\eta_1^{rad}\eta_2^{rad}} \tag{5.4}$$

where $S_{21,s}$ represents the stirred power contribution of S_{21}. η_1^{rad} and η_2^{rad} are the efficiency of the transmitting and the receiving antennas, respectively.

In the following analysis, the transmitting antenna in the RC is denoted by antenna 1, the receiving antenna in the RC is denoted by antenna 2 and the receiving antenna in the EUT is denoted by antenna 3, as can be seen from Figure 5.1(a). Then, the net power transfer function in the RC (T_o) can be extracted as

$$T_o = \frac{\langle |S_{21,s}|^2 \rangle}{(1 - |\langle S_{11} \rangle|^2)(1 - |\langle S_{22} \rangle|^2)\eta_1^{rad}\eta_2^{rad}} \tag{5.5}$$

The net power transfer function between the RC and the EUT (T_i) can be given as

$$T_i = \frac{\langle |S_{31,s}|^2 \rangle}{(1 - |\langle S_{11} \rangle|^2)(1 - |\langle S_{33} \rangle|^2)\eta_1^{rad}\eta_3^{rad}} \tag{5.6}$$

where η_3^{rad} are the efficiency of antenna 3.

Substituting (5.3), (5.5) and (5.6) into (5.1), the SE can be determined from ratio of the net power transfer functions T_i and T_o

$$\text{SE} = -10\log_{10}\left(\frac{T_i}{T_o}\right) = -10\log_{10}\left(\frac{\langle |S_{31,s}|^2 \rangle}{\langle |S_{21,s}|^2 \rangle} \cdot \frac{1 - |\langle S_{22} \rangle|^2}{1 - |\langle S_{33} \rangle|^2} \cdot \frac{\eta_2^{rad}}{\eta_3^{rad}}\right) \tag{5.7}$$

As can be seen from (5.7), three antennas are needed in the measurement. Typically, the net power transfer functions are measured with two high-efficiency antennas using (5.5) and (5.6) with the knowledge of their efficiency ($\eta_2^{rad}, \eta_3^{rad}$). And also, for the measurement using a two-port VNA, two measurements are required (connecting receiving port to antenna 2 and antenna 3, respectively), which is really time consuming.

If an RC is ideally performing, the enhanced backscatter constant [11], [16], [17]

$$e_b = \sqrt{\langle |S_{11,s}|^2 \rangle \langle |S_{22,s}|^2 \rangle} \Big/ \langle |S_{21,s}|^2 \rangle = 2 \tag{5.8}$$

Assuming antenna 1 and antenna 2 are identical, it can be obtained $\langle |S_{11,s}|^2 \rangle = \langle |S_{22,s}|^2 \rangle = 2\langle |S_{21,s}|^2 \rangle$. Now, equation (5.5) can be converted to the form [11]

$$T_o = \frac{\langle |S_{11,s}|^2 \rangle}{2(1 - |\langle S_{11} \rangle|^2)^2 (\eta_1^{rad})^2} \tag{5.9}$$

Substituting (5.9) into (5.7), the SE can be rewritten as

$$\mathrm{SE} = -10 \log_{10} \left(2 \cdot \frac{\langle |S_{31,s}|^2 \rangle}{\langle |S_{11,s}|^2 \rangle} \cdot \frac{1 - |\langle S_{11} \rangle|^2}{1 - |\langle S_{33} \rangle|^2} \cdot \frac{\eta_1^{rad}}{\eta_3^{rad}} \right) \tag{5.10}$$

Thus, only two antennas are needed (one transmitting antenna in the RC and one receiving antenna in the EUT) and the measurement can be completed once, which will greatly simplify the measurement. The precondition for this method is $e_b = 2$. The impact of e_b to the validity of this method will be discussed in Section 5.4. If the transmitting antenna in the RC and the receiving antenna in the EUT are identical, (5.10) can be further simplified as

$$\mathrm{SE} = -10 \log_{10} \left(2 \cdot \frac{\langle |S_{31,s}|^2 \rangle}{\langle |S_{11,s}|^2 \rangle} \right) \tag{5.11}$$

It is interesting to note that the efficiency is eliminated in (5.11) and the knowledge of the efficiency of any antenna used in the measurement is not needed – the condition is both antennas are identical.

5.2.2 Time Domain

In the time domain, the reverberant diffuse fields in each cavity, denoted by subscript *i* = 1, 2, are analysed based on the time-dependent full exchange of radiated EM power between coupled spaces [8], [18] – [20]. The spatially averaged power density is modeled from conservation of energy consideration when the excitation source is in cavity 1

$$V_1 \langle \dot{S_1}(t) \rangle = -(\Lambda_1 + \Lambda_t) \langle S_1(t) \rangle + \Lambda_t \langle S_2(t) \rangle + \delta(t) \tag{5.12}$$

$$V_2\langle \dot{S_2}(t)\rangle = \Lambda_t\langle S_1(t)\rangle - (\Lambda_2 + \Lambda_t)\langle S_2(t)\rangle \tag{5.13}$$

where $\langle S_i\rangle$ is the averaged power density in cavity *i*, $\langle \dot{S_i}(t)\rangle$ signifies the time rate of change of the averaged power density of cavity *i*. V_i is the volume of cavity *i* and $\delta(t)$ is an impulse of EM power fed to the cavity at time $t = 0$. Λ_i and Λ_t are the energy loss rate coefficients for cavity *i* and for coupling between the two cavities, respectively [20].

The analytical solutions to (5.12) and (5.13) are provided in [21] and [22] as

$$\langle S_1(t)\rangle = \frac{U_0}{\alpha-\beta}\left[\frac{\alpha e^{\alpha t} - \beta e^{\beta t}}{V_1} + \frac{(\Lambda_1+\Lambda_2)\left(e^{\alpha t} - e^{\beta t}\right)}{V_1 V_2}\right] \tag{5.14}$$

$$\langle S_2(t)\rangle = \frac{U_0\Lambda_t}{V_1V_2}\cdot\frac{e^{\alpha t} - e^{\beta t}}{\alpha-\beta} \tag{5.15}$$

where the coefficients α and β are defined according to the relationships shown in (5.16) and (5.17)

$$B = \frac{\Lambda_2+\Lambda_t}{V_2} + \frac{\Lambda_1+\Lambda_t}{V_1},\ \ C = \frac{\Lambda_1\Lambda_2 + \Lambda_1\Lambda_t + \Lambda_2\Lambda_t}{V_1V_2} \tag{5.16}$$

$$\alpha = \frac{-B + \sqrt{B^2 - 4C}}{2},\ \ \beta = \frac{-B - \sqrt{B^2 - 4C}}{2} \tag{5.17}$$

and U_0 is the total power injected into cavity 1 by the impulse excitation at time $t = 0$.

(5.14) and (5.15) can be rewritten as

$$\langle U_1(t)\rangle = \frac{U_0}{\alpha-\beta}\left[(\alpha + \frac{\Lambda_1+\Lambda_2}{V_2})e^{\alpha t} - (\beta + \frac{\Lambda_1+\Lambda_2}{V_2})e^{\beta t}\right] \tag{5.18}$$

$$\langle U_2(t)\rangle = \frac{U_0\Lambda_t}{V_1}\cdot\frac{e^{\alpha t} - e^{\beta t}}{\alpha-\beta} \tag{5.19}$$

where $\langle U_1(t)\rangle$ and $\langle U_2(t)\rangle$ are the averaged total power in cavity 1 and cavity 2, respectively. (5.18) and (5.19) describe the dynamics of power level inside the RC (cavity 1) and the EUT (cavity 2) when a short pulse is injected into the RC. As can be seen, the time-domain response of the RC and the EUT is of double-exponential behaviour [23]. The transient response of $\langle U_1(t)\rangle$ and $\langle U_2(t)\rangle$ can be obtained by fitting the PDPs of the RC and the EUT,

respectively. This fitting process can be realized through a least-square-fit optimization routine that minimizes the sum of the squares of the error between overlaid modelled and measured curves. The SE of the EUT can then be obtained by the difference of the fitted PDP (in dB format) of the RC (PDP_{RC}) and that of the EUT (PDP_{EUT}) [20]

$$\mathrm{SE(dB)} = PDP_{RC}(\mathrm{dB}) - PDP_{EUT}(\mathrm{dB}) \tag{5.20}$$

The PDP_{RC} and PDP_{EUT} are obtained from S_{21} data and S_{31} data, respectively. For an ideally stirred RC, it has been proved that in the time domain [16]

$$e_b = \frac{\sqrt{PDP_{RC}^{S11} \cdot PDP_{RC}^{S22}}}{PDP_{RC}^{S21}} = 2 \tag{5.21}$$

where PDP_{RC}^{S11} , PDP_{RC}^{S22} and PDP_{RC}^{S21} (in linear format) are the PDPs (excluding the early-time part) of the RC from the S_{11}, S_{22} and S_{21} data, respectively. Likewise, assuming antenna 1 and antenna 2 are identical, (5.21) then becomes

$$PDP_{RC}^{S21} = \frac{1}{2} \cdot PDP_{RC}^{S11} \tag{5.22}$$

Or in dB format,

$$PDP_{RC}^{S21}(\mathrm{dB}) = PDP_{RC}^{S11}(\mathrm{dB}) - 3\mathrm{dB} \tag{5.23}$$

And (5.20) can be rewritten as

$$\mathrm{SE(dB)} = PDP_{RC}^{S11}(\mathrm{dB}) - 3\mathrm{dB} - PDP_{EUT}(\mathrm{dB}) \tag{5.24}$$

Thus, antenna 2 is eliminated in (5.24) and the formula for the two-antenna method in the time domain is mathematically derived.

5.3 Measurement

Measurements were conducted from 2.8 to 4.2 GHz in our RC to verify the proposed methods. Three antennas were used: two double-ridged waveguide horn antennas were used as antenna 1 (Rohde & Schwarz® HF 906) and antenna 3 (SATIMO® SH 2000),

respectively, one planar monopole antenna was used as antenna 2. Antenna 1 was connected to VNA port 1 and antenna 2 (or antenna 3) was connected to VNA port 2. The step-by-step rotation of the two stirrers was synchronized. 360 positions were obtained (1 degree per step). For each mode stirring position, the VNA swept over the full frequency span and recorded the *S*-parameters. A metallic enclosure with an open-air aperture is employed as the EUT. The EUT has a size of 1.0 m $\times$1.0 m $\times$1.1 m (about 10 λ $\times$10 λ $\times$11 λ at 3.0 GHz). The size of the aperture is about 1.0 m $\times$ 0.1 m. According to Weyl's formula [3], [24], the mode number is around 9,185 inside the EUT at 3.0 GHz, which is large enough for the RC to perform well. The whole measurement system is depicted in Figure 5.1(a). Figure 5.1(b) and (c) illustrate the measurement setup and the detail of the aperture is shown in Figure5.1 (d).

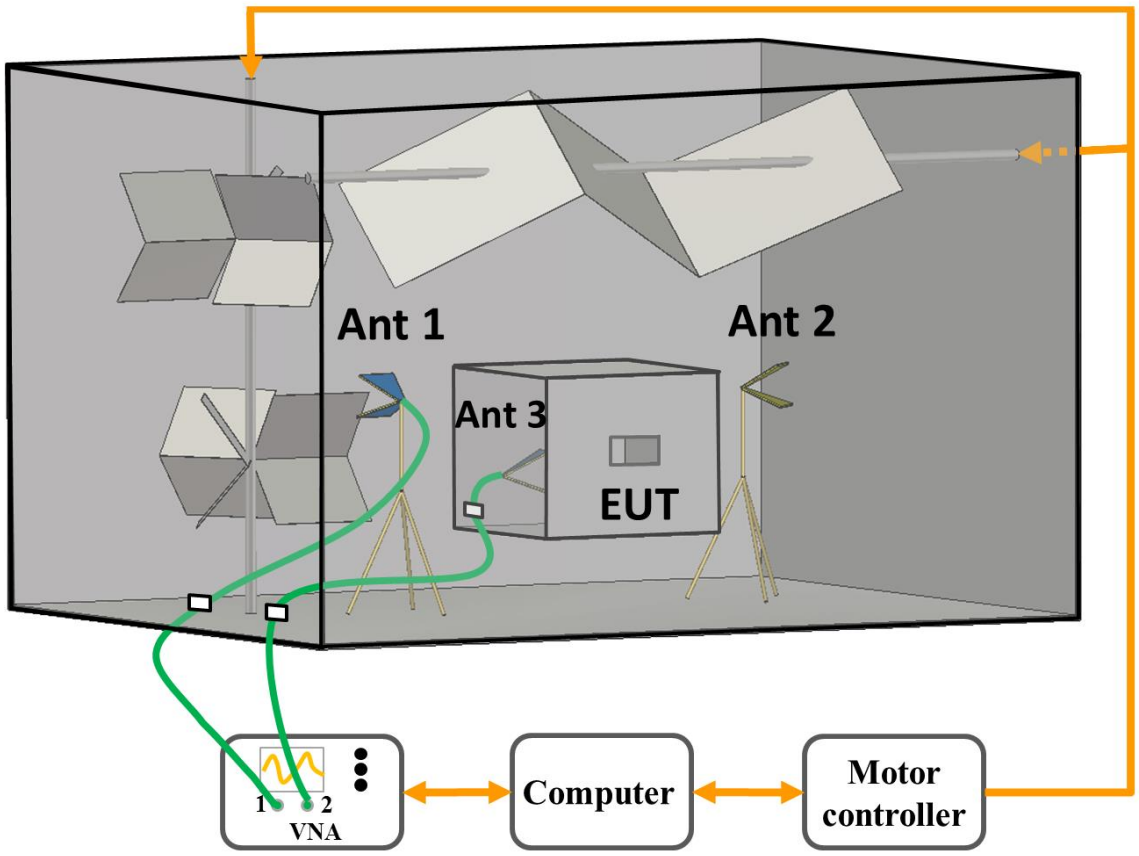

(a)

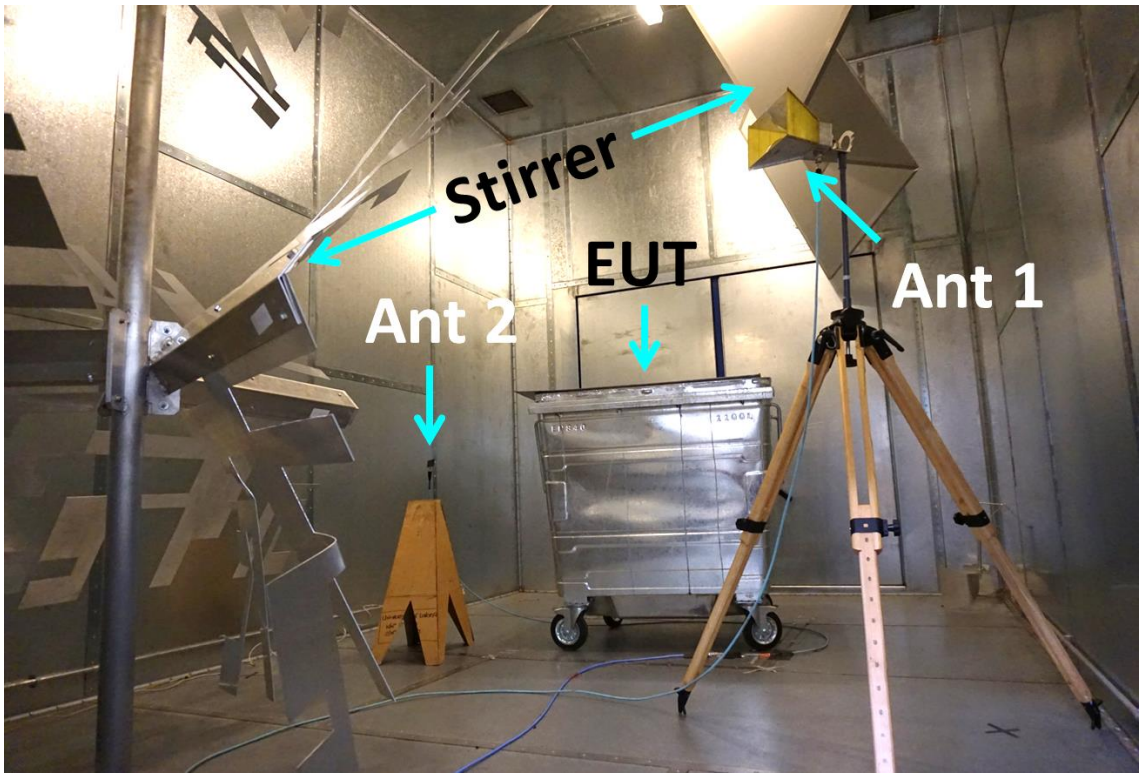

(b)

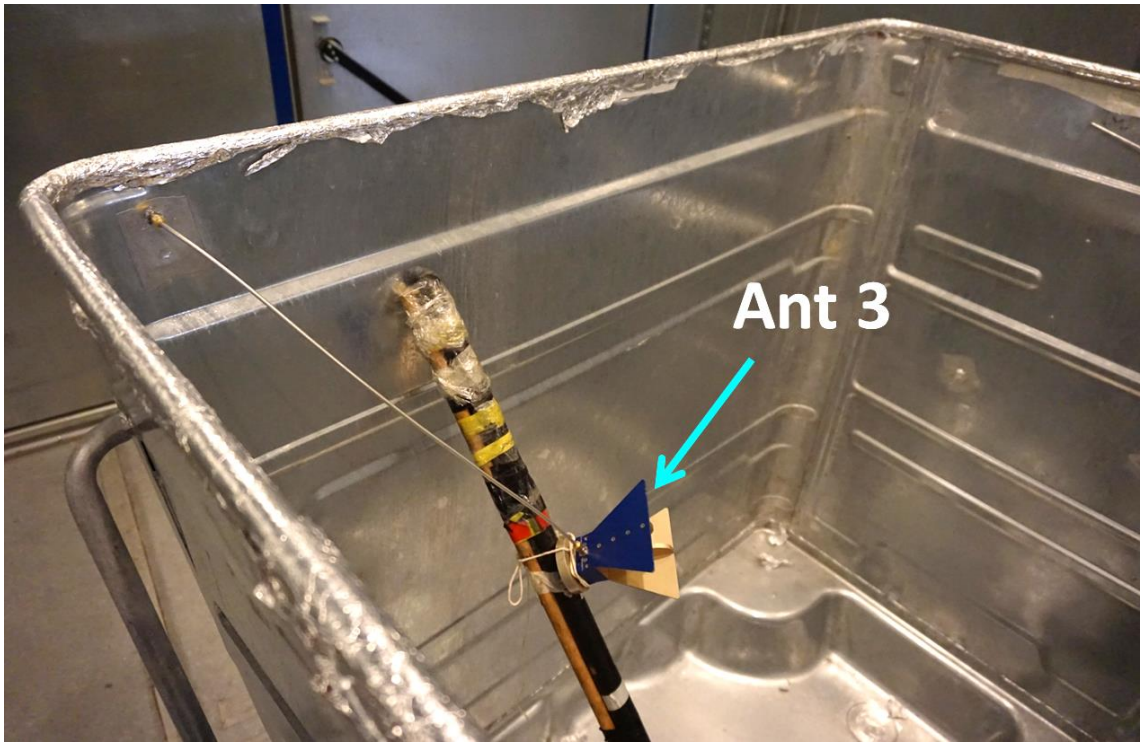

(c)

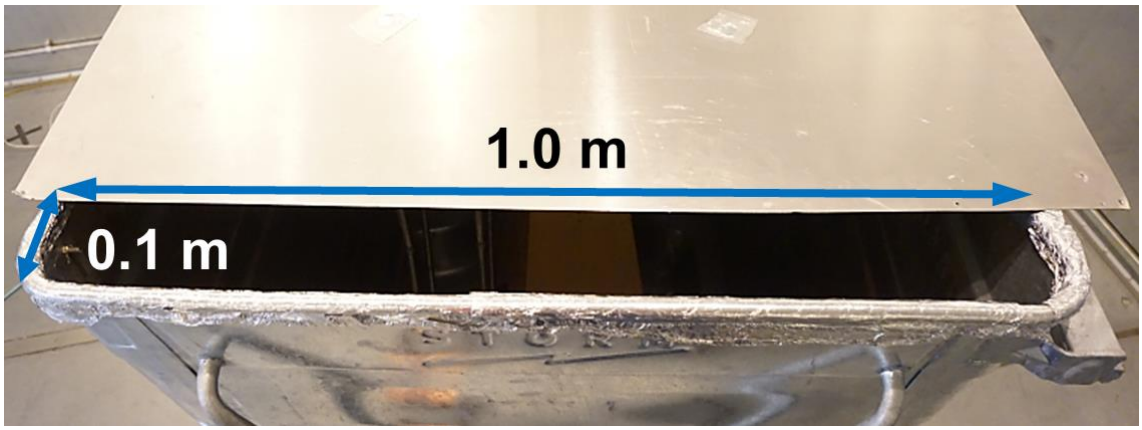

(d)

Figure 5.1 SE measurement setup in the RC: (a) measurement system, (b) measurement setup in the experiment, (c) antenna 3 (SATIMO® horn antenna) in the EUT, (d) the aperture of the EUT.

The measurement was performed according to the following procedure.

Step 1: Do standard calibration process of the VNA including the cables.

Step 2: Place antenna 1 and antenna 2 inside the RC and place antenna 3 inside the EUT. Place all the antenna supports along with the antennas inside the RC to keep the chamber loss constant.

Step 3: Connect antenna 1 to port 1 of the VNA and antenna 2 to port 2 of the VNA, load antenna 3 with a 50 Ω termination and collect the full *S*-parameters for each stirring position.

Step 4: Repeat Step 3 with antenna 3 connected to port 2 of the VNA and antenna 2 loaded with a 50 Ω termination.

In practice, it may not have a chance to introduce mode stirring or source stirring in the EUT, thus only frequency stirring is used here. In the measurement, 10,001 points were sampled in the frequency span of 2.8 to 4.2 GHz. The conventional three-antenna method ($SE_{FD,\ 3}$), the two-antenna method in the frequency domain ($SE_{FD,\ 2}$) and the two-antenna method in the time domain ($SE_{TD,\ 2}$) were adopted respectively to calculate the SE of the EUT. To make the abbreviation clear, the first subscript “FD” or “TD” is used to indicate that the measurement

is conducted in the frequency domain or in the time domain, respectively. "2" or "3" is assigned to the second subscript to signify that two or three antennas were used in the measurement. In the frequency domain, the enhanced backscatter constant (e_b) is calculated and plotted in Figure 5.2. As can be seen, it is close to 2. This means the RC was well performing and the experiment equipment was reasonably set up [11], [16].

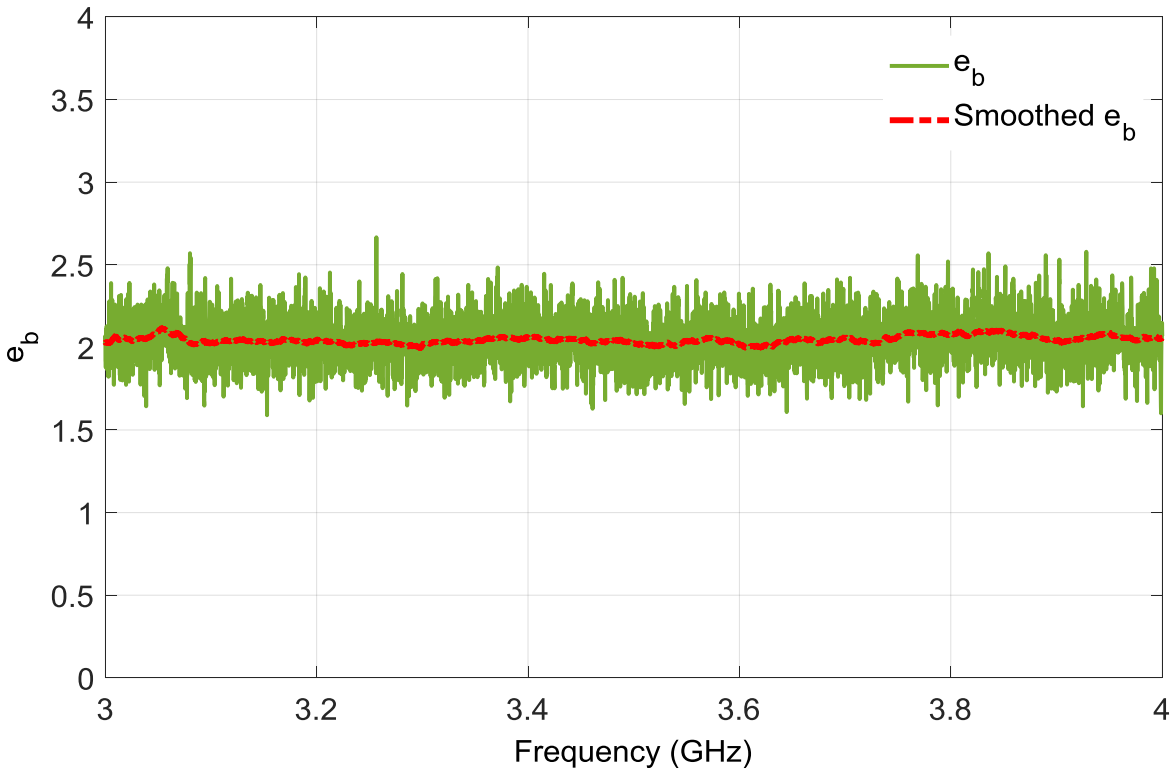

Figure 5.2 The measured e_b in the RC.

The power transfer functions of the RC measured using antenna 1 ($T_{o,1}$) and using antenna 1 and antenna 2 ($T_{o,2}$) are shown in Figure 5.3. The power transfer function from the RC to the EUT ($T_{i,2}$) measured using antenna 1 and antenna 3 is plotted in Figure 5.3 as well. Again, to make the abbreviation clear, "*o*" or "*i*" is assigned to the first subscript to signify that the measurement was done when the receiving antenna was outside or inside the EUT. "1" or "2" in the second subscript means one or two antennas were required in the measurement. As can be seen, $T_{i,2}$ is smaller than $T_{o,1}$ and $T_{o,2}$ because of the shielding of the EUT. $T_{o,1}$ agrees well with $T_{o,2}$, which manifests that the two-antenna method for SE measurement in the frequency domain is effective.

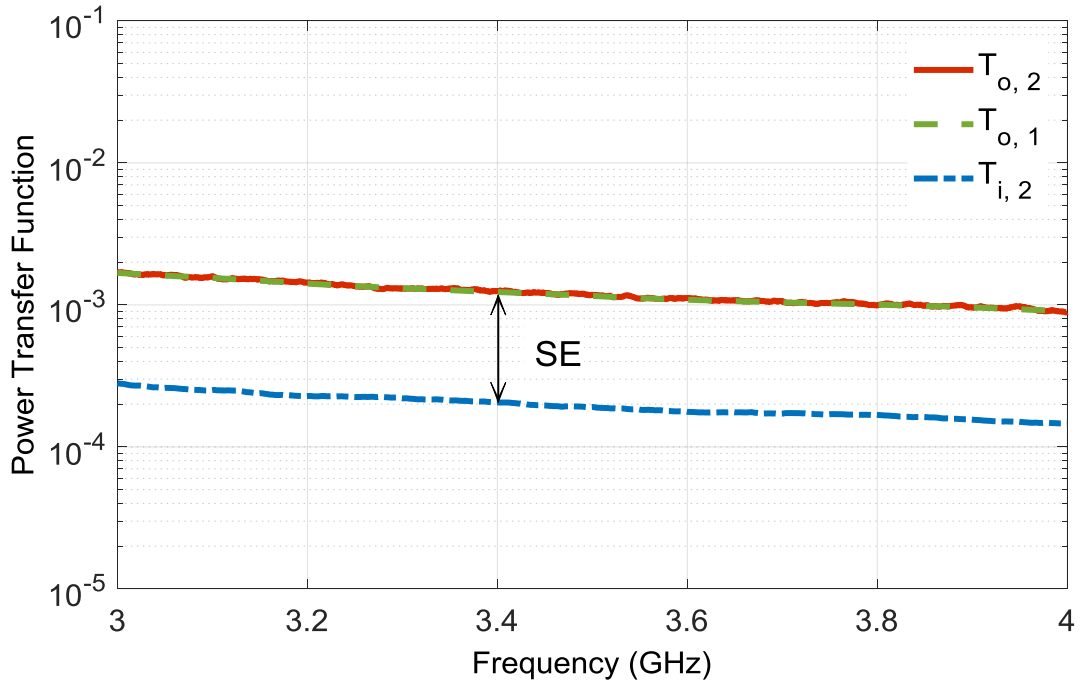

Figure 5.3 The measured power transfer functions in the RC and between the RC and the EUT.

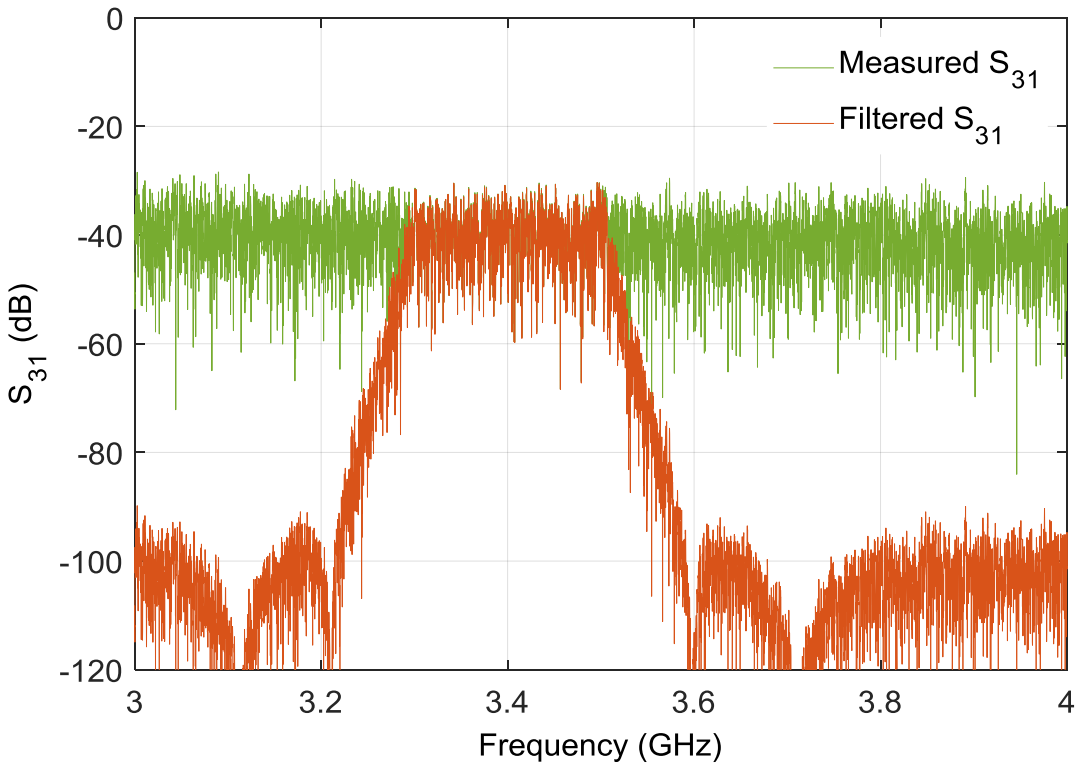

Figure 5.4 Measured S_{31} and filtered S_{31}.

Since the data was measured in the frequency domain, the time-domain method was attained by applying the IFT on the measured data. In the time domain, a 10-order band-pass elliptic filter was used to filter S_{11} and S_{31} with a 200 MHz bandwidth [11], as can be seen from Figure 5.4. Since the transient responses of the power in the RC and in the EUT are of double exponential behaviour, the least-square-fit optimization is applied to the PDPs and the modeled decay behaviour can be obtained, as shown in Figure 5.5(a). The dynamics of power transfer between the RC and the EUT are of particular interest. As can be seen from Figure 5.5(b), the early-time behaviour is observed because of the unstirred reflections from the antenna itself and from the walls of the RC [20]. For $P_2(t)$, at the first 200 ns, it rises slowly and the energy in the RC must leak into the EUT gradually through the leakage aperture described by Λ_t. After the EUT is fully filled, $P_2(t)$ ultimately decreases along with $P_1(t)$. It can be noticed, at the first 20 ns, no rise appears for $P_2(t)$ because the power emitting from the T_x antenna takes certain time to reach the R_x antenna. The 20 ns correspond to about 6 meters for EM wave travelling in free space, which agrees well with the distance between antenna 1 and antenna 3 in the experiment. The difference between $P_1(t)$ and $P_2(t)$ at the late time gives us the information of SE of the EUT. It is worth noting that, to avoid the influence of the early-time behaviour, only part of the PDPs (the late-time part) should be used to evaluate the SE.

The results are illustrated in Figure 5.6. 200 MHz frequency stirring is used in the frequency domain. The average efficiency of antenna 1, antenna 2 and antenna 3 in 3.0 – 4.0 GHz is 95%, 80%, and 82%, respectively. When conducting the measurement using the two-identical-antenna method, antenna 1 was replaced with another SATIMO® SH 2000 horn antenna. It can be seen clearly from Figure 5.6 that the measured SEs using the four methods agree well and the maximum difference is within 0.5 dB.

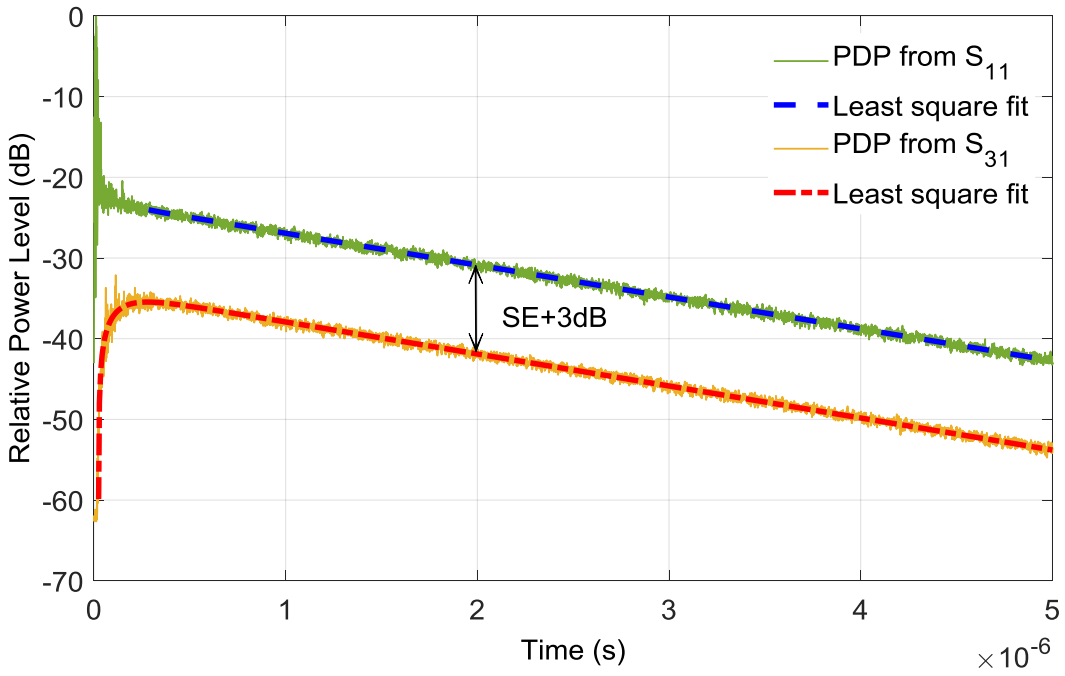

(a)

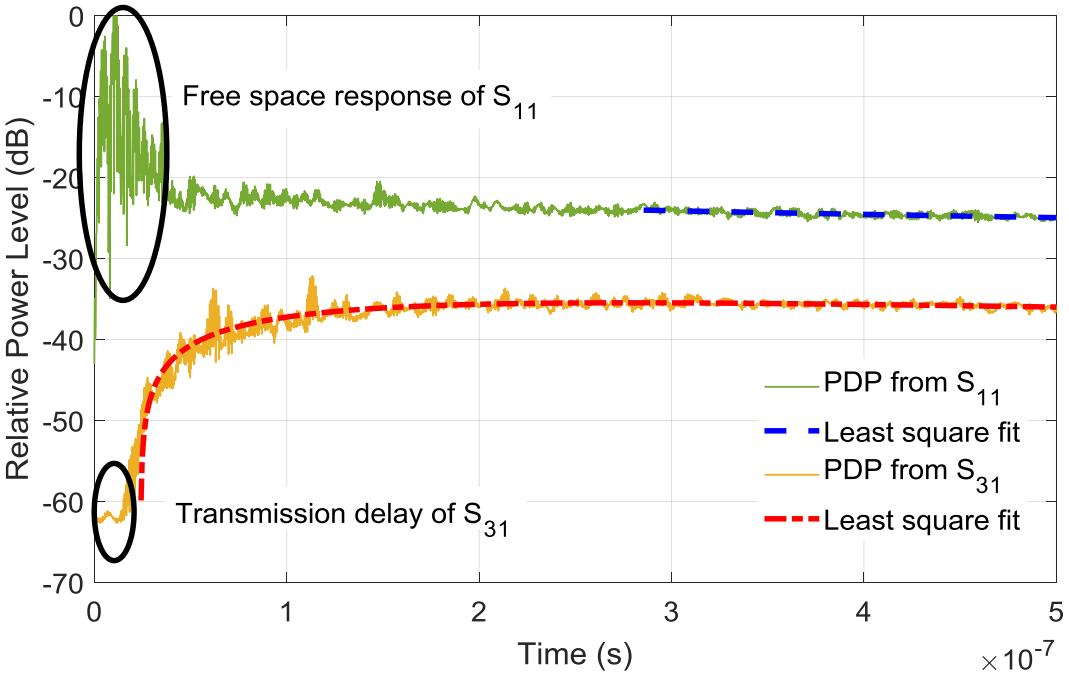

(b)

Figure 5.5 Transient responses of the PDPs in the RC and in the EUT for the impulse excitation injected into the RC: (a) PDPs from S_{11} and from S_{31}, respectively, (b) early-time responses of PDPs.

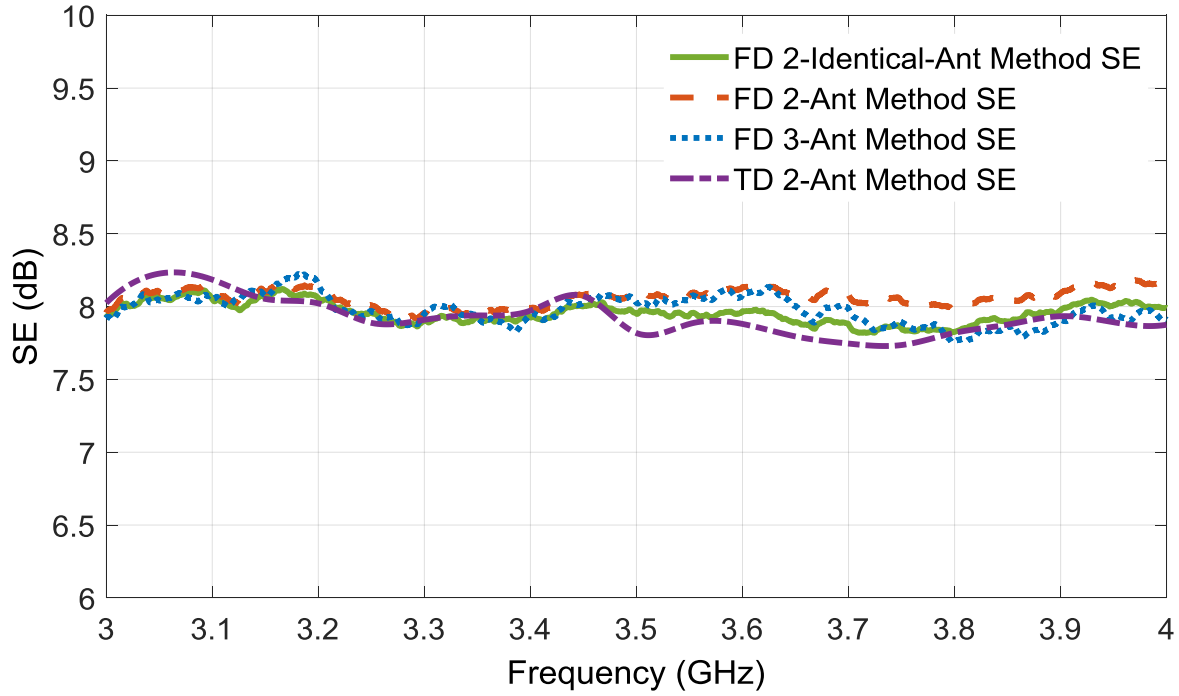

Figure 5.6 The SEs of the EUT measured with different methods.

5.4 Convergence Behaviour

The convergence behaviour of the proposed two-antenna methods in the frequency domain and in the time domain is studied.

As indicated in (5.8) and (5.9), the two-antenna method in the frequency domain requires $e_b = 2$. A basic question is "what is the impact of e_b to the validity of the frequency domain measurement method?" That is, if e_b deviates from 2, what kind of results should be expected? In fact, intuition and experience say that if e_b deviates from 2 a lot, the measured SE should be unreliable because the field in the RC is not well stirred, i.e., the field is not statistically uniform. To investigate this issue, the variation of the measured $SE_{FD,2}$ along with e_b at 3.5 GHz was checked where the SE is 8 dB, as shown in Figure 5.7. It can be seen clearly that the deviation of e_b from 2 fluctuates intensely at about the first 50 stirring positions. Consequently, the measured SE is inaccurate as expected. The maximum difference can reach about 90%. However, e_b begins to converge to 2 gradually with the stirring positions number increasing. For $SE_{FD,2}$, its convergence behaviour is coincident with

e_b. The measured $SE_{FD,\,2}$ becomes stable (it converges to 8 dB) after about 250 stirring positions when the variation of e_b from 2 becomes very small (within 10% variation). From the above analysis, it is known that the accuracy of the frequency domain two-antenna method relies on $e_b = 2$. That is to say, the frequency-domain measurement is sensitive to the deviation of the chamber field from the ideally over-moded case.

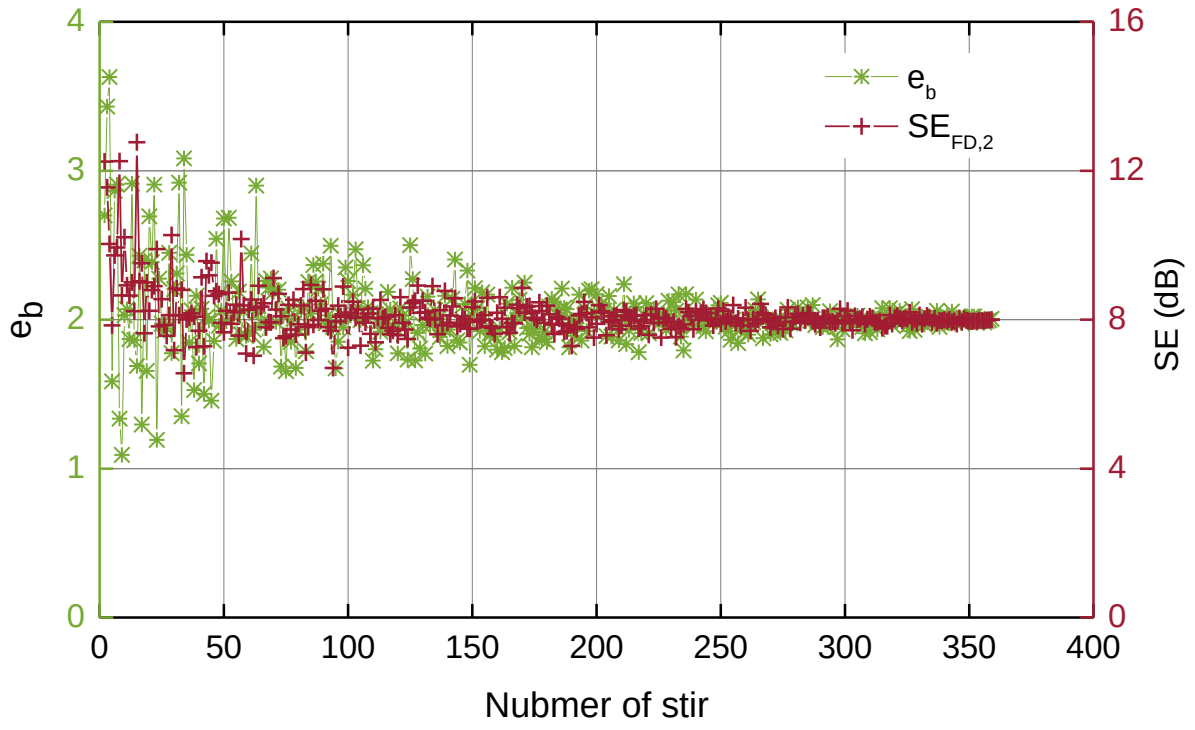

Figure 5.7 The convergence properties of e_b and $SE_{FD,\,2}$ at 3.5 GHz.

The convergence behaviour of the proposed two-antenna methods in the time domain is studied by comparing it with the convergence behaviour in the frequency domain. The root-mean-square-error (RMSE) of the measured SE from 3.0 – 4.0 GHz with different numbers of stirring positions was evaluated [11]. The reference used is the SE measured with 360 stirring positions. The algorithm is expressed as

$$\mathrm{RMSE}_i = \sqrt{\frac{\sum_{j=1}^{N}\left(\mathrm{SE}_{i,j} - \mathrm{SE}_{M,j}\right)^2}{N}} \tag{5.25}$$

In (5.25), *i* represents the number of stirring positions and *M* is the maxima of *i*. *j* signifies the frequency sampling point number and *N* is the maximal value of *j*. In our measurement, *M* =

360 and N = 7144. The comparison of RMSEs of different methods is depicted in Figure 5.8. As can be seen, the convergence speeds of the two-antenna method and the three-antenna method in the frequency domain are close but the time-domain method converges faster than the frequency domain methods. This is because the power transfer function and e_b are very sensitive to deviations of the chamber field from the ideally over-mode case (i.e., how well the RC is stirred). But, the modelled PDP is not susceptible to the boundary conditions. It is mainly determined by the diffuse loss of the RC. That means the PDP is very robust. In other words, the time-domain measurement is far less sensitive to the non-ideal chamber field and appears to yield an average of the PDP. As a result, $SE_{TD,2}$ converges faster than $SE_{FD,2}$ and $SE_{FD,3}$. To be more specific, in the time domain, the RMSE remains less than 10% (in comparison with the averaged SE in the frequency span of interest, about 8 dB from Figure 5.6) and drops below 5% after about 10 stirring positions. However, in the frequency domain, the RMSEs of the two-antenna method and the three-antenna method drop below 5% after about 100 stirring positions. And also, the RMSEs keep exceeding 10% for the first 40 stirring positions and then decline gradually afterwards.

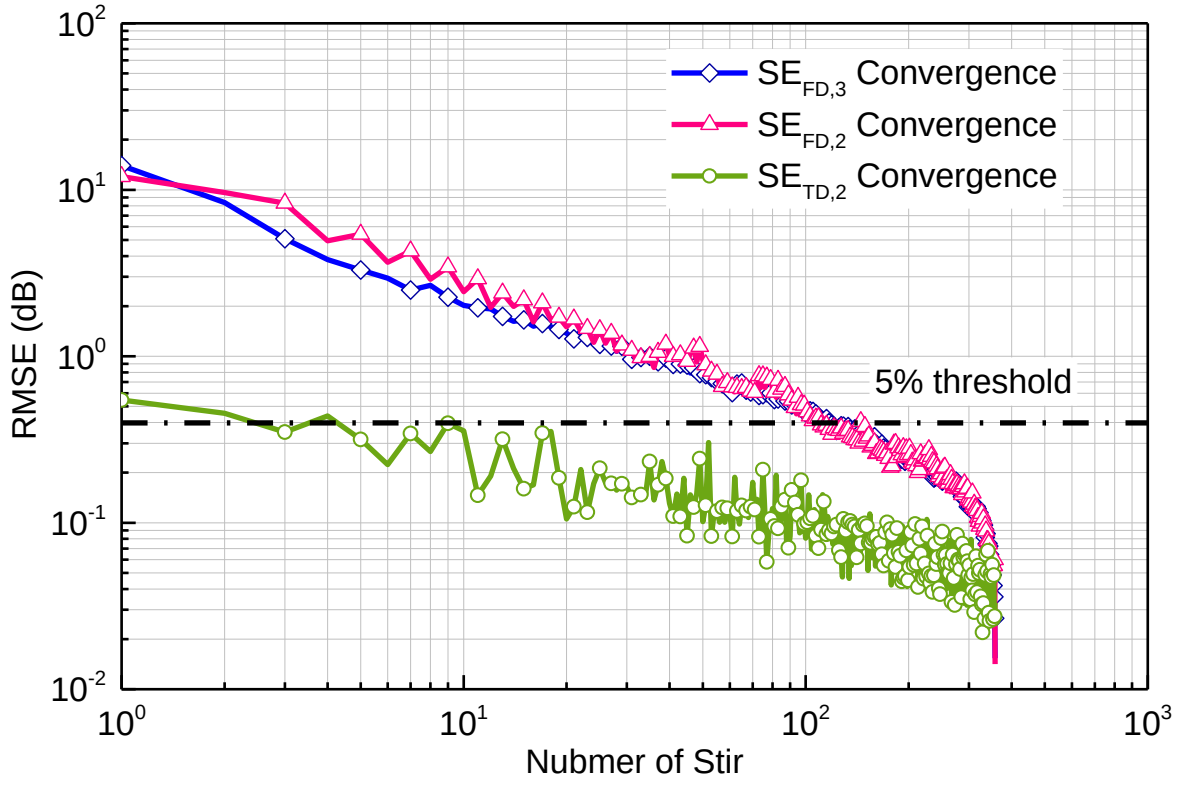

Figure 5.8 The comparison of RMSEs of different methods.

From above analysis, it is known that the PDP is robust and the time-domain method converges fast. Actually, these properties offer us a way to obtain SE with a small number of stirring positions and subsequently result in an efficient measurement method of SE. Basically, for a small number of stirring positions case, source stirring technique can be adopted, which will avoid rotating the stirrers. In practice, the measurement can be completed in an electrically large conducting cavity, i.e., no mode-stirred RC is required. By doing this, the measurement simplification can go a step further. To validate this idea, another set of measurement was performed. In this measurement, the RC stirrers were kept fixed (no mode stirring introduced). Consequently, the RC would just serve as an electrically large enclosure. In order to recover the true PDP, a turn-table platform was rotated on which the transmitting antenna was mounted (thus the source was rotated). Considering the convergence speed of $SE_{TD,\ 2}$, 10 source stirring positions were chosen. The turn-table platform was rotated stepwise to 10 positions (36 degrees for each step). Antenna 1 (Rohde & Schwarz® HF 906) was mounted on the turn-table platform and connected to VNA port 1. Antenna 2 (SATIMO® SH 2000) was placed inside the EUT and connected to VNA port 2. The PDPs of the outer cavity (i.e., the RC with stirrers being fixed) and between the outer cavity and the EUT were extracted from S_{11} and S_{21}, respectively. The measured SEs are plotted in Figure 5.9.

It can be seen that the SEs measured using 360 mode stirring positions and 10 source stirring positions agree well and the maximal variation is less than 10%. Also, the entire time consumed by the source-stir measurement was only approximately 10 minutes. It signifies that the SE can be measured in the time domain instantly and precisely. The consumed time of this method is comparable with the one proposed in [5]. But it is more advisable for EUTs with complex structures because it is no need to cover and uncover the apertures. And therefore, it is quite general and efficient for SE measurement of electrically large enclosures. The aforementioned measurement methods are compared and summarized in Table 5.1. Because the measurement accuracy relies on the number of independent samples in measurement sequences, a sufficient number of independent samples should be obtained at the lowest frequency of the measurement. This makes a request for the size of the outer cavity – it should be suitably large to accommodate sufficient cavity modes. When selecting the outer cavity for the measurement, its size should be carefully considered.

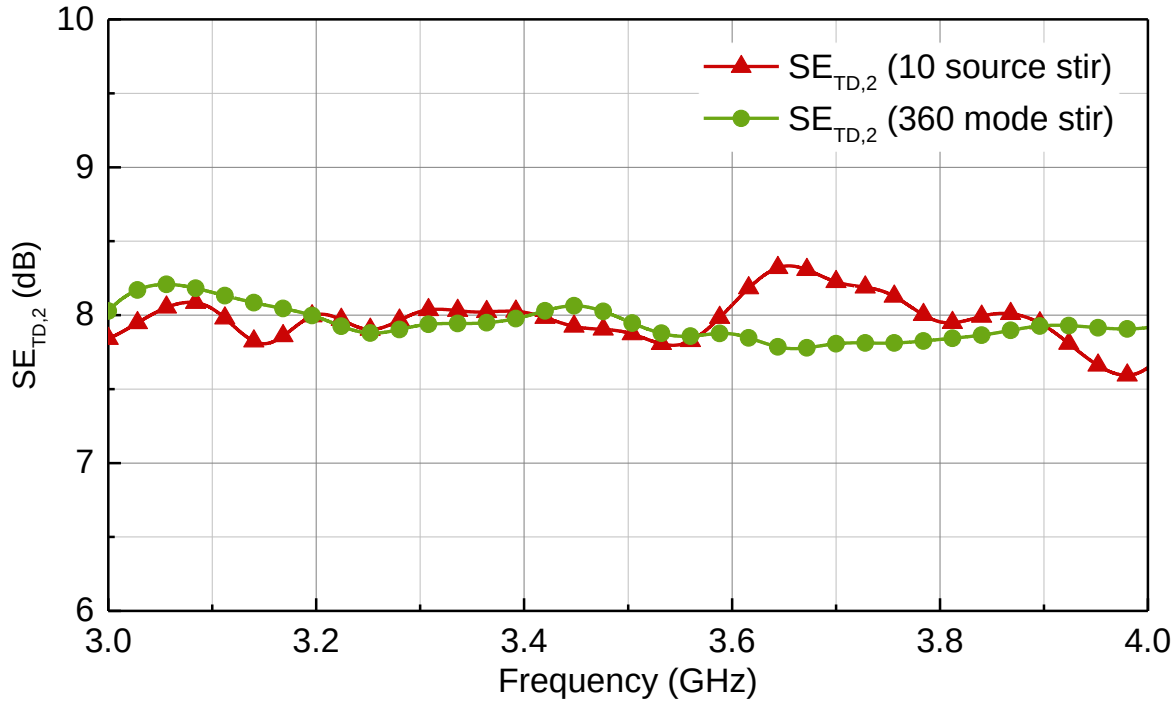

Figure 5.9 The comparison of $SE_{TD,2}$ (10 source stirring positions) and $SE_{TD,2}$ (360 mode stirring positions).

Table 5.1: Summary of the Existing Methods and the Proposed Methods

Measurement methods	Number of antennas	Antenna efficiency requirement	Measurement times	Measurement time	Facility
FD 3-antenna method	3	Yes	2	Approx. 14 hrs	RC
FD 2-antenna method	2	Yes	1	Approx. 7 hrs	RC
FD 2-identical-antenna method	2	No	1	Approx. 7 hrs	RC
TD 2-antenna method (mode stirring)	2	No	1	Approx. 10 mins	RC
TD 2-antenna method (source stirring)	2	No	1	Approx. 10 mins	Electrically large cavity
TD 1-antenna method proposed in [5]	1	No	2	Approx. 20 mins	EUT only

5.5 Discussions and Conclusion

In this chapter, the two-antenna methods for the SE measurement using the nested RC in both the frequency domain and the time domain have been presented. These two-antenna methods have simplified the measurement setup and improved the measurement efficiency. It is demonstrated that the measured SEs using the proposed two-antenna methods and the conventional three-antenna method agree well. The time-domain method goes to convergence much faster than the frequency-domain methods. Consequently, in the time domain, fast and accurate measurement can be realized by using the source stirring technique, which will result in fast SE measurement in reality. Furthermore, in the time-domain approach, by replacing the RC with a suitable conducting cavity (electrically large) and using the source stirring technique, the hardware requirement will be greatly reduced. The aforementioned measurement methods are compared. It is found that the time-domain method outperforms the frequency-domain method with much higher measurement efficiency and much lower hardware requirement.

Note that the proposed methods are based on the assumption that both the RC and the EUT are well stirred, if not, the measured power transfer function and PDP will be of considerable errors. Hence, the measured SE will be inaccurate. Another point that should be noted is that high-efficiency antennas should be used for the time-domain method, i.e., the loss of the antennas used in the measurement should be negligible. Otherwise, the measured PDP will be influenced by the loss of the antennas and (5.20) is no longer valid. However, in the frequency domain, as can be seen from (5.4), (5.5) and (5.6), the antenna efficiency has been calibrated out in the net power transfer function. Thus, it is not necessary for the antennas to be of high efficiency. Moreover, the proposed methods are general for SE measurement no matter the SE is low or high. The measurement uncertainty is only determined by the dynamic range of the VNA. When the EUT is well shielded, the power coupled from the RC into the EUT will be very small. Consequently, S_{31} will be very small. Under this circumstance, The VNA used in the measurement should have a large dynamic range to measure the small S_{31} accurately. Or, the measured SE could be of big error. Finally, during the measurement, the antennas (especially the one in the EUT) should be placed away from

the conducting walls of the cavities (at least quarter-wavelength distance from the nearest walls for the lowest frequency) to avoid the boundary effect [25], [26].

5.6 References

[1] *IEEE Standard Method for Measuring the Effectiveness of Electromagnetic Shielding Enclosures*, IEEE Standard 299, 2006.

[2] D. A. Hill, M. T. Ma, A. R. Ondrejka, B. F. Riddle, M. L. Crawford, and R. T. Johnk, "Aperture excitation of electrically large, lossy cavities," *IEEE Trans. Electromagn. Compat.*, vol. 36, no. 3, pp. 169-178, Aug. 1994.

[3] D. A. Hill, Electromagnetic Fields in Cavities: Deterministic and Statistical Theories. New York, NY, USA: Wiley-IEEE Press, 2009.

[4] C. L. Holloway, D. A. Hill, M. Sandroni, J. M. Ladbury, J. Coder, G. Koepke, A. C. Marvin, and Y. He, "Use of Reverberation Chambers to Determine the Shielding Effectiveness of Physically Small, Electrically Large Enclosures and Cavities," *IEEE Trans. Electromagn. Compat.*, vol. 50, no. 4, pp. 770-782, Nov. 2008.

[5] Q. Xu, Y. Huang, X. Zhu, L. Xing, Z. Tian, and C. Song, "Shielding Effectiveness Measurement of an Electrically Large Enclosure Using One Antenna," *IEEE Trans. Electromagn. Compat.*, vol. 57, no. 6, pp. 1466-1471, Dec. 2015.

[6] C. L. Holloway, D. A. Hill, J. Ladbury, G. Koepke, and R. Garzia, "Shielding effectiveness measurements of materials using nested reverberation chambers," *IEEE Trans. Electromagn. Compat.*, vol. 45, no. 2, pp. 350-356, May 2003.

[7] J. Carlsson, K. Karlsson, and A. Johansson, "Validation of shielding effectiveness measurement method using nested reverberation chambers by comparison with aperture theory," in *Proc. IEEE Int. Symp. Electromagn. Compat.*, Sept. 2012, pp. 1-6.

[8] G. B. Tait, R. E. Richardson, M. B. Slocum, and M. O. Hatfield, "Time-Dependent Model of RF Energy Propagation in Coupled Reverberant Cavities," *IEEE Trans. Electromagn. Compat.*, vol. 53, no. 3, pp. 846-849, Aug. 2011.

[9] S. Greco, and M. S. Sarto, "Hybrid Mode-Stirring Technique for Shielding Effectiveness Measurement of Enclosures Using Reverberation Chambers," in *Proc. IEEE Int. Symp. on Electromagn. Compat.*, Jul. 2007, pp. 1-6.

[10] *Electromagnetic Compatibility (EMC) Part 4-21: Testing and Measurement Techniques-Reverberation Chamber Test Methods*, IEC 61000-4-21, 2003.

[11] Z. Tian, Y. Huang, Y. Shen, and Q. Xu, "Efficient and Accurate Measurement of Absorption Cross Section of a Lossy Object in Reverberation Chamber Using Two One-Antenna Methods," *IEEE Trans. Electromagn. Compat.*, vol. 58, no. 3, pp. 686-693, Jun. 2016.

[12] C. L. Holloway, H. A. Shah, R. J. Pirkl, W. F. Young, D. A. Hill, and J. Ladbury, "Reverberation Chamber Techniques for Determining the Radiation and Total Efficiency of Antennas," *IEEE Trans. Antennas Propag.*, vol. 60, no. 4, pp. 1758-1770, Apr. 2012.

[13] P. S. Kildal, X. Chen, C. Orlenius, M. Franzen, and C. S. L. Patane, "Characterization of Reverberation Chambers for OTA Measurements of Wireless Devices: Physical Formulations of Channel Matrix and New Uncertainty Formula," *IEEE Trans. Antennas Propag.*, vol. 60, no. 8, pp. 3875-3891, Aug. 2012.

[14] Y. Huang, and D. J. Edwards, "A novel reverberating chamber: the source-stirred chamber," *8th Int. Conf. Electromagn. Compat.*, Edinburgh, 1992, pp. 120-124.

[15] D. A. Hill, "Electronic mode stirring for reverberation chambers," *IEEE Trans. Electromagn. Compat.*, vol. 36, no. 4, pp. 294-299, Nov. 1994.

[16] C. R. Dunlap, "Reverberation chamber characterization using enhanced backscatter coefficient measurements," Ph.D. dissertation, Dept. of Elect. Comput. and Eng., Univ. of Colorado, Boulder, USA, 2013.

[17] C. R. Dunlap, C. L. Holloway, R. Pirkl, J. Ladbury, E. F. Kuester, D. A. Hill, and S. van de Beek, "Characterizing reverberation chambers by measurements of the enhanced backscatter coefficient," in *Proc. IEEE Int. Symp. on Electromagn. Compat.*, Aug. 2012, pp. 210-215.

[18] G. B. Tait, R. E. Richardson, M. B. Slocum, M. O. Hatfield, and M. J. Rodriguez, "Reverberant Microwave Propagation in Coupled Complex Cavities," *IEEE Trans. Electromagn. Compat.*, vol. 53, no. 1, pp. 229-232, Feb. 2011.

[19] J. S. Giuseppe, C. Hager, and G. B. Tait, "Wireless RF Energy Propagation in Multiply-Connected Reverberant Spaces," *IEEE Antennas Wireless Propag. Lett.*, vol. 10, pp. 1251-1254, 2011.

[20] R.Richardson, "Reverberant microwave propagation," Naval Surface Warfare Center, Dahlgren Division, Dahlgren, VA, Tech. Rep. NSWCDD/TR-08/127, Oct. 2008.

[21] A. H. Davis, "Reverberation equations for two adjacent rooms connected by an incompletely soundproof partition," *Philos. Mag.*, vol. 50, no. 295, pp. 75–80, Jul. 1925.

[22] A. D. Pierce, *Acoustics: An Introduction to Its Physical Principles and Applications*. New York: McGraw-Hill, 1981, ch. 6.

[23] C. L. Holloway, H. A. Shah, R. J. Pirkl, K. A. Remley, D. A. Hill, and J. Ladbury, "Early Time Behavior in Reverberation Chambers and Its Effect on the Relationships Between Coherence Bandwidth, Chamber Decay Time, RMS Delay Spread, and the Chamber Buildup Time," *IEEE Trans. Electromagn. Compat.*, vol. 54, no. 4, pp. 714-725, Aug. 2012.

[24] S. J. Boyes, "Reverberation Chambers and the Measurement of Antenna Characteristics," Ph.D. dissertation, Dept. of Elect. Eng. and Electron., Univ. of Liverpool, Liverpool, U.K., 2013.

[25] D. A. Hill, "Boundary fields in reverberation chambers," *IEEE Trans. Electromagn. Compat.*, vol. 47, no. 2, pp. 281-290, May 2005.

[26] A. Somani, S. Gorla, M. Magdowski, and R. Vick, “Measurement of boundary fields in a reverberation chamber,” in *Proc. IEEE Int. Symp. on Electromagn. Compat.*, Sept. 2011, pp. 123-127, *IEEE Standard Method for Measuring the Effectiveness of Electromagnetic Shielding Enclosures*, IEEE Standard 299, 2006.

Chapter 6: Antenna Array Efficiency Measurement

6.1 Introduction

As mentioned in Chapter 1, RCs can be used for the characterization of DUTs, such as antennas or wireless devices, and for the EMC testing. Chapter 3 to Chapter 5 have considered the EMC testing/measurement in RCs. In this chapter, the characterization of DUTs using RCs will be considered – antenna array efficiency measurement.

The efficiency of an antenna array is an important indicative measure of the merits of a given design. Conventionally, the efficiency measurement of an antenna array is conducted in an AC with the pattern integration method [1]. However, the measurement setup of this method is complicated and the measurement uncertainty is usually high (>10%) [1]. Over the past few years, the RC is becoming a prevalent alternative facility for performing radiated power measurements of either an antenna or a DUT [2] – [7]. It is very applicable to determine the efficiency of antennas.

In [8], the efficiency of an antenna array was measured with the reference antenna method in an RC. In this approach, to make the array work in an "all-excited" manner, a power divider is used to excite the feeding ports of the array elements simultaneously, that is, all the array elements are excited through a power divider by merely a single excitation source. Thus, the efficiency measurement of the entire array can be effectively treated in a manner similar to a single port antenna, which would simplify the measurement procedure and reduce the overall measurement time. Because of the introduction of the power divider that is external to the array under test, the consequent insertion loss has to be calibrated out. In [8], to measure the insertion loss of the power divider, all outputs except the one were terminated in impedance-matched loads and the transmission coefficient between the input and the one output was measured. Then the measurement proceeded in turn for each output (the insertion loss was measured in the condition of 50 Ohm loads). It is correct for the antenna array that each element is well-matched but it could be a problem when some elements are not well-matched because the reflection from the array elements could contribute to the insertion loss of the power divider, which will result in an inaccurate evaluation of the array efficiency.

In this chapter, it is shown that the array efficiency can be obtained accurately using a power divider even when the elements of the array are not well-matched with the power divider. This is realized by introducing proper attenuators between the array elements and the power divider to alleviate the effect of the reflected power from the array to the insertion loss of the power divider. The theoretical investigation is detailed. Simulations and measurements are conducted to validate the effectiveness of the proposed method.

6.2 The Problem

As mentioned above, there is a problem with the existing method [8] for the efficiency measurement of an antenna array which is hard to reveal it directly and clearly. However, it can be much easier and clearer to start the analysis from a single antenna and then extend it to an antenna array. Thus, the progressive steps in the problem-solving process will be made explicit.

6.2.1 Single Antenna Case

In the single antenna case, a sleeve dipole antenna was selected as an AUT. A 5-dB RF attenuator was connected to the AUT to introduce specific insertion loss, as shown in Figure 6.1(a). Measurements were performed from 2.6 to 2.8 GHz in the RC at the University of Liverpool. In this measurement, the reference antenna method was adopted to obtain the radiation efficiency and the total efficiency of the AUT. Two double-ridged waveguide horn antennas were used as the transmitting antenna (SATIMO® SH 2000) and the reference antenna (Rohde & Schwarz® HF 906), respectively. The antennas were connected to a VNA via cables running through the bulkheads of the chamber. During the measurement, the two stirrers were moved simultaneously and stepwise to 360 positions (1 degree for each step). At each mode stirring position, a full frequency sweep was performed using the VNA and the *S*-parameters were collected. In this measurement, 10,001 points were sampled in the measured frequency range. The measurement setup is shown in Figure 6.1(b).

(a)

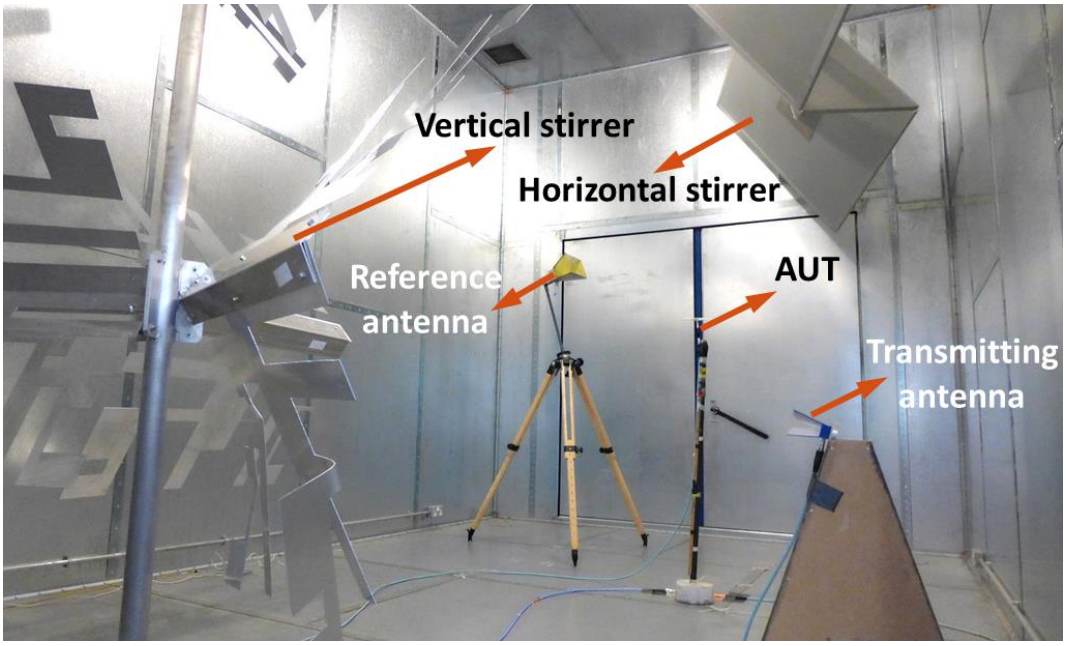

(b)

Figure 6.1 Measurement setup of the efficiency of a dipole antenna: (a) AUT with a 5-dB attenuator, (b) measurement setup in RC.

The measurement procedure is given as follows.

Step1: Calibrate the VNA including the cables according to the standard calibration procedure.

Step2: Place the AUT, the reference antenna, the transmitting antenna and the supports inside the RC to keep the chamber loss constant.

Step3: Connect the AUT to port 1 of the VNA and the transmitting antenna to port 2 of the VNA, terminate the reference antenna with a 50 Ω load and record the full *S*-parameters for each stirring position.

Step4: Disconnect the AUT from port 1 of the VNA and terminate it with a 50 Ω load. Connect the reference antenna to port 1 of the VNA and the transmitting antenna is kept connecting to port 2 of the VNA. Record the full *S*-parameters for each stirring position.

The radiation efficiency of the AUT (η_{aut}^{rad}) is then calculated using the reference antenna method [9] – [11]

$$\eta_{aut}^{rad} = \left[\frac{\langle|S_{12,s}^{aut}|^2\rangle}{\langle|S_{12,s}^{ref}|^2\rangle} \times \frac{1-|\langle S_{11}^{ref}\rangle|^2}{1-|\langle S_{11}^{aut}\rangle|^2} \times \frac{1}{IL}\right] \times \eta_{ref}^{rad} \tag{6.1}$$

where η_{ref}^{rad} is the radiation efficiency of the reference antenna. The quantities $\langle|S_{12,s}^{aut}|^2\rangle$ and $\langle|S_{12,s}^{ref}|^2\rangle$ represent the stirred energy contributions of S_{12}^{aut} and S_{12}^{ref}, respectively [4]. S_{12}^{aut} and S_{12}^{ref} are the transmission coefficients when the VNA port 1 is connecting to the AUT and the reference antenna, respectively. S_{11}^{aut} and S_{11}^{ref} are the reflection coefficients of the AUT and the reference antenna, respectively. *IL* is the insertion loss introduced by the attenuator (5 dB here). The measurement results are shown in Figure 6.2. As can be seen, when the AUT is matched very well (S_{11} is approximately below -15 dB in this case), the measured radiation efficiency agrees well with the real radiation efficiency (the real radiation/total efficiency was measured with the conventional reference antenna method without the attenuator which should be accurate), shown as the shaded band. However, when the AUT is not well matched, considerable errors may occur (the maximum error is approximately 25% in this case). The reason can be explained as follows: when the AUT is very well matched, $S_{11}^{aut} \to 0$ and $(1-|\langle S_{11}^{aut}\rangle|^2) \to 1$, which means η_{aut}^{rad} is not easily influenced by S_{11}^{aut}. The contribution of S_{11}^{aut} to η_{aut}^{rad} is negligible. However, when the AUT is not well matched, the contribution of S_{11}^{aut} to η_{aut}^{rad} cannot be neglected. Actually, the

measured S_{11}^{aut} is not the real reflection coefficient of the AUT because of the influence of the introduced insertion loss. Therefore, the radiation efficiency is not measured correctly. This is because the precondition of (6.1) is that the antenna is well matched with the attenuator.

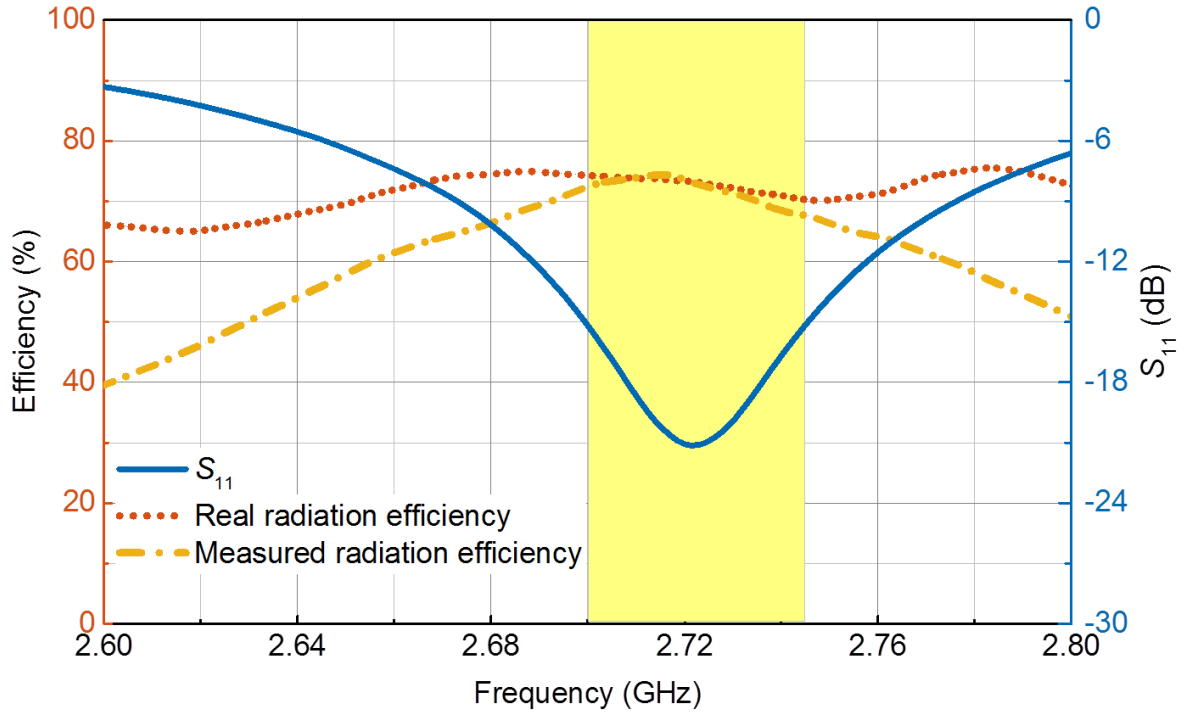

Figure 6.2 Comparison of the measured radiation efficiency and real radiation efficiency of the sleeve dipole antenna with a 5-dB attenuator, along with the antenna S_{11}.

To show this problem quantitatively, an equivalent model in Figure 6.3 is considered, where P_s is the power supplied to the antenna, P_b is the power reflected back at the reference plane and P_r is the power radiated. The relationship between P_b and P_s can be expressed as

$$P_b = P_s \cdot IL \cdot \left|S_{11,r}^{aut}\right|^2 \cdot IL \tag{6.2}$$

where IL is the insertion loss (in linear form) of the attenuator and $S_{11,r}^{aut}$ is the real reflection coefficient of the AUT in free space. (6.2) can be rewritten as

$$|S_{11}^{aut}|^2 = \left|S_{11,r}^{aut}\right|^2 \cdot IL^2 \tag{6.3}$$

where

$$|S_{11}^{aut}|^2 = P_b/P_s \tag{6.4}$$

is the measured reflection coefficient at the reference plane.

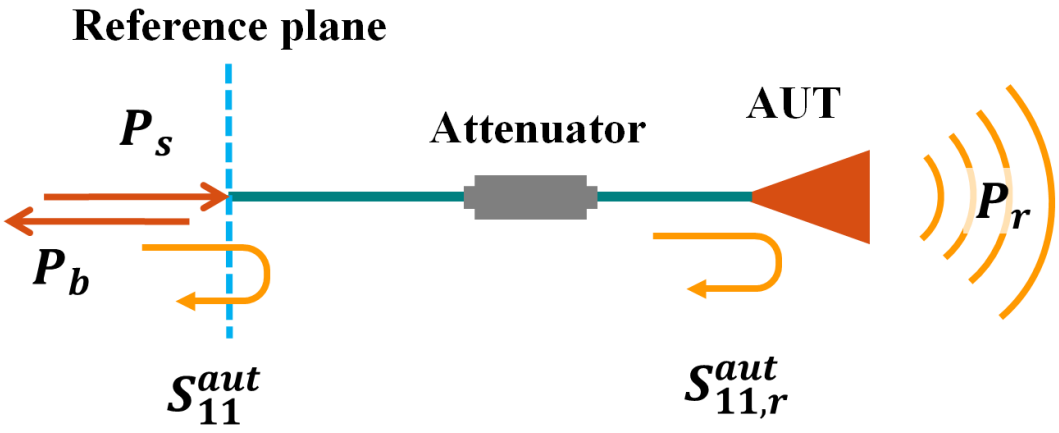

Figure 6.3 The equivalent model.

The radiated power P_r is linked to the supplied power P_s by

$$P_r = P_s \cdot IL \cdot (1 - |S_{11,r}^{aut}|^2) \cdot \eta_{aut}^{rad} \tag{6.5}$$

where η_{aut}^{rad} is the real radiation efficiency of the antenna. The corresponding transformation of (6.5) is

$$\eta_{aut}^{rad} = \eta_{aut}^{tot} \cdot \frac{1}{1 - |S_{11,r}^{aut}|^2} \cdot \frac{1}{IL} \tag{6.6}$$

where

$$\eta_{aut}^{tot} = P_r/P_s \tag{6.7}$$

is the measured total efficiency at the reference plane.

For the reference antenna method, it can be derived

$$\eta_{aut}^{tot}/\eta_{ref}^{tot} = \langle |S_{12,s}^{aut}|^2 \rangle / \langle |S_{12,s}^{ref}|^2 \rangle \tag{6.8}$$

where

$$\eta_{ref}^{tot} = \left(1 - \left|\langle S_{11}^{ref}\rangle\right|^2\right) \cdot \eta_{ref}^{rad} \tag{6.9}$$

Substituting (6.3), (6.6), (6.8) and (6.9) into (6.1) gives

$$\eta_{aut}^{rad} = \left[\frac{\langle\left|S_{12,s}^{aut}\right|^2\rangle}{\langle\left|S_{12,s}^{ref}\right|^2\rangle} \times \frac{1 - \left|\langle S_{11}^{ref}\rangle\right|^2}{1 - |\langle S_{11}^{aut}\rangle|^2/IL^2} \times \frac{1}{IL}\right] \times \eta_{ref}^{rad} \tag{6.10}$$

Thus, the modified equation is mathematically derived. As can be seen from (6.10), when there is no insertion loss (IL = 1) or the insertion loss is negligible ($IL \rightarrow 1$). (6.10) is equivalent to (6.1). However, when the insertion loss is large, there is a big difference between (6.1) and (6.10). That is, when the insertion loss is large, if (6.1) is used to calculate the efficiency of the AUT, considerable errors will occur. The comparison of the calculated radiation efficiency using (6.1) and (6.10) and the real radiation efficiency is shown in Figure 6.4.

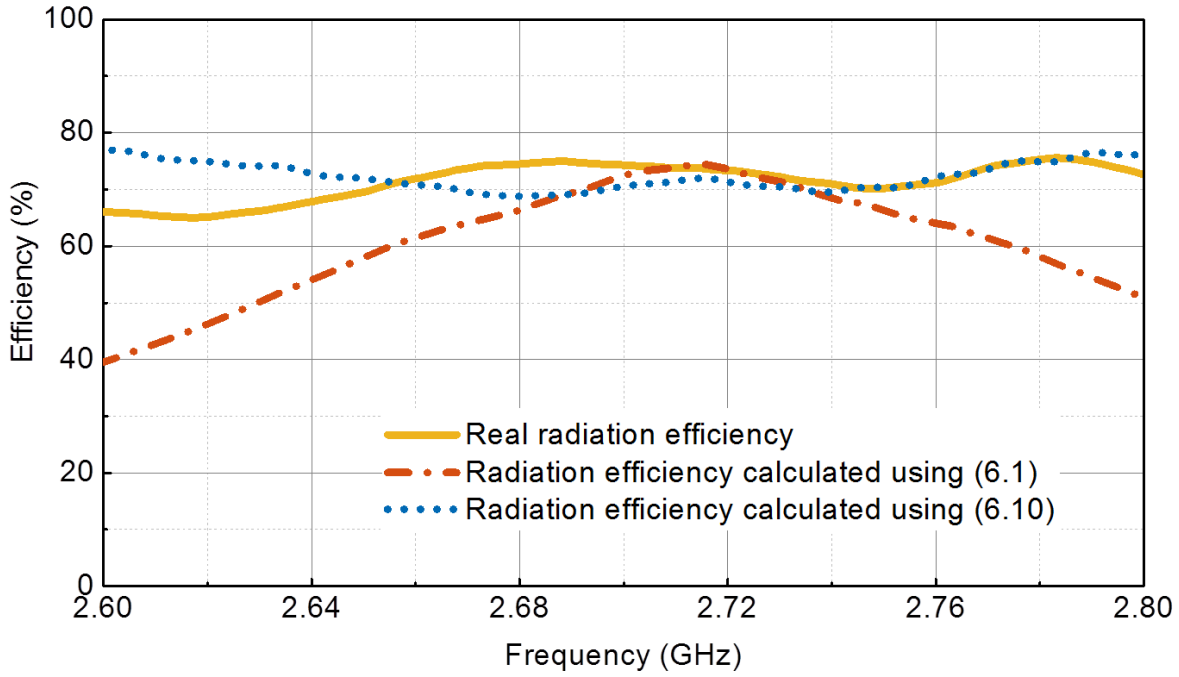

Figure 6.4 The comparison of the measured radiation efficiency using (6.1) and (6.10) and the real radiation efficiency.

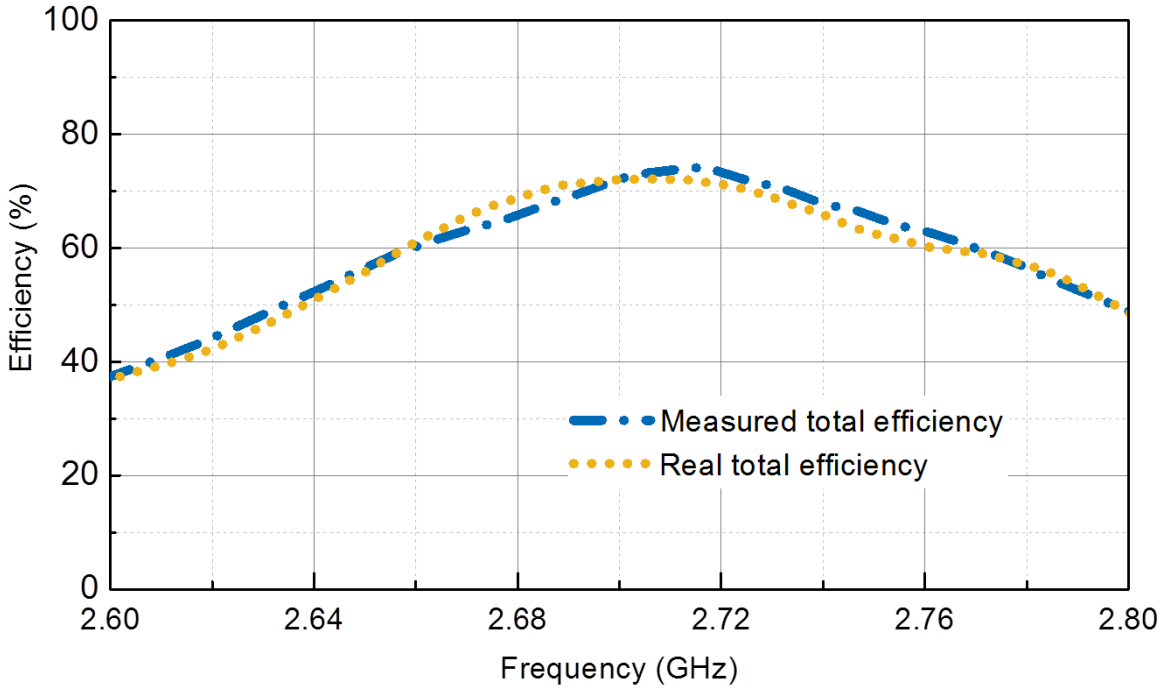

Figure 6.5 Comparison of the real total efficiency and the measured total efficiency.

It can be seen that the radiation efficiency calculated using (6.10) seems closer to the real radiation efficiency in most of the frequency span than that calculated using (6.1). But it does not agree well with the real radiation efficiency as expected. At some frequency bands, say, 2.60 – 2.64 GHz, there is still significant error between the measured radiation efficiency and the real radiation efficiency. This error is caused by the imperfection of the transition section between the antenna and the attenuator or the attenuator and the cable. To be more specific, when the AUT is connected with the attenuator, the reflection coefficient measured at the reference plane is very small. Thus, it is easily affected by the mismatch caused by the imperfection of the transition section. A small mismatch of the transition section may cause a big variation of the reflection coefficient measured at the reference plane. Therefore, it would be very difficult to calibrate the influence of the insertion loss to S_{11} of the AUT in practice. Thus, in reality, the radiation efficiency is hard to be measured accurately when there is insertion loss between the AUT and the feeding port. However, S_{12} is not easily affected by the small mismatch of the transition section because this mismatch is negligible compared with the insertion loss caused by the attenuator. Therefore, the total efficiency can be measured correctly because the total efficiency η_{aut}^{tot} depends only on S_{12}^{aut} while not on S_{11}^{aut},

as indicated in (6.11). The comparison of the real total efficiency and the measured total efficiency are shown in Figure 6.5. It can be seen that the results are in reasonable agreement.

$$\eta_{aut}^{tot} = \left[\frac{\langle|S_{12,s}^{aut}|^2\rangle}{\langle|S_{12,s}^{ref}|^2\rangle} \times (1 - |\langle S_{11}^{ref}\rangle|^2) \times \frac{1}{IL}\right] \times \eta_{ref}^{rad} \tag{6.11}$$

6.2.2 Antenna Array Case

When measuring the efficiency of an antenna array, to make the array work in an "all-excited" manner, a power divider is normally adopted to excite the feeding ports of the array elements simultaneously [8], [12], i.e., all the array elements are excited through a series of power dividers by merely a single excitation source. Thus, the efficiency measurement of the entire array can be effectively treated in a manner similar to a single port antenna. The power divider is such a network with the property of appearing lossless when the output ports are matched and only the reflected power from the output ports is dissipated [13]. The reflected power will be consumed by the isolation resistance (R_{iso}) in the power divider, as can be seen in Figure 6.6.

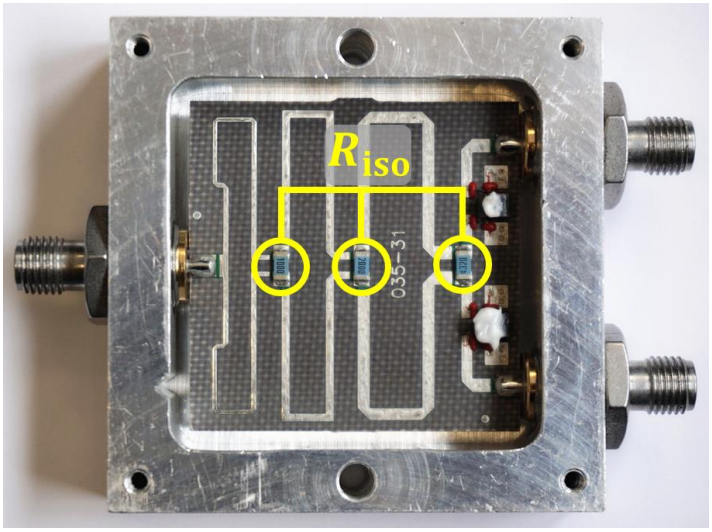

Figure 6.6 A typical 2-way Wilkinson power divider in microstrip line format.

Therefore, the insertion loss of the power divider depends on the impedance of the external device. When the elements of the antenna array are well matched, very small amount of power will be reflected from each element and the insertion loss of the power divider can be neglected. However, when the elements are not well matched, a large amount of power will be reflected from each element and then dissipated on the R_{iso}, thus the insertion loss can be very large. Even worse, unlike the single antenna case, the insertion loss of the power divider caused by the reflection from the antenna array cannot be quantified because it is not possible to know how much power has been dissipated on R_{iso}. Therefore, the measurement problem caused by the insertion loss will become more complicated. Neither the radiation efficiency nor the total efficiency can be measured accurately when the elements of the antenna array are not well matched.

6.3 Improved Method

From the above analysis, it is known that it is difficult to quantify the insertion loss of the power divider when the external device is not well matched. In this case, it is useful to try to minimise the dissipated power on R_{iso} of the power divider, i.e., minimise the reflected power from the antenna array. In this section, we propose to introduce an attenuator of a proper value between each array element and each power divider port. Actually, by introducing an attenuator, the effects of mismatch between the array elements and the power divider ports could be minimized. Thus, the use of the attenuator allows transferring the power that should have been dissipated on R_{iso} to the attenuator. To validate this idea, field-circuit co-simulation is employed in CST (Computer Simulation Technology) Microwave Studio in the frequency range of 2.0 – 3.5 GHz. A two-dipole array is adopted as an antenna under simulation, as can be seen in Figure 6.7. In the two-dipole array, one element is 53.4 mm long and the other is 46.5 mm long. The spacing between these two elements is set to be 25.4 mm. The material for making the array is PEC. The reflection coefficients, the phase of the reflection coefficients and the transmission coefficients of the array are shown in Figure 6.8. As can be seen, S_{11} and S_{22} are interlaced (both in amplitude and phase), which ensures that there will be power loss on the R_{iso}. Another thing that should be noted is that S_{21} and S_{12} are very small

(below -15 dB), which means the mutual coupling between the two dipole elements is negligible.

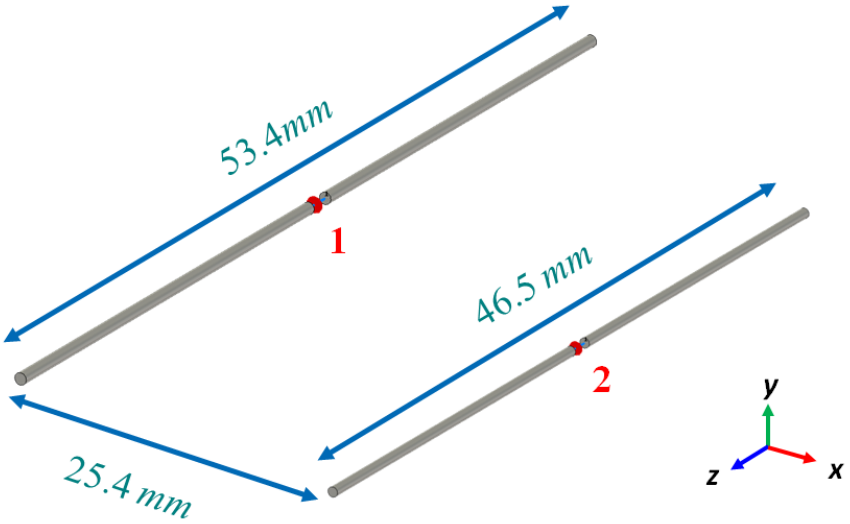

Figure 6.7 The two-dipole array used for simulation in CST.

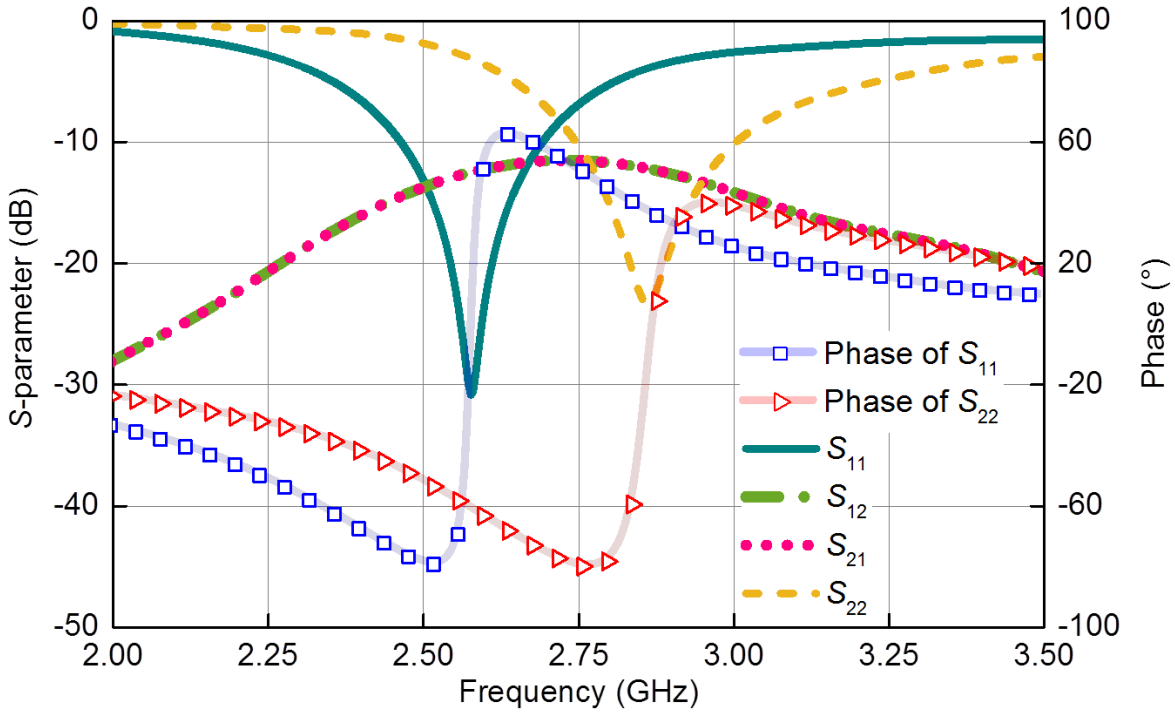

Figure 6.8 The simulated *S*-parameters of the two-dipole array.

In practice, the mutual coupling between elements is an importance issue that needs to be carefully considered in an antenna array. In this section, the impact of the mutual coupling to the validity of the proposed method is studied as well and will be discussed later. The schematic of the field-circuit co-simulation model is given in Figure 6.9. To obtain the power loss on the R_{iso}, a current probe P1 is introduced to monitor the current on the R_{iso}. The feeding power from port 1 is 1 W. The attenuation of the attenuators is tuned stepwise from 0 dB to 10 dB (2 dB per step). The power consumed on the R_{iso} is shown in Figure 6.10. Two things can be identified from this figure. First, because of the mismatch of the array elements, there exists power loss on R_{iso} (when the attenuation is zero, the power consumed is not zero). Second, with the increase of the attenuation, the power consumed on R_{iso} will decrease as expected. When the attenuation is 10 dB, the power consumed on the R_{iso} will be always below 0.002 W, that is, only less than 0.2% power will be consumed by R_{iso}.

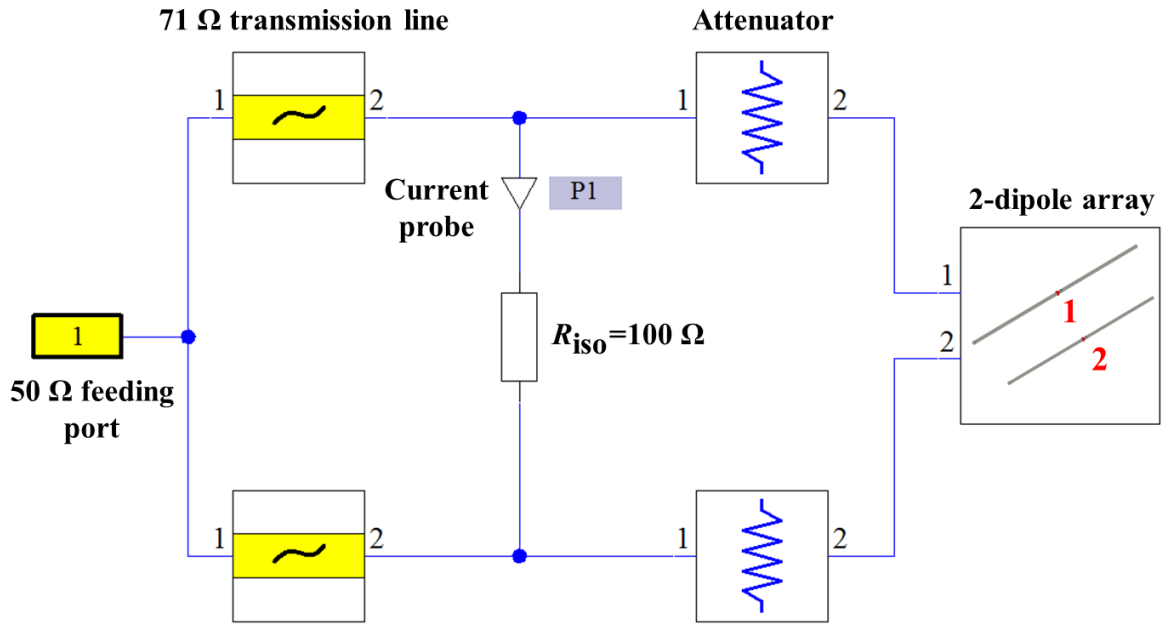

Figure 6.9 Schematic of the circuit.

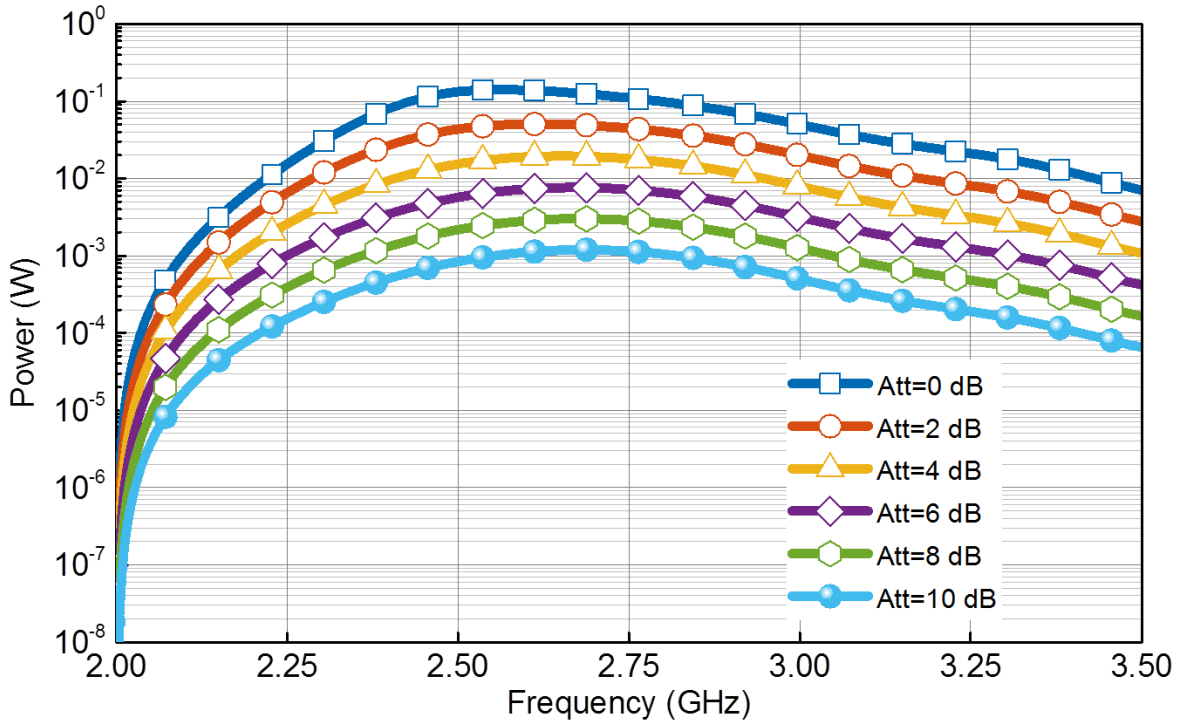

Figure 6.10 Simulated power consumed on the isolation resistance of the power divider for 1 W input power with different attenuators.

From the above simulation analysis, it can be seen that the attenuator can help to reduce the power loss on the R_{iso}. Because the attenuation value is exactly known, the insertion loss caused by the attenuator can be calibrated out for the total efficiency measurement. However, the radiation efficiency measurement is still a problem because the effect of the imperfection of the transition section between the antenna and the attenuator or the attenuator and the cable is hard to remove, as discussed in Section 6.2. In the following part, it will demonstrate that the radiation efficiency can be measured accurately using the proposed method.

To demonstrate the effectiveness of the proposed method, a measurement was performed in our RC. A 2-way 0° power divider (Mini-Circuits® ZAPD-4-S+) with a voltage standing wave ratio (VSWR) < 1.33:1 from 2.0 – 4.2 GHz was employed in this study. The spacing of the two output ports is 25.4 mm. The AUT in this study is a two-dipole array consisting of two parallel dipole elements with the spacing of 25.4 mm. The *S*-parameters of the two dipole elements are shown in Figure 6.11. The power divider is connected to the AUT to feed the two dipole elements with equal weights, as can be seen from Figure 6.12.

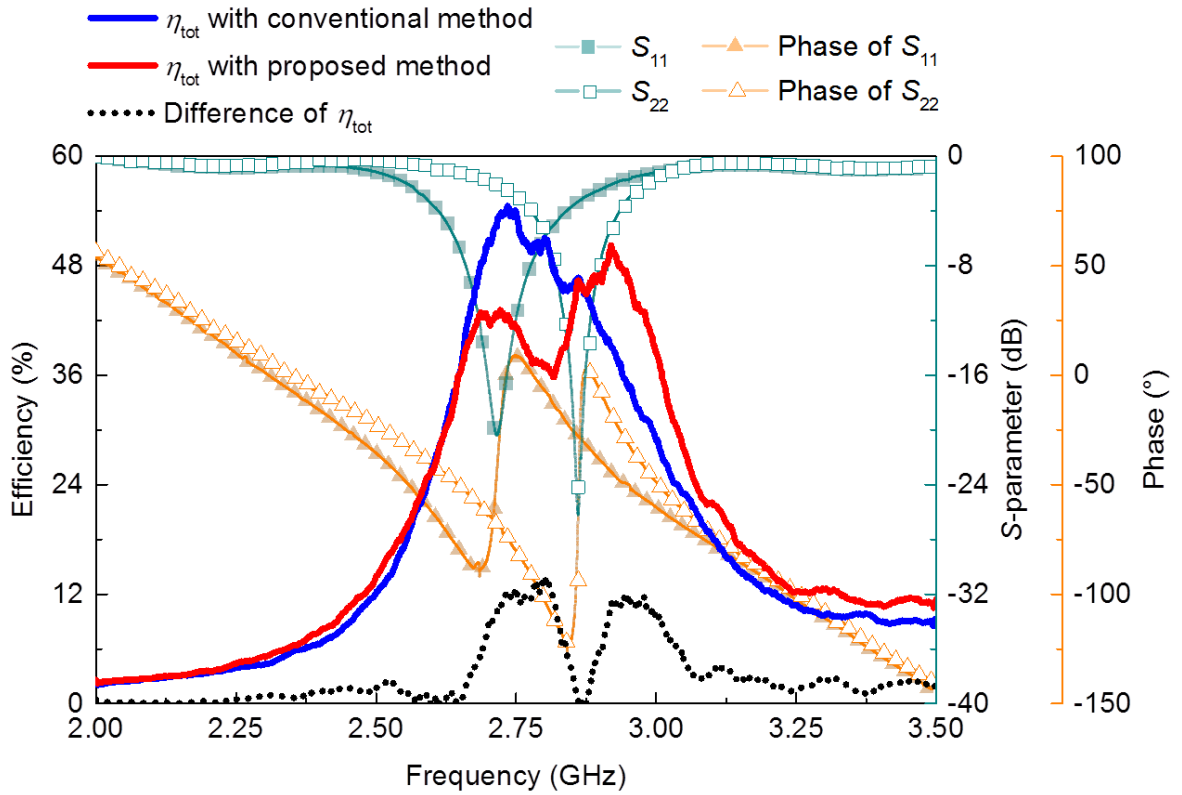

Figure 6.11 **Comparison of the measured total efficiency of the two-dipole array with the conventional method and with the proposed method.**

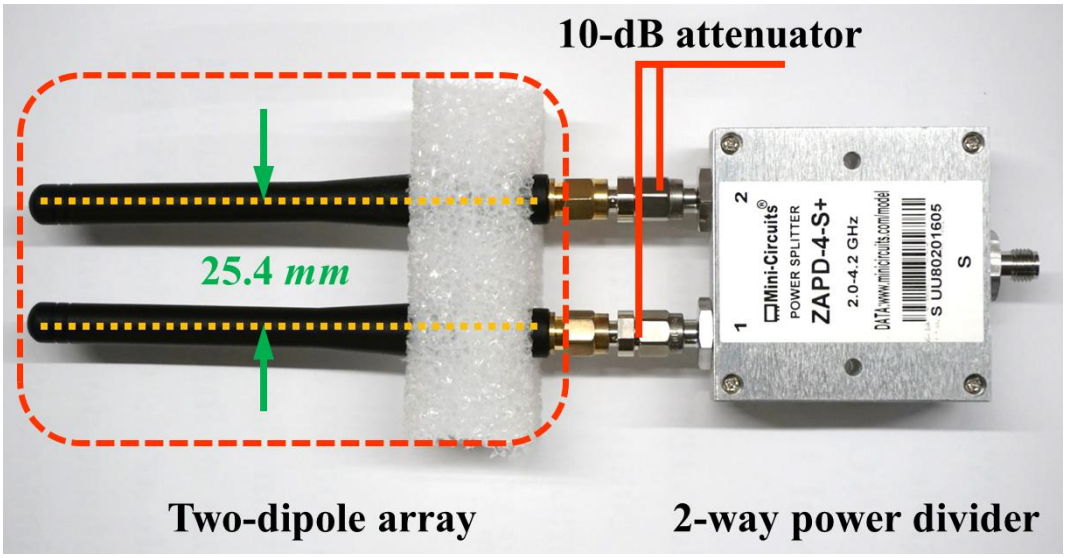

Figure 6.12 **The two-dipole array connected with the 2-way power divider.**

The measurement was conducted in the frequency range of 2.0 – 3.5 GHz. The reference antenna method is adopted in this measurement. The measurement setup and measurement procedure are the same as detailed in Section 6.2.1. The comparison of the measured total efficiency of the two-dipole array with the conventional method and with the proposed method is shown in Figure 6.11. It can be seen that, in the frequency range of 2.0 – 2.6 GHz and 3.1 – 3.5 GHz, there is not much difference of the amplitude and phase between S_{11} and S_{22}. Therefore, very little power will be consumed on the R_{iso}. Thus, the total efficiency measured with the conventional method and with the proposed method agrees well. However, in the frequency range of 2.6 – 3.1 GHz, there is a significant difference of the amplitude or phase between S_{11} and S_{22}, i.e., a considerable amount of power will be consumed by R_{iso}. In this case, the *IL* in (6.11) cannot be accurately obtained. The *IL* of the power divider measured (using the method in [8]) is not correct because it is accurate only when the power divider ports are terminated with impedance-matched loads, i.e., no reflection occurs. Thus, considerable errors could occur if the conventional method is adopted for the not-well-matched case. Conversely, for the proposed method, the *IL* is dominated by the attenuators and the contribution of the power divider to the *IL* can be neglected. Besides, the reflected power from the array elements will be attenuated by the attenuators as well. Hence, the *IL* of the power divider including the reflection effect will have little influence on *IL* in (6.11). As can be seen in Figure 6.11, the total efficiency measured using the conventional method has obvious errors compared with that measured using the proposed method in the frequency range of 2.6 – 3.1 GHz where the amount of the power consumed on R_{iso} is big. The maximum error can reach 15% at about 2.76 GHz, which cannot be neglected in practice.

One thing to be noted is that there is always some uncertainty on the attenuation value of the attenuator. That is, the actual attenuation value is not always exactly the same as the nominal value. The attenuator used in the experiment has about $\pm$ 0.5 dB deviation in the frequency range of DC to 3.0 GHz [14]. To show the impact of the deviation of the attenuation value on the efficiency of the antenna array, the field-circuit co-simulation was conducted in the above-mentioned two-dipole array model in CST. The total efficiency of the two-dipole array was calculated with the attenuation value of 9.5 dB, 10 dB, and 10.5 dB, respectively. The results are shown in Figure 6.13.

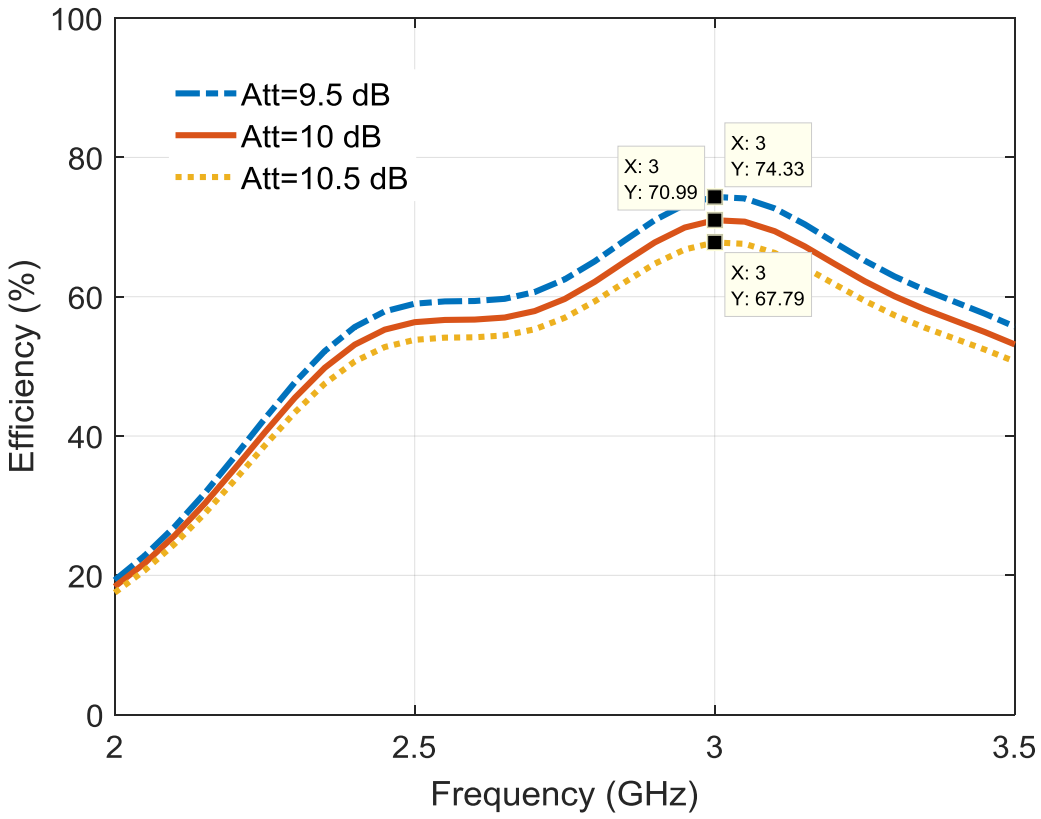

Figure 6.13 The total efficiency of the two-dipole array in CST with different attenuation values.

As can be seen, only a very small difference can be observed for the total efficiency of the array calculated with different attenuation values in the full frequency span. The maximum difference is only about 4% which is small. Thus, the impact of the uncertainty from the attenuation value of the attenuator can be neglected. Another point that may be concerned is the impact of the mutual coupling between antenna elements on the validity of the proposed method. To investigate this issue, a simulation is done using CST. In this simulation, the spacing between the two elements of the dipole array (as shown in Figure 6.7) is set to be 5.0 mm, which results in significant increase in the mutual coupling of the two dipole elements. Thus, a new dipole array with higher mutual coupling is created. As can be seen from Figure 6.14, the mutual coupling of the new dipole array exceeds -10 dB from 2.5 GHz to 3.45 GHz and can reach about -3 dB at 2.9 GHz. The array total efficiency predicted by CST (used as a benchmark here) and that obtained from the field-circuit model using our proposed method are plotted and compared in Figure 6.14. The total efficiency of the array with a low mutual

coupling (the array shown in Figure 6.7 and Figure 6.8) is also plotted for reference here. It can be seen that no matter the mutual coupling is high or low, the efficiency obtained from our proposed method does not have a big difference from the benchmark. The maximum difference is only about 3% for both high coupling and low coupling scenarios, which is very small. That is, the mutual coupling does not influence the validity of the proposed method. The proposed method is general for the efficiency measurement of antenna arrays regardless of the mutual coupling.

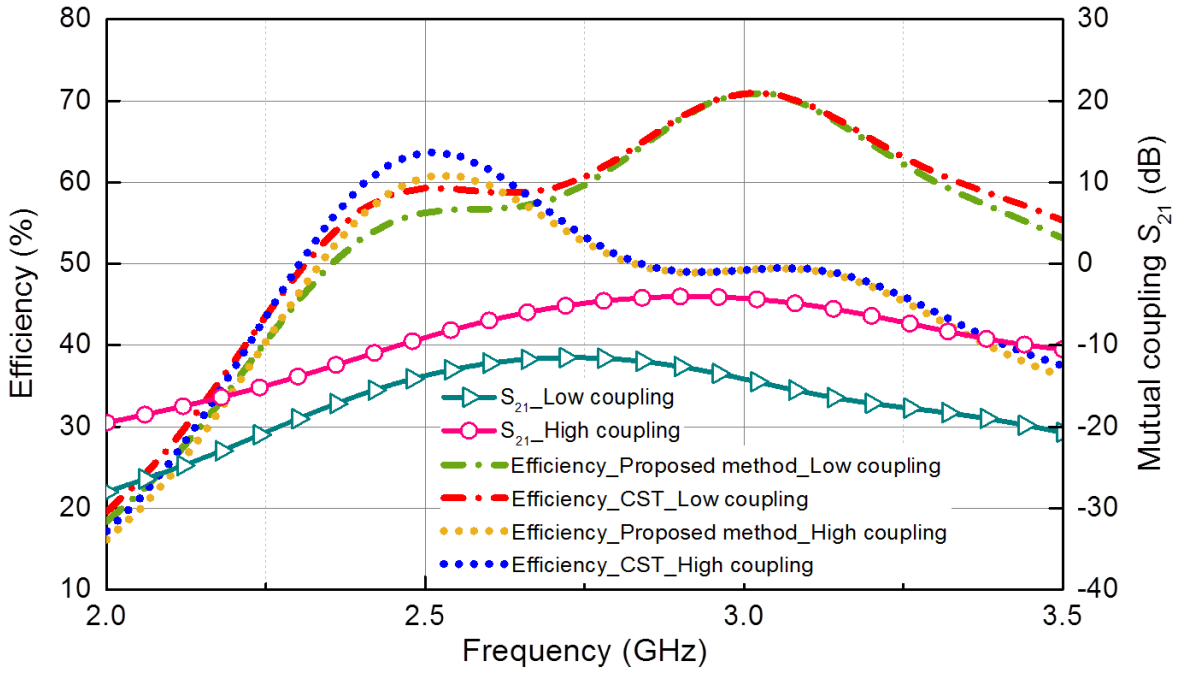

Figure 6.14 The two-dipole array total efficiency predicted by CST and that obtained from the field-circuit model using our proposed method with low and high mutual coupling.

Once the total efficiency has been known, the radiation efficiency can be calculated by excluding the impedance mismatch effect of the antenna elements. The radiation efficiency can then be expressed as

$$\eta_{rad} = \frac{\eta_{tot}}{1 - \frac{1}{2}(|S_{11}|^2 + |S_{22}|^2)} \tag{6.12}$$

The array radiation efficiency, the array total efficiency and the mutual coupling S_{21} of the two dipole elements are shown in Figure 6.15. As can be seen, the radiation efficiency is reasonable and the mutual coupling between array elements is negligible.

Generally, for an antenna array with N elements, the total efficiency can be obtained using (6.11) and the radiation efficiency will become

$$\eta_{rad} = \frac{\eta_{tot}}{1 - \frac{1}{N}\sum_{i=1}^{N}|S_{ii}|^2} \tag{6.13}$$

where i is the element number.

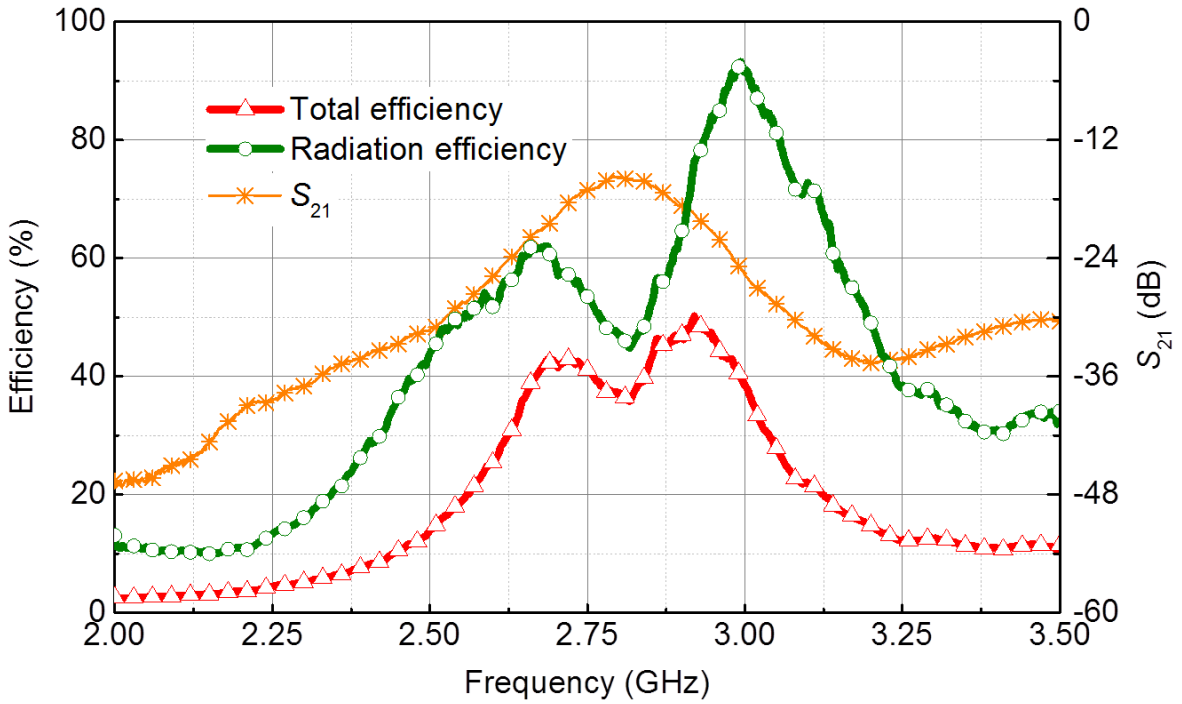

Figure 6.15 The comparison of the radiation efficiency and the total efficiency of the two-dipole array and the mutual coupling S_{21} of the two dipole elements.

6.4 Measurement Uncertainty

To quantify the measurement uncertainty, the method proposed in [15] has been adopted. As demonstrated in [15], the direct coupling can be a major source of uncertainty inherent during over-the-air measurements in an RC. Therefore, the direct coupling (normally expressed as

the Rician *K*-factor) should be as small as possible. Furthermore, the uncertainty model presented in [15] combines the random NLoS process and the random LoS process, and the combined standard deviation can be written as

$$\sigma = \frac{\sqrt{\sigma_{NLoS}^2 + K^2\sigma_{LoS}^2}}{\sqrt{1+K^2}} \tag{6.14}$$

where $\sigma_{NLoS} = 1/\sqrt{N_{NLoS,ind}}$, $\sigma_{LOS} = 1/\sqrt{N_{LoS,ind}}$ and K = average Rician *K*-factor, comprising the samples obtained from mechanical stirring, source stirring and polarization stirring. $N_{NLoS,ind}$ and $N_{LoS,ind}$ are the NLoS independent samples and LoS independent samples, respectively. The Rician *K*-factor is calculated as follows

$$K = \frac{|\langle S_{12}^{aut}\rangle|^2}{\langle|S_{12}^{aut} - \langle S_{12}^{aut}\rangle|^2\rangle} \tag{6.15}$$

The standard σ is presented in dB scale by averaging the dB values of $(1+\sigma)$ and $(1-\sigma)$, i.e.,

$$\sigma_{dB} = \frac{10\{\log(1+\sigma) - \log(1-\sigma)\}}{2} = 5\log\left(\frac{1+\sigma}{1-\sigma}\right) \tag{6.16}$$

$N_{NLoS,ind}$ is computed by applying the standardized circular autocorrelation to a 1D (one dimensional) array written using the received power samples during one rotation cycle [16]. The critical value *r* suggested by the standard [7] is applied.

$$r = \frac{1}{e}\left(1 - \frac{7.22}{n^{0.64}}\right) \tag{6.17}$$

where *n* is the number of the checked samples (120 in our case). The autocorrelation coefficient of the received power samples at the lowest frequency 2.0 GHz is shown in Figure 6.16. As can be seen, it is always below the critical value for the lag number from 1 to 199, which means the 120 samples are independent. $N_{LOS,ind}$ can be calculated via

$$N_{LOS,ind} = N_{ap} \cdot N_{ant,ind} \tag{6.18}$$

where N_{ap} is the number of antenna positions, and $N_{ant,ind}$ is the number of independent antennas used in the chamber. In our case, $N_{ap} = N_{ant,ind} = 1$. The measured Rician *K*-

factor and standard deviation in decibel format are shown in Figure 6.17. It can be seen that any contribution toward the uncertainty from LoS coupling is small and the overall uncertainty inherent in the measurements is acceptably low.

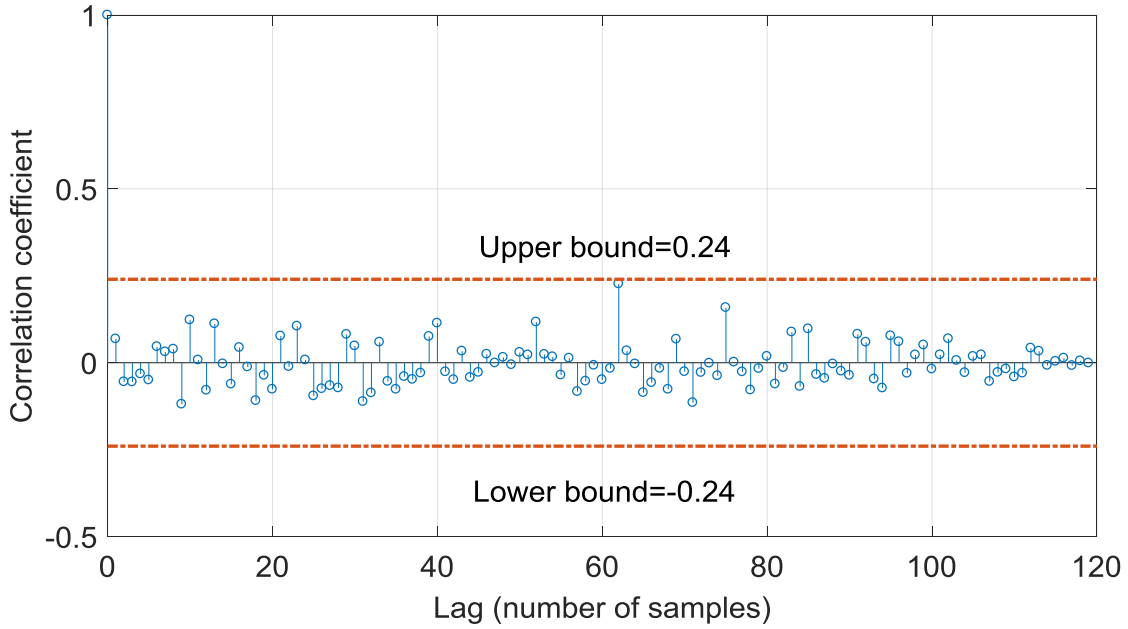

Figure 6.16 The autocorrelation coefficient of the received power samples and the lag at which the correlation is lost (@ 2.0 GHz).

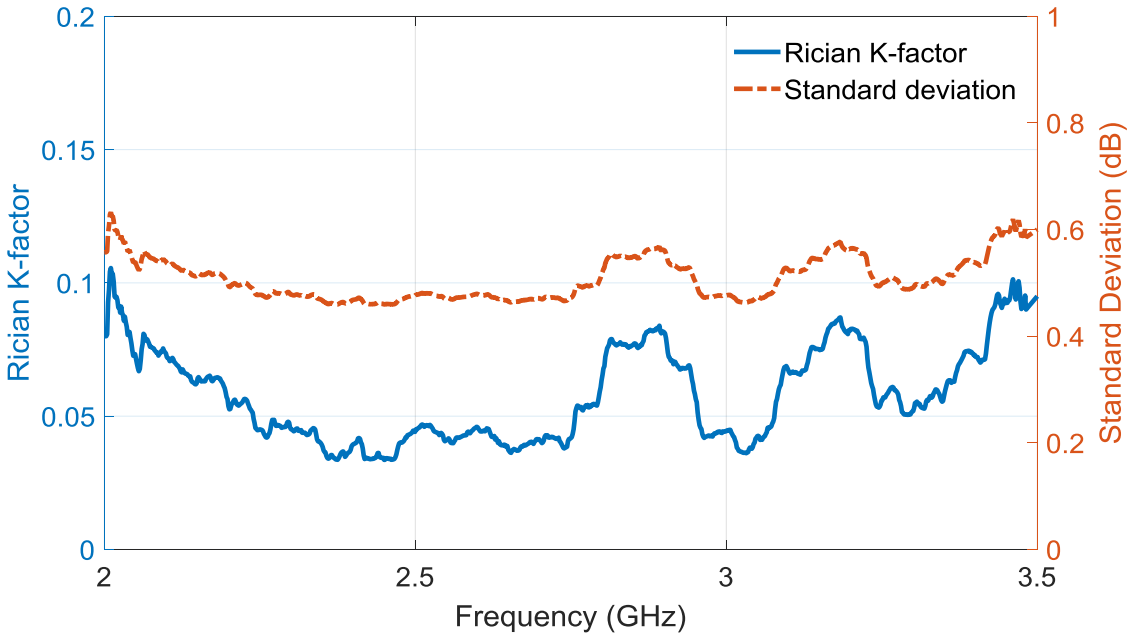

Figure 6.17 Rician *K*-factor and standard deviation.

6.5 Discussions and Conclusion

In this chapter, an improved measurement-based method to obtain the efficiency of an all-excited antenna array in an RC has been presented. When measuring the efficiency of an antenna array in an RC, to make the array work in an "all-excited" manner, a power divider is normally employed to excite the feeding ports of the array elements simultaneously, that is, all the array elements are excited through a series of power dividers by merely a single excitation source. Thus, the efficiency measurement of the entire array can be effectively treated in a manner similar to a single port antenna, which would simplify the measurement procedure and reduce the overall measurement time. However, the introduction of the power divider will inevitably bring in insertion loss which needs to be quantified and calibrated out. In our previous work, the calibration of the insertion loss of the power divider was implemented by terminating all outputs in impedance-matched loads and measured the transmission coefficient between the input and the output port. By repeating this procedure for each output port, the *S*-parameters from the input to all output ports can be obtained. The total insertion loss is calculated by summating the measured transmission coefficient of each port. It is correct if each element of the antenna array is well matched. However, if some elements of the array antenna are not well matched, a considerable error may occur. The reason is, when the element is not well matched, a non-ignorable amount of the power fed to the element will be reflected back to the power divider and then dissipated on the R_{iso}. The power dissipated on the R_{iso} is very difficult to quantify. Therefore, the insertion loss of the power divider cannot be exactly known.

In this study, the power dissipated on the R_{iso} of the power divider has been minimized by introducing 10-dB attenuators between array elements and power divider ports. The attenuators would alleviate the reflection from the array antenna to the power divider and thus reduce the dissipated power on the attenuator. Moreover, because the attenuation of the attenuator is known, thus it can be calibrated out accurately. Simulations and measurements have been done to validate the proposed method. The results show that this method is effective to measure the efficiency of an antenna array especially for an antenna array that some elements of it are not well matched. It is advantageous especially for wideband antenna arrays where good impedance matching of array elements is difficult to maintain.

There are some points that need to be emphasized. Firstly, the attenuation of the attenuators used in the measurement should be large enough. Otherwise, when the attenuator is loaded with the mismatched antenna, the attenuation value will be changed [13]. In our case, a 10-dB attenuator is suitable. Theoretically, the bigger the attenuation, the less sensitive the attenuation to the impedance of the mismatched antenna, and consequently, the more accurate the measured results will be. However, considering the dynamic range of the VNA, the attenuation cannot be too large to ensure the accurate measurement of the *S*-parameters. Therefore, the attenuation value should be carefully selected before the measurement. Secondly, the proposed method is time-saving as the whole array is treated in a manner similar to a single port antenna, and also it is no need to calibrate the insertion loss of power divider. This is advantageous especially for arrays of a large number of elements. However, no verification of this method has been performed for such arrays, and it is left as a topic for future work.

6.6 References

[1] Y. Huang, "Radiation efficiency measurements of small antennas," in *Handbook of Antenna Technologies, ed by Z. Chen, Singapore: Springer, 2015*.

[2] D. A. Hill, Electromagnetic Fields in Cavities: Deterministic and Statistical Theories. New York, NY, USA: Wiley-IEEE Press, 2009.

[3] C. L. Holloway, H. A. Shah, R. J. Pirkl, W. F. Young, D. A. Hill, and J. Ladbury, "Reverberation chamber techniques for determining the radiation and total efficiency of antennas," *IEEE Trans. Antennas Propag*., vol. 60, no. 4, pp. 1758-1770, Apr. 2012.

[4] C. L. Holloway, D. A. Hill, J. M. Ladbury, P. F. Wilson, G. Koepke, and J. Coder, "On the Use of Reverberation Chambers to Simulate a Rician Radio Environment for the Testing of Wireless Devices," *IEEE Trans. Antennas Propag., Special Issue on Wireless Communications*, vol. 54, no. 11, pp. 3167-3177, Nov. 2006.

[5] H. G. Krauthäuser, and M. Herbrig, "Yet another antenna efficiency measurement method in reverberation chambers," in *Proc. IEEE Int. Symp. Electromagn. Compat.*,Jul. 25-30, 2010, pp. 536-540.

[6] P.-S. Kildal, and K. Rosengren, "Correlation and capacity of MIMO systems and mutual coupling, radiation efficiency, and diversity gain of their antennas: simulations and measurements in a reverberation chamber," *IEEE Commun. Mag.*, vol. 42, no. 12, pp. 104-112, Dec. 2004.

[7] *Electromagnetic Compatibility (EMC) part 4-21: Testing and measurement techniques-Reverberation chamber test methods*, IEC 61000-4-21, 2003.

[8] S. J. Boyes, Y. Zhang, A. K. Brown, and Y. Huang, "A Method to De-Embed External Power Dividers in Efficiency Measurements of All-Excited Antenna Arrays in Reverberation Chamber," *IEEE Antennas Wireless Propag. Lett.*, vol. 11, pp. 1418-1421, 2012.

[9] K. Rosengren, and P.-S. Kildal, "Radiation efficiency, correlation, diversity gain and capacity of a six-monopole antenna array for a MIMO system: Theory, simulation and measurement in reverberation chamber," *IEE Proc. Microw. Antennas Propag.*, vol. 152, pp. 7-16, 2005.

[10] G. le Fur, C. Lemoine, P. Besnier, and A. Sharaiha, "Performances of UWB wheeler cap and reverberation chamber to carry out efficiency measurements of narrowband antennas," *IEEE Antennas Wireless Propag. Lett.*, vol. 8, pp. 332-335, 2009.

[11] S. J. Boyes, P. J. Soh, Y. Huang, G. A. E. Vandenbosch, and N. Khiabani, "Measurement and Performance of Textile Antenna Efficiency on a Human Body in a Reverberation Chamber," *IEEE Trans. Antennas Propag.*, vol.61, no.2, pp. 871-881, Feb. 2013.

[12] M. V. Ivashina, M. N. M. Kehn, P.-S. Kildal, and R. Maaskant, "Decoupling efficiency of a wideband Vivaldi focal plane array feeding a reflector antenna," *IEEE Trans. Antennas Propag.*, vol. 57, no. 2, pp. 373-382, 2009.

[13] David M. Pozar, "Power dividers and directional couplers," in *Microwave Engineering*, 4th ed., 2011, Singapore: Wiley, pp. 317-379.

[14] [Online]. Available: http://uk.rs-online.com/web/p/products/2859551/?tpr=3. [Accessed: 04-Nov-2016].

[15] P. S. Kildal, X. Chen, C. Orlenius, M. Franzen, and C. S. L. Patane, "Characterization of Reverberation Chambers for OTA Measurements of Wireless Devices: Physical Formulations of Channel Matrix and New Uncertainty Formula," *IEEE Trans. Antennas Propag.*, vol. 60, no. 8, pp. 3875-3891, Aug. 2012.

[16] F. Moglie, and V. M. Primiani, "Analysis of the Independent Positions of Reverberation Chamber Stirrers as a Function of Their Operating Conditions," *IEEE Trans. Electromagn. Compat.*, vol. 53, no. 2, pp. 288-295, May 2011.

Chapter 7: Conclusions and Future Work

In this thesis, efficient measurement techniques in an RC have been discussed, including the efficient measurement of the averaged ACS with only one antenna, the rapid volume measurement method using the averaged ACS, the simplified SE measurement using the nested RC with two antennas, and the improved antenna array efficiency measurement in an RC. The efficient measurement is realized by using the enhanced backscatter effect or the robustness of the chamber decay time for averaged ACS, cavity volume, and SE measurement. And for the antenna array efficiency measurement, it has been pointed out the RC method is much more efficient than the conventional AC method. Our contribution is to make the measurement more accurate.

To be more specific, the ***key contributions*** in each chapter are summarized as follows:

Chapter 3: Averaged ACS measurement

The commonly used RC technique for determining the averaged ACS of a lossy object requires two antennas and the radiation efficiency of the two antennas should be known. In this chapter, the one-antenna method in both the frequency domain and the time domain was presented [1]. The measurement setup is greatly simplified and moreover, in the time domain, the knowledge of the antenna efficiency is not required. From the experimental results, it is found that the measured averaged ACSs by the three methods the conventional two-antenna method, the proposed frequency-domain one-antenna method, and the proposed time-domain one-antenna method are in good agreement. It is found that the time-domain method converges much faster than the frequency-domain methods because of the robustness of the chamber decay time (which is only determined by the diffuse loss of the chamber). A rapid and accurate measurement can be achieved in the time domain based on this finding by using source stirring technique. Furthermore, in the time-domain approach, the RC can be replaced by a suitable electrically large conducting cavity, which will further reduce the hardware requirement. The method was validated in the RC by setting the paddles stationary and the results agree well with that measured in the RC using mechanical stirring. It is demonstrated

that the time-domain method is much more efficient and its hardware requirement is much lower than the frequency-domain method.

Chapter 4: Cavity volume measurement using statistical EM theory

In this chapter, an efficient and effective method for measuring the volume of a large cavity is proposed [2]. A piece of RAM with a known averaged ACS is selected to aid the measurement. The cavity volume can be obtained by measuring its decay time constants with and without the RAM. Both the theory and measurement studies are conducted. It is found that the measurement can be completed rapidly with a simple measurement setup using the proposed method, which makes it an attractive method for the cavity volume measurement. Moreover, by using acoustic waves, the proposed method can be generalized and the cavity under test does not have to be metallic.

Chapter 5: SE measurement using nested RC

The conventional method for SE measurement of a physically small but electrically large cavity in an RC requires three antennas. And the efficiency of the two receiving antennas should be known. In this chapter, two-antenna methods for the SE measurement using the nested RC were proposed in both the frequency domain and the time domain [3]. The measurement setup is simplified and the measurement efficiency is improved. It is demonstrated that the measured SE using the proposed two-antenna methods and the conventional three-antenna method agrees well. The time-domain method converges much faster than the frequency-domain methods. Consequently, in the time domain, fast and accurate measurement can be realized by using the source stirring technique, which will result in fast SE measurement in reality. Furthermore, in the time-domain approach, by replacing the RC with a suitable conducting cavity (electrically large) and using the source-stir technique, the hardware requirement will be greatly reduced. The aforementioned measurement methods are compared. It is found that the time-domain method outperforms the frequency-domain method with much higher measurement efficiency and much lower hardware requirement.

Chapter 6: All-excited antenna array efficiency measurement

Chapter 6 proposes an improved measurement-based method to obtain the efficiency of an all-excited antenna array in an RC [4]. When measuring the efficiency of an antenna array in an RC, to make the array work in an "all-excited" manner, a power divider is normally employed to excite the feeding ports of the array elements simultaneously, that is, all the array elements are excited through a series of power dividers by merely a single excitation source. Thus, the efficiency measurement of the entire array can be effectively treated in a manner similar to a single port antenna, which would simplify the measurement procedure and reduce the overall measurement time. However, the introduction of the power divider will inevitably bring in insertion loss which needs to be quantified and calibrated out. The previous calibration method is correct when each element of the antenna array is well matched but not if some elements of the array antenna are mismatched. In this chapter, a new method to remove the insertion loss effect of the power divider by introducing attenuators between array elements and power divider ports was proposed. The attenuators would alleviate the reflection from the array antenna to the power divider and thus reduce the dissipated power on the power divider. Simulations and measurements have been done to validate the proposed method. The results show that this method is effective to measure the efficiency of an antenna array especially for an antenna array that some elements of it are not well matched. It is advantageous especially for wideband antenna arrays where good impedance matching of array elements is difficult to maintain.

There are also some possible ***future works*** related to this thesis:

Based on the conclusions drawn from above and taking into account the limitations of the work present in each chapter, future work can be carried out in the following area.

From Chapter 3, the calculation of the ACS requires the difference in the net power transfer function (in the frequency domain) or the chamber decay time (in the time domain) with and without the OUT. If the loss of the OUT is too small compared with that of the chamber itself, it will be very difficult for the chamber to distinguish the difference of the loss, which will result in the inaccuracy of the measurement. How to measure the ACS of a small OUT in a big RC is still a problem. Is there any method to improve the "sensitivity" of the RC? This work is still under investigation. Another possible future work may include the real

application of the proposed one-antenna method for, e.g., the measurement of the ACS of human bodies in the RC [5].

In Chapter 4, the condition of the proposed method is that the environment inside the cavity under test should be reverberant, i.e., the cavity should not be too lossy. How to realize a statistically uniform field inside a relatively lossy cavity is still a problem. Another issue is if the cavity is partially filled with liquid or dielectric materials either absorb or reflect waves completely (inhomogeneous cavity), the wave velocity is changed which could increase the measurement error [6]. How the inhomogeneous materials affect the results is still unknown. Finally, another possible extension of this work would be on-site measurement practice.

From Chapter 5, the assumption of the proposed method is that the EM field inside both the RC and the EUT is statistically uniform. What if the EUT is very lossy? When the EUT is very lossy, it is very difficult to stir the field inside the EUT well. Hence, the measured SE will be inaccurate. Another problem is when the EUT is shielded very well the power coupled from the RC into the EUT will be very small, even out of the VNA dynamic range sometimes. Under this circumstance, a power amplifier is probably required to measure the SE accurately. In this chapter, only a two-coupled-cavities scenario was considered. What will the results be for a multiple-couple-cavities scenario (i.e., three or more cavities coupled)? The relevant theory has been established in [7], but more practical investigations or applications are needed. The industrial applications of the proposed simplified methods for real reverberant environments such as the below-deck compartments in ships and aircraft cabins and bays are also possible future work [8].

In Chapter 6, the time-saving merit of the proposed method is advantageous especially for arrays of a large number of elements. For now, no verification of this method has been performed for such arrays, and it is left as a topic for future work.

References

[1] Z. Tian, Y. Huang, Y. Shen, and Q. Xu, "Efficient and Accurate Measurement of Absorption Cross Section of a Lossy Object in Reverberation Chamber Using Two One-Antenna Methods," *IEEE Trans. Electromagn. Compat.*, vol. 58, no. 3, pp. 686-693, Jun. 2016.

[2] Z. Tian, Y. Huang, Q. Xu, and Gaosheng Li, "A Rapid Method for Measuring the Volume of a Large Cavity Using Averaged Absorption Cross Section," *IEEE Access*, in revision.

[3] Z. Tian, Y. Huang, and Q. Xu, "Efficient Methods of Measuring Shielding Effectiveness of Electrically Large Enclosures Using Nested Reverberation Chambers with Only Two Antennas," *IEEE Trans. Electromagn. Compat.*, DOI: 10.1109/TEMC.2017.2696743.

[4] Z. Tian, Y. Huang, and Q. Xu, "An Improved Method for Efficiency Measurement of All-Excited Antenna Array in Reverberation Chamber Using Power Divider," *IEEE Trans. Antennas Propag.*, vol. 65, no. 6, pp. 3005-3013, Jun. 2017.

[5] I. D. Flintoft, G. C. R. Melia, M. P. Robinson, J. F. Dawson, and A. C. Marvin. "Rapid and accurate broadband absorption cross-section measurement of human bodies in a reverberation chamber," *Meas. Sci. Technol.*, vol. 26, no. 6, pp. 65701-65709, Jun. 2015.

[6] Q. Xu, Y. Huang, L. Xing, Z. Tian, Z. Fei, and L. Zheng, "A Fast Method to Measure the Volume of a Large Cavity," *IEEE Access*, vol. 3, pp. 1555-1561, 2015.

[7] G. B. Tait, R. E. Richardson, M. B. Slocum, M. O. Hatfield, and M. J. Rodriguez, "Reverberant Microwave Propagation in Coupled Complex Cavities," *IEEE Trans. Electromagn. Compat.*, vol. 53, no. 1, pp. 229-232, Feb. 2011.

[8] G. B. Tait, and M. B. Slocum, "Electromagnetic environment characterization of below-deck spaces in ships," in *Proc IEEE Int. Symp. on Electromagn. Compat.*, Detroit, MI, 2008, pp. 1-6.

Appendix A. Vector and Dyadic Analysis

In a rectangular coordinate, a general vector $\vec{A}$ can be written as

$$\vec{A} = \hat{x}A_x + \hat{y}A_y + \hat{z}A_z \tag{A.1}$$

where $(\hat{x}, \hat{y}, \hat{z})$ denotes the unit vector for the rectangular coordinate system.

Vector addition is defined as

$$\vec{A} + \vec{B} = \hat{x}(A_x + B_x) + \hat{y}(A_y + B_y) + \hat{z}(A_z + B_z) \tag{A.2}$$

Scalar multiplication or dot product is defined as

$$\vec{A} \cdot \vec{B} = A_x B_x + A_y B_y + A_z B_z \tag{A.3}$$

Vector multiplication or cross product is defined as

$$\vec{A} \times \vec{B} = \begin{vmatrix} \hat{x} & \hat{y} & \hat{z} \\ A_x & A_y & A_z \\ B_x & B_y & B_z \end{vmatrix} \tag{A.4}$$

The frequently used differential operators are the gradient ($\nabla\varphi$), divergence ($\nabla \cdot \vec{A}$), curl ($\nabla \times \vec{A}$), and Laplacian ($\nabla^2\varphi$). In a rectangular coordinate, the vector operator del (∇) is

$$\nabla = \hat{x}\frac{\partial}{\partial x} + \hat{y}\frac{\partial}{\partial y} + \hat{z}\frac{\partial}{\partial z} \tag{A.5}$$

and the differential operations are written as [1]

$$\nabla\varphi = \hat{x}\frac{\partial\varphi}{\partial x} + \hat{y}\frac{\partial\varphi}{\partial y} + \hat{z}\frac{\partial\varphi}{\partial z} \tag{A.6}$$

$$\nabla \cdot A = \hat{x}\frac{\partial A_x}{\partial x} + \hat{y}\frac{\partial A_y}{\partial y} + \hat{z}\frac{\partial A_z}{\partial z} \tag{A.7}$$

$$\nabla \times \vec{A} = \begin{vmatrix} \hat{x} & \hat{y} & \hat{z} \\ \dfrac{\partial}{\partial x} & \dfrac{\partial}{\partial y} & \dfrac{\partial}{\partial z} \\ A_x & A_y & A_z \end{vmatrix} \tag{A.8}$$

$$\nabla^2\varphi = \frac{\partial^2\varphi}{\partial x^2} + \frac{\partial^2\varphi}{\partial y^2} + \frac{\partial^2\varphi}{\partial z^2} \tag{A.9}$$

Vector identities exist for the following dot products, cross products, and differentiation [1] – [3]

$$\vec{A}\cdot\left(\vec{B}\times\vec{C}\right) = \vec{B}\cdot\left(\vec{C}\times\vec{A}\right) = \vec{C}\cdot\left(\vec{A}\times\vec{B}\right) \tag{A.10}$$

$$\vec{A}\times\left(\vec{B}\times\vec{C}\right) = \left(\vec{A}\cdot\vec{C}\right)\vec{B} - \left(\vec{A}\cdot\vec{B}\right)\vec{C} \tag{A.11}$$

$$\nabla(\varphi\psi) = \varphi\nabla\psi + \psi\nabla\varphi \tag{A.12}$$

$$\nabla\cdot\left(\varphi\vec{B}\right) = \varphi\nabla\cdot\vec{B} + \vec{B}\cdot\nabla\varphi \tag{A.13}$$

$$\nabla\times\left(\varphi\vec{B}\right) = \varphi\nabla\times\vec{B} - \vec{B}\times\nabla\varphi \tag{A.14}$$

$$\nabla\cdot\left(\vec{A}\times\vec{B}\right) = \vec{B}\cdot\nabla\times\vec{A} - \vec{A}\cdot\nabla\times\vec{B} \tag{A.15}$$

$$\nabla\cdot\left(\vec{A}\cdot\vec{B}\right) = \left(\vec{A}\cdot\nabla\right)\vec{B} + \left(\vec{B}\cdot\nabla\right)\vec{A} + \vec{A}\times\left(\nabla\times\vec{B}\right) + \vec{B}\times\left(\nabla\times\vec{A}\right) \tag{A.16}$$

$$\nabla\times\left(\vec{A}\times\vec{B}\right) = \vec{A}\nabla\cdot\vec{B} - \vec{B}\nabla\cdot\vec{A} - \left(\vec{A}\cdot\nabla\right)\vec{B} + \left(\vec{B}\cdot\nabla\right)\vec{A} \tag{A.17}$$

$$\nabla\cdot(\nabla\varphi) = \nabla^2\varphi \tag{A.18}$$

$$\nabla\cdot\left(\nabla\vec{A}\right) = \nabla^2\vec{A} \tag{A.19}$$

$$\nabla\times\left(\nabla\times\vec{A}\right) = \nabla(\nabla\cdot\vec{A}) - \nabla^2\vec{A} \tag{A.20}$$

$$\nabla\times(\nabla\varphi) = 0 \tag{A.21}$$

$$\nabla\cdot\left(\nabla\times\vec{A}\right) = 0 \tag{A.22}$$

Dyadic identities also exist for the following dot products, cross products, and differentiation [2]

$$\vec{A}\cdot\left(\vec{B}\times\overleftrightarrow{C}\right) = -\vec{B}\cdot\left(\vec{A}\times\overleftrightarrow{C}\right) = \left(\vec{A}\times\vec{B}\right)\cdot\overleftrightarrow{C} \tag{A.23}$$

$$\vec{A}\times\left(\vec{B}\times\overleftrightarrow{C}\right) = \vec{B}\cdot\left(\vec{A}\cdot\overleftrightarrow{C}\right) - \left(\vec{A}\cdot\vec{B}\right)\overleftrightarrow{C} \tag{A.24}$$

$$\nabla \cdot \left(\varphi \vec{C}\right) = \varphi \nabla \cdot \vec{C} + (\nabla \varphi) \cdot \vec{C} \quad \text{(A. 25)}$$

$$\nabla \times \left(\varphi \vec{C}\right) = \varphi \nabla \times \vec{C} + (\nabla \varphi) \times \vec{C} \quad \text{(A. 26)}$$

$$\nabla \times \left(\nabla \times \vec{C}\right) = \nabla\left(\nabla \cdot \vec{C}\right) - \nabla^2 \vec{C} \quad \text{(A. 27)}$$

$$\nabla \cdot \left(\nabla \times \vec{C}\right) = 0 \quad \text{(A. 28)}$$

Appendix B. Probability Density Function

For a random variable g, the probability that g lies within a small range between g and $g + dg$ can be written as $f(g)dg$. The function $f(g)$ is called the probability density function (PDF). Since probabilities cannot be negative, all PDFs must be positive or zero

$$f(g) \geq 0, \quad \text{for all } g \tag{B.1}$$

PDFs do not have to be continuous or even finite. However, since the random variable g must lie between -∞ and +∞, the following integral relationship must hold [4]

$$\int_{-\infty}^{\infty} f(g)dg = 1 \tag{B.2}$$

The mean value or ensemble average (normally designated μ) of g is $\langle g \rangle$ which can be determined from the following integral using the PDF

$$\mu = \langle g \rangle = \int_{-\infty}^{\infty} gf(g)dg \tag{B.3}$$

The variance (frequently designated as σ^2) of g is defined as $\langle (g-\mu)^2 \rangle$. It can also be determined from the PDF as

$$\langle (g-\mu)^2 \rangle = \sigma^2 = \int_{-\infty}^{\infty} (g-\mu)^2 f(g)dg \tag{B.4}$$

The standard deviation σ is the square root of the variance.

References

[1] R. F. Harrington, Time-Harmonic Electromagnetic Fields, 2nd Edition. New York: Wiley-IEEE Press, 2001.

[2] C. T. Tai, Dyadic Green Functions in Electromagnetic Theory. New York: IEEE Press, 1997.

[3] D. L. Sengupta, and V. V. Liepa, Applied Electromagnetics and Electromagnetic Compatibility. Hoboken, NJ: Wiley, 2006.

[4] D. A. Hill, Electromagnetic Fields in Cavities: Deterministic and Statistical Theories. New York, NY, USA: Wiley-IEEE Press, 2009.